**The Dissertation Committee for Alexander John Edward Rettie Certifies that this is the approved version of the following dissertation:**

# Metal Oxide Photoelectrodes for Solar Water Splitting

**Committee:**

Charles Buddie Mullins, Supervisor

Allen J. Bard

Simon M. Humphrey

Gyeong S. Hwang

Brian A. Korgel

# Metal Oxide Photoelectrodes for Solar Water Splitting

**by**

**Alexander John Edward Rettie, B.S.E.**

**Dissertation**

Presented to the Faculty of the Graduate School of

The University of Texas at Austin

in Partial Fulfillment

of the Requirements

for the Degree of

**Doctor of Philosophy**

**The University of Texas at Austin**

**August, 2015**

# Dedication

To my family

# Acknowledgements

Chiefly, I express my sincere appreciation to my supervisor, Prof. C. Buddie Mullins. Working with Buddie has been a joy, his steadfast support and spirit for collaboration has facilitated research that I am extremely proud of. I will emulate those qualities in my future career and if I am one tenth of the teacher he is, I'll be doing well.

I would like to thank the members of my committee for their input and guidance, especially Prof. Bard, who, with Hank Lee and Sean Berglund, piqued my interest in bismuth vanadate early on.

I have been so fortunate to have many wonderful collaborators during my time at UT. Together they have made this a transformative experience. Indeed this list is very long, so my apologies if anyone is missed out. Firstly, Drs. Luke Marshall and Jianshi Zhou helped me grow single crystals and taught me everything I know about fundamental property measurements. Dr. Zhou I am especially indebted to, as without the instruments in his lab, none of this work have been possible. Drs. John McCloy, Cigdem Capan and Tim Droubay were invaluable during my time at Pacific Northwest National Laboratory, another transformative experience. The written word cannot communicate my appreciation for Dr. Jeff Lindemuth at LakeShore Cryotronics. Jeff did the impossible in measuring takes the Hall effect in $BiVO_4$ and since has contributed many important measurements in our studies of metal oxides. Additionally I acknowledge Prof. Afu Lin for the use of his Raman system and lively discussions, Shirin Mozaffari and Prof. John Markert for use of their pulsed laser deposition system and Drs. DJ McDaniel and Agham Posadas who taught me a great deal about epitaxial thin films.

I was lucky to be surrounded by many talented and bright people in the Mullins' research group. I am indebted to Drs. Nathan Hahn, Sean Berglund, Son Hoang, Paul Abel and Yong Mao Lin for listening to my questions and setting the bar high. I thank Paul personally for his love of cycling and excellent coffee (coffee in general perhaps deserves a place in these acknowledgments). Many Bard group members deserve thanks: Hank Lee, Hyun Park, David Eisenberg and Ben Meekins to name a few.

My colleagues in the group, Will Chemelewski, Kyle Klavetter, Greg Mullen, Wen-Yueh Yu, Adrian Brush, Hoang Dang and Sean Wood have all aided this work and have extremely bright futures. Of special note, working with Will and Dr. Emin to understand small polarons has been a highlight of my career so far, may the journey continue. Additional thanks goes to my undergraduate research assistants, Ashioma Ishiekwene, Susanna Beal, Heather Bolton and Kristen Pearson for their tireless work on my half-thought-out ideas.

Finally, I thank my family and friends in Austin (and abroad). Your support means everything and my successes are yours as well.

# Metal Oxide Photoelectrodes for Solar Water Splitting

Alexander John Edward Rettie, Ph.D.

The University of Texas at Austin, 2015

Supervisor: Charles Buddie Mullins

Efficient solar water splitting – using sunlight to produce hydrogen from water – has been an ambitious goal of the scientific community for over 40 years. At its heart this is a materials problem, with the photoelectrodes used in a photoelectrochemical cell having to satisfy all the constraints of a photovoltaic material (light absorption, charge transport) as well as being stable in water and having appropriately positioned band edges. Of the metal oxide systems studied for this purpose, we identified iron oxide (hematite, $\alpha$-$Fe_2O_3$), tungsten trioxide ($WO_3$) and an emerging (at the time) material, bismuth vanadate ($BiVO_4$) as the most promising. In this dissertation we sought to understand and address the shortcomings of these materials, namely, carrier transport in $BiVO_4$ and $\alpha$-$Fe_2O_3$ and light absorption in $WO_3$.

We synthesized high quality single crystals of undoped and Mo and W-doped $BiVO_4$ using the floating zone technique and carried out fundamental transport measurements. Electrons were shown to form small polarons and the Hall effect mobility was low, $\sim 10^{-1}$ $cm^2$ $V^{-1}$ $s^{-1}$ at 300 K. Critically, the mobility measured by the Hall effect may be vastly different from the drift mobility. Small-polaron hopping was found to be in the adiabatic regime and anisotropic conductivity was related to the structural arrangement of vanadium ions.

Electrons are also thought to form small polarons in α-$Fe_2O_3$, but a thorough analysis had not been performed. We grew single crystals of Ti:α-$Fe_2O_3$ and characterized their electron transport to evaluate this model and probe the large anisotropy thought to occur between the basal planes. These revealed that the adiabatic small-polaron model was appropriate**.** Interestingly, electron transport in Ti:α-$Fe_2O_3$ was shown to be near-isotropic, contradicting the common view in the literature.

Finally, we studied the effects of sulfur or iodine incorporation in $WO_3$ with the aim to improve its visible light harvesting ability. Both of these impurities did increase visible light absorption, but performance was degraded in all cases except for very low concentrations of sulfur doping. These impurities likely form inter-gap defect bands which allow the absorption of longer wavelength light, but also degrade transport properties if present in large amounts.

# Table of Contents

# List of Tables

# List of Figures

# Chapter 1: Introduction

## 1.1 Energy Problem

Humankind's extensive use of fossil fuels has heralded unprecedented advances over the last century. This extensive, ever increasing use is also the reason we need sources of clean, sustainable energy. Without them, we will run out of fuel, and do irreparable harm to our planet in the process. Currently, ~15 TW of power is consumed on earth every year, and demand is estimated to grow to 30 TW by 2050 due to population growth and modernization [1]. Our future energy portfolio must include terawatt-scale, sustainable resources such as wind, hydroelectric, tidal, nuclear and solar power in addition to fossil fuels.

Out of these alternatives, only solar energy is plentiful enough to meet our future energy demands [2]. However, the sun is an intermittent energy source and large scale storage is a major obstacle. One solution to this problem is to store solar energy in chemical fuels, such as hydrogen, with the most elegant method being directly splitting water into hydrogen and oxygen using sunlight. This process has been termed "solar water splitting" [3].

Water splitting is comprised of two half reactions; the reduction of protons and the oxidation of water, shown in equations 1.1and 1.2 respectively (RHE: reference $H_2$ electrode):

$$4H^+ (aq) + 4e^- \rightleftharpoons 2H_2 (g) \qquad E_0 = +0.00\ \text{V vs. RHE} \qquad (1.1)$$

$$2H_2O (l) + 4h^+ \rightleftharpoons 4H^+ (aq) + O_2 (g) \qquad E_0 = +1.23\text{V vs. RHE} \qquad (1.2)$$

The Gibbs free energy for the overall water splitting reaction is +237 kJ $mol^{-1}$ (1.23 eV). It should be noted that this value represents the thermodynamic *minimum* energy for the reaction to proceed. In practice, overpotentials and system losses must be overcome to evolve $H_2$ and $O_2$ at appreciable rates, setting this energy requirement closer to ~1.8 eV [4].

## 1.2 PHOTOELECTROCHEMICAL CELLS

The most practical configuration to accomplish water splitting today would be to couple a solar cell to an electrolyzer. This is a baseline to which all other water splitting technologies should be compared. With existing technologies, this configuration results in a cost greater than $8/kg of $H_2$ [1], far above the $2-4/kg target set by the Department of Energy [5]. The photoelectrochemical (PEC) systems discussed here have two main advantages over the solar cell-electrolyzer pairing:

1) Higher potential efficiency. The large current density (~1 A $cm^{-2}$), and hence, the overpotential required for commercial electrolyzers limits the efficiency of these devices to ~65%. In contrast, efficient PEC systems would operate between 10 and 30 mA $cm^{-2}$.
2) Lower capital cost. Integration of light absorption and water electrolysis into a single device would have a lower physical footprint and no need for the intermediate power conversion devices between the solar array and electrolyzer.

We will discuss photoelectrochemical (PEC) cells in this dissertation, but we should briefly mention suspended photocatalyst powder systems. These have definite cost

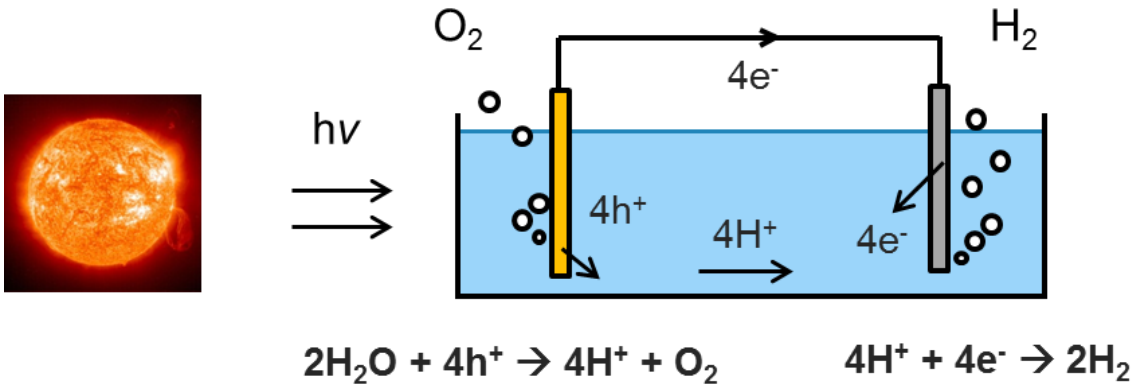


**Figure 1.1:** Cartoon of PEC cell with a photoanode (yellow) and metal cathode (grey).

advantages PEC cells [6], but severe challenges in achieving necessary efficiencies, preventing parasitic back reactions and the mixing of explosive gases remain. At this time, we believe the PEC cell arrangement holds the most promise.

PEC cells use one or two semiconducting electrodes to split water. Several configurations are possible, but for simplicity a system consisting of a n-type photoanode and metal cathode immersed in electrolyte will be discussed initially (Figure 1.1).

When photons with energy greater than the band gap of the semiconductor are absorbed they excite an electron from the valence band to the conduction band, generating an electron-hole pair (Figure 1.2). In a PEC cell we wish to use this charge in equations 1.1 and 1.2, driving electrons to the surface of the cathode, and holes to the surface of the anode.

This is aided by the formation of an electric field at the semiconductor-electrolyte interface due to the difference in electrochemical potential, termed the depletion layer (Fig. 1.2 Region I). Carriers that are generated in, or are able to diffuse to this region are

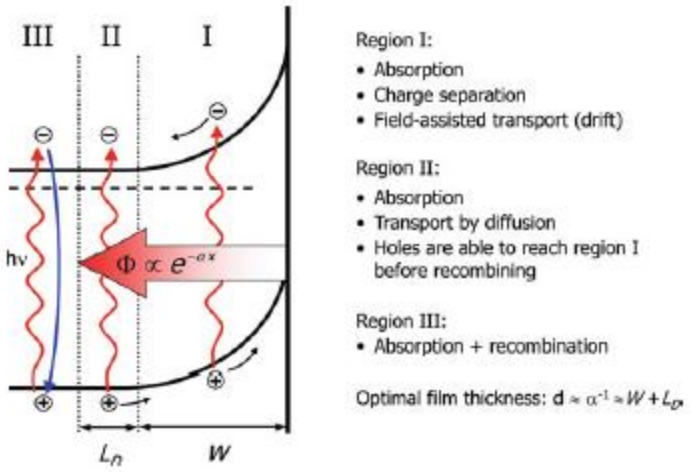


**Figure 1.2:** Energy diagram of light absorption and carrier fate in an n-type photoanode [1]. ϕ: light intensity, α: absorption coefficient, *W*: depletion width and $L_D$: diffusion length

efficiently separated and can be used to split water. In contrast, electron-hole pairs that are generated in the bulk material have a high probability of recombining (Fig. 1.2 Region III). Finally, once carriers reach the interface they must overcome kinetic limitations associated with the reactions in equations 1.1 and 1.2.

A solar to hydrogen conversion efficiency of ~10 % and lifetime of 10 years have been suggested for practical deployment [7]. High efficiency cells based on $GaInP_2$ and GaAs have been demonstrated [8], but are expensive to fabricate and unstable in aqueous electrolytes. This has motivated the search for efficient metal oxide photoelectrode materials, which have the potential to be cheap and stable. In order to produce hydrogen efficiently, potential semiconductors must meet the following stringent criteria:

- Absorb a majority of the visible spectrum
- Band edges suitably positioned for proton reduction and/or water oxidation
- Good charge transport properties

- Relative abundancy
- Long term stability in aqueous electrolyte
- Fast kinetics for the reaction(s) of interest

Two recent developments have softened these requirements somewhat. Detailed modeling of PEC systems indicate that a single photoelectrode is unlikely to achieve the required 10% solar to hydrogen efficiency required for commercialization [4,9-11]. A tandem cell, where both a photoanode and photocathode are employed has the advantages of potential higher efficiencies and allows us to separately optimize photoelectrodes for water oxidation and proton reduction. Thus, we can focus on materials for either half reaction with respect to band edge positions and stability.

Additionally, earth abundant electrocatalysts based on cobalt [12,13], iron [14] and nickel [15] have been recently developed that are far superior for the oxygen evolution reaction compared to bare metal oxide surfaces and can be deposited on the photoelectrode with minimal blocking of incident light. Light absorption, band edge positions and charge transport requirements are therefore the most salient when evaluating new photoelectrode materials. As water oxidation is a four electron process, it requires greater overpotentials than the hydrogen evolution reaction and consequently limits the overall efficiency of the PEC cell. Hence, we have focused on the photoanode.

### 1.3 METAL OXIDE PHOTOELECTRODES

Metal oxides satisfy both the stability and abundance criteria better than traditional photovoltaic materials. As they cannot be oxidized further, they are particularly well suited as photoanodes. The most studied metal oxides for this purpose

| | $TiO_2$ | $\gamma$-$WO_3$ | $\alpha$-$Fe_2O_3$ | $BiVO_4$ |
|---|---|---|---|---|
| Band gap (eV) | 3.0/3.2 | 2.7 | 2.1 | 2.5 |
| Charge Transport | Medium/Good | Good | Poor | Poor |
| Conduction Band edge (V vs. RHE) | ~0.2/0 | ~0.4 | ~0.4 | ~0.1 |

**Figure 1.3:** General properties of widely studied photoanodes. The two values for $TiO_2$ refer to the rutile/anatase polymorphs.

are titanium dioxide ($TiO_2$), tungsten trioxide ($WO_3$), iron oxide ($\alpha$-$Fe_2O_3$) and bismuth vanadate ($BiVO_4$). Their strengths and weaknesses are summarized in Figure 1.3. It should be noted that, at the time of writing, no material fully satisfies all the constraints for a photoanode material listed in the previous section. Our approach was to identify the most promising photoanodes and investigate their limitations, with the aim to mitigate them.

In the cases of $BiVO_4$ and $\alpha$-$Fe_2O_3$, bulk charge transport is limiting and poorly understood. In order to meaningfully probe charge transport, model systems such as bulk single crystals (Chapters 2, 3 and 5) or epitaxial thin films (Chapter 4) are needed so that the data can be simply interpreted, i.e. without the confounding effects of grain boundaries. In the case of $WO_3$, visible light absorption was limiting and therefore dopants that might increase the visible light harvesting ability were investigated (Chapter

6). As it is central to the work on BiVO4 and α-$Fe_2O_3$ presented in this dissertation, the remainder of this chapter will focus on small-polaron transport and experimental characterization of small-polaron conductors.

## 1.4 SMALL POLARONS

All charge carriers in solids interact to some degree with the lattice they travel through. The degree of this interaction distinguishes free carrier (fast) and polaronic (slow) transport and the severity of the localization between large (slow) and small-polaron (slowest) transport. A polaron is defined as a carrier and its associated lattice distortion as illustrated in Figure 1.4. When the carrier moves slowly and the lattice is easily polarizable, strong localization of the carrier may be favorable and it becomes self-trapped. The carrier is then confined to a site usually less than a unit cell distance. Alternatively stated, small-polaron formation is favorable when the energy gained by the lattice due to localization of the carrier (the binding energy) exceeds the strain caused by the accompanying lattice deformation [16]. These conditions are satisfied in materials with narrow transport bands, i.e. carriers with large effective masses, and large dielectric constants. These strongly localized carriers require thermal energy to move from site to site, via a so-called "thermally-activated hopping mechanism". Transport in these materials is characterized by a thermally activated drift mobility that is extremely small: $<< 1\ cm^2\ V^{-1}\ s^{-1}$. By contrast, large polarons have an accompanying lattice distortion that is spread over many sites, a drift mobility that is moderate in size and decreases with increasing temperature [17]. Small polarons have been observed in metal oxides [18-20], amorphous [21-23] and organic semiconductors [24,25], even dry DNA [26]!

Small polarons belong to the theoretical physicists. While the theory is relatively well developed, difficulties in measuring low mobility, highly resistive compounds mean experimental studies and robust analysis of real materials is lacking. Of particular note is a chapter by Nagels [19] where the transport of reduced $LiNbO_3$ is systematically analyzed in the context of the small-polaron models developed by Holstein, Friedman and Emin. This text lays the foundation for how small-polaron conductors should be analyzed experimentally, though we note that a calculation error led the author to conclude that hopping is in the non-adiabatic regime. Generally, non-adiabatic hopping requires transfer integrals that are too small to be physical in real materials, except at low temperatures.

Full transport characterization of small-polaron conductors requires that the conductivity, Seebeck coefficient and Hall effect be measured versus temperature. Additionally, optical measurements can be utilized to distinguish between large and small polarons.


**Figure 1.4:** Cartoon of the distortion arising from a carrier trapped in a polarizable lattice.

### 1.4.1 Conductivity

Electronic transport studies should start with conductivity, $\sigma$ (or its reciprocal, resistivity, $\rho$) measurements. These experiments will inform aspects of other transport

measurements such as the Seebeck and Hall effects e.g. Ohmic contacts, the magnitude of the sample resistance, metallic or semiconducting behavior. Clearly, the sample geometry will affect the raw values of resistance, as will the nature of the electrical contact. Four point conductivity, either van der Pauw [27] or collinear geometries should be used, shown in Figure 1.5, so that contact resistances are removed. Even in highly resistive samples ($R_{2pt}$ > 1 MΩ), the contact resistance can dominate two-point measurements, obscuring the material's true conductivity. Ohmic contact, i.e. current being linear with voltage to the sample over the measurement range are essential for conductivity measurements. This is determined by the type of junction created at the metal-semiconductor interface [28]. In general, low work function metals such as Ag, Ti, In or InGa eutectic are suitable for n-type semiconductors, and vice versa for p-type semiconductors where Au or Pd are most appropriate. Even when the work function difference predicts an Ohmic contact, a poor interface or reaction between the sample and the contact material can lead to non-Ohmic behavior. Making robust contacts is a true art and the literature should be your starting point when you first start making contacts to a new material.

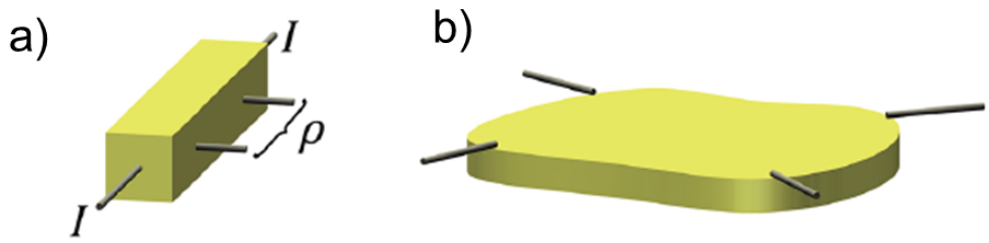


**Figure 1.5:** Contact geometries for conductivity measurements. a) 4-point collinear contacts on a bar-shaped sample. b) van der Pauw (vdP) contacts on the periphery of a thin sample of arbitrary shape. Modified from ref 29.

A prerequisite for small-polaron conduction is a temperature-activated conductivity. In an n-type semiconductor the electronic conductivity is given in equation 1.3:

$$\sigma = ne\mu_d \qquad (1.3)$$

where $n$ is the carrier concentration, $e$ is the elementary charge and $\mu_d$ is the electron drift mobility. Looking at equation 1.3, a temperature dependent conductivity can be due to a strong temperature dependence of the carrier concentration or the drift mobility. Complimentary transport experiments must be performed to decouple these variables. The temperature-activated conductivity is given by equation 1.4,

$$\sigma(T) = \sigma_0(T)exp\left(-\frac{E_\sigma}{\kappa T}\right) \qquad (1.4)$$

where $E_\sigma$ is the conductivity activation energy and $\kappa$ is the Boltzmann constant.

The key parameters and are obtained by plotting ln($\sigma T$) vs. reciprocal temperature. This should yield a linear fit, with the slope being $E_\sigma$ and the $y$-intercept yielding the pre-factor multiplied by the absolute temperature: $\sigma_0 T$. Comparison of $\sigma_0$ with should be in agreement with calculated values for simple adiabatic small polaron hopping:

$$\sigma_0 = \frac{ne^2a^2v_0}{\kappa T} \qquad (1.5)$$

where $a$ is the hopping distance and $v_0$ is the characteristic phonon frequency. Additional phenomena can lead to a much larger measured value for the pre-factor, such as carrier-induced softening [30,31]. A measured pre-factor that is much lower than that calculated from equation 1.5 implies that the non-adiabatic regime may be valid [18].

### 1.4.2 Seebeck Coefficient

When a temperature gradient is applied to a metal or semiconductor, a voltage is established due to the thermoelectric effect. Simply, this is the migration of majority carriers from the hot end to cold end of the sample. The Seebeck coefficient. *S* is this voltage divided by the temperature gradient:

$$S = \frac{\Delta V}{\Delta T} \qquad (1.4)$$

where, $\Delta V$ is the thermoelectric voltage and $\Delta T$ is the temperature difference. The Seebeck coefficient is often called the thermoelectric power or thermopower in older publications.

For metals, *S* is small; < 86 μV $K^{-1}$, while for semiconductors and insulators it may be hundreds of μV $K^{-1}$. This is because the Seebeck coefficient is generally due to the change in the entropy of mixing when a carrier is added. Intuitively, a metal has many carriers, so the relative change upon carrier addition is small. Conversely, the relative change when adding a carrier to insulator may be very large, hence a large Seebeck coefficient is produced.

Many sample geometries are used for measuring *S* (Figure 1.6) and all have their drawbacks.[29] In general, uncertainties of ± 5-10% in *S* are usual and should be kept in mind when calculating carrier concentrations and activation energies. Ohmic contacts should be used and the thermoelectric voltage should be linear with temperature gradient. It is by its nature a relative measurement and contributions from the voltage sensing wires must be taken into account. Because of this, metals such as copper and gold are typically used as they have very small Seebeck coefficients.

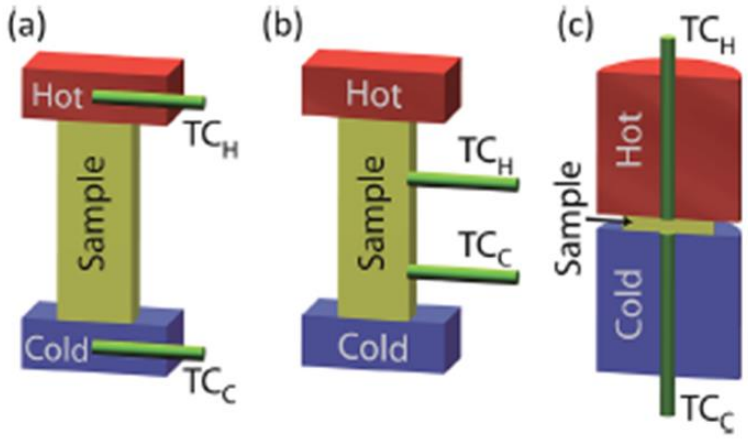


**Figure 1.6:** Various geometries for Seebeck coefficient measurements. TC: thermocouple, where H and C denote hot and cold. Modified from ref 29.

Firstly the magnitude and sign of the Seebeck coefficient should be considered. The sign of the Seebeck voltage unambiguously gives the character of the majority carriers in the material: negative for electrons and positive for holes. Principally the Seebeck coefficient gives insight into the carrier concentration of the sample and, in conjunction with the conductivity, the carrier mobility as discussed in Section 1.4.1.

Compared to the conductivity, the thermopower is considerably more complex to interpret. The Seebeck coefficient for transport in a single, infinitely narrow small polaron band can be described by equation 1.5.

$$S = -\frac{\kappa}{e}\left(\frac{E_S}{\kappa T} + A\right) \qquad (1.5)$$

where $E_S$ is the Seebeck coefficient activation energy and $A$ is the heat of transport constant. $A$ is related to the steepness of the onset of the density of transport states, with a large value of $A$ (>1) in agreement with narrow transport bands. It should be noted that while $E_\sigma > E_S$ is consistent with small-polarons being the charge carriers, a Seebeck

coefficient that increases with increasing temperature does not rule out the carriers being small polarons, but hints that effects other than carrier generation determine the magnitude of *S*. $E_\sigma$ is equal to $E_a$,+ $E_S - t$, where $t$ is the transfer integral. Assuming $t$ to be small, $E_a$ is simply the difference between $E_\sigma$ and $E_S$. From these measured values the drift mobility may be estimated via the relation,

$$\mu_d = \frac{ea^2 v_0}{\kappa T} exp\left(-\frac{(E_\sigma - E_S)}{\kappa T}\right) \qquad (1.6)$$

Assuming adiabatic small-polaron hopping model to be valid, the y-intercept of $\ln(\mu_d)$ vs. $1/T$ is 1 $cm^2$ $V^{-1}$ $s^{-1}$. This analysis yields an estimate of the drift mobility from conductivity and Seebeck coefficient measurements alone. Additionally, the Seebeck coefficient for transport in a single, infinitely narrow band in the high temperature limit is given by:[17]

$$S = \frac{\kappa}{e} ln\left(\frac{1-c}{c}\right) \qquad (1.7)$$

where $c = n/N$, and $N$ is the density of thermally accessible transport states.

### 1.4.3 Hall Effect

The Hall effect is a classic semiconductor characterization experiment, occasionally termed "the Queen of transport measurements" [32] due to its near universal use in characterizing the carrier mobilites in wide band semiconductors such as Si, Ge, GaAs etc. Essentially, it measures the deflection of majority carriers in a magnetic field. Note that this phenomenon has no fundamental relationship to the velocity of carriers under an electric field: the drift mobility. Rather, in wide band semiconductors, solution of the Boltzmann transport equation conveniently results in these two quantities being

comparable [33]. In small-polaron conductors, where transport takes place in narrow bands, the situation is very different. Indeed, the Hall effect mobility, $\mu_{Hall}$ can differ from the drift mobility in magnitude, temperature dependence and even sign! These differences are in fact, indicators for the presence of small-polaronic carriers.

The Hall effect in these materials is instead strongly related to the hopping site geometry. Only the cases of triangular [34,35] and square [36] geometries have been treated theoretically. If the hopping geometry is more complex, it is more valuable to use the general features to support or rule out the assignment of small-polaron hopping.

The magnetic field is applied perpendicular to current flow to a sample with vdP contact configuration as in Figure 1.5b or with more complex 5- or 6-contact arrangements [29]. The applied field can be static or alternating current (AC). The AC field Hall effect has the advantage being able to discern the very small Hall voltages found in low mobility materials [37,38].

### 1.4.4 Optical Properties

Small polarons also possess distinct optical properties. An absorption event is due to the excitation of the trapped carrier to a higher energy state. This state is typically another ion, hence absorption events are equivalent to small-polaron hops [17]. This small-polaron absorption results in a broad band centered around $4E_a$ that broadens with increasing temperature. The optical spectra of materials (usually in the near to mid-IR) can be used to distinguish between small, large and bi-polarons [39].

## REFERENCES


(1) van de Krol, R.; Grätzel, M. *Photoelectrochemical Hydrogen Production*, 2012.

(2) Lewis, N. S.; Nocera, D. G. *Proceedings of the National Academy of Sciences* **2006**, *103*, 15729.

(3) Walter, M. G.; Warren, E. L.; McKone, J. R.; Boettcher, S. W.; Mi, Q.; Santori, E. A.; Lewis, N. S. *Chemical Reviews* **2010**, *110*, 6446.

(4) Seitz, L. C.; Chen, Z.; Forman, A. J.; Pinaud, B. A.; Benck, J. D.; Jaramillo, T. F. *ChemSusChem* **2014**, *7*, 1372.

(5) James, B. D.; Baum, G. N.; Perez, J.; Baum, K. N. *DOE Report* **2009**.

(6) Pinaud, B. A.; Benck, J. D.; Seitz, L. C.; Forman, A. J.; Chen, Z.; Deutsch, T. G.; James, B. D.; Baum, K. N.; Baum, G. N.; Ardo, S. *Energy & Environmental Science* **2013**, *6*, 1983.

(7) Bard, A. J.; Fox, M. A. *Acc. Chem. Res.* **1995**, *28*, 141.

(8) Khaselev, O.; Turner, J. A. *Science* **1998**, *280*, 425.

(9) Weber, M. F.; Dignam, M. *International Journal of Hydrogen Energy* **1986**, *11*, 225.

(10) Weber, M. F.; Dignam, M. J. *Journal of the Electrochemical Society* **1984**, *131*, 1258.

(11) Bolton, J. R.; Strickler, S. J.; Connolly, J. S. *Nature* **1985**, *316*, 495.

(12) Reece, S. Y.; Hamel, J. A.; Sung, K.; Jarvi, T. D.; Esswein, A. J.; Pijpers, J. J.; Nocera, D. G. *Science* **2011**, *334*, 645.

(13) Zhong, D. K.; Choi, S.; Gamelin, D. R. *J. Am. Chem. Soc.* **2011**, *133*, 18370.

(14) Chemelewski, W. D.; Lee, H.-C.; Lin, J.-F.; Bard, A. J.; Mullins, C. B. *J. Am. Chem. Soc.* **2014**, *136*, 2843.

(15) Kim, T. W.; Choi, K.-S. *Science* **2014**, *343*, 990.

(16) Kweon, K. E.; Hwang, G. S.; Kim, J.; Kim, S.; Kim, S. *Phys. Chem. Chem. Phys.* **2014**, *advance online publication*.

(17) Emin, D. *Polarons*; 1st ed.; Cambridge University Press: New York, 2013.

(18) Jaime, M.; Hardner, H.; Salamon, M.; Rubinstein, M.; Dorsey, P.; Emin, D. *Phys. Rev. Lett.* **1997**, *78*, 951.

(19) Nagels, P. In *The Hall Effect and Its Applications*; Springer: 1980, p 253.

(20) Zhao, B.; Kaspar, T. C.; Droubay, T. C.; McCloy, J.; Bowden, M. E.; Shutthanandan, V.; Heald, S. M.; Chambers, S. A. *Phys. Rev. B* **2011**, *84*, 245325/1.

(21) Emin, D.; Seager, C.; Quinn, R. K. *Phys. Rev. Lett.* **1972**, *28*, 813.

(22) Sayer, M.; Mansingh, A. *J. Non-Cryst. Solids* **1983**, *58*, 91.

(23) Baily, S. A.; Emin, D. *Phys. Rev. B* **2006**, *73*, 165211.

(24) Yoo, K.-H.; Ha, D.; Lee, J.-O.; Park, J.; Kim, J.; Kim, J.; Lee, H.-Y.; Kawai, T.; Choi, H. Y. *Phys. Rev. Lett.* **2001**, *87*, 198102.

(25) Venkateshvaran, D.; Nikolka, M.; Sadhanala, A.; Lemaur, V.; Zelazny, M.; Kepa, M.; Hurhangee, M.; Kronemeijer, A. J.; Pecunia, V.; Nasrallah, I.; Romanov, I.; Broch, K.; McCulloch, I.; Emin, D.; Olivier, Y.; Cornil, J.; Beljonne, D.; Sirringhaus, H. *Nature* **2014**, *advance online publication*.

(26) Alexandre, S. S.; Artacho, E.; Soler, J. M.; Chacham, H. *Phys. Rev. Lett.* **2003**, *91*, 108105.

(27) Van der Pauw, L. *Philips Technical Review* **1958**, *20*, 220.

(28) Streetman, B. G.; Banerjee, S. *Solid state electronic devices*; 6th ed.; Prentice Hall New Jersey, 2006.

(29) Borup, K. A.; de Boor, J.; Wang, H.; Drymiotis, F.; Gascoin, F.; Shi, X.; Chen, L.; Fedorov, M. I.; Müller, E.; Iversen, B. B. *Energy & Environmental Science* **2015**, *8*, 423.

(30) Emin, D. *Monatshefte für Chemie-Chemical Monthly* **2013**, *144*, 3.

(31) Emin, D. *Phys. Rev. Lett.* **2008**, *100*, 166602.

(32) Nagaosa, N.; Sinova, J.; Onoda, S.; MacDonald, A.; Ong, N. *Reviews of Modern Physics* **2010**, *82*, 1539.

(33) Emin, D. In *The Hall Effect and Its Applications*; Springer: 1980, p 281.

(34) Emin, D.; Holstein, T. *Ann. Phys.* **1969**, *53*, 439.

(35) Friedman, L.; Holstein, T. *Ann. Phys.* **1963**, *21*, 494.

(36) Emin, D. *Ann. Phys.* **1971**, *64*, 336.

(37) J. Lindemuth and S.-I. Mizuta, presented at the SPIE Solar Energy + Technology, 2011 (unpublished)

(38) J. Lindemuth, A. J. Rettie, L. G. Marshall, J. Zhou, and C. B. Mullins, presented at the MRS Proceedings, 2014 (unpublished).

(39) Emin, D. *Phys. Rev. B* **1993**, *48*, 13691

.

# Chapter 2: Combined Charge Carrier Transport and Photoelectrochemical Characterization of $BiVO_4$ Single Crystals[1]

## 2.1 INTRODUCTION

Photoelectrochemical (PEC) water splitting has great potential as a route to renewable hydrogen production using solar energy [1,2]. However, a lack of efficient, inexpensive and stable photoelectrodes inhibits this technology. Metal oxides are promising candidate materials due to their stability and relative abundance, but often have poor light absorption and charge transport properties. Pertinent examples of metal oxide photoelectrode materials include titania ($TiO_2$ [3]), hematite ($\alpha$-$Fe_2O_3$ [4]), and tungsten oxide ($WO_3$ [5]). In the continuing search for higher efficiencies, complex metal oxides – having two or more cations – are coming to the forefront of this field.

Monoclinic bismuth vanadate ($BiVO_4$) is one such promising material for water oxidation [6-8]. It is attractive due to its direct band gap of ~2.4 eV, favorably positioned band edges and stability when coupled with co-catalysts. The monoclinic structure ("clinobisvanite") is the most common at ambient conditions and has also been shown to be the most photocatalytically active [9]. The crystal is a slightly distorted tetragonal scheelite structure, which converts to an undistorted scheelite structure with temperature [10], pressure [11] or the addition of dopants [12]. Recently, polycrystalline $BiVO_4$

[1] A.J.E. Rettie, H.C. Lee, L.G. Marshall, J.-F. Lin, C. Capan, J. Lindemuth, J.S. McCloy, J. Zhou, A.J. Bard, C.B.Mullins. "Combined Charge Carrier Transport and Photoelectrochemical Characterization of $BiVO_4$ Single Crystals: Intrinsic Behavior of a Complex Metal Oxide", *J. Am. Chem. Soc*., **2013**, 135 (30), pg 11389.
A. J. E. Rettie, L. G. Marshall and J.-S. Zhou synthesized the single crystal samples, A. J. E. Rettie and H.C. Lee performed electrochemistry experiments and A. J. E. Rettie, C. Capan, J. Lindemuth, and J.S. McCloy performed transport measurements. J.-F. Lin aided in Raman spectroscopy experiments. A. J. E. Rettie, H.C. Lee, A. J. Bard and C. B. Mullins designed the project. All authors wrote and revised the manuscript.

photoelectrodes singly doped with molybdenum (Mo) [13-16], tungsten (W) [15,17-19], or co-doped with Mo/W [20,21], have led to increased efficiencies and thus motivated us to perform a fundamental study of the electrical properties of this system using well characterized single crystals.

In 1979, Sleight et al. first made synthetic single crystals of $BiVO_4$ using the Czochralski technique [22]. Additionally, Hoffart et al. measured the conductivity of $BiVO_4$ single crystals at high temperatures (550-700 °C) where the tetragonal scheelite phase is dominant and conduction is primarily ionic [23]. Several investigations of conduction in polycrystalline samples have been performed [24-28], but variation in syntheses and grain boundary effects limit general application of these results. Determinations of carrier properties, such as mobility and diffusion length, are inherently difficult, as most metal oxides are highly electrically resistive at temperatures applicable to PEC cell operation (room temperature to 100 °C for aqueous electrolytes).

The aim of this study was to measure the intrinsic electrical properties of $BiVO_4$. To the best of our knowledge, this is the first report of doped $BiVO_4$ single crystals. Once these crystals were obtained, they were oriented and either characterized electrically or used as photoelectrodes. The term “doping” will be used in this paper to describe the addition of impurities to change a material’s electrical properties, without the formation of secondary phases.

Crystal phase and composition were studied using X-ray diffraction, inductively coupled plasma mass spectrometry and Raman spectroscopy. Electrical properties were obtained by measuring resistivity and the Hall effect as functions of temperature. Oriented samples were used to probe potential anisotropy. Finally, the behavior of the crystals as photoelectrodes under illumination, Mott-Schottky analyses and estimation of the hole diffusion length using the Gärtner model were performed.

## 2.2. EXPERIMENTAL METHODS

### 2.2.1 Single crystal synthesis

Starting ceramic powders were made by a solid state reaction of $Bi_2O_3$ (99.999%, Sigma-Aldrich), $V_2O_5$ (99.6%, Sigma-Aldrich), $MoO_3$ (99.95%, Alfa Aesar) and $WO_3$ (99.99%, Kurt J. Lesker). After mixing in an agate mortar, these mixtures were calcined first at 600°C for 10 hrs before further reaction at 900°C for 10 hrs in air with intermediate mixing. Mo and W were added based on the chemical formula,

$$Bi_{1-x/3}\,\emptyset_{x/3}V_{1-x}M_xO_4 \qquad (2.1)$$

where ∅ = Bi vacancies and M = Mo or W [12,29].

Single crystals were grown using an infrared-heating image furnace (NEC SC-M35HD). The ceramic powders were isostatically pressed to form the feed and seed rods before a final annealing step of 700 °C for 10 hrs. A slight excess of V (Bi:V = 48:52 at.%) was added to these powders to account for volatilization losses [23]. The feed and seed rods were counter-rotated at 30 rpm in a static $O_2$ atmosphere of 1.8 atm during the growth. Typical growth rates were between 1-3 mm $hr^{-1}$. In some cases, the feed rods were pre-melted prior to growth to suppress bubble formation in the melt zone.

### 2.2.2 Composition

Powder X-ray diffraction (XRD) was performed using a Philips X'Pert diffractometer equipped with monochromatic Cu Kα x-rays ($\lambda$ = 1.54056 Å). Laue back reflection XRD was employed to check single crystal quality and to orient crystals in the

3 principal crystallographic axes to within 1°. Multiple Laue images were taken on samples to ensure they were single domain throughout. Inductively-coupled plasma mass spectrometry (ICP-MS) measurements were conducted using an Agilent 7500ce Quadrupole ICP-MS. To prepare samples for ICP-MS, powders from the single crystals were dissolved in 4 M $HNO_3$ (Fisher) and reacted at 180°C for 2 hrs in a Teflon-lined autoclave (Parr). De-ionized water was used throughout the ICP-MS sample preparation. An optical Raman system with a Verdi V2 532 nm green laser, Andor spectrometer, iCCD detector and a 1800 grating was utilized for vibrational spectroscopy measurements. Diffuse reflectance UV−vis spectra were measured with a Cary 500 spectrophotometer attached to an integrating sphere (Labsphere DRA-CA-5500).

### 2.2.3 Electrical measurements

DC resistivity and DC field Hall effect measurements were made using a Physical Property Measurement System (PPMS, Quantum Design) specially modified for high resistivity samples at Pacific Northwest National Laboratory [30]. A custom sample probe with triax connectors was used for this work. AC field Hall effect measurements were conducted at Lake Shore Cryotronics on a 8404 AC/DC Hall measurement system. Some resistivity measurements at room temperature were conducted using a Keithley 2400 source meter.

Sample geometry was rectangular, oriented such that measurements could be made along principal crystallographic axes (Figure A.1 in Appendix A). It was not practical to differentiate between the *a* and *b* axes using Laue XRD due to the near-structural symmetry in these directions, therefore they were combined and termed ab. The thicknesses of the single crystals ranged from 160-220 μm.

Ohmic contact was achieved by using In-Ga eutectic (Sigma-Aldrich), held in place with Ag paste (Circuit-Works). When indium metal or only Ag paste was used, high resistances and diode behavior were observed (Figure A.2 in Appendix A). Contact areas at the edges were kept small (~0.1 $mm^2$) to minimize measurement errors. Current-voltage curves taken at all chosen temperatures confirmed that the contacts were Ohmic (Figure A.3).

DC resistivity was measured from 400 to 140 K in the van der Pauw (vdP) configuration. DC field Hall effect data were obtained with a magnetic field of -6 to 6 T applied perpendicular to the sample. DC current was applied in both polarities at each field and temperature to eliminate intrinsic errors resulting from misaligned contacts [31]. Experimental errors commonly found in high resistivity samples due to sample capacitance and temperature transients were minimized by waiting for the current and voltage signal to reach steady state after changing temperature, field, or current. AC field Hall effect data were obtained with a magnetic field frequency of 0.1 Hz. This frequency is large enough such that AC conductivity effects can be ignored (further explanation in Appendix A). DC current was applied in both polarities to remove the inductive pickup signal from the Hall voltage [32].

### 2.2.4 Photoelectrochemical measurements

Single crystals were incorporated in electrodes using an In-Ga eutectic/Ag paste back contact embedded in non-conductive epoxy (Loctite). A freshly cleaved (001) face was exposed and electrode areas were between 1-2 $mm^2$. The crystal thicknesses ranged from 80-150 μm.

Photoelectrochemical measurements were conducted in a 3-electrode cell using the single crystal as the working electrode, Ag/AgCl (saturated KCl) as the reference electrode and Pt wire as the counter electrode. All potentials reported here are versus the reversible $H_2$ electrode (RHE). Illumination was the full output of a 150 W Xe lamp (Osram, Munich, Germany) calibrated to 100 mW $cm^{-2}$. A monochromator (Photon Technology International), silicon photodetector (model 818-UV, Newport), and optical power meter (model 1830-C, Newport) were used to obtain the incident photon to current conversion efficiency (IPCE). IPCE values were calculated using the formula [33]:

$$\mathrm{IPCE}(\lambda) = \frac{1240 \cdot j(\lambda)}{\lambda \cdot E(\lambda)} \times 100 \qquad (2.2)$$

where, $\lambda$ is the wavelength (nm), $j$ is the photocurrent density and $E$ is the incident power of the monochromated light.

The electrolyte solution was 0.1 M phosphate buffer with 0.1 M $Na_2SO_4$ (Fisher) in de-ionized Milli-Q water (pH 7). In some experiments, 0.1 M $Na_2SO_3$ (Fisher) was added to this solution as a hole scavenger (pH 7). A CH Instruments 630D potentiostat was used for all current-voltage scans. The scan rate was 20 mV $s^{-1}$. Capacitance-voltage measurements were made using a CH Instruments 660D potientiostat. The amplitude of the applied voltage was 5 mV at fixed frequencies of 500, 1000 and 1500 Hz.

## 2.3. Results and Discussion

### 2.3.1 Synthesis

Crystal boules of undoped and doped (< 1 at.%) $BiVO_4$, ~6 mm in diameter and 20 mm long were prepared, but were rarely single-domain throughout. This is in

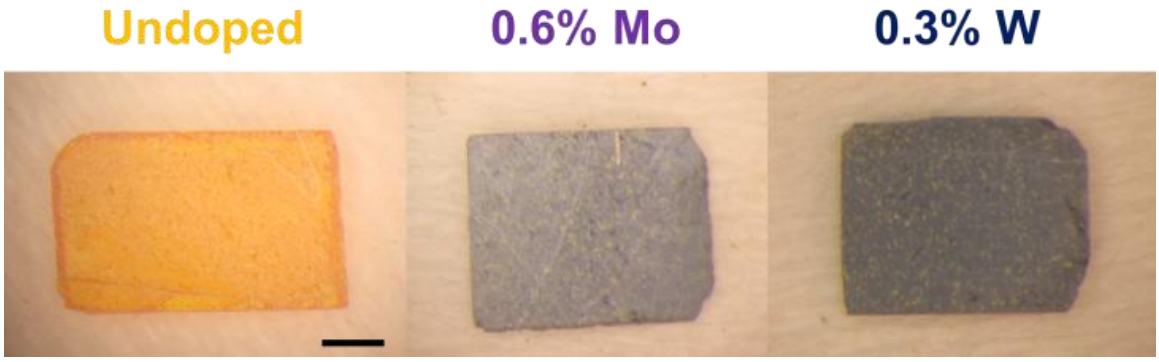


**Figure 2.1:** Photographs of undoped and doped oriented and polished single crystal *c*-plates. The scale bar is 1 mm.

agreement with other studies, where $BiVO_4$ crystals grown by the Czochralski technique contained extensive twinning [22,23]. Regardless, large single crystals (up to 4 × 3 × 2 mm in our case) could be cut from the boules. Laue back-reflection XRD confirmed that the prepared samples were not macroscopically twinned (Figure A.4). The undoped crystals were transparent orange and we saw cleavage perpendicular to the *c*-axis as observed by other workers [22,23]. Figure 2.1 shows that doping with Mo and W changed the apparent color to a dark purple. Observed color can be due to a variety of mechanisms [34], in this case we rationalize the color change using semiconductor band theory. Mo and W are predicted to act as shallow donor impurities [20,35], which gives rise to a low-energy transition between the impurity states and the conduction band, capable of absorbing all visible photons. Grinding of both doped and undoped crystals resulted in yellow powder characteristic of $BiVO_4$, indicating that the dark purple color is only observed in specimens where the crystal domains are large enough. This phenomena is well known in mineralogy, where "streak" (dragging a sample across a hard plate to produce a fine powder) is used to identify compounds [36].

Higher doping concentrations, up to 10%, were at-tempted, but resulted in an unstable melt zone, which was presumably due to incongruent melting. Incongruently melting materials can be grown using the travelling solvent floating zone technique [37], but the use of a suitable solvent is essential. Several solvents in the $Bi_2O_3$-$V_2O_5$ phase diagram were tried, but none resulted in stable crystal growth. More exotic solvent materials may be successful.

### 2.3.2 Compositional analysis

Final dopant concentrations were determined by inductively coupled plasma mass spectrometry (ICP-MS), confirming that Mo and W were present in the samples. Results are shown in Table 2.1. From these values it appears that *x* in Equation 2.1 is limited to ~0.3% for W in $BiVO_4$ grown from the melt. In fact, the value of *x* decreased for all samples, except sample 1, where the increase in Mo concentration is attributed to V evaporation during growth. Hereafter, all data in this chapter refer to either undoped, 0.6% Mo or 0.3% W doped $BiVO_4$ single crystals. The doped samples will be referred to as Mo:$BiVO_4$ and W:$BiVO_4$. In this analysis we have assumed that the doping in the

| Dopant | Sample | Starting *x* (%) | Final *x* (%) |
|---|---|---|---|
| Mo | 1 | 0.54 | 0.57 |
| | 2 | 1.08 | 0.78 |
| W | 3 | 0.52 | 0.31 |
| | 4 | 1.04 | 0.31 |
| x is based on Equation 1 | | | |

**Table 2.1:** Initial calculated dopant concentrations in the feed rods compared to the concentrations determined by ICP-MS in $BiVO_4$ single crystals

samples is homogeneous, i.e. no surface segregation takes place. As mentioned in Section 2.3.1, the melt-growth technique produces large boules of crystal-line material, from which samples are cut. As the samples are obtained from the bulk of the boules, surface segregation is unlikely.

Analyses of the powder x-ray diffraction (XRD) spectra showed that the resulting crystals were single phase monoclinic $BiVO_4$ (PDF #14-0688) as shown in Figure 2.2. The addition of Mo and W have been shown to stabilize the tetragonal scheelite structure of polycrystalline $BiVO_4$ at room temperature with high (> 5 at.%) dopant concentrations [12,20,21]. The dopant concentrations achievable using the floating zone growth process (< 1%) were too small to have any significant change in the lattice parameters, and so the

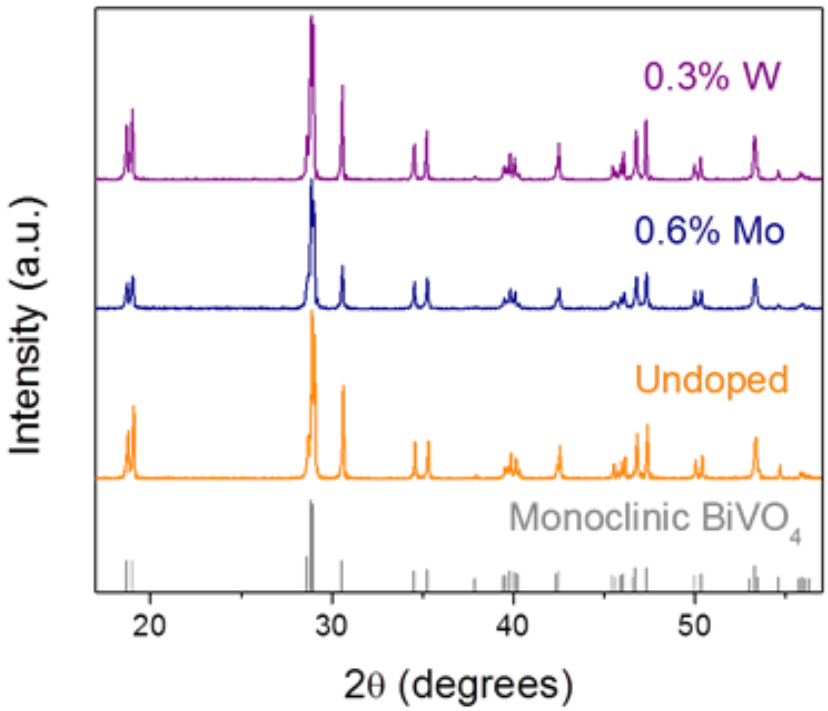


**Figure 2.2:** XRD patterns for pulverized $BiVO_4$ single crystals. Grey vertical ticks show the pattern for the monoclinic phase of $BiVO_4$ (PDF #14-0688).

incorporation of Mo and W could not be studied using XRD.

Raman spectra were collected from the c-plates of the single crystals to probe potential changes in the V-site in the $BiVO_4$ lattice. All peaks could be indexed to Raman bands of the monoclinic $BiVO_4$ [38,39]. Luo et al. recently performed Raman spectroscopy on $BiVO_4$ thin films doped with 3 at.% Mo or W [15]. Doping resulted in little change between spectra, except for a shift of ~7 $cm^{-1}$ in the peak around 829 $cm^{-1}$ associated with stretching of the V-O bond. We measured a comparable shift of ~2 $cm^{-1}$ in this peak, which we also assign to Mo and W substitution in the V-site (Figure 2.3). Though the shift was small, it was repeatable. The low concentration of dopants made analyses of their charge state and local environment by X-ray photoelectron spectroscopy

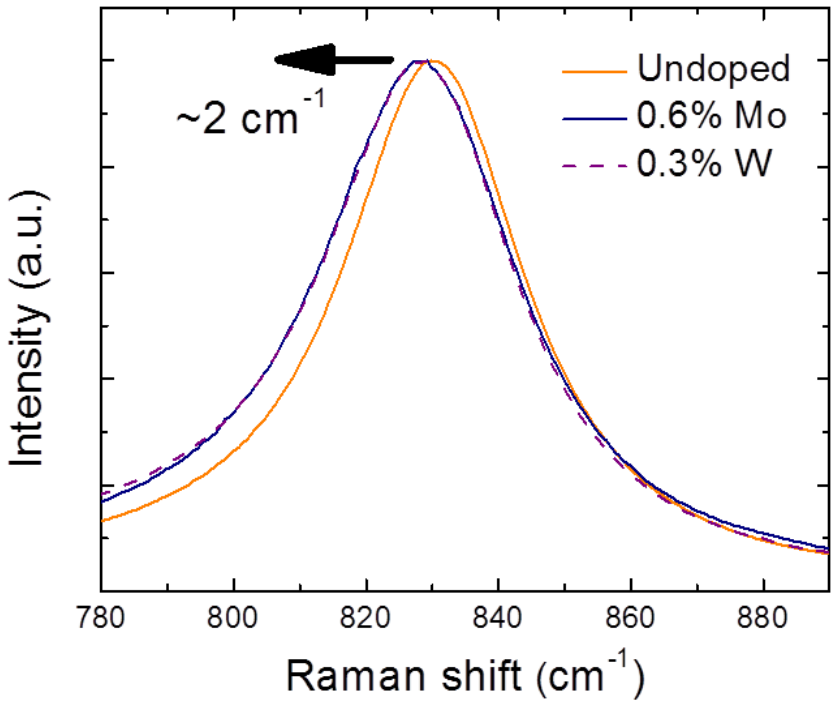


**Figure 2.3:** Raman spectra of single crystal *c*-plates, illustrating a shift in the peak around 830 $cm^{-1}$

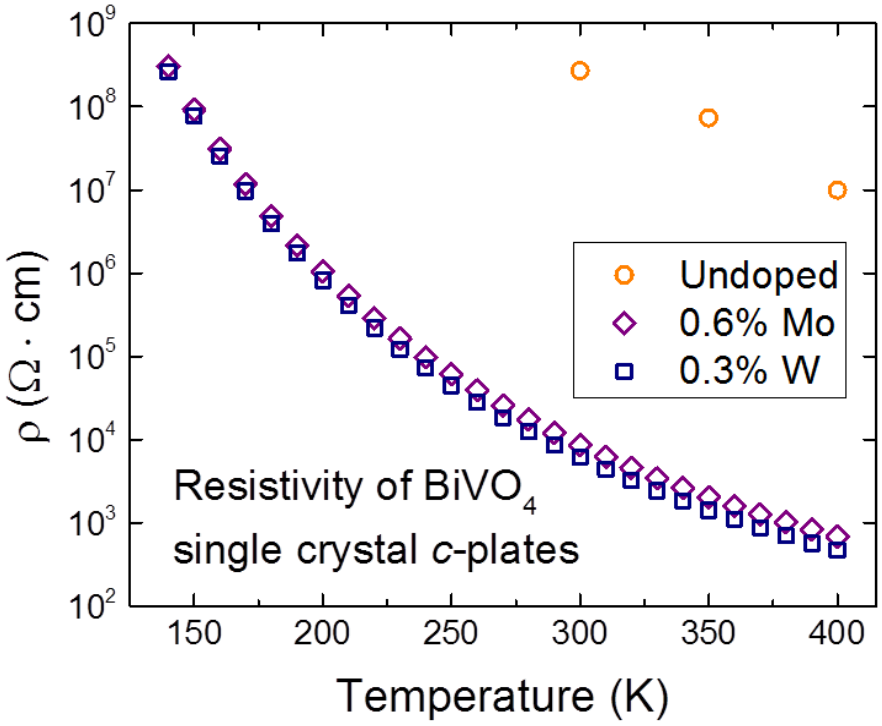


**Figure 2.4:** Resistivity *vs.* temperature for $BiVO_4$ single crystals.

(XPS) impossible.

### 2.3.3 Electrical transport

Resistivity was measured from 400 to 140 K, increasing by 5 orders of magnitude as temperature was decreased (Figure 2.4). The similarity in the resistivity values for Mo and W doping was expected as their concentrations are comparable and both are typically in the 6+ oxidation state [20,21], therefore adding a single electron to the lattice per dopant atom. Undoped crystals were highly resistive, ~5 × $10^8$ Ω • cm, compared with ~$10^4$ Ω • cm for doped samples at 300 K. The van der Pauw (vdP) configuration was used and there was little difference between the resistances along the *a* or *b* axes indicating that $\rho_a \approx \rho_b$. Thus c-plates were assumed to be isotropic.

### 2.3.3.1 Transport models

In many metal oxides (i.e. Ti:$Fe_2O_3$ [40,41] and Nb:$TiO_2$ [42]), carrier transport is described by a thermally activated small polaron hopping (SPH) mechanism first proposed by Mott [43]. In this model, the charge carrier distorts the surrounding lattice, impeding its transport and resulting in low mobility: an upper limit of 0.1-1 $cm^2\ V^{-1}\ s^{-1}$ has been calculated [44]. Based on density functional theory calculations [20], small polaron hopping was suggested to be dominant in Mo:$BiVO_4$ and W:$BiVO_4$, with electron transport taking place between $V^{4+}$ and $V^{5+}$, $Mo^{6+}$ or $W^{6+}$ atoms. The small polaron model is described by [45]:

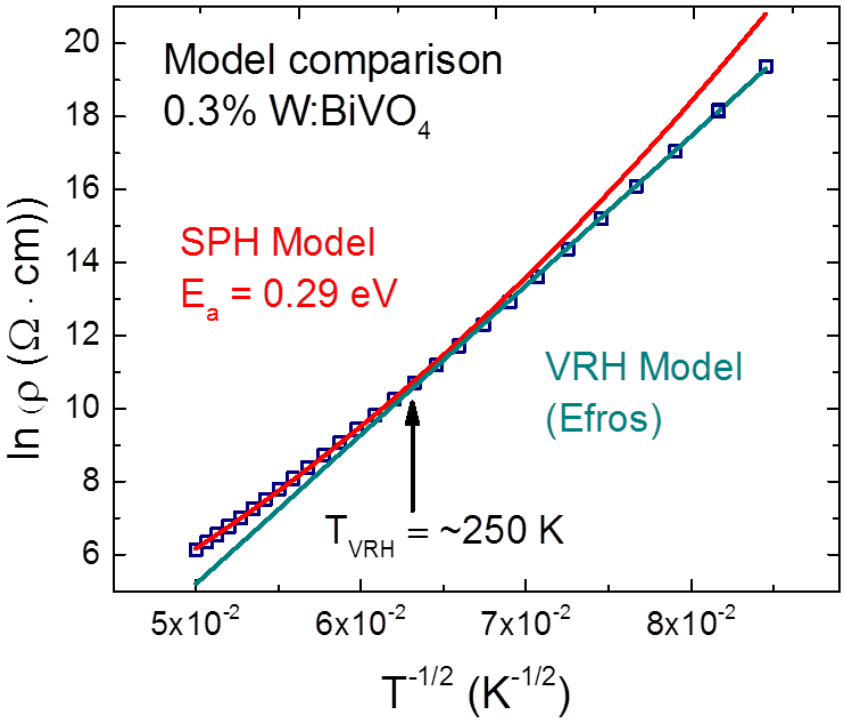


**Figure 2.5:** Fits of small polaron hopping (SPH) and variable range hopping (VRH) transport models to resistivity data. Arrow indicates transition to the VRH mechanism.

$$\rho\,(T) \propto T\exp\left(\frac{E_a}{k_B T}\right) \qquad (2.3)$$

where $E_a$ is the hopping activation energy, $k_B$ is the Boltzmann constant and $T$ is the absolute temperature. As shown in Figure 2.5, this model fits the data closely from 250-400 K, and activation energies of 0.286(1) and 0.290(1) eV were determined for Mo and W:$BiVO_4$ respectively. These results indicate that Mo and W have electrically similar behavior as dopants in the $BiVO_4$ system at concentrations less than 1%.

A transition to a variable range hopping (VRH) mechanism is expected at low temperatures, at approximately one half the Debye temperature; $\Theta_D/2$ [46]. At the time of writing, no literature values for the Debye temperature of $BiVO_4$ exist, so based on our data we estimate a value of ~500 K. In the VRH regime, conduction occurs by hopping from localized dopant centers and so is applicable in doped semiconductors and amorphous glasses containing metal ions. Several VRH mechanisms exist: Mott 3D, 2D [43] and Efros-Shkolvskii [47]. The Efros-Shkolvskii model gave the best fit to our data and is described by:

$$\rho\,(T) \propto \exp\left(\frac{1}{T^{1/2}}\right) \qquad (2.4)$$

though it should be noted that all models mentioned fit the data adequately ($R^2 > 0.999$). Interestingly, ln $\rho\ \alpha\ T^{-3/4}$ matched the resistivity data excellently over the entire temperature range (data not shown), but no conduction model was of this form. The data for 0.6% W:$BiVO_4$ crystals (Figure A.5 in Appendix A) produced nearly identical results to those described above for 0.3% Mo:$BiVO_4$. Certainly, our understanding of transport

in $BiVO_4$ would benefit from rigorous computational studies as have been performed for hematite [48,49] and titania [50].

### 2.3.3.2 Resistivity anisotropy

Monoclinic $BiVO_4$ (space group $I2/b$, $a$ = 5.1935 Å, $b$ = 5.0898 Å, $c$ = 11.6972 Å, $\gamma$ = 90.387° [22]) has a layered structure, consisting of edge sharing $BiO_8$ and $VO_4$ groups, separated by weakly bonded oxygen planes perpendicular to the c-direction (Figure 2.6). Hoffart et al. investigated anisotropy in undoped single crystals at elevated temperatures (550-700 °C), where conduction is primarily ionic and due to oxygen vacancies [23]. The authors showed 50 times greater ionic resistivity in the $c$ direction

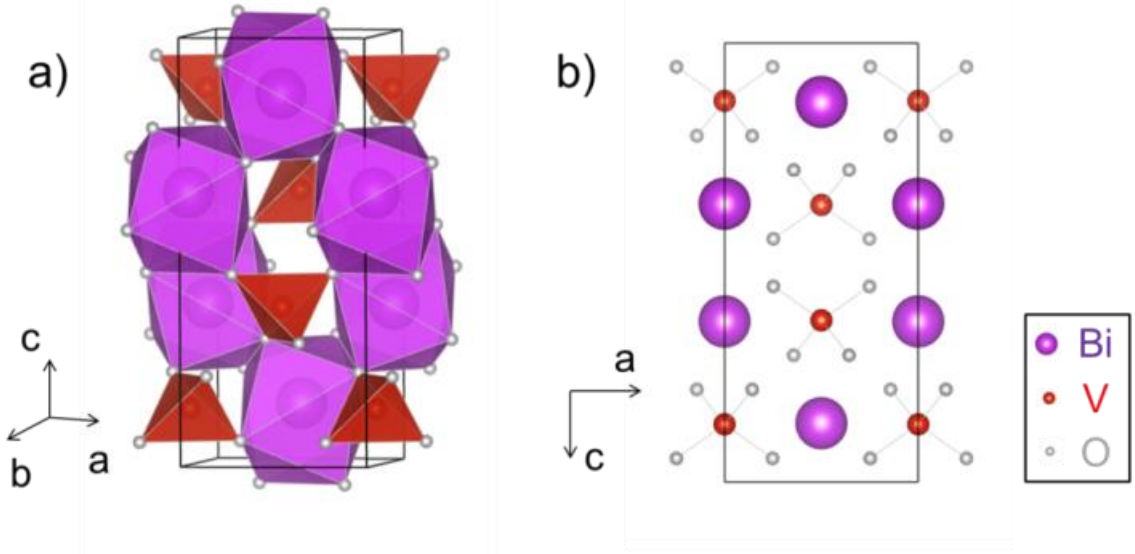


**Figure 2.6:** Schematic of monoclinic $BiVO_4$ structure a) showing edge sharing $BiO_8$ (purple) and $VO_4$ (red) units and b) illustrating oxygen planes perpendicular to the c-direction [57]

compared with *a*, which was attributed to the layered structure of $BiVO_4$. We measured a resistivity anisotropy ratio, $\rho_c$ / $\rho_{ab}$, of ~3 over multiple single crystal samples at room temperature (Table 2), where $\rho_a \approx \rho_b = \rho_{ab}$ as discussed in Section 2.3.3. This was first observed in the vdP geometry; however direction-dependent resistivities could not be extracted using the traditional vdP method, which assumes that the sample is isotropic [51]. Several authors have presented techniques to determine resistivity anisotropy from vdP data [52-55]. Here, we have used Kazani et al.'s method [5], which indicated an anisotropy ratio between 2.6-3.7. To verify this result, bar-shaped samples (0.5 × 0.3 × 2 mm) were cut in the directions of interest and 4-point collinear measurements confirmed an anisotropy ratio of ~3 as shown in Table 2.2.

| Sample | Geometry | Technique | $\rho_c$ / $\rho_{ab}$ |
|---|---|---|---|
| 1 | *ab*-plate | vdP | 2.6 |
| 2 | *ab*-plate | vdP | 3.7 |
| 3 | Bar | 4-point collinear | 2.9 |
| [a]van der Pauw (vdP) | | | |

**Table 2.2:** Resistivity anisotropy of 0.3% W $BiVO_4$ single crystals (300 K)

Though the degree of anisotropy is modest, this difference could be significant in $BiVO_4$-based photoelectrodes where charge transport is limiting. High aspect ratio nanostructures that minimize electron transport in the *c*-direction are therefore predicted to be beneficial in this case. Other recent work has emphasized the importance of crystal orientation in photoelectrochemical processes, in that case, on different crystal facets of $BiVO_4$ [58].

Kazani et al.'s method was further tested by applying the technique to vdP data for *c*-plates which were expected to be isotropic. This analysis yielded resistivities that only varied by 20-30% (Table A.1 in Appendix A).

#### 2.3.3.3 Hall effect measurements

We attempted to measure the Hall effect using a static magnetic field in the doped samples, but no clear signal above the instrument noise could be obtained. For these samples it was noticed that several hours were required to reach a steady state after a current had been applied, and spurious Hall voltages could be easily obtained by insufficient wait time. A potential explanation for the small signal is that the samples were too thick. The Hall voltage, $V_H$, is inversely proportional to sample thickness, t [59],

$$V_H = \frac{iB\rho\mu}{t} \qquad (2.5)$$

where, $i$ is the applied current, $B$ is the field strength and $\mu$ is the mobility. Thin films (on the order of nm) would improve the Hall signal dramatically, but also increase the misalignment voltage which is directly proportional to sample thickness [32].

AC field Hall effect measurements were used to obtain values for carrier mobility, $\mu$ and carrier concentration, $n$ for the doped single crystals. This technique applies an oscillating magnetic field to the sample, making the resulting Hall voltage (given in Equation 2.5) time dependent. This signal is boosted by a lock-in amplifier, facilitating measurement of the Hall effect in low mobility materials [32] Though this is an uncommon technique, it is well established in the literature with work dating from the 1960s developing and utilizing it [60,61]. AC field Hall effect measurements showed

both W:$BiVO_4$ and Mo:$BiVO_4$ crystals were n-type with electron mobility of ~0.2 $cm^2$ $V^{-1}$ $s^{-1}$ at 300 K (Table A.2 in Appendix A). In the temperature range 250-300 K, the mobility was effectively constant, while the carrier concentration decreased as the sample was cooled (Figure 2.7), consistent with the resistivity increase at lower temperatures (Figure 2.4). Similar behavior was observed for 0.6% Mo:$BiVO_4$ (Figure A.6). Below 250 K the signal was too noisy to discern a Hall voltage in the doped crystals and undoped samples were too resistive to measure the Hall effect at all temperatures considered. There was variability in the measurements (factor of ~2) as the Hall voltage was small (Table A.3), but this did not change the observed trends or the values for $n$ or $\mu_e$ appreciably. For an n-type semiconductor, carrier concentration is

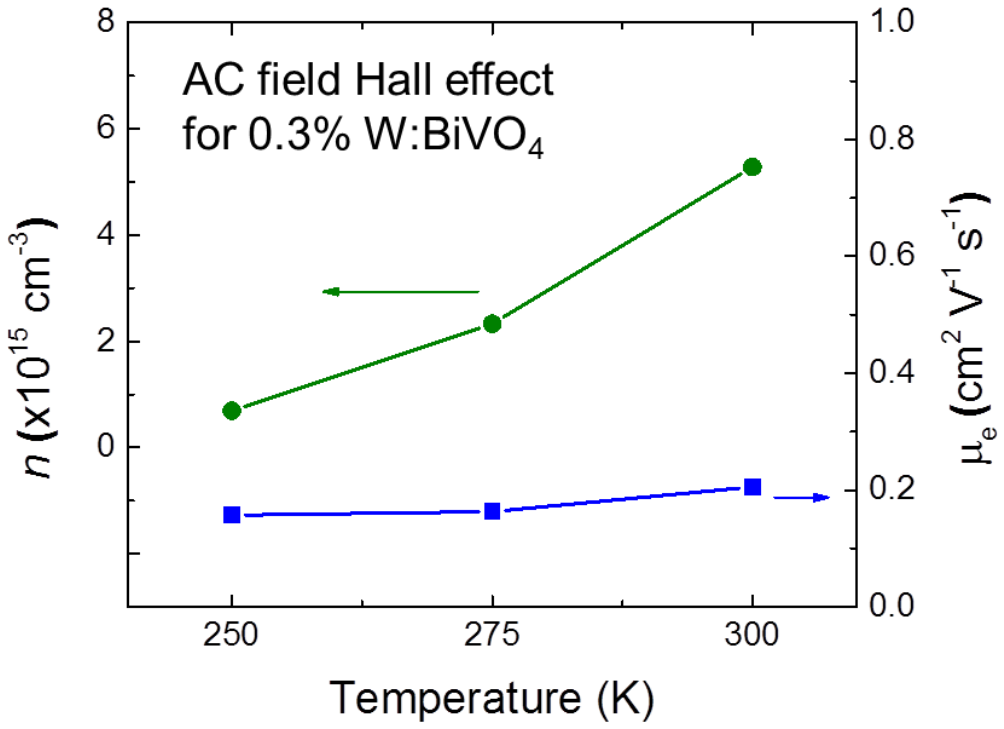


**Figure 2.7:** Carrier concentration ($n$) and electron mobility ($\mu_e$) AC field Hall effect as a function of temperature for a 0.3% W:$BiVO_4$ $c$-plate.

given by,

$$n = \frac{1}{\rho e \mu_e} \qquad (2.6)$$

Using Equation 2.6, *n* was determined as ~5 × $10^{15}$ $cm^{-3}$ at 300 K (Table A.2 in Appendix A), significantly lower than the impurity concentrations – between 4-8 × $10^{19}$ $cm^{-3}$ for 0.3% W and 0.6% Mo doping respectively – calculated from ICP-MS measurements (Table 2.1). This unexpected result suggests partial charge compensation in these single crystals, which can complicate the intentional doping of complex metal oxides [62]. Under the O-rich and Bi-poor growth conditions employed, we hypothesize that singly ionized impurities substituted on the V-site ($M_V^{\bullet}$) are the main source of donors and triply-charged Bi vacancies ($V_{Bi}^{'''}$) are the main source of acceptors (Equation 2.4), using Kröger-Vink notation:

$$n - p = [M_V^{\bullet}] - 3[V_{Bi}^{'''}] \qquad (7)$$

where *p* is the carrier concentration of holes, *M* = Mo or W and the subscript refers to the lattice site. Bi vacancies have been observed in heavily doped (Mo and W) poly-crystalline $BiVO_4$ [12,29] and are predicted to be shallow acceptors that can easily be accommodated in the $BiVO_4$ lattice [35,63]. Unfortunately, the very low predicted concentration of these vacancies mean they could not be observed in our lightly doped samples. From the charge balance in Equation 2.7 it is clear that only a small concentration of Bi vacancies would be needed to provide significant degree of charge compensation. Addition of excess Bi in the feed rods may promote less compensation and

more efficient n-type doping of $BiVO_4$ [62,64], however a slight excess of V was required for stable growth of crystals experimentally.

### 2.3.4 Photoelectrochemistry

All photoelectrochemical testing was done with doped samples, as we could not obtain a measureable photocurrent from electrodes using undoped $BiVO_4$ crystals. This is attributed to recombination of generated electron-hole pairs before reaching the back contact based on the inherently low conductivity of undoped crystals (Figure 2.4) and relatively large crystal thickness (~100 μm). Linear sweep voltammetry (LSV) was used to evaluate the performance of doped single crystal $BiVO_4$ electrodes with the (001) face exposed, which exhibited behavior characteristic of an n-type photoanode (Figure 2.8a). Only Mo:$BiVO_4$ data are shown as the behavior of W:$BiVO_4$ electrodes were comparable (Figure A.7 in Appendix A).

Photocurrents reached ~0.4 mA $cm^{-2}$ at 1.2 V vs. RHE (Figure 2.8a). A hole scavenger ($Na_2SO_3$) was used to evaluate electrode performance with facile oxidation kinetics (Figure 2.8b). Here, we observed the onset of photocurrent at lower potentials than for water oxidation, demonstrating that hole transfer from the $BiVO_4$ surface to solution is limiting when used for water oxidation. This has been reported by other authors and illustrates the importance of co-catalysts for this material [21,65,66]. Relatively small cathodic dark currents were observed at more negative potentials (Figures 2.8a and b, A.7 in Appendix A) and may result from reduction of the electrode surface or dissolved oxygen in the electrolyte. Incident photon conversion efficiency (IPCE) spectra agreed well with polycrystalline $BiVO_4$ photoanodes with a tail extending to ~520 nm (Figure 2.9) [65,67]. This indicates a band gap, $E_g$ of ~2.4 eV, despite the

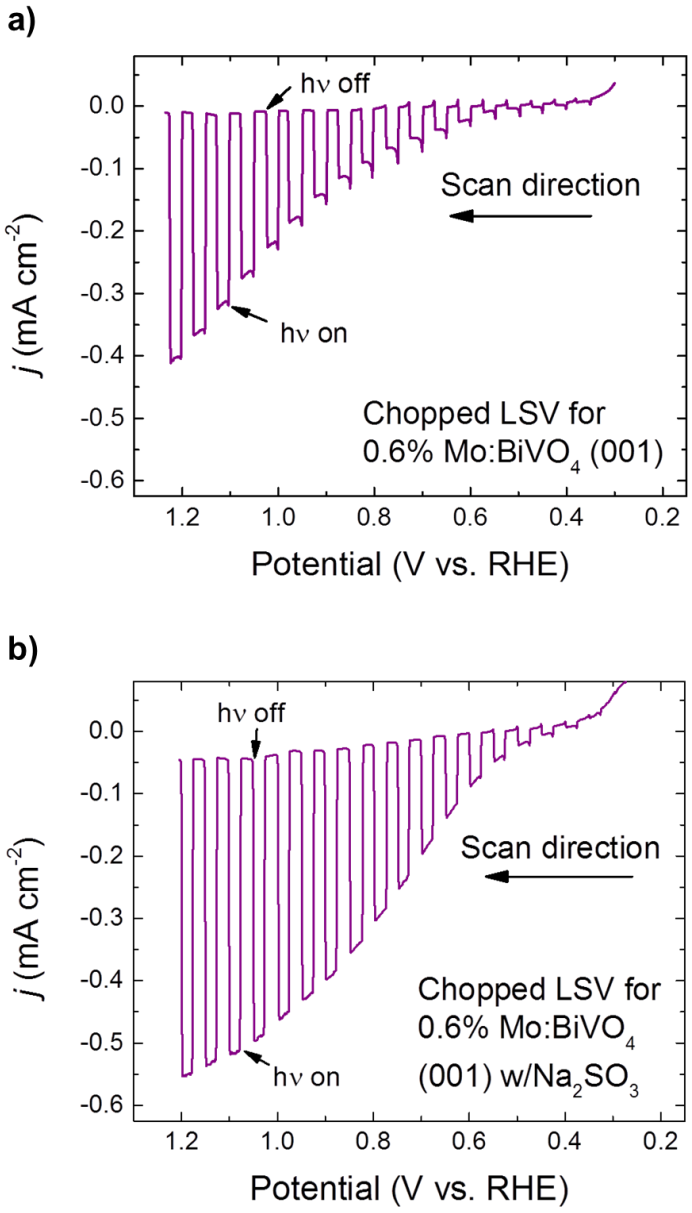


**Figure 2.8:** Chopped illumination linear sweep voltammograms (LSVs) of a Mo:$BiVO_4$ electrode with the (001) face exposed. Scan rate was 20 mV $s^{-1}$ and light intensity was 100 mW $cm^{-2}$ from a full xenon lamp. The electrolyte solution was 0.1 M phosphate buffer with a) 0.1 M $Na_2SO_4$ b) 0.1 M $Na_2SO_4$ and 0.1 M $Na_2SO_3$ (hole scavenger).

dark coloration of the doped single crystals (Figure 2.1). Diffuse reflectance UV-Vis spectra showed that these samples absorb at all wavelengths of visible light (Figure A.8), but clearly these do not contribute to useful electron-hole generation. This phenomena has been observed in reduced single crystal $TiO_2$ [68] and $SrTiO_3$ [69], doped ZnO [70] and most recently, $H_2$-treated polycrystalline $BiVO_4$ films [63], but the underlying mechanism remains unclear. Future work will involve photoluminescence measurements to probe the role of impurity states and carrier recombination in our crystals.

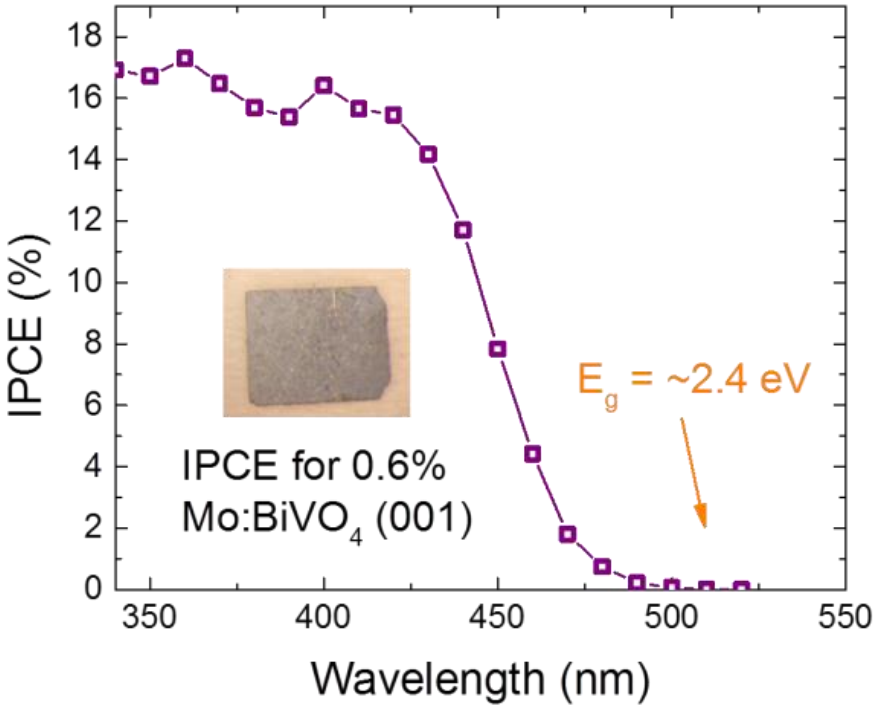


**Figure 2.9:** Incident photon to current efficiency at 1.2 V *vs*.RHE in 0.1 M phosphate buffer with 0.1 M $Na_2SO_4$. Photograph of Mo:$BiVO_4$ *c*-plate (inset) shows dark coloration of doped single crystal.

### 2.3.4.1 Mott-Schottky analysis

Mott-Schottky (M-S) analysis is commonly used in photoelectrode characterization, and relies on measuring the capacitance of the space charge region at the semiconductor-liquid junction. The flat band potential, $V_{fb}$, is determined from a plot of $C_{SC}^{-2}$ vs. potential as the *x*-intercept and the carrier concentration can be calculated using the slope of the linear region according to Equation 2.8 for an n-type semiconductor,

$$\frac{1}{C_{SC}^{2}} = \left(\frac{2}{\varepsilon\varepsilon_0 en}\right)\left(V - V_{fb} - \frac{k_B T}{e}\right) \qquad (2.8)$$

where, $\varepsilon$ is the dielectric constant of the material, $\varepsilon_0$ is the permittivity of free space and $V$ is the applied potential. The term $k_B T/e$ is small at room temperature and therefore neglected.

Both the calculated flat band potential and carrier concentrations were shown to vary with frequency (Figure S9 in the SI). The flat band potential was 0.03 – 0.08 V vs. RHE, in good agreement with the on-set potential of ~0.05 V (Figure A.7, inset, in Appendix A). The calculated range of carrier concentration from these plots was 0.3 to 1 $\times$ $10^{18}$ $cm^{-3}$. This value does not agree with $n$ from Hall effect measurements and illustrates the need for independent measurement of this quantity. The frequency dispersion indicates that M-S analysis may not be adequate for accurate n determination for these single crystals. This finding has also been observed for other single crystal electrodes, such as hematite [69].

### 2.3.4.2 Estimation of hole diffusion length

By applying the model of Gärtner [71], a useful relationship can be derived for estimating the hole diffusion length [72,73]:

$$\ln(1-\eta) = -\alpha\left(\frac{\varepsilon\varepsilon_0}{2en}\right)^{1/2}\left(V - V_{fb}\right)^{1/2} - \ln\left(1+\alpha L_p\right) \qquad (2.9)$$

where, $\eta$ is the IPCE in Equation 2.2 corrected for reflection at the electrode surface and expressed as a fraction, $\alpha$ is the absorption coefficient and $L_p$ is the minority carrier diffusion length. At sufficiently positive potentials, a plot of $\ln(1-\eta)$ vs. $\left(V - V_{fb}\right)^{1/2}$ results in a linear region that can be extrapolated to the *y*-intercept to determine Lp (Figure A.10). Application of this analysis yielded a value for α of ~2,600 $cm^{-1}$ using *n* from Hall effect measurements and a resulting hole diffusion length of ~100 nm at $\lambda$ = 400 nm. This value is in agreement with the estimated range of 100 to 200 nm calculated by other authors for polycrystalline undoped and doped $BiVO_4$ electrodes [18]. Detailed calculations are given in Appendix A.

### 2.3.5 Comparison to other metal oxide photoanode materials

The electron mobility of Mo:$BiVO_4$ and W:$BiVO_4$ are low, but in the correct range for metal oxide semiconductors where thermally activated small polaron hopping is the dominant conduction mechanism. In comparison to other metal oxides studied as photoanodes, its intrinsic mobility is on the low side, similar to iron oxide (Table A.4 in Appendix A). However, the hole diffusion length is moderate, being greater than reported values for single crystal $TiO_2$ and polycrystalline hematite (at the time of writing, no single crystal data for comparison could be found), but significantly less than monoclinic $WO_3$ (Table A.5).

It is important to note that mobility is a function of total impurity concentration due to scattering, and although the *n* of these single crystals was low due to charge compensation, the impurity concentration was on the order of $10^{19}$ $cm^{-3}$ (calculated based

on ICP-MS measurements). If fewer of the donor impurities were compensated, samples with lower resistivity and lower impurity concentrations could be synthesized, potentially resulting in higher electron mobility due to reduced impurity scattering. Further studies of doping on grain boundaries and surface states as has been performed for other materials [74,75] are essential to an in-depth understanding of this material and optimization of $BiVO_4$ for water splitting applications.

## 4. CONCLUSIONS

We have synthesized single crystals of undoped and Mo, W:$BiVO_4$ via the floating zone technique, with up to 0.6% and 0.3% respectively. Mo and W substitute for V in $BiVO_4$ and act as donor impurities, doping crystals n-type. Between 250 and 400 K conduction is governed by small polarons, with an associated activation energy of 0.3 eV. At temperatures lower than 250 K a transition to a variable range hopping mechanism occurs. Resistivity anisotropy of ~3 was observed in the *c*-direction and was attributed to the layered structure of $BiVO_4$. Attempts to measure the DC field Hall effect were unsuccessful, but the AC field technique yielded an electron mobility of ~0.2 $cm^2\ V^{-1}\ s^{-1}$ at 300 K. Comparison of the impurity level to the carrier concentration indicated partial charge compensation in these crystals. Mott-Schottky analysis yielded a flat band potential of 0.03-0.08 V vs. RHE, while IPCE tests showed that the dark coloration of the doped single crystals did not contribute to additional photocurrent. By application of the Gärtner model we estimate a hole diffusion length of ~100 nm. These results provide new insights into the fundamental transport properties of $BiVO_4$, and should be of great value in optimizing this material further for photoelectrochemistry and other applications.

## REFERENCES


(1) Bard, A. J.; Fox, M. A. *Accounts of Chemical Research* **1995**, *28*, 141.

(2) Grätzel, M. *Nature* **2001**, *414*, 338.

(3) Ni, M.; Leung, M. K.; Leung, D. Y.; Sumathy, K. *Renewable and Sustainable Energy Reviews* **2007**, *11*, 401.

(4) Sivula, K.; Le Formal, F.; Grätzel, M. *ChemSusChem* **2011**, *4*, 432.

(5) Liu, X.; Wang, F.; Wang, Q. *Physical Chemistry Chemical Physics* **2012**, *14*, 7894.

(6) Park, Y.; McDonald, K. J.; Choi, K.-S. *Chemical Society Reviews* **2013**.

(7) Li, Z.; Luo, W.; Zhang, M.; Feng, J.; Zou, Z. *Energy & Environmental Science* **2013**, *6*, 347.

(8) Berglund, S. P.; Flaherty, D. W.; Hahn, N. T.; Bard, A. J.; Mullins, C. B. *J. Phys. Chem. C* **2011**, *115*, 3794.

(9) Tokunaga, S.; Kato, H.; Kudo, A. *Chem. Mater.* **2001**, *13*, 4624.

(10) Bierlein, J. D.; Sleight, A. W. *Solid State Communications* **1975**, *16*, 69.

(11) Pinczuk, A.; Welber, B.; Dacol, F. *Solid State Communications* **1979**, *29*, 515.

(12) Sleight, A. W.; Aykan, K.; Rogers, D. B. *J. Solid State Chem.* **1975**, *13*, 231.

(13) Pilli, S. K.; Furtak, T. E.; Brown, L. D.; Deutsch, T. G.; Turner, J. A.; Herring, A. M. *Energy & Environmental Science* **2011**, *4*, 5028.

(14) Luo, W.; Yang, Z.; Li, Z.; Zhang, J.; Liu, J.; Zhao, Z.; Wang, Z.; Yan, S.; Yu, T.; Zou, Z. *Energy & Environmental Science* **2011**, *4*, 4046.

(15) Luo, W.; Wang, J.; Zhao, X.; Zhao, Z.; Li, Z.; Zou, Z. *Phys. Chem. Chem. Phys.* **2013**, *15*, 1006.

(16) Luo, W.; Li, Z.; Yu, T.; Zou, Z. *The Journal of Physical Chemistry C* **2012**, *116*, 5076.

(17) Ye, H.; Park, H. S.; Bard, A. J. *The Journal of Physical Chemistry C* **2011**.

(18) Zhong, D. K.; Choi, S.; Gamelin, D. R. *Journal of the American Chemical Society* **2011**, *133*, 18370.

(19) Abdi, F. F.; Firet, N.; van de Krol, R. *ChemCatChem* **2013**, *5*, 490.

(20) Park, H. S.; Kweon, K. E.; Ye, H.; Paek, E.; Hwang, G. S.; Bard, A. J. *The Journal of Physical Chemistry C* **2011**, *115*, 17870.

(21) Berglund, S. P.; Rettie, A. J. E.; Hoang, S.; Mullins, C. B. *Phys. Chem. Chem. Phys.* **2012**, *14*, 7065.

(22) Sleight, A. W.; Chen, H. Y.; Ferretti, A.; Cox, D. E. *Mater. Res. Bull.* **1979**, *14*, 1571.

(23) Hoffart, L.; Heider, U.; Huggins, R. A.; Witschel, W.; Jooss, R.; Lentz, A. *Ionics* **1996**, *2*, 34.

(24) Hoffart, L.; Heider, U.; Joerissen, L.; Huggins, R. A.; Witschel, W. *Solid State Ionics* **1994**, *72*, 195.

(25) Hoffart, L.; Heider, U.; Jorissen, L.; Huggins, R. A.; Witschel, W. *Ionics* **1995**, *1*, 131.

(26) Hartmanova, M.; Le, M. T.; Jergel, M.; Smatko, V.; Kundracik, F. *Russ. J. Electrochem.* **2009**, *45*, 621.

(27) Beg, S.; Haneef, S.; Al-Areqi, N. A. S. *Phase Transitions* **2010**, *83*, 1114.

(28) Vinke, I. C.; Diepgrond, J.; Boukamp, B. A.; De, V. K. J.; Burggraaf, A. J. *Solid State Ionics* **1992**, *57*, 83.

(29) Cesari, M.; Perego, G.; Zazzetta, A.; Manara, G.; Notari, B. *J. Inorg. Nucl. Chem.* **1971**, *33*, 3595.

(30) McCloy, J. S.; Ryan, J. V.; Droubay, T.; Kaspar, T. C.; Chambers, S.; Look, D. C. *Review of Scientific Instruments* **2010**, *81*, 063902.

(31) Look, D. C. *Electrical characterization of GaAs materials and devices*; Wiley, 1989.

(32) Lindemuth, J.; Mizuta, S.-I. In *SPIE Solar Energy + Technology*; International Society for Optics and Photonics: 2011, p 81100I.

(33) Chen, Z.; Jaramillo, T. F.; Deutsch, T. G.; Kleiman-Shwarsctein, A.; Forman, A. J.; Gaillard, N.; Garland, R.; Takanabe, K.; Heske, C.; Sunkara, M. *J. Mater. Res* **2010**, *25*, 3.

(34) Nassu, K. *American Mineralogist* **1978**, *63*, 219.

(35) Yin, W.-J.; Wei, S.-H.; Al-Jassim, M. M.; Turner, J.; Yan, Y. *Physical Review B* **2011**, *83*, 155102.

(36) Klein, C.; Hurlbut, C. S.; Dana, J. D. *Manual of mineralogy*; Wiley New York, 1993; Vol. 527.

(37) Koohpayeh, S.; Fort, D.; Abell, J. *Progress in Crystal Growth and Characterization of Materials* **2008**, *54*, 121.

(38) Frost, R. L.; Henry, D. A.; Weier, M. L.; Martens, W. *Journal of Raman Spectroscopy* **2006**, *37*, 722.

(39) Zhang, H. M.; Liu, J. B.; Wang, H.; Zhang, W. X.; Yan, H. *Journal of Nanoparticle Research* **2008**, *10*, 767.

(40) Bosman, A.; Van Daal, H. *Advances in Physics* **1970**, *19*, 1.

(41) Zhao, B.; Kaspar, T. C.; Droubay, T. C.; McCloy, J.; Bowden, M. E.; Shutthanandan, V.; Heald, S. M.; Chambers, S. A. *Phys. Rev. B: Condens. Matter Mater. Phys.* **2011**, *84*, 245325/1.

(42) Yildiz, A.; Lisesivdin, S.; Kasap, M.; Mardare, D. *Physica B: Condensed Matter* **2009**, *404*, 1423.

(43) Mott, N. F.; Davis, E. A. *Electronic processes in non-crystalline materials*; 2nd ed.; OUP Oxford, 1979.

(44) Emin, D.; Seager, C.; Quinn, R. K. *Physical Review Letters* **1972**, *28*, 813.

(45) Austin, I. G.; Mott, N. F. *Advances in Physics* **1969**, *18*, 41.

(46) Holstein, T. *Annals of Physics* **1959**, *8*, 343.

(47) Efros, A.; Shklovskii, B. *Journal of Physics C Solid State Physics* **1975**, *8*, L49.

(48) Rosso, K. M.; Smith, D. M.; Dupuis, M. *The Journal of chemical physics* **2003**, *118*, 6455.
(49) Iordanova, N.; Dupuis, M.; Rosso, K. M. *The Journal of chemical physics* **2005**, *122*, 144305.
(50) Deskins, N. A.; Dupuis, M. *Physical Review B* **2007**, *75*, 195212.
(51) Van der Pauw, L. *Philips Technical Review* **1958**, *20*, 220.
(52) Price, W. *Journal of Physics D: Applied Physics* **2002**, *5*, 1127.
(53) Bierwagen, O.; Pomraenke, R.; Eilers, S.; Masselink, W. *Physical Review B* **2004**, *70*, 165307.
(54) Montgomery, H. *Journal of Applied Physics* **1971**, *42*, 2971.
(55) dos Santos, C. A. M.; de Campos, A.; da Luz, M. S.; White, B. D.; Neumeier, J. J.; de Lima, B. S.; Shigue, C. Y. *Journal of Applied Physics* **2011**, *110*, 083703.
(56) Kazani, I.; De Mey, G.; Hertleer, C.; Banaszczyk, J.; Schwarz, A.; Guxho, G.; Van Langenhove, L. *Textile Research Journal* **2011**, *81*, 2117.
(57) Momma, K.; Izumi, F. *Journal of Applied Crystallography* **2011**, *44*, 1272.
(58) Li, R.; Zhang, F.; Wang, D.; Yang, J.; Li, M.; Zhu, J.; Zhou, X.; Han, H.; Li, C. *Nat Commun* **2013**, *4*, 1432.
(59) Streetman, B. G.; Banerjee, S. *Solid state electronic devices*; 6th ed.; Prentice Hall New Jersey, 2006.
(60) Hermann, A.; Ham, J. *Review of Scientific Instruments* **1965**, *36*, 1553.
(61) Parker, D.; Yahia, J. *Physical Review* **1968**, *169*, 605.
(62) van de Krol, R.; Grätzel, M. *Photoelectrochemical Hydrogen Production*, 2012.
(63) Wang, G.; Ling, Y.; Lu, X.; Qian, F.; Tong, Y.; Zhang, J. Z.; Lordi, V.; Rocha Leao, C.; Li, Y. *The Journal of Physical Chemistry C* **2013**, *117*, 10957.
(64) Abdi, F. F.; Firet, N.; van de Krol, R. *ChemCatChem* **2013**, *5*, 490.
(65) Seabold, J. A.; Choi, K.-S. *Journal of the American Chemical Society* **2012**, *134*, 2186.
(66) Abdi, F. F.; van de Krol, R. *The Journal of Physical Chemistry C* **2012**, *116*, 9398.
(67) Liang, Y.; Tsubota, T.; Mooij, L. P.; van de Krol, R. *The Journal of Physical Chemistry C* **2011**, *115*, 17594.
(68) Kavan, L.; Grätzel, M.; Gilbert, S. E.; Klemenz, C.; Scheel, H. J. *Journal of the American Chemical Society* **1996**, *118*, 6716.
(69) Finklea, H. O. *Semiconductor electrodes*; Elsevier Science Ltd, 1988.
(70) Paulauskas, I. E.; Jellison, G. E.; Boatner, L. A.; Brown, G. M. *International Journal of Electrochemistry* **2011**, *2011*.
(71) Gärtner, W. W. *Physical Review* **1959**, *116*, 84.
(72) Kennedy, J. H.; Frese, K. W. *Journal of the Electrochemical Society* **1976**, *123*, 1683.

(73) Kennedy, J. H.; Frese, K. W. *Journal of the Electrochemical Society* **1978**, *125*, 709.
(74) Chen, Z.; Forman, A. J.; Jaramillo, T. F. *The Journal of Physical Chemistry C* **2013**, *117*, 9713.
(75) Frank, S. N.; Bard, A. J. *Journal of the American Chemical Society* **1975**, *97*, 7427.

# Chapter 3: Anisotropic Small-Polaron Hopping in W:$BiVO_4$ Single Crystals[2]

## 3.1 INTRODUCTION

Monoclinic bismuth vanadate ($BiVO_4$ or BVO) is a promising photo-anode for solar water splitting because (1) its band edges are well positioned for water oxidation, (2) its band gap is modest, ~ 2.5 eV and (3) it is stable in aqueous environments when coupled with co-catalysts [1-3] However, the low electrical conductivity of BVO limits its utility as a photo-electrode [4-6]. This low conductivity was preliminarily ascribed to its charge carriers forming small polarons and a low temperature-independent Hall mobility [4].

Small polarons can form when electronic charge carriers move slowly enough to displace surrounding atoms from their equilibrium positions [7]. Thus small polarons are found in non-crystalline solids [8-10] as well as in well-ordered transition-metal [11-14] and organic [15-17] compounds where slow electronic motion is attributed to disorder and to narrow electronic energy bands respectively.

Here, we report measurements of the dc conductivity, Seebeck and Hall coefficients of n-type tungsten-doped BVO single crystals from 300-450 K. Detailed analysis of the anisotropic transport of W:BVO finds it consistent with adiabatic small-

[2] A.J.E. Rettie, W.D. Chemelewski, J. Lindemuth, J.S. McCloy, L.G. Marshall, J. Zhou, D. Emin and C.B. Mullins. "Anisotropic Small-Polaron Hopping in W:$BiVO_4$ Single Crystals", *Appl. Phys. Lett.*, **2015**, 106, 022106.
A. J. E. Rettie, L. G. Marshall and J.-S. Zhou synthesized the single crystal samples, J. Lindemuth performed electronic transport measurements. A. J. E. Rettie, W.D. Chemelewski and D. Emin performed data analysis. A. J. E. Rettie and C. B. Mullins designed the project. All authors wrote and edited the manuscript.

polaron hopping. Furthermore, we demonstrate that the anisotropy of transport is plausibly linked to structural differences in the arrangement of V ions.

## 3.2 Experimental Methods

The synthesis of single crystal samples of BVO with 0.3% W has been described in detail in Chapter 2. Four point collinear conductivity and AC field Hall effect were conducted at Lake Shore Cryotronics on an 8404 AC/DC Hall measurement system. Measurement of the Seebeck coefficient was performed using a laboratory-built apparatus at UT Austin. Experimental details, calculation of geometrical factors and a full description of the data analysis are provided in Appendix C [18].

## 3.3 Results and discussion

The unit cell of monoclinic BVO is only slightly distorted from that for a tetragonal structure (where $a = b$). Thus we describe the transport as that for a tetragonal structure, only differentiating between transport in the *ab*-plane (perpendicular to the *c*-axis) and that along the *c*-axis.

The electrical conductivities ($\sigma$) measured in the *ab*-plane and parallel to the *c*-axis are plotted versus temperature in Figure 3.1a. These measurements agree with our previous work (See Chapter 2). The anisotropy ratio of the conductivity $\sigma_{ab}/\sigma_c = 2.3 \pm 0.4$ is constant over the temperature range 300-450 K. As shown in Figure 3.1b, this data can be described with the formula:

$$\sigma(T) = \sigma_0(T) exp\left(-\frac{E_\sigma}{\kappa T}\right), \qquad (3.1)$$

with the pre-exponential factor $\sigma_0(T) \propto 1/T$, where $E_\sigma$ is the conductivity activation energy, $\kappa$ is the Boltzmann constant and $T$ is the absolute temperature. The first two columns of Table I list the activation energies and pre-exponential factors at 300 K for

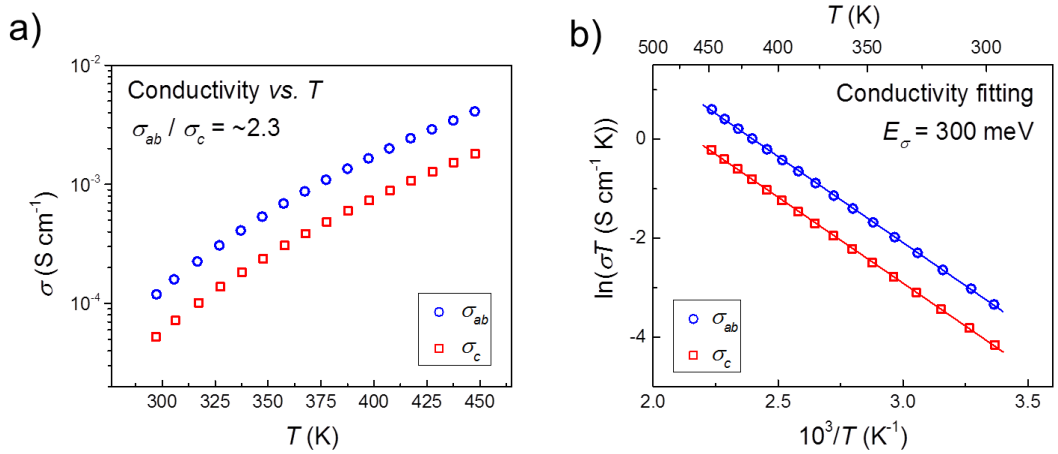


**Figure. 3.1:** The dc electrical conductivities in the *ab*-plane and parallel to the *c*-axis are plotted versus temperature in sub-figure **a)**. The solid lines in sub-figure **b)** show the data's fit to Eq. (3.1).

transport in the *ab*-plane and in the *c*-direction.

The Seebeck coefficients are plotted versus 103/T in Fig. 2. This data has been fit to

$$S = -\frac{\kappa}{e}\left(\frac{E_S}{\kappa T} + A\right), \qquad (3.2)$$

where $e$ is the magnitude of an electron's charge, $E_S$ is the Seebeck coefficient's characteristic energy, and $A$ is a dimensionless constant [7,10]. The third and fourth columns of Table 3.1 list these fitting parameters. Significantly, the characteristic Seebeck energies are much smaller than $E_\sigma$ (300 meV). These energy differences indicate that the activated conductivity is produced by carriers' thermally assisted hopping rather than from trap-modulated transport [7,19].

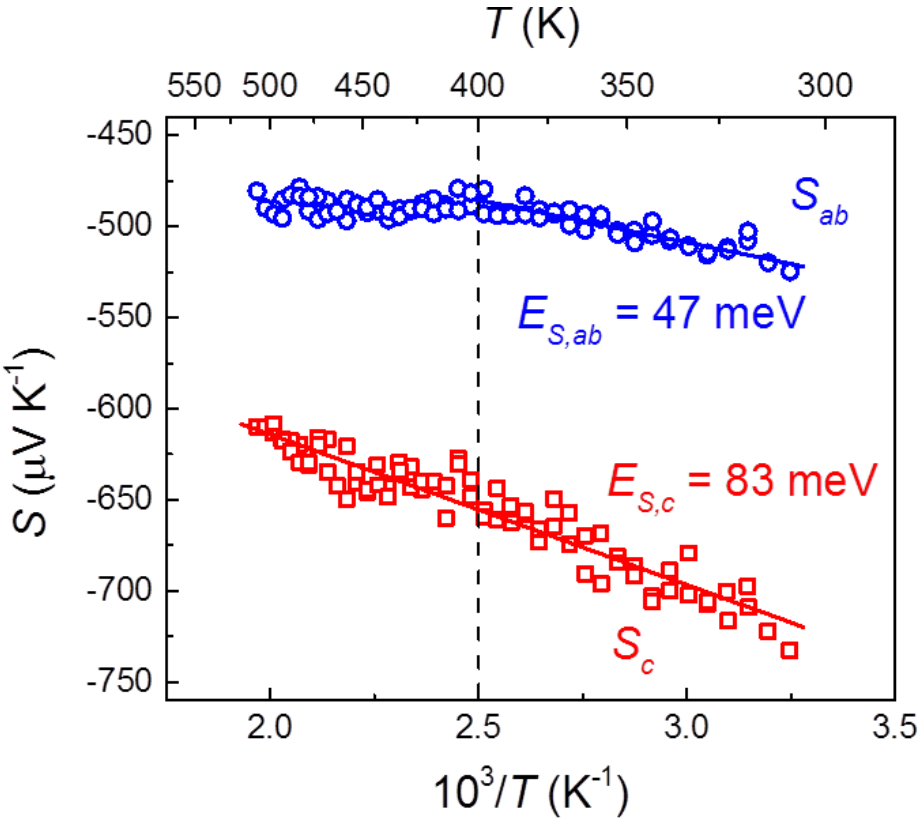


**Figure. 3.2:** Seebeck coefficients measured in the *ab*-plane and along the *c*-axis are plotted versus reciprocal temperature. Fits to Eq. (3.2) are shown with solid lines. The dashed vertical line at 400 K highlights a change of slope.

| | $E_\sigma$ (meV) | $\sigma_0$ (S cm$^{-1}$) at 300 K | $E_S$ (meV) | $A$ (dimensionless) |
|---|---|---|---|---|
| *ab*-plane | 300 ± 1 | 14.2 ± 0.4 | 47 ± 4 | 4.3 ± 0.1 |
| *c*-axis | 300 ± 1 | 6.1 ± 0.2 | 83 ± 3 | 5.2 ± 0.1 |

**Table 3.1:** Conductivity and Seebeck coefficient fitting parameters

The Hall mobility in the *ab*-plane is the product of the Hall constant $R_{Hall}$ measured with the magnetic field parallel to the *c*-axis and the electrical conductivity in the *ab*-plane, $\mu_{Hall} \equiv \sigma_{ab} R_{Hall}$. The Hall mobility in the *ab*-plane is plotted against reciprocal temperature in Figure 3.3. For comparison we also plot the drift mobility in the

*ab*-plane deduced from measurements of the conductivity and Seebeck coefficients in the *ab*-plane, $\mu_{d,ab} \propto \exp[-(E_\sigma - E_{s,ab})/\kappa T]$, where we have chosen the intercept at $1/T = 0$ to be 1 $cm^2\ V^{-1}\ s^{-1}$. This assumption is consistent with small-polaron hopping in the adiabatic regime, whose validity will be demonstrated in the following analysis.

BVO adopts a monoclinic scheelite structure at ambient conditions (space group *I*2/*b*, $a$ = 5.1935 Å, $b$ = 5.0898 Å, $c$ = 11.6972 Å, and $\gamma$ = 90.387°, Figure 3.4a) [20]. Although dopants can alter the lattice parameters, the changes are negligible at the dopant concentrations considered here [21] The conduction band of BVO is of primarily V 3*d*

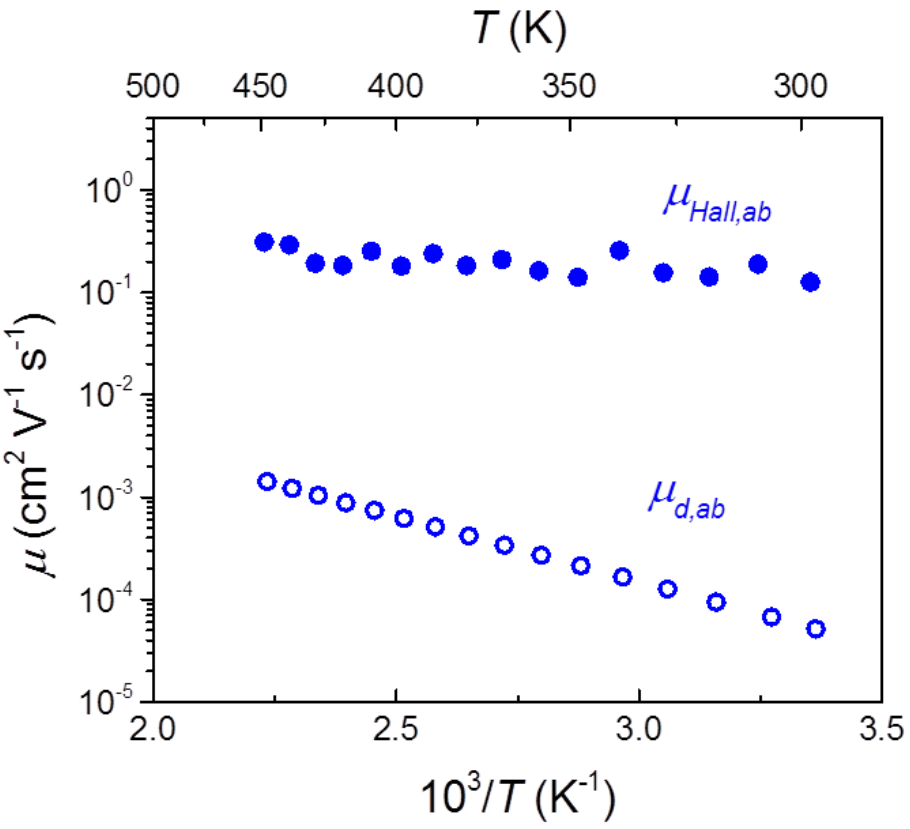


**Figure. 3.3:** Hall and deduced-drift mobilities in the *ab*-plane are plotted versus reciprocal temperature.

character while the valence band is made up of O 2*p* and Bi 6*s* states [22]. W dopants substitute for V atoms and act as electron donors [4]. Excess electrons in BVO have been predicted to favorably localize on vanadium atoms, [23] thus we presume hopping to occur between the V sites.

Let us consider the physical origin of the transport anisotropy in W:BVO (Figures 3.1 and 3.2). Nearest-neighbor (NN) jumps can be viewed as proceeding along zig-zag chains in the *a*-*c* and *b*-*c* directions with jump lengths of 3.8 Å and 4 Å, respectively. As seen in Figure 3.4b, a combination of such NN hops generates motion along the *c*-axis. By themselves NN jumps would generate nearly isotropic hopping. However, as depicted by the dashed lines in Figure 3.4b, next-nearest-neighbor (NNN) hops in the *ab*-plane (~5.2 Å) are only slightly longer than NN hops. By contrast, NNN hops with a significant *c*-axis component (~6.9 Å) are much longer than NN hops. Therefore the structure of BVO appears to support anisotropic hopping transport. For example, such anisotropic transport would result if *c*-axis motion is dominated by NN hopping while *ab*-plane transport is a convolution of NN and NNN jumps. Alternatively stated, the band of small-polaron states is anisotropic with it being wider for motion in the *ab*-plane than along the *c*-axis (Figure 3.4c).

An anisotropic small-polaron conduction band that is populated by thermally exciting electrons from lower-lying donor states of energy $E_d$ is akin to that of a conventional semiconductor. The position of the chemical potential $\mu$ is then determined from the requirement that the number of holes in the donor band equals the number of small-polarons in the conduction band:

$$N_d e^{(E_d-\mu)/\kappa T} = N_{ab}(T) e^{-(E_{m,ab}-\mu)/\kappa T} + N_c(T) e^{-(E_{m,c}-\mu)/\kappa T}, \qquad (3.3)$$

where $N_d$ denotes the density of donors while $N_{ab}(T)$ and $N_c(T)$ represent the densities of small-polaron states near their minima at energies $E_{m,ab}$ and $E_{m,c}$. The chemical potential is then

$$\mu = \frac{E_{m,ab}+E_d}{2} + \frac{\kappa T}{2} ln\left[\frac{N_d}{N_{ab}(T)}\right] - \frac{\kappa T}{2} ln\left[1 + \frac{N_c(T)}{N_{ab}(T)} e^{-(E_{m,c}-E_{m,ab})/\kappa T}\right] \cong \frac{E_{m,ab}+E_d}{2} + \frac{\kappa T}{2} ln\left[\frac{N_d}{N_{ab}(T)}\right]. \quad (3.4)$$

Analogous to $\sigma = ne\mu_d$, the anisotropic values of $\sigma_0$ are the electronic charge $e$ multiplied by the pre-exponential factors from the thermally activated carrier density and small-polaron mobility. The pre-exponential factors for the densities of carriers in the appropriate transport states for motion in the *ab*-plane and in the *c*-direction are $\cong [N_d N_{ab}(T)]^{1/2}$ and $\cong N_c(T)[N_d/N_{ab}(T)]^{1/2}$ respectively. Since electronic carriers are usually able to adjust to the relatively slow movements of the solid's atoms, small-polaron hops are generally adiabatic [7]. The corresponding pre-exponential factors of the anisotropic mobilities are then $ega^2 \nu_0/\kappa T$, where a denotes the jump distance, $\nu_0$ represents the characteristic vibration frequency and $g$ is a numerical factor associated with the hopping sites' geometrical arrangement. In accord with the results of Table 3.1, the calculated conductivity pre-exponential factors for hopping within the *ab*-plane and in the *c*-direction are respectively $\sigma_{o,ab} \cong 10$ S cm$^{-1}$ and $\sigma_{o,c} \cong 5$ S cm$^{-1}$ with $\nu_0 = 2 \times 10^{13}$ Hz, thus hopping is adiabatic. Since the doping level of our W:BVO is quite small (0.3%), our values for $\sigma_0$ are orders-of-magnitude smaller than those for intrinsic small-polaron hopping, $10^2 - 10^3$ S cm$^{-1}$ [7,8].

The Seebeck coefficient is the entropy transported with a charge carrier divided by its charge [25]. In most instances, the transported entropy is just the entropy-of-mixing

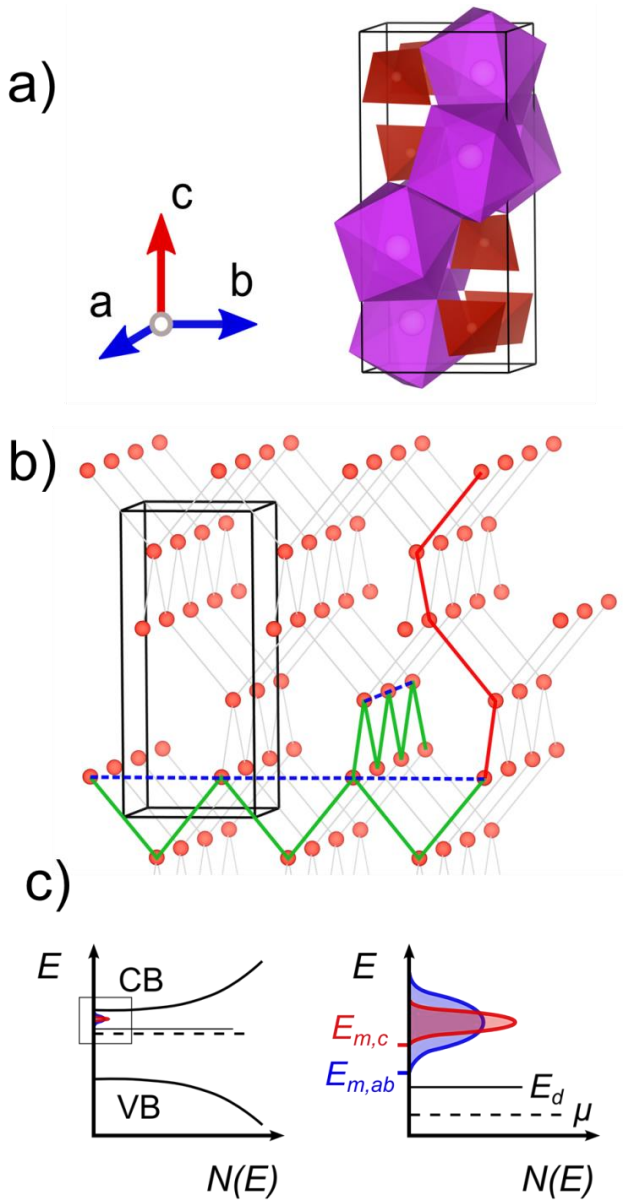


**Figure 3.4: a)** Monoclinic BVO unit cell showing $BiO_8$ (purple) and $VO_4$ units (red) and principal axes created with VESTA software [24]. **b)** VESTA rendition of a 3 × 2 × 1 super-cell illustrating the vanadium atom sub-lattice. NN hopping paths are indicated in *ab*-plane and *c*-axis with green and red solid lines respectively. NNN jumps in the *ab*-plane are shown with blue dashed lines. **c)** Left: The location of small-polaron states. Right: Schematic illustration of the anisotropy of the width of the small-polaron band. Symmetrical distributions have been used for simplicity.

arising from adding a charge carrier to the relevant transport states. Then the Seebeck coefficient depends on the carrier density and the density of thermally accessible transport states. Increasing the carrier density (e.g. by raising the temperature) decreases the Seebeck coefficient's magnitude. Conversely increasing the number of thermally accessible transport states (by raising the temperature) increases the Seebeck coefficient's magnitude. The decrease of the magnitudes of the Seebeck coefficients of Figure 3.2 with rising temperature implies the predominance of the former effect, that is, the W donors are partially ionized at room temperature.

The Seebeck coefficient for transport within the *ab*-plane and *c*-direction just depends on the energies of small-polaron states associated with transport in these directions, $E_{ab}$ and $E_c$ [7,25],

$$S_{ab} = -\frac{\kappa}{e}\frac{\langle E_{ab}-\mu\rangle_{ab}}{\kappa T} \tag{3.5}$$

and

$$S_c = -\frac{\kappa}{e}\frac{\langle E_c-\mu\rangle_c}{\kappa T}, \tag{3.6}$$

where the brackets denote an average over the thermally accessible transport states. Incorporating Eq. (3.4) into Eqs. (3.5) and (3.6) these Seebeck coefficients become

$$S_{ab} \cong -\frac{\kappa}{e}\left\{\frac{(E_{m,ab}-E_d)/2}{\kappa T} + \frac{1}{2}ln\left[\frac{N_{ab}(T)}{N_d}\right] + \frac{\langle E_{ab}-E_{m,ab}\rangle_{ab}}{\kappa T}\right\} \tag{3.7}$$

and

$$S_c \cong -\frac{\kappa}{e}\left\{\frac{(E_{m,c}-E_{m,ab})+(E_{m,ab}-E_d)/2}{\kappa T} + \frac{1}{2}ln\left[\frac{N_{ab}(T)}{N_d}\right] + \frac{\langle E_c-E_{m,c}\rangle_c}{\kappa T}\right\}. \tag{3.8}$$

There are three terms within the curly brackets of both Eqs. (3.7) and (3.8). The first term falls with increasing temperature, the second term rises weakly with increasing temperature and the final term is the nearly temperature-independent "heat-of-transport" constant, $A$. The relatively strong temperature dependence of the first term ensures that the magnitude of the Seebeck coefficient falls with increasing temperature. The competition between the first and second terms is responsible for the change in slope observed at ~400 K in the *ab*-plane (Figure 3.2). Furthermore, the first term in the expression for the Seebeck coefficient for motion in the *c*-direction, Eq. (3.8), exceeds that for motion within the *ab*-plane, Eq. (3.7), by the energy difference $E_{m,c} - E_{m,ab}$. Twice this energy difference, 2(0.08 eV – 0.05 eV) = 0.06 eV, is compatible with the requirement that the net small-polaron-bandwidth be less than the characteristic phonon energy. The relatively large heat-of-transport constants, $A_{ab} = 4.3$ and $A_c = 5.2$, are also consistent with an anisotropic small-polaron band whose width is less than the phonon energy but greater than or comparable to the thermal energy $\kappa$T [7,8,10]. Finally, finding $A_c > A_{ab}$ implies that the anisotropic small-polaron band is more sharply peaked in the *c*-direction than in the *ab*-plane [10] (Figure 3.4c).

The customary drift mobility is defined as a carrier's drift velocity per unit applied electric field. For high-temperature adiabatic small-polaron hopping this mobility is the product of the pre-exponential factor given above, $ega^2\nu_0/\kappa T$ (~1 cm$^2$ V$^{-1}$ s$^{-1}$ at 300 K) and an Arrhenius factor $\exp(-E_a/\kappa T)$, where the mobility activation energy, $E_a$ is usually greater than $h\nu_0$. The mobility activation energies are the differences between $E_\sigma$ and $E_S$ in the *ab*-plane and *c*-direction. Semiclassical small-polaron hopping is implied since these energy differences (250 meV and 220 meV respectively) greatly exceed the characteristic phonon energy (on the order of 0.1 eV). For motion in the *ab*-plane the drift mobility at 300 K is about $5 \times 10^{-5}$ cm$^2$ V$^{-1}$ s$^{-1}$. This value is consistent with that inferred

from time-resolved microwave conductivity (TRMC) measurements, ~ $10^{-4}$ $cm^2$ $V^{-1}$ $s^{-1}$ at 300 K [5]. The larger mobility activation energy in the *ab*-plane is in accord with slightly longer NNN transfers, as $E_a$ increases with the length of the hop [for example, c.f. Fig. 11.4 of Ref. (5)].

The Hall mobility is defined as the angle per unit applied magnetic field that a drifting carrier is deflected by this field's application. For free carriers the drift and Hall mobilities equal one another. However, for small-polaron hopping the activation energy of the Hall mobility is < $E_a/3$ [7,26-28]. As a result a small-polaron's Hall mobility is generally much larger and much less temperature dependent than its drift mobility. The data of Figure 3.3 shows that the Hall mobility we measure for our W:BVO is consistent with small-polaron hopping.

### 3.4 CONCLUSIONS

In summary we have reported electronic transport measurements of W:BVO single crystals and established that electrons in this material form small polarons. The anisotropic transport was reconciled by including NNN transfers, which foster enhanced hopping in the ab-plane. Based on our findings, the low electrical conductivity which limits the utility of W:BVO as a photo-anode for water splitting results from the very low thermally activated mobility intrinsic to small polarons. However, knowing that the carriers are small polarons suggests a means of circumventing this deficiency. In particular, a small-polaron generally exhibits a broad absorption band centered near ~ $4E_a$, about 1 eV for BVO [7,29]. For BVO this small-polaron absorption band lies well below the strong intrinsic inter-band absorption that begins at 2.5 eV. Significantly, small-polarons' absorptions produce small-polaron hops [c.f. Fig 9.3 of Ref. (5)]. Thus,

sub-bandgap illumination of a W:BVO photo-anode should increase its electrical conductivity. This optical remedy for the low dark conductivity of W:BVO exploits its carriers being small polarons and is the subject of further study in our laboratory.

## REFERENCES


(1) Kim, T. W.; Choi, K.-S. *Science* **2014**, *343*, 990.

(2) Abdi, F. F.; Han, L.; Smets, A. H. M.; Zeman, M.; Dam, B.; van de Krol, R. *Nat. Commun.* **2013**, *4*, 1.

(3) Berglund, S. P.; Rettie, A. J. E.; Hoang, S.; Mullins, C. B. *Phys. Chem. Chem. Phys.* **2012**, *14*, 7065.

(4) Rettie, A. J. E.; Lee, H. C.; Marshall, L. G.; Lin, J.-F.; Capan, C.; Lindemuth, J.; McCloy, J. S.; Zhou, J.; Bard, A. J.; Mullins, C. B. *J. Am. Chem. Soc.* **2013**, *135*, 11389.

(5) Abdi, F. F.; Savenije, T. J.; May, M. M.; Dam, B.; van de Krol, R. *J. Phys. Chem. Lett.* **2013**, *4*, 2752.

(6) Park, H. S.; Kweon, K. E.; Ye, H.; Paek, E.; Hwang, G. S.; Bard, A. J. *J. Phys. Chem. C* **2011**, *115*, 17870.

(7) Emin, D. *Polarons*; 1st ed.; Cambridge University Press: New York, 2013.

(8) Emin, D.; Seager, C.; Quinn, R. K. *Phys. Rev. Lett.* **1972**, *28*, 813.

(9) Sayer, M.; Mansingh, A. *J. Non-Cryst. Solids* **1983**, *58*, 91.

(10) Baily, S. A.; Emin, D. *Phys. Rev. B* **2006**, *73*, 165211.

(11) Bosman, A.; Van Daal, H. *Adv. Phys.* **1970**, *19*, 1.

(12) Nagels, P. In *The Hall Effect and Its Applications*; Springer: 1980, p 253.

(13) Jaime, M.; Hardner, H.; Salamon, M.; Rubinstein, M.; Dorsey, P.; Emin, D. *Phys. Rev. Lett.* **1997**, *78*, 951.

(14) Zhao, B.; Kaspar, T. C.; Droubay, T. C.; McCloy, J.; Bowden, M. E.; Shutthanandan, V.; Heald, S. M.; Chambers, S. A. *Phys. Rev. B* **2011**, *84*, 245325/1.

(15) Yoo, K.-H.; Ha, D.; Lee, J.-O.; Park, J.; Kim, J.; Kim, J.; Lee, H.-Y.; Kawai, T.; Choi, H. Y. *Phys. Rev. Lett.* **2001**, *87*, 198102.

(16) Alexandre, S. S.; Artacho, E.; Soler, J. M.; Chacham, H. *Phys. Rev. Lett.* **2003**, *91*, 108105.

(17) Venkateshvaran, D.; Nikolka, M.; Sadhanala, A.; Lemaur, V.; Zelazny, M.; Kepa, M.; Hurhangee, M.; Kronemeijer, A. J.; Pecunia, V.; Nasrallah, I.; Romanov, I.; Broch, K.; McCulloch, I.; Emin, D.; Olivier, Y.; Cornil, J.; Beljonne, D.; Sirringhaus, H. *Nature* **2014**, *advance online publication*.

(18) See Supplemental Material at [URL will be inserted by publisher] for experimental details, calculation of geometrical factors and a full description of the data analysis.

(19) Lago, J.; Battle, P.; Rosseinsky, M.; Coldea, A.; Singleton, J. *J. Phys. Condens. Matter* **2003**, *15*, 6817.
(20) Sleight, A. W.; Chen, H. Y.; Ferretti, A.; Cox, D. E. *Mater. Res. Bull.* **1979**, *14*, 1571.
(21) Sleight, A. W.; Aykan, K.; Rogers, D. B. *J. Solid State Chem.* **1975**, *13*, 231.
(22) Walsh, A.; Yan, Y.; Huda, M. N.; Al-Jassim, M. M.; Wei, S.-H. *Chem. Mater.* **2009**, *21*, 547.
(23) Kweon, K. E.; Hwang, G. S.; Kim, J.; Kim, S.; Kim, S. *Phys. Chem. Chem. Phys.* **2014**, *advance online publication*.
(24) Momma, K.; Izumi, F. *J. Appl. Crystallogr.* **2011**, *44*, 1272.
(25) Emin, D. In *Wiley Encyclopedia of Electrical and Electronics Engineering*; Webster, J. G., Ed.; Wiley: New York, 2002.
(26) Friedman, L.; Holstein, T. *Ann. Phys.* **1963**, *21*, 494.
(27) Emin, D.; Holstein, T. *Ann. Phys.* **1969**, *53*, 439.
(28) Emin, D. *Ann. Phys.* **1971**, *64*, 336.
(29) Emin, D. *Phys. Rev. B* **1993**, *48*, 13691.

# Chapter 4: Pulsed Laser Deposition of Epitaxial and Polycrystalline Bismuth Vanadate Thin Films[3]

## 4.1 INTRODUCTION

Efficient photoelectrochemical (PEC) water splitting has been lofty goal of the scientific community for over 40 years. [1,2]. A potential system for accomplishing this process is a tandem cell arrangement, that consists of a photo-anode and cathode illuminated by sunlight and submerged in a suitable aqueous electrolyte [3,4]. Monoclinic bismuth vanadate ($BiVO_4$, BVO) is a popular candidate material for the photoanode due to its moderate band gap (2.4-2.6 eV), well positioned band edges (conduction band at ~0 V vs. reversible hydrogen electrode (RHE)) and stability when coupled with water oxidation electrocatalysts [5].

BVO thin films have been synthesized by numerous techniques including metal-organic deposition [6,7], drop casting [8,9], electrodeposition [10], spray pyrolysis [11], physical vapor deposition [12,13], reactive sputtering [14], chemical vapor deposition [15], dip-coating [16] and molecular-beam epitaxy (MBE) [17]. There has been a focus on nanostructured electrodes, as these have led to the highest photocurrents. However, many of the desirable properties of nanostructured films: high surface area, short carrier transport lengths and light scattering make them problematic to characterize electrically and electrochemically. Thus, there is a need for well-defined model systems.

---

[3] A.J.E. Rettie, S. Mozaffari, M.D. McDaniel, K.N. Pearson, J.G. Ekerdt, J.T. Markert and C.B. Mullins. "Pulsed Laser Deposition of Epitaxial and Polycrystalline Bismuth Vanadate Thin Films", *J. Phys. Chem. C*, **2014**, 11 (46), p 26543.
A. J. E. Rettie, S. Mozaffari and K. N. Pearson synthesized the samples. M.D. McDaniel performed XPS measurements. A. J. E. Rettie performed experiments, analyzed data and wrote the paper. A. J. E. Rettie and C. B. Mullins designed the project. All authors wrote and edited the manuscript.

Single crystals are invaluable to advancing fundamental understanding of materials. Further, they often exhibit better charge transport properties – a critical bottleneck for BVO photoanodes [8,13,18] – than their polycrystalline counterparts. Despite this, photoelectrodes made using bulk single crystals of metal oxides exhibit low photocurrents [19,20], likely due in part to the sample thickness (tens of microns) that prevents carriers from reaching the back contact. We decided to explore techniques capable of producing epitaxial thin films with thicknesses on the order of hundreds of nanometers. Typically, material is deposited from the gas phase onto a heated substrate, whose lattice parameters are matched to those of the desired film. Of the available methods, pulsed laser deposition (PLD) has had remarkable success in producing a wide range of epitaxial metal oxide thin films [21]. A target (usually similar in composition to the desired film) is ablated by laser, producing a plume of material that lands on the substrate. Facets of PLD that distinguish it from other techniques are the high flux of incident material followed by a relatively long period before the next pulse and the large pressure of reactive or inert gas used during deposition.

The choice of an appropriate substrate is essential to obtain epitaxial films of high quality. Cubic yttria-stabilized zirconia (YSZ, $a$ = 5.145 Å [17]) is well lattice-matched to the base of the monoclinic BVO unit cell ($a$ = 5.1956 Å, b = 5.0935 Å [22]) and should result in $c$-oriented crystal growth. Indeed, Stoughton et al. synthesized epitaxial BVO (001) on YSZ (100) by reactive MBE [17]. Other candidates with excellent lattice matching were cubic indium oxide ($In_2O_3$, $a$ = 10.118 Å [23]), tetragonal cerium vanadate ($CeVO_4$, $a$ = 7.4 Å [24]), and lutetium aluminate ($LuAlO_3$, $a$ = 5.1 Å, $b$ = 5.33 Å [25,26]). YSZ was chosen due to the availability of large single crystal substrates. To the best of our knowledge, this is the first report of epitaxial BVO films via PLD.

Additionally, dense, continuous polycrystalline BVO films are desirable for fundamental measurements and are difficult to prepare, with most techniques leaving areas of exposed substrate [13,16,18]. Chen et al. recently showed that continuous films could be made by reactive sputtering of $Bi_2O_3$ and V targets [14] and we hypothesized that PLD-grown films would also have this desirable morphology. The PLD of polycrystalline BVO films is relatively unstudied [27].

First, we describe the experimental conditions used to achieve epitaxial and polycrystalline growth. Next, we analyzed the film quality, morphology and composition by X-ray diffraction (XRD), atomic force microscopy (AFM), scanning electron microscopy (SEM) and x-ray photoelectron spectroscopy (XPS). UV-Vis spectroscopy was used to characterize the optical properties of the films. Finally, polycrystalline films on conductive substrates were evaluated as photoanodes for water oxidation.

### 4.2 Experimental Methods

Films were synthesized in a custom-built PLD vacuum chamber with a base pressure of $10^{-6}$ Torr and a Lambda Physik COMPex 201 KrF (248 nm) pulsed excimer laser. The laser ablated a rotating ceramic target, producing a plume of material that deposited on a substrate positioned in the center of the chamber. The laser pulse energy was 100 mJ and the fluence was ~3-6 J $cm^{-2}$. Repetition rates ranged from 1-10 Hz. Single crystal yttria-stabilized zirconia (YSZ) substrates (5×5 $mm^2$, MTI) were fixed to a heater puck using silver paste (Epoxy Technology), while conductive glass substrates (fluorine-doped tin oxide (FTO, Hartford Glass) were held in place with double-sided Scotch tape. The glass substrates were typically 10×10 $mm^2$ in size. YSZ and FTO substrates were cleaned prior to deposition by sonication in acetone or in a Contrex

detergent and ethanol mixture, respectively. Pre-ablation to clean the target surface and ample wait time for the temperature and pressure to reach steady state preceded each run. After growth, the heater was turned off immediately and the samples were cooled under the atmosphere used for deposition. Substrate temperatures were determined by a calibrating a type K thermocouple adhered directly to the substrate holder with silver epoxy, against a sceond type K thermocouple in close proximity to the substrate holder that could be monitored during deposition. Post-annealing in air at 500 °C for 1 hr in a box furnace (Neytech) was performed to crystallize the polycrystalline films. As-deposited polycrystalline films were translucent black/grey.

Ceramic targets were made by solid-state methods from powders of bismuth oxide ($Bi_2O_3$, 99.999%) and vanadium oxide ($V_2O_5$, 99.6%, both Sigma-Aldrich). These were ground into a homogeneous mixture (8-10 g total), fired at 600 °C for 10 hr, ground again and fired at 800 °C for 10 hr to complete the solid-state reaction. After grinding for a final time, PVA binder was added (1% by weight) and the powder was pressed into a ~1.375 in. diameter target. Heating at 400 °C for 10 hrs was performed to decompose the binder, followed by sintering at 700-800 °C for 10 hr. All annealing was done in air in a box furnace and all samples were allowed to cool naturally. A commercial ITO ($In_2O_3$:$SnO_2$; 90%:10%) sputtering target (Alfa Aesar) was used for deposition of ITO films.

The crystal phase was determined by XRD using a Philips X'PERT diffractometer equipped with Cu Kα X-rays ($\lambda$ = 1.54056 Å). For epitaxial films, each sample was mounted on non-diffracting putty in a stainless steel holder and pressed flat using a glass slide. Alignment was achieved using the (200) reflection of YSZ. Off-axis phi scans were performed using a Bruker-Nonius D8 diffractometer with Cu Kα X-rays. Topographical images of the film surfaces were taken with a Veeco Atomic Force

Microscope (AFM), ex situ at room temperature using the tapping mode. Al-coated silicon cantilevers (Bruker) with resonance frequencies of 300-350 kHz and force constants of 20-80 N/m were used. Gwyddion software (version 2.32) was used to process the raw AFM images. The composition of the films was determined using a custom-built X-ray photoelectron spectrometer (XPS) with a VG Scienta R3000 analyzer and monochromated Al Kα source at 1486.6 eV. High resolution spectra of the Bi 4*f*, V 2p, and O 1*s* core levels were measured using a pass energy of 100 eV with an analyzer slit width of 0.4 mm. Each high-resolution scan was measured four times and summed, using 50 meV steps with a dwell time of 157 ms per step. CasaXPS (Version 2.3.15) software and Wagner sensitivity factors were used to analyze the XPS spectra. The adventitious carbon 1*s* peak was used as a reference with a binding energy (BE) of 285 eV. The error in the measurement of the BE associated with this procedure varies from ±0.1 to 0.2 eV [28,29]. Diffuse reflectance UV−vis spectra were measured with a Cary 500 spectrophotometer attached to an integrating sphere (Labsphere DRA-CA-5500). Film thickness on insulating substrates was obtained with a Veeco NT9100 Optical Profiler.

Photoelectrochemical (PEC) measurements were conducted in a glass 3-electrode cell using the BVO film as the working electrode, Ag/AgCl (1 M KCl) as the reference electrode and Pt wire as the counter electrode. All potentials reported here are versus the reversible $H_2$ electrode (RHE),

$$E_{RHE} = E_{Ag/AgCl} + 0.059\times\text{pH} + E^{\circ}_{Ag/AgCl}\,(1\text{ M KCl}) \qquad (4.1)$$

where, $E^{\circ}_{Ag/AgCl}$ (1 M KCl) = 0.236 V at 25 °C [30].

Illumination was accomplished using a 150 W Xe lamp (Newport) with an AM1.5G filter (Newport) calibrated to 100 mW $cm^{-2}$ using a thermopile. A monochromator (Photon Technology International), silicon photodetector (model 818-UV, Newport), and optical power meter (model 1830-C, Newport) were used to determine the incident photon to current conversion efficiency (IPCE). IPCE values were calculated using the formula:

$$\mathrm{IPCE}(\lambda) = (1240 \cdot j(\lambda)) / (\lambda \cdot P(\lambda)) \times 100 \qquad (4.2)$$

where, $\lambda$ is the wavelength (nm), $j$ is the photocurrent density (mA $cm^{-2}$) and $P$ is the incident power density of the monochromated light (mW $cm^{-2}$). Illumination was from the back-side of the PEC cell in most cases, passing through the FTO-glass substrate unless otherwise indicated. The glass-side of the films was masked off, so that the illuminated area closely matched the area of the sample in contact with electrolyte: ~0.212 $cm^2$.

The electrolyte solution was 0.1 M potassium phosphate buffer and 0.1 M sodium sulfate ($Na_2SO_4$) solution with 0.1 M sodium sulfite ($Na_2SO_3$, all Fisher) added as a hole scavenger in some cases. A CH Instruments 660D potentiostat was used for all electrochemical measurements. The scan rate was 10 mV $s^{-1}$.

## 4.3 Results and Discussion

### 4.3.1 Synthesis

Several parameters are controlled during PLD growth of epitaxial oxides: substrate temperature ($T_{sub}$), $O_2$ pressure ($p_{O2}$), target composition, laser energy and

repetition rate. Bi is known to be a highly volatile component in other Bi-containing materials synthesized at elevated temperatures [31-33]. To determine the target composition that would result in a stoichiometric film at the temperatures required for epitaxy, Si substrates were used with targets of various Bi:V ratios and the film composition measured by XPS. Increasing oxygen pressure was found to increase the yield of Bi in the films, but was a less critical parameter than target composition. Laser energy was varied between 3 and 6 J $cm^{-2}$ and with a repetition rate between 1 and 10 Hz – neither of these variables affected film composition noticeably. Targets ranged from orange (Bi:V = ~1:1) to pale yellow (Bi:V = ~6:1) in appearance (Figure C.1 in Appendix C). A blue-purple plume was produced from all targets during ablation.

At the optimized synthesis conditions for epitaxial films detailed in Table 4.1, a characteristic yellow color was observed after deposition. The thickness of epitaxial films was determined by masking off a corner of the film and using phase sensitive optical profilometry to measure the step height (Figure C.2 in Appendix C). Unless otherwise specified, epitaxial BVO films were ~65 nm thick, corresponding to a growth rate of ~0.36 Å/pulse.

| Substrate | $T_{sub}$ (°C) | Bi:V ratio of target | Rate (Hz) | $pO_2$ (Torr) | Film composition (%) | | FWHM (004) peak (°) |
|---|---|---|---|---|---|---|---|
| | | | | | Bi | V | |
| YSZ (100) | 600 | 6:1 | 1 | | 47 | 53 | 0.33 |
| FTO-glass | 30 | 1:1 | 10 | | 50 | 50 | - |

**Table 4.1:** Optimized deposition conditions for epitaxial and polycrystalline growth.

### 4.3.2 Crystal Structure and Phase

X-ray diffraction (XRD) techniques were used to analyze film orientation, quality and phase. Figure 4.1a depicts a typical $\theta$-$2\theta$ scan of epitaxial BVO on cubic YSZ (100).

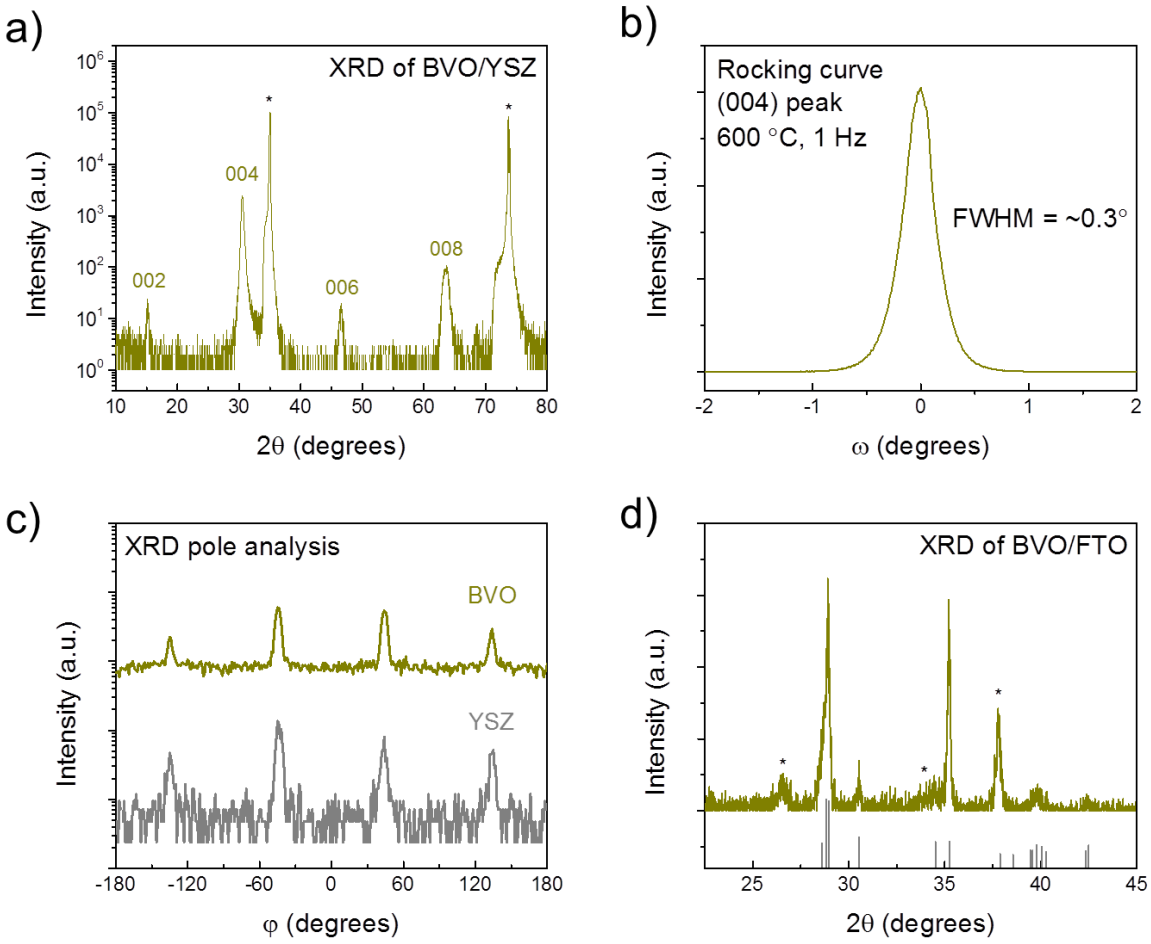


**Figure 4.1: a)** $\theta$-$2\theta$ XRD scan of BVO(65 nm)/YSZ showing only (00*l*) reflections of BVO. **b)** Rocking curve around the (004) peak of the epitaxial BVO film in Table 1, around $2\theta = 30.545°$. **c)** Off-axis phi scans of the (118) reflection of monoclinic BVO with a tilt angle, $\psi = 21.88^{\circ}$ and of the (115) reflection of the YSZ. **d)** XRD of a 300 nm thick polycrystalline BVO film on FTO glass. Grey vertical lines represent the reference pattern for monoclinic BVO (PDF#01-074-4893) [22]. The * symbol indicates peaks from the underlying substrate.

Only the (00*l*) reflections of the BVO were present, indicating that growth was *c*-axis oriented: BVO (001) || YSZ (001). Rocking curves around the (004) film peak displayed an optimized full width half maximum (FWHM) of ~0.3° (Figure 4.1b). The repetition rate was found to have a slight influence on the film quality (Figure C.3 in Appendix C) with slower grown films having a smaller FWHM of the (004) peak. $\varphi$-scans were used to discern in-plane epitaxy. Suitable off-axis reflections were chosen based on their intensity and the geometry of the diffractometer. The near-identical azimuthal positions of the BVO (118) peaks relative to the YSZ (115) peaks shown in Figure 4.1c confirm that the in-plane relationship was BVO [100] || YSZ [100] or BVO [010] || YSZ [010].

The monoclinic scheelite phase of BVO is the most photochemically active [34] and the most stable at ambient conditions. However, BVO undergoes a ferroelastic phase transition upon application of high temperature ($T_c$ = 528 K [35]), pressure [36] or doping [37] to the tetragonal scheelite structure ($a$ = 5.147 Å, PDF#01-074-4892 [22]). We questioned whether the superior lattice match of YSZ to the tetragonal scheelite structure could stabilize this less active phase at room temperature, however the (002) and (006) reflections at 15.136° and 46.547°, respectively, (Figure 4.1a) are unique to monoclinic BVO. It is likely that the films crystallized as the tetragonal scheelite BVO (as $T_{sub} > T_c$) and underwent a phase transition during cooling.

Polycrystalline films were confirmed as monoclinic BVO via XRD (Figure 4.1d), but with a slight preferred *b*-axis orientation (higher intensity 020 peak at 35.238°). The reason for slightly preferred *b*-orientation relative to a randomly oriented sample is not known, but has also been observed in sputtered films on ITO-glass [14].

### 4.3.3 Film Morphology

AFM was utilized to gain information about the film surface as undoped BVO films on YSZ substrates were highly insulating. The epitaxial films consisted of irregularly shaped, smooth grains, hundreds of nanometers in size (Figure 4.2a and C.4a). AFM images of the early stages of deposition (Figure 4.2b and C.4b) clearly show a 3-

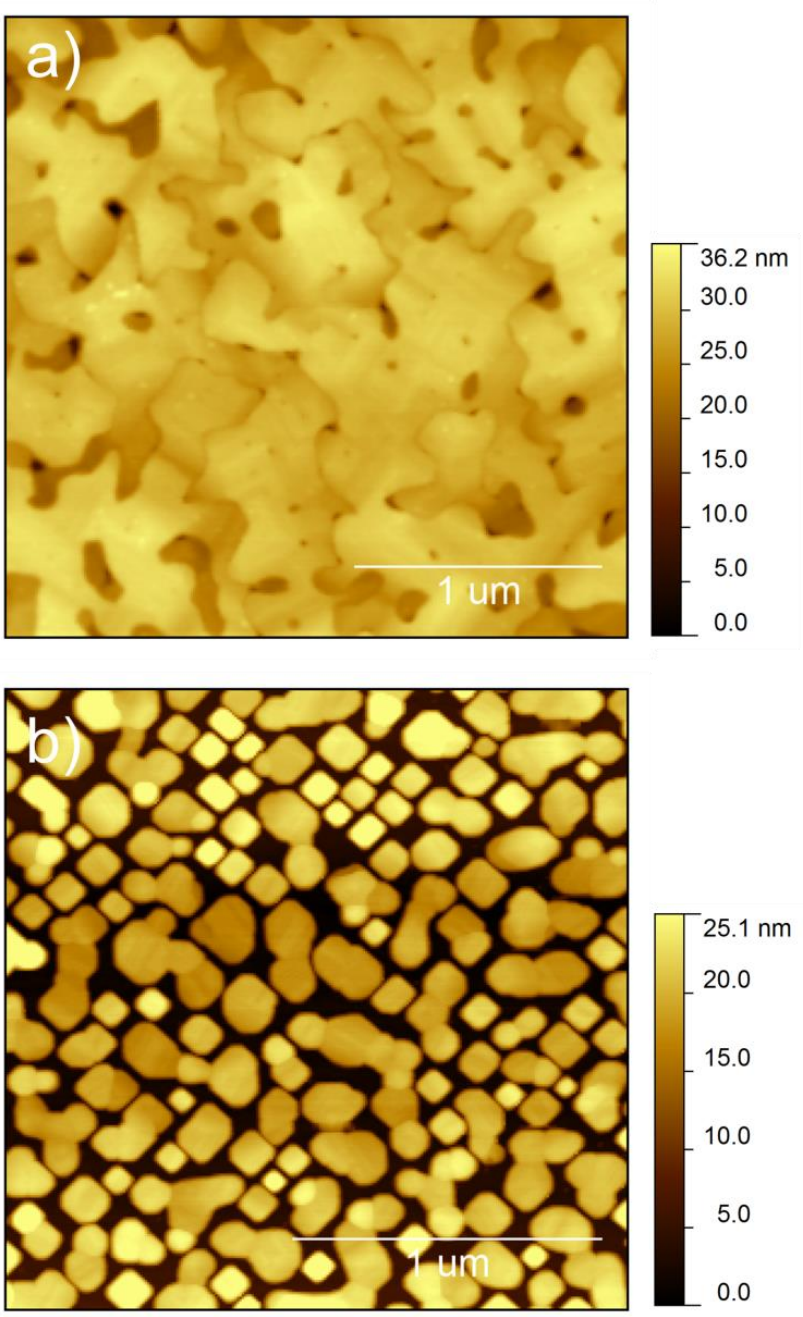


**Figure 4.2: a)** AFM image of irregular, discontinuous BVO(65 nm)/YSZ film morphology **b)** image at early stage of film growth, depicting isolated islands of material.

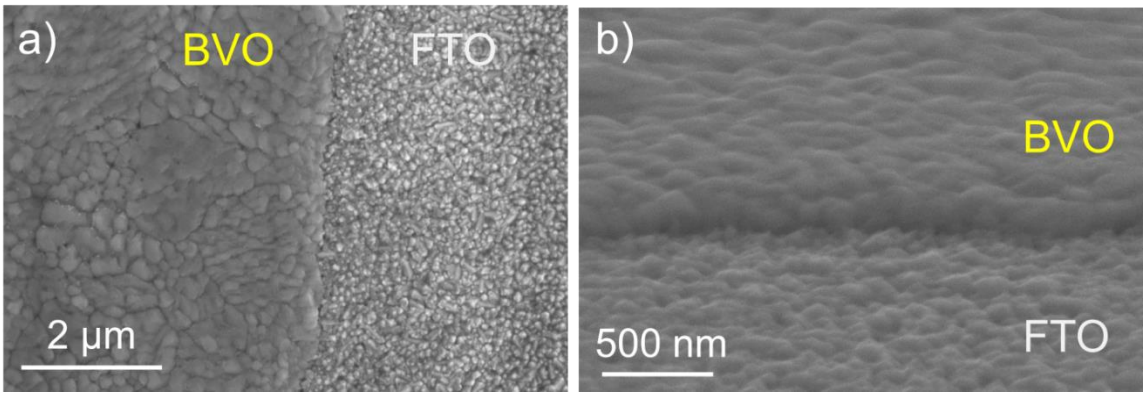


**Figure 4.3: a)** Top view SEM image of polycrystalline BVO/FTO interface. **b)** 45˚ view of the interface showing a film thickness of ~100 nm.

dimensional growth process (Volmer-Weber) [21], where the isolated islands coalesce as the deposition proceeds. The resultant porous films are not desirable for fundamental studies, where compact, well-defined samples are ideal. We hypothesized that the absorption and re-evaporation of Bi during growth was the cause, but this is not consistent with other Bi-containing oxides such as $BiFeO_3$ where continuous films were grown by absorption-controlled MBE [31]. The porous nature is more likely related to the energetics of BVO growth on the YSZ (100) surface. Other substrates or experimental approaches such as interval deposition [38] or low temperature growth followed by annealing may be successful in obtaining dense epitaxial BVO by PLD.

Scanning electron microscopy (SEM) was employed to analyze the BVO films deposited on FTO (Figure 4.3a and b). The films were dense and continuous with grains a few hundred nm in size. Film thickness was measured by cross-sectional SEM, yielding a deposition rate of ~0.5 Å/pulse for the conditions used in synthesizing the polycrystalline films.

### 4.3.4 X-ray Photoelectron Spectroscopy (XPS)

Stoichiometry and oxidation state information were obtained by XPS (Figure 4.4). Determining the stoichiometry of the resultant film is especially important in PLD, as the film composition may differ markedly from that of the target [39]. The Bi 4*f* (Figure 4.4a), V 2*p* and O 1*s* (Figure 4.4b) regions agreed well with previously reported spectra for BVO [13]. Peaks corresponding to Bi $4f_{7/2}$ (158.9 eV) and $4f_{5/2}$ (164.2eV), with the correct spin orbit coupling area ratio (4:3) and peak splitting (~5.3 eV) indicated that only $Bi^{3+}$ was present [13,14,40]. In the BE range ~510-540 eV, V $2p_{3/2}$, $2p_{1/2}$ and O 1*s* were present at 516.6, 524.1 and 529.7eV, respectively. The area ratio (2:1) and ~7.5 eV peak splitting for the V 2*p* spectra, combined with the peak positions imply that the charge states for vanadium and oxygen were $V^{5+}$ and $O^{2-}$ [40,41]. The higher BE shoulder on the O 1*s* peak has been observed in many oxides and is attributed to either defective oxygen sites [42,43] or surface hydroxides. XPS data and fitting for an epitaxial BVO/YSZ sample were nearly identical to the spectra for polycrystalline BVO and are provided in Appendix C (Figure C.5). Bi and V stoichiometry (Table 4.1) was close to 1:1 for both BVO/FTO and BVO/YSZ deposited at optimized conditions.

### 4.3.5 UV-Vis Spectroscopy

A characteristic yellow color was visually observed for crystalline BVO films grown on both YSZ and FTO by PLD (Figure 4.5 inset). We used UV-Vis spectroscopy to quantitatively measure visible light absorption and determine the nature of optical transitions. While a band gap of 2.4-2.5 eV is regularly quoted for BVO, light absorption is a complicated function of electronic properties, morphology and particle size. BVO powder (micron size particles) exhibits an optical band gap of ~2.4 eV [34], while band

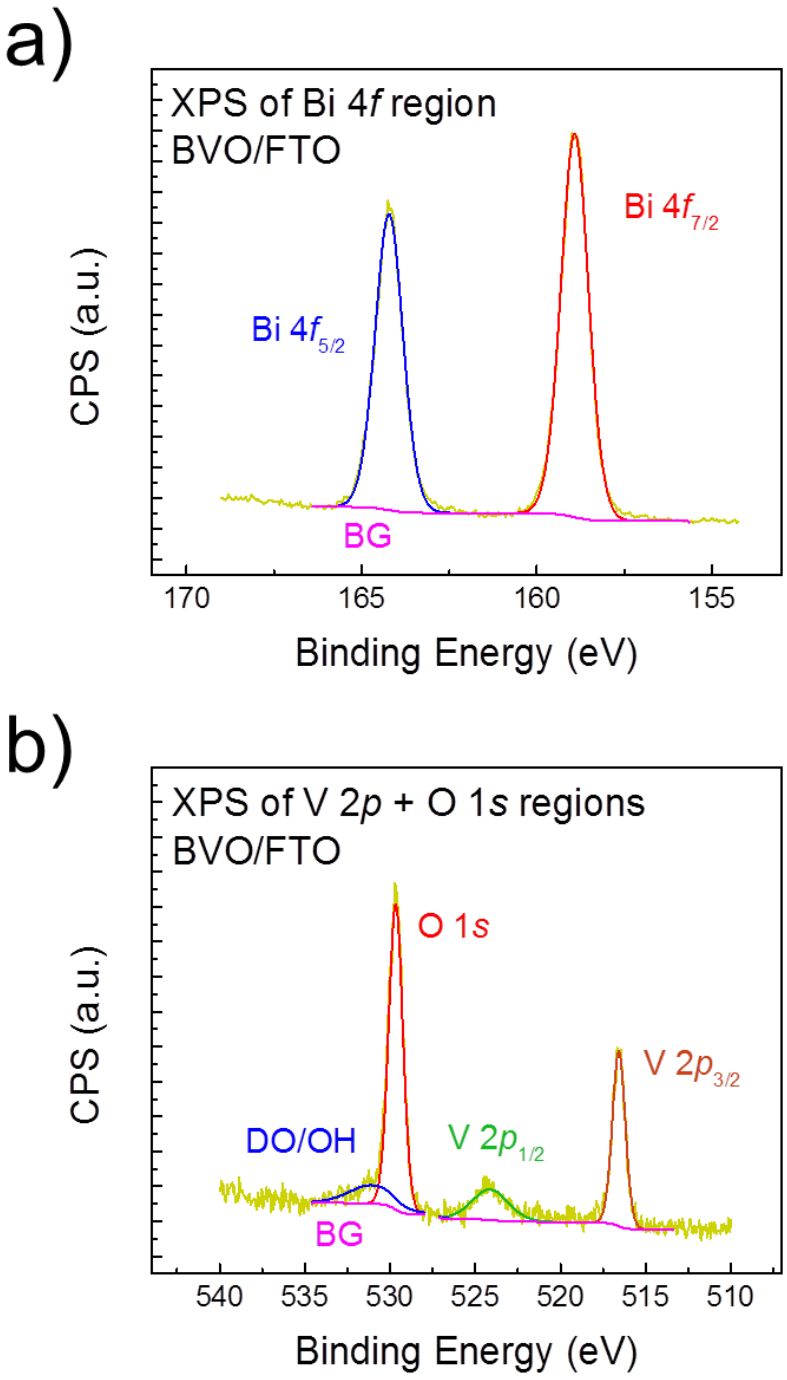


**Figure 4.4:** XPS data and fitting for a BVO/FTO film. **a)** Bi 4*f* and **b)** V 2*p* and O 1*s* region data with peak designations. DO/OH: defect oxide or hydroxide, BG: background.

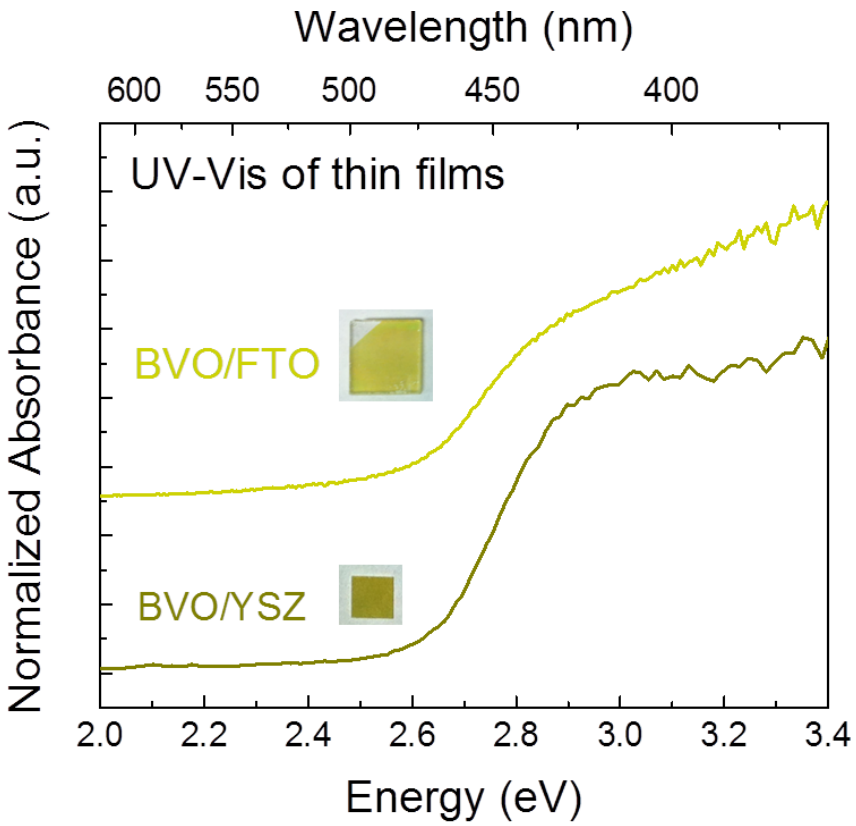


**Figure 4.5:** UV-Vis spectra of epitaxial and polycrystalline BVO films deposited by PLD. Inset: photographs of the samples. The apparent darker shade of the BVO/YSZ is due to lighting in the photograph.

gaps of ~2.5-2.6 eV have been reported for thin films [13,17,44]. Epitaxial and polycrystalline thin films had very similar light absorption properties, being on the upper bound of those in the literature with direct transitions of 2.65 eV and a smaller indirect transitions of ~2.55 eV as determined by Tauc plot analyses (Figure C.6). This is in agreement with those reported by Chen et al. for dense polycrystalline films [14], though we acknowledge that our indirect gap is slightly larger than theirs: ~2.4 eV. Epitaxial BVO transitions agree well with the work of Stoughton et al [17].

### 4.3.6 Photoelectrochemistry

While the morphology shown in Figure 4.2 is non-ideal for transport measurements, nanostructured films with high surface areas are highly desirable as photoelectrodes. Therefore, we attempted to fabricate fully epitaxial devices using lattice-matched conductive substrates for PEC testing. Cubic ITO is lattice matched to both BVO and YSZ [45], so we deposited an ITO buffer layer between the YSZ and BVO (details and XRD in Appendix C). As an example, this approach has facilitated magnetoelectric measurements of epitaxial $GdFeO_3$ films [46]. Despite our best efforts, we did not observe crystalline BVO on the ITO layer by XRD. As the lattice parameters agree excellently and highly oriented growth of BVO on ITO via solution-based methods has been demonstrated [45], we hypothesize that the ITO interface was the main issue, either being of low quality or the site of undesired reactions at growth temperatures, inhibiting crystallization. Therefore, our discussion of PEC properties will focus on the polycrystalline BVO samples deposited on FTO-glass.

Linear scanning voltammetry (LSV) with simulated solar light was used to probe the PEC properties of the polycrystalline samples. Photocurrents of ~0.15 and ~0.05 mA $cm^{-2}$ were observed at 1.23 V vs. RHE with and without a hole scavenger, respectively (Figure 4.6a). Water oxidation is kinetically limited at the undoped BVO surface [6,47], as illustrated by the lower photocurrents and higher on-set potentials without $Na_2SO_3$. This is further evidenced by small transient spikes at the beginning and end of each chop, indicative of charge trapping and recombination at the electrode surface [44]. As expected, these transients were suppressed in the presence of a hole scavenger. Only very small photocurrents were observed from films with thicknesses greater than 100 nm (Figure C.8).

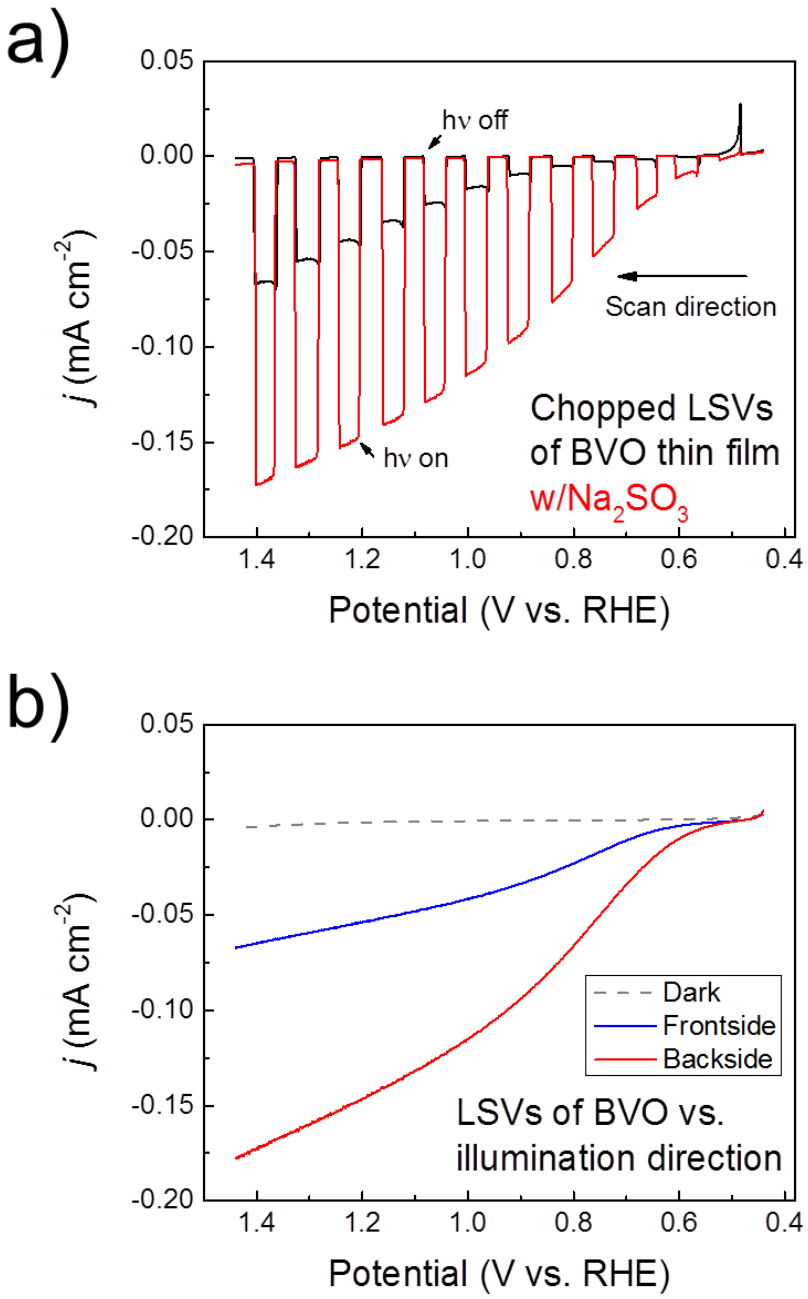


**Figure 4.6: a)** Chopped LSVs of BVO(100nm)/FTO with (red) and without (black) $Na_2SO_3$. **b)** LSVs of front (blue) and backside (red) illumination. The electrolyte was 0.1 M phosphate buffer with 0.1 M $Na_2SO_4$ and 0.1 M $Na_2SO_3$ as a hole scavenger under AM1.5G simulated solar light (100 mW $cm^{-2}$). The scan rate was 10 mV $s^{-1}$.

The effect of illumination direction – through the solution (frontside) or through the FTO-glass substrate (backside) – was significant, with backside illumination always resulting in higher PEC performance (Figure 4.6b). There are many examples of this behavior for nanostructured BVO films in the literature [13,47,48], but interestingly the only other example of dense BVO thin films found illumination direction to have a negligible effect on photocurrent for undoped films of 100 nm thickness [14]. This effect is quite complex however, being a convolution of electron-hole transport and recombination. Charged defects can have large effects on carrier transport as we will discuss later.

Incident photon conversion efficiency is an invaluable test for photoelectrodes as it identifies how photons of different wavelengths contribute to the overall photocurrent. This data is presented in Figure 4.7. The onset of ~500 nm corresponds to a band gap of ~2.5 eV and is consistent with the afore-mentioned UV-Vis spectra (Figure 4.5). Integration of the IPCE data with respect to the AM1.5G reference spectrum [49] were close to the observed photocurrents (Table C.1 in Appendix C). A typical IPCE power density spectrum is supplied in Appendix C (Figure C.9).

Comparison between our samples and others in the literature is warranted. In general, the photoresponse of our samples was on the low end, but reasonable for undoped BVO with low surface area [13,47]. The best comparison can be made against samples with similar morphology, namely the reactively sputtered BVO films of Chen et al., which had larger photocurrents (~0.4 mA $cm^{-2}$ at 1.23 V vs. RHE without a hole scavenger). The magnitude of the photocurrents observed for the films synthesized via PLD in the presence of $Na_2SO_3$ imply that charge transport through the BVO film is likely the limiting factor. In the $BiVO_4$ system, n-type conductivity will be governed chiefly by oxygen vacancies, and suppressed under O-rich conditions [50]. As the films

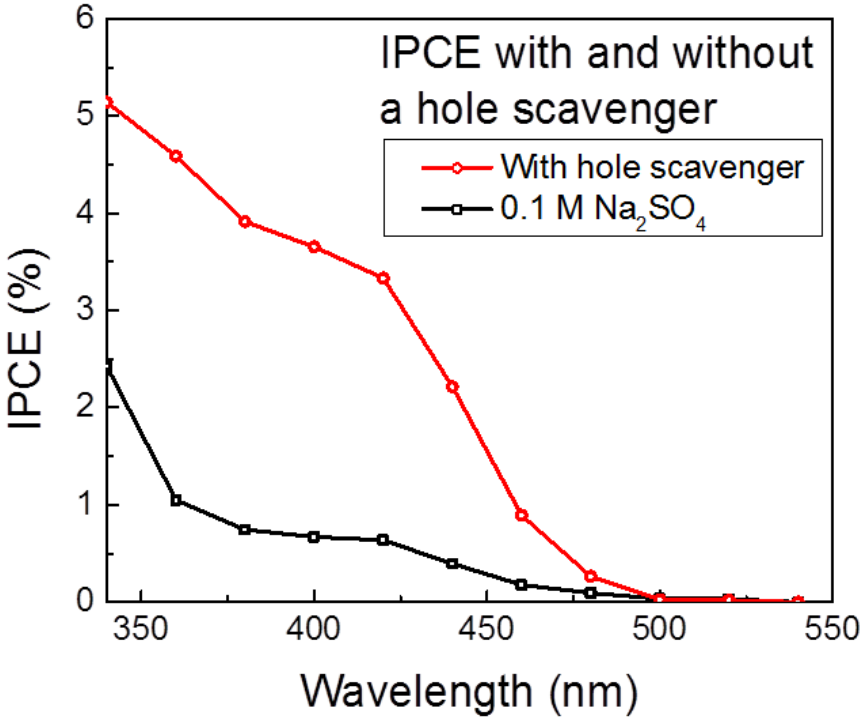


**Figure 4.7:** Incident photon conversion efficiency (IPCE) of BVO(100nm)/FTO. A hole scavenger ($Na_2SO_3$, red open circles) was added to better visualize the spectral shape due to low IPCE values in the 0.1 M phosphate buffer and 0.1 M $Na_2SO_4$ electrolyte (black open squares).

appear comparable to those synthesized by reactive sputtering by numerous characterization techniques (XRD, SEM, XPS, UV-vis), we speculate that the differences in PEC performance can be attributed to a smaller concentration of oxygen-related defects and hence greater resistivity of the PLD films.

Oxygen vacancies are hard to measure and minute quantities (< 1 at%) could have large effects on electrical properties. Other work in our laboratory found that undoped BVO films deposited by ballistic deposition in O-poor conditions exhibited markedly better PEC performance [13]. We attempted to apply this principle to PLD-grown films,

but growing without background gas had no noticeable effect (Figure C.10 in Appendix C), probably because there is already a significant amount of oxygen present in the PLD targets (being comprised of $Bi_2O_3$ and $V_2O_5$). In contrast, the sputtered films used $Bi_2O_3$ and V metal targets with a lower oxygen pressure during growth (0.6 mTorr) [14].

The ability of PLD to provide planar BVO films with high oxygen content mean these samples may be useful in studying the effects of oxygen and oxygen-related defects. The ability to heat the substrate during growth in controlled atmospheres (as opposed to annealing in air) could yield insights into how to engineer intrinsic defects in this photoanode. Further, studying the interplay between oxygen vacancies and extrinsic dopants such as Mo or W by conductivity or time-resolved spectroscopy would be fascinating avenues for future work.

## 4.4 CONCLUSIONS

We have fabricated epitaxial and polycrystalline BVO thin films using PLD. X-ray diffraction and X-ray photoelectron spectroscopy measurements confirmed that both film types were single-phase monoclinic $BiVO_4$. Epitaxial BVO was realized on YSZ (100) single crystals, employing a Bi-rich target. Optimized deposition conditions resulted in high quality films, with FWHM values of ~0.3° and the epitaxial relationship was shown to be BVO (001) || YSZ (001) and BVO (100) || YSZ (100). These films had a porous morphology, consisting of irregular, smooth grains. Dense, continuous polycrystalline films were grown on FTO-glass at room temperature with post-deposition annealing. Photoelectrochemical testing of these films resulted in photocurrents of ~0.15 and ~0.05 mA $cm^{-2}$ at 1.23 V vs. RHE with and without a hole scavenger respectively. We attribute the photocurrents of these films to a lack of oxygen defects, due to the O-

rich growth conditions of the PLD process. Thus, we think the high quality thin films produced by PLD will be useful model systems and aid in gaining a fundamental understanding of BVO in terms of defects, dopants and grain boundaries.

## REFERENCES


(1) Bard, A. J.; Fox, M. A. *Acc. Chem. Res.* **1995**, *28*, 141.

(2) Fujishima, A.; Honda, K. *Nature* **1972**, *238*, 37.

(3) Sivula, K. *J. Phys. Chem. Lett.* **2013**, *4*, 1624.

(4) Grätzel, M. *Nature* **2001**, *414*, 338.

(5) Park, Y.; McDonald, K. J.; Choi, K.-S. *Chem. Soc. Rev.* **2013**, *42*, 2321.

(6) Zhong, D. K.; Choi, S.; Gamelin, D. R. *J. Am. Chem. Soc.* **2011**, *133*, 18370.

(7) Sayama, K.; Nomura, A.; Arai, T.; Sugita, T.; Abe, R.; Yanagida, M.; Oi, T.; Iwasaki, Y.; Abe, Y.; Sugihara, H. *J. Phys. Chem. B* **2006**, *110*, 11352.

(8) Park, H. S.; Kweon, K. E.; Ye, H.; Paek, E.; Hwang, G. S.; Bard, A. J. *J. Phys. Chem. C* **2011**, *115*, 17870.

(9) He, H.; Berglund, S. P.; Rettie, A. J. E.; Chemelewski, W. D.; Xiao, P.; Zhang, Y.; Mullins, C. B. *J. Mater. Chem. A* **2014**, *2*, 9371.

(10) Kim, T. W.; Choi, K.-S. *Science* **2014**, *343*, 990.

(11) Abdi, F. F.; Han, L.; Smets, A. H. M.; Zeman, M.; Dam, B.; van de Krol, R. *Nat. Commun.* **2013**, *4*, 1.

(12) Berglund, S. P.; Flaherty, D. W.; Hahn, N. T.; Bard, A. J.; Mullins, C. B. *J. Phys. Chem. C* **2011**, *115*, 3794.

(13) Berglund, S. P.; Rettie, A. J. E.; Hoang, S.; Mullins, C. B. *Phys. Chem. Chem. Phys.* **2012**, *14*, 7065.

(14) Chen, L.; Alarcón-Lladó, E.; Hettick, M.; Sharp, I. D.; Lin, Y.; Javey, A.; Ager, J. W. *J. Phys. Chem. C* **2013**, *117*, 21635.

(15) Alarcon-Llado, E.; Chen, L.; Hettick, M.; Mashouf, N.; Lin, Y.; Javey, A.; Ager, J. W. *Phys. Chem. Chem. Phys.* **2014**, *16*, 1651.

(16) Seabold, J. A.; Zhu, K.; Neale, N. R. *Phys. Chem. Chem. Phys.* **2014**, *16*, 1121.

(17) Stoughton, S.; Showak, M.; Mao, Q.; Koirala, P.; Hillsberry, D.; Sallis, S.; Kourkoutis, L.; Nguyen, K.; Piper, L.; Tenne, D. *Appl. Phys. Lett. Mater.* **2013**, *1*, 0421121.

(18) Liang, Y.; Tsubota, T.; Mooij, L. P.; van de Krol, R. *J. Phys. Chem. C* **2011**, *115*, 17594.

(19) Rettie, A. J. E.; Lee, H. C.; Marshall, L. G.; Lin, J.-F.; Capan, C.; Lindemuth, J.; McCloy, J. S.; Zhou, J.; Bard, A. J.; Mullins, C. B. *J. Am. Chem. Soc.* **2013**, *135*, 11389.

(20) Quinn, R. K.; Nasby, R. D.; Baughman, R. J. *Mater. Res. Bull.* **1976**, *11*, 1011.

(21) Chrisey, D. B.; Hubler, G. K. *Pulsed laser deposition of thin films*; 2nd ed.; Wiley-VCH: New York, NY, 2003.

(22) Sleight, A. W.; Chen, H. Y.; Ferretti, A.; Cox, D. E. *Mater. Res. Bull.* **1979**, *14*, 1571.

(23) Swanson, H. E. C.-M., M.; Evans, E. H.; Ulmer, L. *National Bureau of Standards Circular 539* **1955**, *5*, 26.

(24) Tsipis, E. V.; Patrakeev, M. V.; Kharton, V. V.; Vyshatko, N. P.; Frade, J. R. *J. Mater. Chem.* **2002**, *12*, 3738.

(25) Vasylechko, L.; Senyshyn, A.; Bismayer, U. In *Handbook on the Physics and Chemistry of Rare Earths*; North Holland: Amsterdam, 2009; Vol. 39, p 113.

(26) Schlom, D. G.; Chen, L.-Q.; Fennie, C. J.; Gopalan, V.; Muller, D. A.; Pan, X.; Ramesh, R.; Uecker, R. *MRS Bull.* **2014**, *39*, 118.

(27) Liu, Z.; Yan, F. *J. Am. Ceram. Soc.* **2012**, *95*, 1944.

(28) Biesinger, M. C.; Payne, B. P.; Lau, L. W.; Gerson, A.; Smart, R. S. C. *Surf. Interface Anal.* **2009**, *41*, 324.

(29) Miller, D.; Biesinger, M.; McIntyre, N. *Surf. Interface Anal.* **2002**, *33*, 299.

(30) Light, T. S. *Anal. Chem.* **1972**, *44*, 1038.

(31) Ihlefeld, J.; Kumar, A.; Gopalan, V.; Schlom, D.; Chen, Y.; Pan, X.; Heeg, T.; Schubert, J.; Ke, X.; Schiffer, P. *Appl. Phys. Lett.* **2007**, *91*, 0719221.

(32) Migita, S.; Kasai, Y.; Ota, H.; Sakai, S. *Appl. Phys. Lett.* **1997**, *71*, 3712.

(33) Theis, C.; Yeh, J.; Schlom, D.; Hawley, M.; Brown, G.; Jiang, J.; Pan, X. *Appl. Phys. Lett.* **1998**, *72*, 2817.

(34) Tokunaga, S.; Kato, H.; Kudo, A. *Chem. Mater.* **2001**, *13*, 4624.

(35) Bierlein, J. D.; Sleight, A. W. *Solid State Commun.* **1975**, *16*, 69.

(36) Pinczuk, A.; Welber, B.; Dacol, F. *Solid State Commun.* **1979**, *29*, 515.

(37) Sleight, A. W.; Aykan, K.; Rogers, D. B. *J. Solid State Chem.* **1975**, *13*, 231.

(38) Blank, D. H.; Koster, G.; Rijnders, G. A.; van Setten, E.; Slycke, P.; Rogalla, H. *J. Cryst. Growth* **2000**, *211*, 98.

(39) Droubay, T.; Qiao, L.; Kaspar, T. C.; Engelhard, M. H.; Shutthanandan, V.; Chambers, S. A. *Appl. Phys. Lett.* **2010**, *97*, 1241051.

(40) National Institute of Standards and Technology X-ray Photoelectron Spectroscopy Database. [Online Early Access]. http://srdata.nist.gov/xps/ (accessed 1st August, 2014).

(41) Silversmit, G.; Depla, D.; Poelman, H.; Marin, G. B.; De Gryse, R. *J. Electron. Spectrosc. Relat. Phenom.* **2004**, *135*, 167.

(42) Biesinger, M. C.; Lau, L. W.; Gerson, A. R.; Smart, R. S. C. *Appl. Surf. Sci.* **2010**, *257*, 887.

(43) Biesinger, M. C.; Payne, B. P.; Grosvenor, A. P.; Lau, L. W.; Gerson, A. R.; Smart, R. S. C. *Appl. Surf. Sci.* **2011**, *257*, 2717.

(44) Abdi, F. F.; van de Krol, R. *J. Phys. Chem. C* **2012**, *116*, 9398.

(45) Zhou, M.; Bao, J.; Bi, W.; Zeng, Y.; Zhu, R.; Tao, M.; Xie, Y. *ChemSusChem* **2012**, *5*, 1420.

(46) Trassin, M.; Viart, N.; Versini, G.; Loison, J.-L.; Vola, J.-P.; Schmerber, G.; Cregut, O.; Barre, S.; Pourroy, G.; Lee, J. *Appl. Phys. Lett.* **2007**, *91*, 2025041.

(47) Seabold, J. A.; Choi, K.-S. *J. Am. Chem. Soc.* **2012**, *134*, 2186.

(48) Luo, W.; Li, Z.; Yu, T.; Zou, Z. *J. Phys. Chem. C* **2012**, *116*, 5076.

(49) National Renewable Energy Laboratory Reference Solar Spectral Irradiance: ASTM G-173. [Online Early Access]. http://rredc.nrel.gov/solar/spectra/am1.5/ASTMG173/ASTMG173.html (accessed 1st August, 2014).

50) Yin, W.-J.; Wei, S.-H.; Al-Jassim, M. M.; Turner, J.; Yan, Y. *Phys. Rev. B* **2011**, *83*, 1551021.

# Chapter 5: Electron Small Polarons and Near-Isotropic Transport in Ti:α-$Fe_2O_3$ Single Crystals

## 5.1 INTRODUCTION

Photoelectrochemical (PEC) cells offer a route to clean, renewable hydrogen ($H_2$) by splitting water using solar energy. Metal oxide semiconductors offer promise as photoelectrodes for these systems due to their stability and relative abundance. Of these, α-$Fe_2O_3$ is one of the most studied, due to its band gap of ~2.1 eV and stability in basic electrolyte [1]. However, its notoriously bad transport properties are regularly cited as a bottleneck to high photocurrents, specifically severe recombination on the order of picoseconds [2] and low carrier mobilities (< 1 $cm^2\ V^{-1}\ s^{-1}$) [3]. Hence, doping and nanostructuring [4-8] have been vital in optimizing this material's PEC performance. Electronic transport in hematite agrees well with the small-polaron model [9] but a thorough analysis in this framework has not been performed. Recent work by our group utilized conductivity, Seebeck and Hall effect measurements as functions of temperature on single crystalline tungsten-doped bismuth vanadate ($BiVO_4$) samples [10,11] to probe the nature of small polarons.

Although many studies concerning hematite's charge transport exist [12-14], several open questions remain, especially regarding transport near room temperature where PEC cells would operate. Elucidation of these currently unknown transport parameters: drift mobility, activation barriers and anisotropy in well-defined synthetic crystals will have implications for future iron oxide devices as well as geochemical research, as electron transport in hematite plays a vital role in many biogeochemical processes [15].

Between ~260 and 960 K, hematite is in a weakly ferromagnetic state (WFS), with an in-plane moment of ~0.4 emu/g [16] and a very weak, but detectable *c*-axis moment [17] both due to spin canting. Spins are coupled antiferromagnetically between basal planes [18]. Below ~260 K spins flop parallel to the c-axis and hematite is a near-perfect antiferromagnet. This has been termed the Morin transition temperature, $T_M$. The transition is due to the competition between single-ion and magnetic dipole fields [19,20]. In this chapter, $T < T_M$ will be termed the antiferromagnetic state (AFS). Due to the anisotropic crystal structure and nuanced magnetic environment, anisotropic conductivity was expected.

Anisotropic conductivity in hematite was first reported in impure, natural single crystals by Nakau in 1960 [21]. Unfortunately, this study had a number of issues: (i) the two samples were highly impure (up to several percent of both donor and acceptor type impurities), (ii) conductivity measurements were 2-pt and so include unknown contact resistances and (iii) very different behavior between the two samples, making it difficult to draw any strong conclusions. The most that can be said about this study is that a conductivity anisotropy between 1-4 orders of magnitude may exist in impure hematite crystals. Acket and Volger [22] performed more thorough transport measurements, noting – no data is presented – that they did not observe significant conductivity anisotropy in or out of plane. Again however, the sample was natural and impure. The large anisotropy observed by Nakau was consistent with the idea that electrons will have difficulty crossing the anisotropic spin environment in hematite due to Hund's rule, and so became widely accepted [23].

An investigation of pure, synthetic crystals came in 1984 with the work of Benjelloun et al. [13] These samples were grown by chemical vapor transport and were highly resistive, meaning transport measurements were conducted above room

temperature from 500-1200 K. Linear extrapolation to room temperature does imply a conductivity anisotropy of 3-4 orders of magnitude (see Figure 5.9a for this plot). A computational study using Marcus theory replicated this anisotropy [24]. The main difference between this treatment and the classically accepted argument is that it did not consider electron transfer across planes to be forbidden. Three orders of magnitude difference in electron mobilities was predicted and found to depend most strongly on the electronic coupling. We note that the most important factor appears to be the spin states of the initial and final sites, i.e. the spin environment is consistently the most important factor governing transport in the *c*-axis. A recent study exploited this fact and showed significantly higher photocurrents in undoped hematite thin films with the basal planes oriented parallel to current flow [25].

The vast majority of research over the last 50 years has been focused on studying the properties of pure hematite [26]. The necessity of doping this material for use as a photoanode has renewed interest in the properties of doped α-$Fe_2O_3$, specifically Ti-doping [27]. Ti incorporates substitutionally for $Fe^{3+}$ as $Ti^{4+}$, doping hematite n-type. Surprisingly, there appear to be no studies concerned with anisotropic transport of doped α-$Fe_2O_3$ around room temperature. Perhaps this is because the anisotropy is linked to the spin structure, which does not change appreciably with doping. Additionally, like Fe, Ti is an abundant element in the earth's crust and is often incorporated in natural hematite. Thus these studies may have relevance in explaining the properties of the impure, natural crystals that are ubiquitous in nature.

This chapter has three main thrusts: (i) describing the synthesis and characterization of the Ti:α-$Fe_2O_3$ grown by CVT, (ii) evaluating transport and optical measurements within the small-polaron hopping model and (iii) reporting the directional-

dependence of the conductivity and Seebeck coefficient of Ti:α-$Fe_2O_3$ single crystals for the first time.

## 5.2. EXPERIMENTAL METHODS

### 5.2.1 Synthesis

Chemical vapor transport (CVT) was used to grow millimeter-sized Ti:$Fe_2O_3$ crystals for transport measurements [14,28]. α-$Fe_2O_3$ (99.995%, Sigma-Aldrich) and titanium metal powder (99.7%, Pfaltz and Bauer) were transported at 1040 and 930 °C in the hot and cold zones respectively using tellerium tetrachloride ($TeCl_4$, 99.9%, Alfa-Aesar) as the transport agent in a 3-zone tube furnace (ThermCraft). The tubes were charged with approximately 1 g of hematite, enough Ti to replace 1% of the Fe sites (60 mg) and 5 mg $cm^{-3}$ of $TeCl_4$. As $TeCl_4$ is air and moisture sensitive, this compound was loaded into the tubes in an Ar-filled glovebox, before being evacuated to ca. $10^{-5}$ Torr and sealed. Back-transport (inverted temperature gradient) was performed for 24 hrs before the growth. The transport lasted 10-13 days.

The silica tubes were cleaned to remove small dust particles and imperfections that could act as nucleation sites using the following procedure: an HF acid rinse followed by soaking in aqua regia for 3 hrs before another HF acid rinse and finally drying under vacuum overnight. De-ionized water was used throughout. Post-reaction the tube was opened in a fume hood and the resultant crystals washed and sonicated in DI water and acetone. All crystals were annealed in air at 500 °C for 1 hr to remove any undesired iron oxide phases.

### 5.2.2 Compositional Characterization

Powder X-ray diffraction (XRD) was performed using a Philips X'Pert diffractometer equipped with monochromatic Cu Kα x-rays (λ = 1.54056 Å). Laue back-reflection XRD was utilized to determine crystal quality and orientation using Rigaku Geigerflex with Mo radiation. Samples were oriented within 2 degrees of the principal axes. An optical Raman system with a Verdi V2 532 nm green laser, Andor spectrometer, iCCD detector and a 1800 grating was used for vibrational spectroscopy measurements. Titanium incorporation will be determined using laser-ablation inductively coupled plasma mass spectrometry (LA-ICP-MS). These experiments are on-going. In this chapter we will assume that conductivity scales with conductivity of the crystals, based on similar samples in the literature this assumption appears to be reasonable [29].

### 5.2.3 Transport Measurements

4-point conductivity and Hall effect measurements were conducted at Lake Shore Cryotronics on an 8404 AC/DC Hall measurement system and DC field Hall effect experiments up to 9 T on a 9700A DC Hall system. Some room temperature conductivity measurements were performed on a Keithley 4200-SCS. Ohmic contact was achieved using In-Ga eutectic (Sigma-Aldrich) or e-beam evaporated Ag metal pads, attached to fine Cu wires with Ag epoxy (EPO-TEK). An example i-V curve is given in Appendix D (Figure D1). Use of just Ag epoxy produced a highly resistive, non-ohmic contact. Evaporated contacts were defined on the small crystals using hand-made wire masks. Contact geometry was either 4-point van der Pauw on plate-like samples or 4-point collinear on bar shaped samples. Measurement of the Seebeck coefficient was performed using a laboratory-built apparatus at UT Austin. In the case of the Seebeck

measurements, high quality contacts were made by evaporating Ag over opposite crystal faces.

### 5.2.4 Optical Measurements

Crystals were pulverized for optical characterization and either used directly or mixed with KBr and pressed into pellets. Diffuse reflectance UV−vis-NIR spectra were measured with a Cary 500 spectrophotometer attached to an integrating sphere (Labsphere DRA-CA-5500). A Tensor 37 FT-IR spectrometer (Bruker Optics) equipped with an integrating sphere at Pacific Northwest National Laboratory was used to measure reflectance from 1.3 to 13.6 μm. All optical measurements were performed at room temperature.

### 5.2.5 Methodology

Inherent to CVT and flux growth techniques, local variations in temperature and reactant flux in the reaction vessel may result in compositional variation from crystal to crystal. Thus, it was vital to grow millimeter-sized samples, on which a battery of characterization and transport measurements could be made for comparison and analysis. Generally, once large crystals were identified, their quality was checked by XRD and Raman spectroscopy. Seebeck coefficient measurements were then performed on the crystals, before being diced and polished into smaller samples for conductivity and Hall effect measurements. Finally these samples will be analyzed using LA-ICP-MS to determine [Ti]/[Fe] (on-going). Conductivity measurements in the basal plane were consistent between the larger crystals and the smaller samples cut from them, indicating that doping was macroscopically homogeneous.

## 5.3 Results and Discussion

### 5.3.1 Synthesis

The CVT process produced black, specular crystals ranging from thin (~20 μm) platelets with large (up to 10 $mm^2$) (0001) faces to prismatic samples hundreds of microns in thickness (Figure 5.1). Once a large (0001) or (1000) plane was identified by Laue XRD, crystals were cut and polished along principal axes relative to it. Laue XRD was employed to check orientation and quality on many areas of the crystals (See Figure D2 in Appendix D for example Laue patterns). Crystals grew in both ends of the tube, as was observed in the case of CVT growth of Nb:α-$Fe_2O_3$ crystals [29]. Upon grinding in a mortar and pestle, the material turned a dark red color characteristic of α-$Fe_2O_3$.

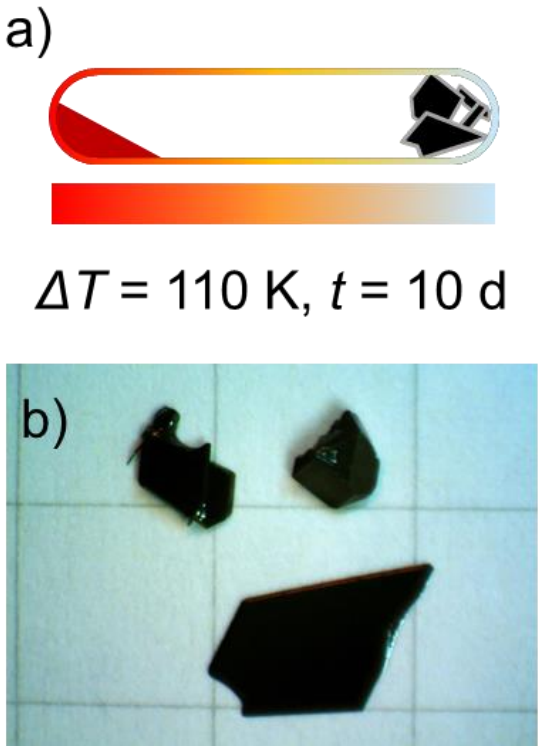


**Figure 5.1: a)** Cartoon of CVT synthesis. **b)** Photograph of typical Ti:α-$Fe_2O_3$ crystals grown by CVT on 5×5 $mm^2$ square paper.

### 5.3.2 Phase and Composition

X-ray diffraction (XRD) spectra for pulverized crystals could only be indexed to α-$Fe_2O_3$ (PDF # 01-071-5088) as shown in Figure 5.2. The unit cell is rhombohedral (illustrated in Figure 5.3a) but is best thought of as distorted hexagonal (R3c space group, $a$ = 5.0238 Å, $c$ = 13.772 Å), consisting of edge-sharing $FeO_6$ units in the basal planes and face-sharing along the $c$-axis (0001) [31]. One third of the Fe sites are vacant, forming the hexagonal arrangement illustrated in Figure 3b.

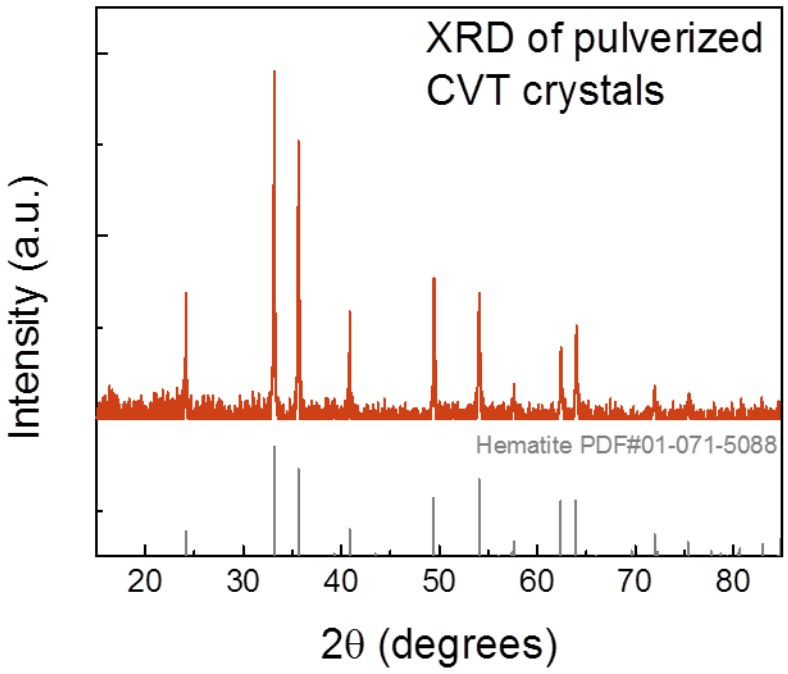


**Figure 5.2:** XRD of pulverized Ti:α-$Fe_2O_3$ crystals.

Raman spectroscopy showed the expected vibrational modes for hematite: two $A_{1g}$ modes at ~226 and 500 and five $E_g$ modes at 245, 283, 293, 300 and 612 $cm^{-1}$ respectively [31]. The 293 and 300 $cm^{-1}$ bands can only be resolved at low temperature

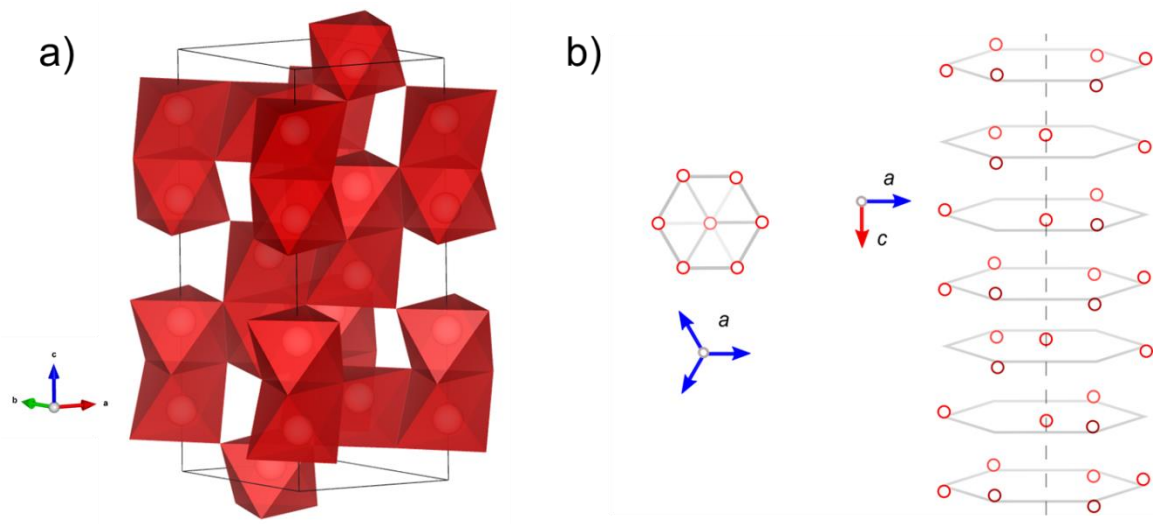


**Figure 5.3: a)** Rhombohedral unit cell of hematite showing $FeO_6$ units (red). Created using VESTA software.[33] **b)** Cartoon of the hexagonal arrangement of Fe atoms, depicting hexagonal arrangement and basal planes.

[32]. The weak feature at ~660 $cm^{-1}$ has been assigned to a IR-active and Raman-inactive $E_u$(LO) mode in synthetic single crystals [34] and high purity (99.998%) α-$Fe_2O_3$ powder [35].

Moderate laser powers will convert other iron oxide phases to hematite, complicating their detection [32]. Thus, low powers (10 mW) and long acquisition times (~6 mins) were employed. In one large crystal, a weak feature at ~670 $cm^{-1}$ was observed, possibly corresponding to either magnetite or maghemite [36]. Annealing in air at 500 °C or intense laser excitation is known to convert these phases to hematite [32], which we confirmed in this sample (Figure D3 in Appendix D). Annealing in air at 500 °C for 1 hr did not noticeably affect the crystallinity or electronic properties of the crystals and so was performed on all as-grown samples to ensure phase purity.

The level of titanium incorporation in the grown crystals was too low to induce

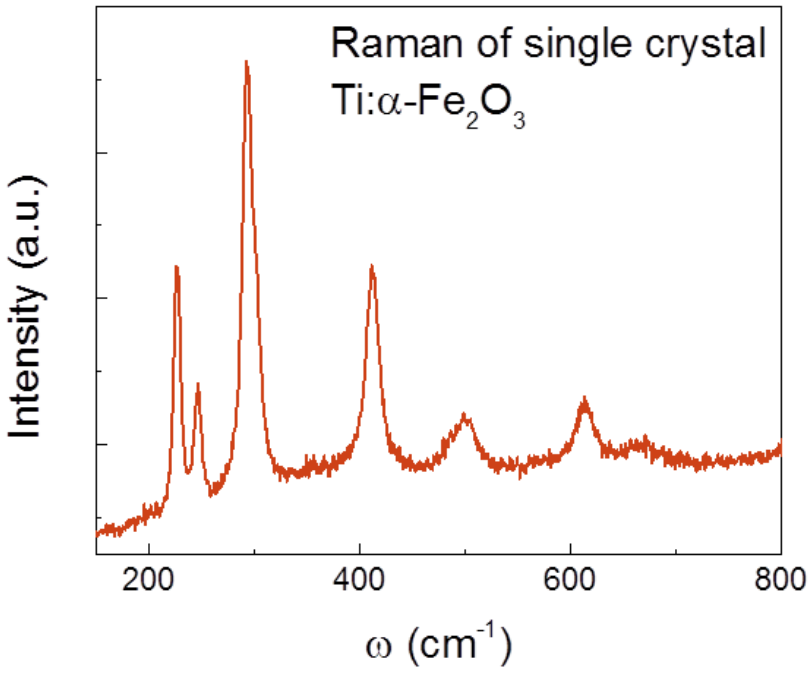


**Figure 5.4:** Raman spectrum of single crystalline Ti:α-$Fe_2O_3$.

changes detectable by XRD or Raman spectroscopy. However, preliminary 2-point resistance measurements were in the kΩ range, indicating some degree of Ti incorporation (undoped α-$Fe_2O_3$ grown by CVT is highly insulating [13,14,29]).

### 5.3.3 Basal Plane Electronic Transport

***Conductivity***

Room temperature crystal resistivity ranged from $10^1$-$10^2$ Ω-cm, which are typical values for n-type hematite single crystals via CVT using various dopants [14,29,37]. DC conductivity from 200-400 K showed semiconducting behavior, decreasing by ~2 orders

of magnitude over this temperature range (Figure 5.5 These data were fit to the adiabatic small-polaron conductivity equation [11]:

$$\sigma(T) = \sigma_0(T) exp\left(-\frac{E_\sigma}{\kappa T}\right) \qquad (5.1)$$

where, $\sigma$ is the conductivity, $E_\sigma$ is the conductivity activation energy, $\kappa$ is the Boltzmann constant, and $T$ is the absolute temperature. The fitting revealed two linear regimes that were differentiated at the characteristic Morin or "spin-flop" transition at ~260 K of hematite (Figure 5.6). No noticeable hysteresis in the conductivity was observed upon either cooling or heating through $T_M$. Doping with $Ti^{4+}$ can suppress $T_M$ to lower temperatures, but drastic suppression is not expected at the low concentrations of Ti in our crystals [16,38]. This was confirmed by magnetization measurements (Figure D4 in Appendix D). The relevant fitting parameters from equation 5.1 (plotted in Figure 5.6) are summarized in Table 5.1. First, we will discuss the high temperature, WFS regime.

**Table 5.1:** Adiabatic small-polaron fitting parameters.

| | $E_\sigma$ (meV) | $\sigma_0 T$ (S cm$^{-1}$ K) | $\sigma_0$ (S cm$^{-1}$) at 300 K |
|---|---|---|---|
| WFS | 90 ± 1 | 46.9 ± 0.4 | 0.156 ± 0.001 |
| AFS | 189 ± 3 | 3359 ± 58 | 11.2 ± 0.2 |

The measured activation energy of ~0.1 eV in the WFS is in excellent agreement with previous experimental values for doped α-$Fe_2O_3$ [9,14]. Further, it is also consistent with *ab initio* calculations for adiabatic transfers between nearest neighbor Fe ions in the basal plane.[39] Estimation of the adiabatic pre-factor yielded $\sigma_0 T$ = 51 S cm$^{-1}$ K (details in Appendix D). Comparison with the measured pre-factor (Table 5.1) again supports the

use of the adiabatic model. Note that the low donor concertation in our crystals means that $\sigma_0$ is significantly smaller than that for intrinsic small-polaron hopping [40,41].

Below $T_M$, both $E_\sigma$ and $\sigma_0$ increased significantly (Table 5.2, Figure 5.6). Interestingly, this behavior does not appear to have been previously reported – likely due to the higher doping levels common to transport studies around room temperature (> 1%)[9,42] $T_M$ is suppressed to very low temperatures [38]. We interpret this behavior within the small-polaron model as an increase in the hopping barrier brought about by the flopping of spins from slightly canted in-plane to parallel to the *c*-axis. The magnetic nature of a carrier's initial and final sites has an effect on the hopping rate and the behavior may suggest that hopping between antiferromagnetically-coupled Fe ions occurs

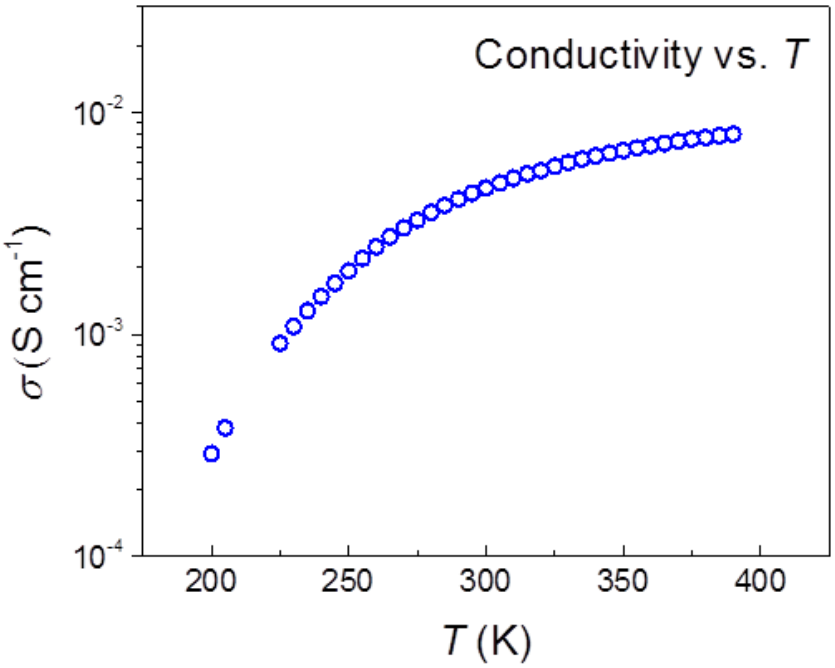


**Figure 5.5:** Conductivity versus temperature for a doped Ti: α-$Fe_2O_3$ crystal in the basal plane.

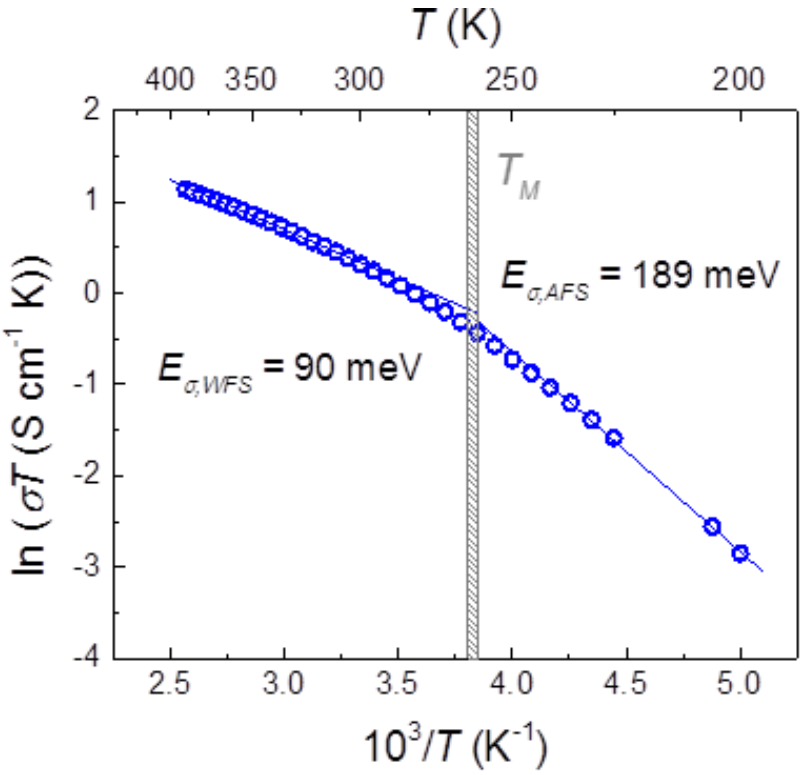


**Figure 5.6:** Fitting of the conductivity data in Figure 5.5 to equation 5.1 in the main text.

in the AFS, while in-plane hops between near-parallel spin Fe sites dominate transport in the WFS. However, this hypothesis raises the question, why are these more difficult hops preferred in the AFS over the in-plane transfers which are still presumably available? Theoretical calculations are needed to provide guidance on this issue.

***Seebeck coefficient***

The Seebeck coefficient in the basal plane was large and negative, consistent with the crystals being lightly doped n-type (Figure 5.7). The magnitude of the Seebeck coefficient increased with increasing temperature and was not significantly affected by the Morin transition. This is consistent with doped semiconductor behavior and the

magnetic contributions to the Seebeck coefficient being small at relatively low temperatures [43,44].

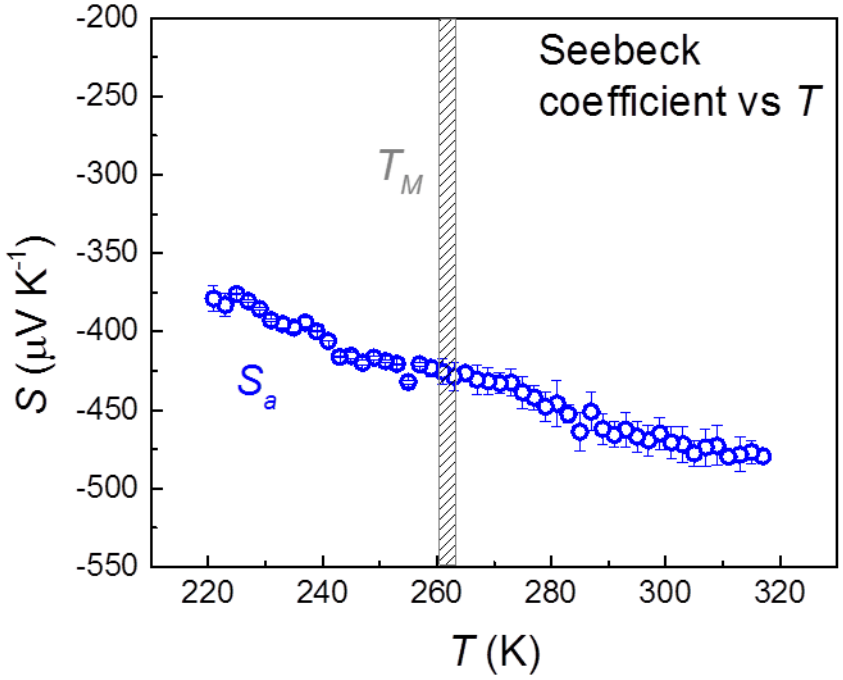


**Figure 5.7:** Seebeck coefficient vs. temperature in the basal plane.

***Hall effect***

Considerable variation exists in the literature regarding the Hall effect in hematite. In most cases, anomalous behavior common in ferromagnets has been observed with the field applied in the *c*-axis [22,42], however in others no Hall effect was observed with this field orientation [45,46]. Additionally, in heavily doped (> 1%) epitaxial films, conventional Hall effect behavior (i.e. the Hall voltage being linear with Hall voltage being linear with field strength) was found from 190 to 290 K [9].

We observed an anomalous Hall voltage above the Morin transition (Figures D5a and b in Appendix D). In this regime the Hall resistivity was fit to the empirical relation [47,48]:

$$\rho_H = R_H B + R_A \mu_0 M \qquad (5.2)$$

where, $\rho_H$ is the Hall resistivity, $R_H$ is the conventional Hall coefficient, $B$ is the applied field, $R_A$ is the anomalous Hall coefficient, $\mu_0$ is the magnetic susceptibility and $M$ is the magnetization. At sufficient field strength the slope of the Hall resistivity was linear with field and $R_H$ could be extracted.

Below $T_M$, the Hall effect was too small to detect via the DC field Hall effect. In this state, large anomalous behavior returned once a critical field was applied (Figures D5c-e in Appendix D). This behavior correlates well with the spin-flop transition from the AFS to WFS state that occurs in hematite when a sufficient field is applied parallel to *c*-axis below $T_M$ [26,49,50] and suggests that net magnetization is a requirement for the AHE in our samples. This is in agreement with the empirical relation for the AHE (equation 5.2). Thus, the AC Hall effect (RMS field of 0.67 T) was used to discern the small Hall coefficient at $T < T_M$. We should mention that net magnetization is not strictly a requirement for the AHE [51].

The conventional Hall coefficients over the temperature range 200-400 K measured by both the DC and AC techniques are shown in Figure 5.8. At all temperatures the Hall coefficient was positive, opposite to the negative sign of the Seebeck coefficient. Anomalously-signed Hall coefficients are common in small-polaron conduction, and the sign depends on the product of transfer energies and number of members in the hopping loop.[43] Further, for small-polaron hopping in a triangular lattice the Hall coefficient is related to the activation energy of the conductivity by [52],

$$R_H \propto exp\left(\frac{2E_\sigma}{3\kappa T}\right) \quad (5.3)$$

The activation energy that characterizes $R_H$ in the AFM regime is 129 ± 8 meV; ~2/3 of $E_\sigma$ (190 meV). This is plotted with the linear fitting in the inset of Figure 5.8. Finally, the Hall effect mobility is in the $10^{-1}$ $cm^2$ $V^{-1}$ $s^{-1}$ range between 200-400 K and is not a strong function of temperature (Figure 5.8). These observations are consistent with small-polaronic transport both above and below $T_M$ in our samples.

The conventional Hall effect in the WFS measured in Zhao et al.'s [9] epitaxial thin films may indicate that there are additional effects of high Ti concentrations that affect the magnetotransport properties of hematite. That this behavior is not observed in bulk single crystal or polycrystalline α-$Fe_2O_3$ is not surprising. Such high Ti concentrations are not usually attainable using bulk single crystal growth techniques

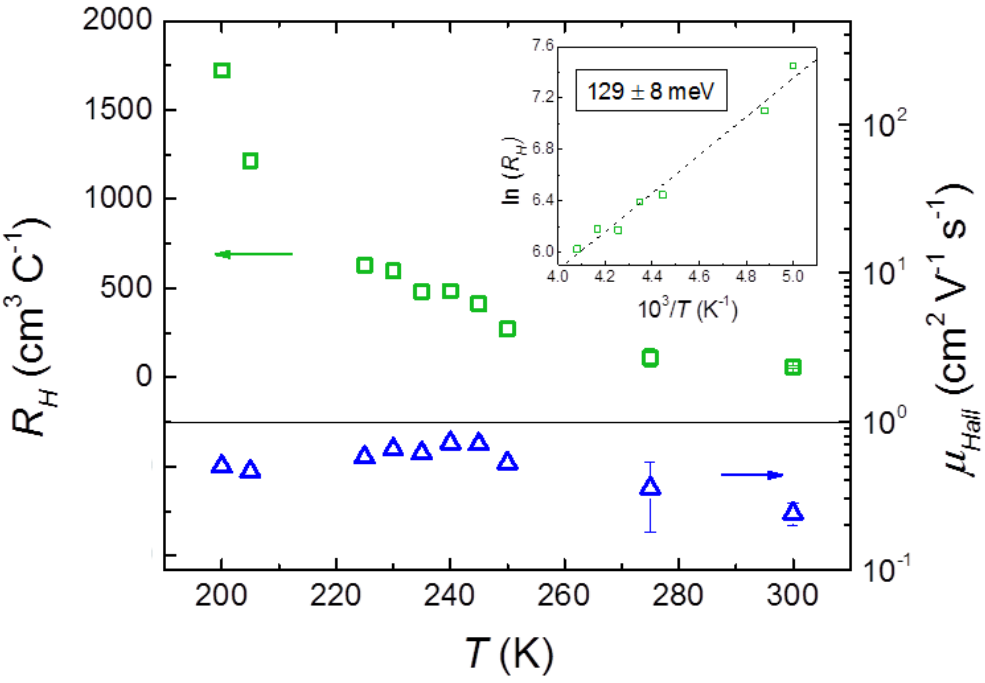


**Figure 5.8:** Hall coefficient and mobility versus temperature. Inset shows fitting of ln($R_H$) vs. reciprocal temperature from 200-245 K.

(typically < 1 at.%) and though achievable in ceramics, the effects of Ti-incorporation are often dampened in polycrystalline samples, e.g. the suppression of the Morin transition temperature [38]. Further investigations of single crystal transport as a function of doping over a wide range would therefore be extremely interesting.

### 5.3.5 Near-Isotropic Electronic Transport

To investigate any effects of Ti-doping on the anisotropy, conductivity measurements were also conducted in the *c*-axis for the Ti:α-$Fe_2O_3$ crystals. These are presented in Figure 5.9a for two crystals of different doping levels, with the undoped, single crystal α-$Fe_2O_3$ data from the work of Benjelloun et al. [13] also plotted for reference. Near-isotropic behavior over the temperature range 200-400 K was found, in contrast to the strongly anisotropy transport in undoped hematite. This is most clearly seen in Figure 5.9b where an anisotropy factor, $\Sigma$ (defined as = $\sigma_a$ / $\sigma_c$) is plotted verses reciprocal temperature. Linear extrapolation of the undoped data results in an anisotropy

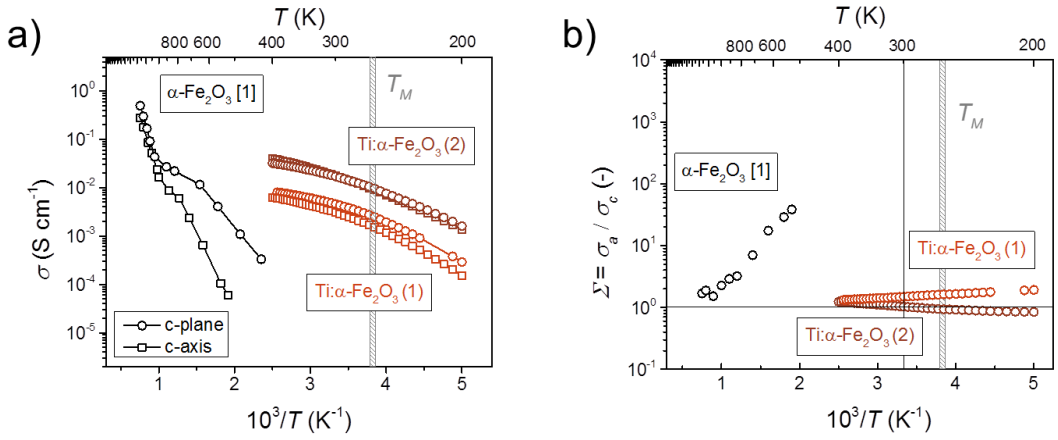


**Figure 5.9: a)** Conductivity in the *c*-plane and *c*-axis versus reciprocal temperature compared with the undoped data of Benjelloun et al.[13] **b)** Anisotropy factor versus reciprocal temperature calculated from the data in a).

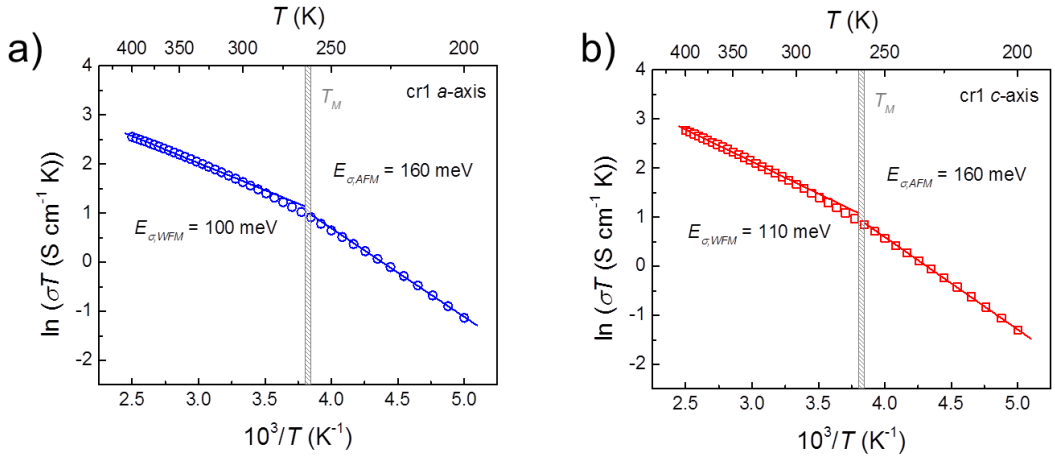


**Figure 5.10:** Fitting of conductivity data to equation 5.1 for **a)** *a*-axis conductivity and **b)** *c*-axis conductivity.

factor of 3- 4 orders of magnitude. Over the admittedly modest doping range achievable with CVT, all samples exhibited qualitatively the same behavior, although the crystals differed slightly; having either small positive or negative trends of $\Sigma$ with temperature.

We performed fitting of these conductivity data to the adiabatic small-polaron model to learn more about electron transport in the *c*-axis (Figure 5.10). Only minor differences exist between the fitting parameters (Table 5.2), indicating that the hopping mechanism is near-identical between them.

As shown in Figure 5.11, near-isotropic values and temperature dependences were also observed for the Seebeck coefficient. In agreement with the analysis of the basal plane transport, the Morin transition has only minimal effects on $S_c$, consistent with the electrons being small polarons. The Seebeck coefficient is related to the carrier concentration and number of thermally accessible transport states. The isotropy shown in Figure 5.11 indicates that there is no significant direction-dependence of these parameters and thus that the electron mobility is also isotropic in the *a* and *c*-axes.

**Table 5.2:** Adiabatic small-polaron fitting parameters.

| | Orientation | $E_\sigma$ (meV) | $\sigma_0 T$ (S cm$^{-1}$ K) | $\sigma_0$ (S cm$^{-1}$) at 300 K |
|---|---|---|---|---|
| WFS | *a*-axis | 94 ± 1 | 199 ± 1 | 0.664 ± 0.004 |
| | *c*-axis | 113 ± 1 | 424 ± 2 | 1.413 ± 0.01 |
| AFS | *a*-axis | 156 ± 2 | 2721 ± 26 | 9.1 ± 0.1 |
| | *c*-axis | 162 ± 1 | 3369 ± 20 | 11.2 ± 0.1 |

Clearly, these results are at odds with the conductivity anisotropy in undoped hematite and the conventional spin state arguments used to explain that anisotropy. In fact, is it as if the spin-barrier has been completely removed in the Ti:α-$Fe_2O_3$ crystals. This is puzzling, as Ti-doping does not affect the WFS of hematite: the magnetic moment is known to be unchanged within experimental error regardless of doping level [16], and this was confirmed by magnetization measurements on our samples (Figure D4 in Appendix D). Additionally, the Morin transition is clearly observed, further indicating that the spin environment is relatively unchanged from the undoped case. The exact mechanism is not known, but these results clearly demonstrate the complexity of Ti-doping in hematite and that these impurities have effects other than simply donating electrons to the lattice. Additionally, Zr:α-$Fe_2O_3$ single crystals exhibited much diminished conductivity anisotropy at high temperatures, hinting that these phenomena may be common to $M^{4+}$ dopants [12].

Distinct differences in magnetic properties have however been observed between pure hematite and Ti:α-$Fe_2O_3$ single crystals in a few electron magnetic resonance (EMR) spectroscopy studies. A shift and broadening of the resonance line was explained by considering a third sublattice of ferrous ($Fe^{2+}$) ions (induced by doping) that is antiferromagnetically coupled to the other two sub-lattices [53,54]. At this time, we

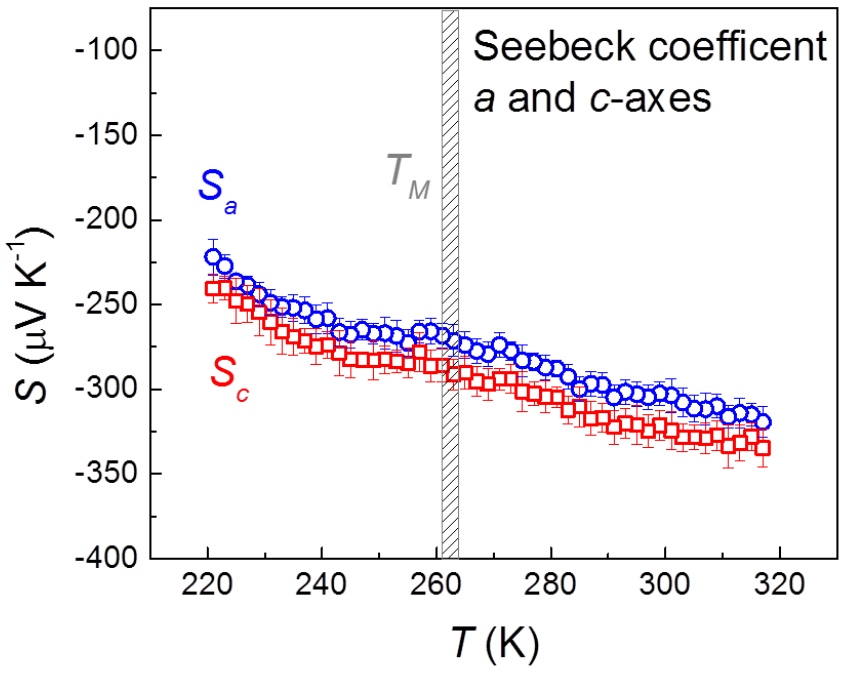


**Figure 5.11:** The Seebeck coefficient of a single crystal measured in both the *a* and *c*-axes.

speculate that the ions in this $Fe^{2+}$ sublattice are involved in hopping and are stabilized in minority spin configurations, softening the transport anisotropy between planes. This has also been postulated to be the origin of the oft-reported $T_M$ suppression with $M^{4+}$ ions, [53] the mechanism of which remains unresolved. Future experiments should include detailed EMR spectroscopy measurements to probe the nature of the ferrous ions, which are difficult to detect even in heavily doped samples [9]. The transport data presented here over a greater range of doping levels may also help rule in or out some of these ideas.

### 5.3.6 Optical Properties

Of special interest was low energy absorption in the mid-IR, characteristic of small-polarons. Three main features were observed in the reflectance spectra from 0.9 to 2.5 eV (Figure 5.12). The band gap, $E_g$ (~2.1 eV) and features at ~1.75 and ~1.4 eV, were evident of hematite. The latter features have been as-signed to (1) $^6A_1 \rightarrow 4E$ and (2) $^6A_1 \rightarrow {}^4A_2$ crystal field or ligand transitions [55]. The third feature was broad and centered around 0.7 eV. This was first observed by Morin in 1% Ti-doped polycrystalline thin films (~10 um thick) and attributed to transitions between Fe and Ti, where Ti ions act as electron donors [56].

At energies less than 0.5 eV, absorption bands corresponding to water and hydroxyl vibrational modes were observed [57,58]. These are most clear in the undoped powder spectrum and convoluted by broad infrared absorption in the doped powder spectra. Small-polaron conductors are best thought of as discrete ions with strongly trapped carriers. Photon absorption can cause the trapped carrier to be excited from its initial low energy state to a higher energy state on a neighboring ion: a small-polaron hop.[43] This broad peak is centered at ~$4E_a$ or ~0.4 eV in Ti:α-$Fe_2O_3$ [59]. Indeed, broad adsorption was observed across nearly the infrared range in the doped samples. The peak's width is related to the atoms thermal displacement, being most narrow at low temperatures and becoming broader as the temperature is increased. Temperature-dependent experiments would be necessary to fully decouple small-polaron absorption from any low energy crystal field or defect related transitions. However, in the context of our transport analysis we believe its assignment to be reasonable. The absorption does not scale with increased Ti-doping, but as mentioned previously, the effects of Ti-incorporation are often more strongly observed in single crystals than polycrystalline samples, e.g. the suppression of the Morin transition temperature [38].

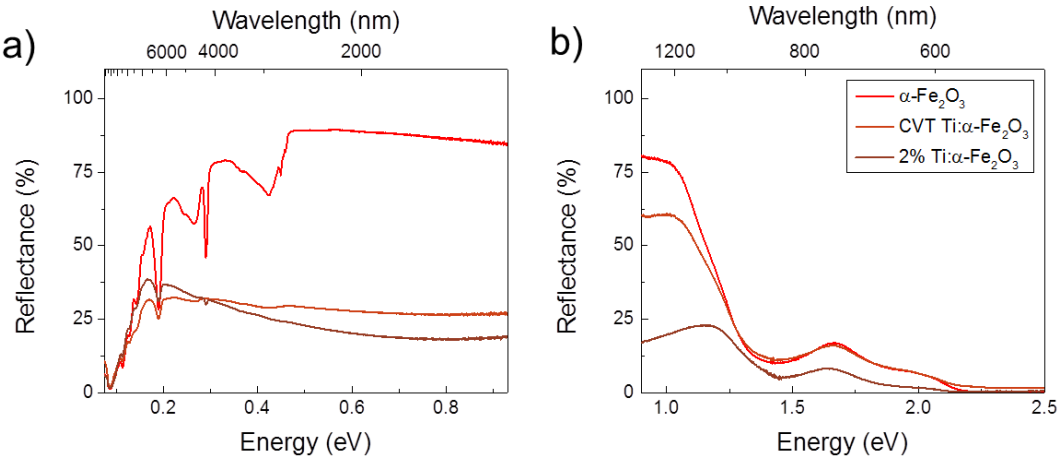


**Figure 5.12:** Reflectance vs. photon energy of undoped and Ti-doped hematite powders.

### 6.4. CONCLUSIONS

In summary, we synthesized single crystals of Ti:$Fe_2O_3$ via chemical vapor transport. The titanium concentration was too low to induce changes detectable by XRD or Raman spectroscopy. Basal plane transport was characterized by conductivity, Seebeck and Hall effect measurements between 200-400 K and found to be consistent with the adiabatic small-polaron hopping model. Below $T_M$, a larger barrier to electron hopping was observed. The Seebeck coefficient was large and negative, consistent with a doped n-type semiconductor. As observed in other small polaronic systems, the sign of the Hall coefficient (positive) was opposite to that of the Seebeck coefficient (negative). In the AFS, the activation energy of the Hall coefficient was consistent with a hopping loop with an odd number of members. Optical measurements revealed broad infrared absorption, again consistent with Ti donating electrons to the hematite lattice that form small polarons.

Conductivity was shown to be near-isotropic between the basal planes and perpendicular to them – in direct contradiction to the behavior reported for undoped

single crystals. The traditional spin state arguments for this behavior are invalid in the case of Ti:α-$Fe_2O_3$ single crystals, as no obvious changes to the magnetic properties occur with doping. Our results prompt a re-evaluation of the models for charge transfer and magnetic properties in hematite.

## REFERENCES


(1) Sivula, K.; Le Formal, F.; Grätzel, M. *ChemSusChem* **2011**, *4*, 432.

(2) Joly, A. G.; Williams, J. R.; Chambers, S. A.; Xiong, G.; Hess, W. P.; Laman, D. M. *Journal of Applied Physics* **2006**, *99*, 053521.

(3) Bosman, A.; Van Daal, H. *Adv. Phys.* **1970**, *19*, 1.

(4) Hahn, N. T.; Ye, H.; Flaherty, D. W.; Bard, A. J.; Mullins, C. B. *ACS Nano* **2010**, *4*, 1977.

(5) Hahn, N. T.; Mullins, C. B. *Chem. Mater.* **2010**, *22*, 6474.

(6) Hu, Y.-S.; Kleiman-Shwarsctein, A.; Forman, A. J.; Hazen, D.; Park, J.-N.; McFarland, E. W. *Chem. Mater.* **2008**, *20*, 3803.

(7) Ling, Y.; Wang, G.; Wheeler, D. A.; Zhang, J. Z.; Li, Y. *Nano Letters* **2011**, *11*, 2119.

(8) Cesar, I.; Sivula, K.; Kay, A.; Zboril, R.; Grätzel, M. *J. Phys. Chem. C* **2008**, *113*, 772.

(9) Zhao, B.; Kaspar, T. C.; Droubay, T. C.; McCloy, J.; Bowden, M. E.; Shutthanandan, V.; Heald, S. M.; Chambers, S. A. *Phys. Rev. B* **2011**, *84*, 245325/1.

(10) Rettie, A. J. E.; Lee, H. C.; Marshall, L. G.; Lin, J.-F.; Capan, C.; Lindemuth, J.; McCloy, J. S.; Zhou, J.; Bard, A. J.; Mullins, C. B. *J. Am. Chem. Soc.* **2013**, *135*, 11389.

(11) Rettie, A. J.; Chemelewski, W. D.; Lindemuth, J.; McCloy, J. S.; Marshall, L. G.; Zhou, J.; Emin, D.; Mullins, C. B. *Appl. Phys. Lett.* **2015**, *106*, 022106.

(12) Benjelloun, D.; Bonnet, J.; Doumerc, J.; Launay, J.; Onillon, M. *Mater. Chem. Phys.* **1988**, *20*, 1.

(13) Benjelloun, D.; Bonnet, J.-P.; Doumerc, J.-P.; Launay, J.-C.; Onillon, M.; Hagenmuller, P. *Mater. Chem. Phys.* **1984**, *10*, 503.

(14) Gharibi, E.; Hbika, A.; Dupre, B.; Gleitzer, C. *Eur. J. Solid State Inorg. Chem.* **1990**, *27*, 647.

(15) Katz, J. E.; Zhang, X.; Attenkofer, K.; Chapman, K. W.; Frandsen, C.; Zarzycki, P.; Rosso, K. M.; Falcone, R. W.; Waychunas, G. A.; Gilbert, B. *Science* **2012**, *337*, 1200.

(16) Flanders, P.; Remeika, J. *Philosophical Magazine* **1965**, *11*, 1271.

(17) Flanders, P. *Journal of Applied Physics* **1972**, *43*, 2430.

(18) Shull, C. G.; Strauser, W. A.; Wollan, E. O. *Physical Review* **1951**, *83*, 333.
(19) Besser, P.; Morrish, A.; Searle, C. *Physical Review* **1967**, *153*, 632.
(20) Artman, J.; Murphy, J.; Foner, S. *Physical Review* **1965**, *138*, A912.
(21) Nakau, T. *J. Phys. Soc. Japan* **1960**, *15*, 727.
(22) Acket, G.; Volger, J. *Physica* **1966**, *32*, 1543.
(23) Goodenough, J. B. *Prog. Solid State Chem.* **1971**, *5*, 145.
(24) Iordanova, N.; Dupuis, M.; Rosso, K. M. *J. Chem. Phys.* **2005**, *122*, 144305.
(25) Kment, S.; Schmuki, P.; Hubicka, Z.; Machala, L.; Kirchgeorg, R.; Liu, N.; Wang, L.; Lee, K.; Olejnicek, J.; Cada, M. *ACS Nano* **2015**.
(26) Morrish, A. H. *Canted antiferromagnetism: hematite*; World Scientific, 1994.
(27) Kronawitter, C.; Zegkinoglou, I.; Shen, S.-H.; Liao, P.; Cho, I.; Zandi, O.; Liu, Y.-S.; Lashgari, K.; Westin, G.; Guo, J.-H. *Energy & Environmental Science* **2014**, *7*, 3100.
(28) Binnewies, M.; Glaum, R.; Schmidt, M.; Schmidt, P. *Chemical vapor transport reactions*; Walter de Gruyter, 2012.
(29) Launay, J.; Horowitz, G. *J. Cryst. Growth* **1982**, *57*, 118.
(30) Sanchez, C.; Sieber, K.; Somorjai, G. *Journal of electroanalytical chemistry and interfacial electrochemistry* **1988**, *252*, 269.
(31) Cornell, R. M.; Schwertmann, U. *The iron oxides: structure, properties, reactions, occurrences and uses*; John Wiley & Sons, 2003.
(32) De Faria, D.; Venâncio Silva, S.; De Oliveira, M. *Journal of Raman Spectroscopy* **1997**, *28*, 873.
(33) Momma, K.; Izumi, F. *J. Appl. Crystallogr.* **2011**, *44*, 1272.
(34) Massey, M.; Baier, U.; Merlin, R.; Weber, W. *Phys. Rev. B* **1990**, *41*, 7822.
(35) Shim, S.-H.; Duffy, T. S. *American Mineralogist* **2002**, *87*, 318.
(36) Oh, S. J.; Cook, D.; Townsend, H. *Hyperfine Interact.* **1998**, *112*, 59.
(37) Sanchez, C.; Hendewerk, M.; Sieber, K.; Somorjai, G. *J. Solid State Chem.* **1986**, *61*, 47.
(38) Curry, N.; Johnston, G.; Besser, P.; Morrish, A. *Philosophical Magazine* **1965**, *12*, 221.
(39) Rosso, K. M.; Smith, D. M.; Dupuis, M. *The Journal of chemical physics* **2003**, *118*, 6455.
(40) Quinn, R. K.; Nasby, R. D.; Baughman, R. J. *Mater. Res. Bull.* **1976**, *11*, 1011.
(41) Baily, S. A.; Emin, D. *Phys. Rev. B* **2006**, *73*, 165211.
(42) Morin, F. J. *Physical Review* **1951**, *83*, 1005.
(43) Emin, D. *Polarons*; 1st ed.; Cambridge University Press: New York, 2013.
(44) Liu, N.-L. H.; Emin, D. *Phys. Rev. B* **1984**, *30*, 3250.
(45) Ransom, C. L., Montana State University, 1968.

(46) Vlasov, K.; Rozenberg, E. *SOV. PHYS. SOL. ST.* **1980**, *22*, 967.
(47) Ovsyannikov, S. V.; Morozova, N. V.; Karkin, A. E.; Shchennikov, V. V. *Phys. Rev. B* **2012**, *86*, 205131.
(48) Shchennikov, V. V.; Ovsyannikov, S. V.; Karkin, A. E.; Todo, S.; Uwatoko, Y. *Solid State Commun.* **2009**, *149*, 759.
(49) Voskanyan, R.; Levitin, R.; Shchurov, V. *Soviet Physics JETP* **1968**, *26*.
(50) Kaneko, T.; Abe, S. *J. Phys. Soc. Jpn.* **1965**, *20*, 2001.
(51) Chen, H.; Niu, Q.; MacDonald, A. *Phys. Rev. Lett.* **2014**, *112*, 017205.
(52) Jaime, M.; Hardner, H.; Salamon, M.; Rubinstein, M.; Dorsey, P.; Emin, D. *Phys. Rev. Lett.* **1997**, *78*, 951.
(53) Searle, C.; Morrish, A. *Journal of Applied Physics* **1966**, *37*, 1141.
(54) Searle, C.; Wang, S. *Journal of Applied Physics* **1968**, *39*, 1025.
(55) Marusak, L. A.; Messier, R.; White, W. B. *Journal of Physics and Chemistry of Solids* **1980**, *41*, 981.
(56) Morin, F. *Physical Review* **1954**, *93*, 1195.
(57)
(58) Farmer, V. C. *Infrared spectra of minerals*; Mineralogical society, 1974.
(59) Emin, D. *Phys. Rev. B* **1993**, *48*, 13691.

# Chapter 6: Improved Visible Light Harvesting of $WO_3$ by Incorporation of Sulfur or Iodine[4]

## 6.1 INTRODUCTION

Monoclinic tungsten trioxide ($WO_3$) [1] is a well-studied photoanode material due to its good charge transport properties and relative stability in acidic electrolytes. These characteristics and modest photocurrents under solar illumination have led to its use in multi-junction photoelectrochemical (PEC) systems [2-4]. However, its band gap of 2.6-2.7 eV limits its solar-to-hydrogen (STH) efficiency for PEC applications to 4-6% assuming a faradaic efficiency and quantum yield of unity [5].

Therefore, significant research efforts have been made to increase this material's visible light harvesting ability. The majority of these studies have focused on transition metal [6,7] or non-metal doping [8], and sensitization approaches using dyes [9] or other semiconductors [10-14]. Cole et al. investigated nitrogen-incorporation in $WO_3$ thin films, synthesized by reactive RF magnetron sputtering using $N_2$ as a background gas [15]. Though a significant reduction in the band gap was observed (< 2.0 eV), PEC performance was impaired due to lattice defects. However, other studies where films were treated in ammonia gas to add N are conflicting, showing improved light absorption and overall PEC performance in some cases [16], but poorer PEC performance in others [17]. Whether these impurities have positive or detrimental effects on the overall

[4] A.J.E. Rettie, K.C. Klavetter, J.-F. Lin, A. Dolocan, H. Celio, A. Ishiekwene, H.L. Bolton, K.N. Pearson, N.T. Hahn, C.B. Mullins. "Improved Visible Light Harvesting of WO3 by Incorporation of Sulfur or Iodine: A Tale of Two Impurities", *Chem. Mater.*, **2014**, 26 (4), pp 1670.
A. J. E. Rettie, A. Ishiekwene, H.L. Bolton, and K.N. Pearson synthesized the thin film samples, A. J. E. Rettie, K.C. Klavetter, H. Celio and A. Dolocan performed XPS and ToF-SIMS experiments and data analysis. J.-F. Lin aided in Raman spectroscopy experiments. All authors wrote and revised the manuscript.

photocurrent depends on how they affect the electronic structure of the material, their concentration and how they are incorporated into the host lattice.

Recent ab initio [18] and density functional theory (DFT) studies [19] have indicated that substitution of S at O-sites may create an impurity band that can reduce the band gap of $WO_3$. The incorporation of S is relatively unstudied experimentally [20]. Additionally, iodine-incorporation in $TiO_2$ particulate photocatalysts has led to improved visible light absorption and photocatalytic activity [21]. By analogy one may assume that I-incorporation may also have a positive effect on $WO_3$'s visible light absorption. To the best of our knowledge there are no reports on iodine doped $WO_3$. We have developed a simple, scalable spray pyrolysis procedure to synthesize sulfur and iodine-incorporated monoclinic $WO_3$ ($S:WO_3$ and $I:WO_3$ respectively) films and probe the effects of these impurities on visible light absorption and PEC performance.

First, we characterized the phase and morphology of the samples using X-ray diffraction (XRD) and scanning electron microscopy (SEM). Changes in optical properties were characterized by diffuse reflectance UV-Vis spectroscopy. PEC and incident photon conversion efficiency (IPCE) testing were used to evaluate the performance of the films as photoanodes and determine if the extra photons absorbed contributed to the photocurrent. The very low levels of impurities in the samples and their bonding environments were determined by a combination of time of flight secondary ion mass spectrometry (ToF-SIMS), X-ray photoelectron spectroscopy (XPS) and Raman spectroscopy. Finally, we discuss and provide evidence for the creation of defect states and their effect on the performance of $WO_3$ photoanodes.

In the interest of clarity, this chapter will focus on the 0.1% and 2% $S:WO_3$ and $I:WO_3$ films, with data for all doping concentrations in Appendix E. These were chosen because the lightly doped films showed the best PEC performance but the smallest

change in physical properties and vice versa for the heavily doped films. Further, to avoid repetition, the term "doping" will be used interchangeably with "incorporation" when discussing the addition of S or I to $WO_3$.

## 6.2. EXPERIMENTAL METHODS

### 6.2.1 Synthesis

Films were deposited using a spray pyrolysis set-up described previously [22,23]. Ammonium tungsten oxide hydrate, $(NH_4)_{10}W_{12}O_{41}•5H_2O$ (99.999%, Alfa Aesar), ammonium sulfide, $(NH_4)_2S$ (20% in water, Sigma-Aldrich) and ammonium iodide, $NH_4I$ (99%, Acros) were dissolved in demineralized water for use as precursor solutions. The precursor concentration was 0.075 M (based on moles of W), with dopant concentrations added based on the fractional substitution of oxygen (O) sites, i.e. a 0.5% doping level corresponds to enough S or I to replace 0.5% of the oxygen sites in fully oxidized $WO_3$. Hereafter, samples will be referred to as undoped $WO_3$, S:$WO_3$ or I:$WO_3$ with concentrations determined as above. In this study the concentrations investigated were 0, 0.1, 0.5, 1, 2 and 5% of the total O sites.

Ammonium tungsten oxide hydrate powder was dissolved in demineralized water by stirring for 30 minutes on a hot plate with a set point of 80 °C. Precursor solutions were pumped intermittently (~10 s on, 25 s off) through an ultrasonic spray nozzle (130 Hz, Sonotech) positioned above a hot plate in a ventilated enclosure under atmospheric conditions. The flowrate was 1.3 mL min-1, the volume per cycle was 0.4 mL and typically 25 cycles were required for good coverage of the substrate. Prior to deposition, substrates were ultrasonically cleaned in a mixture of detergent (Contrex), water and ethanol. After this step they were rinsed in water, ethanol and finally air dried. The heater

temperature set point was 300 °C, resulting in a substrate temperature of ~250 °C during deposition, as measured using an optical pyrometer (Microepsilon).

As-deposited films were translucent white and amorphous. Samples were annealed in at 550 °C for 1 hr in air and allowed to cool naturally to crystallize the monoclinic phase of $WO_3$.

### 6.2.2 Compositional Characterization

X-ray diffraction (XRD) was performed using a Philips X'Pert diffractometer equipped with monochromatic Cu Kα x-rays (λ = 1.54056 Å). The films were of sufficient thickness to use θ-2θ scans (without the need for grazing incidence XRD, required for thin films). Film morphology and thickness were determined using a Quanta 650 (FEI) scanning electron microscope (SEM). Diffuse reflectance UV−vis spectra were measured with a Cary 500 spectrophotometer attached to an integrating sphere (Labsphere DRA-CA-5500). X-ray photoelectron spectroscopy (XPS) measurements were performed on a Kratos AXIS Ultra DLD spectrometer with a monochromated Al-Kα X-ray source (hν = 1486.5 eV), hybrid optics (employing a magnetic and electrostatic lens simultaneously) and a multi-channel plate coupled to a hemispherical photoelectron kinetic analyzer. The photoelectrons take-off angle was normal to the surface of the sample and 45° with respect to the X-ray beam. An electron flood gun was employed to prevent charging of the samples and the pressure in the analysis chamber was typically $2\times10^{-9}$ Torr during data acquisition. CasaXPS (Version 2.3.15) software was used to analyze the XPS spectra. The adventitious carbon 1s peak was used as a reference with a binding energy (B.E.) of 285 eV. The error in the measurement of the B.E. associated with this procedure varies from ±0.1 to 0.2 eV [24,25]. ToF-SIMS data were acquired on a TOF.SIMS 5 instrument (ION-TOF GmbH, Germany, 2010) at a base pressure of <

$2\times10^{-9}$ Torr. Elemental concentrations of the species of interest were recorded as function of depth (i.e. depth profiling) by using a pulsed primary ion beam ($Bi_1^+$ at 30 kV energy and 3 pA measured sample current) for ultra-sensitive (parts-per-billion) surface chemical analysis and a secondary ion beam ($Cs^+$ at 2 kV energy and 90 nA measured sample current) for sputtering. The depth profiles were acquired in noninterlaced mode (i.e. sequential analysis and sputtering) from an analysis area of 100 × 100 $\mu m^2$ centered within a previously Cs sputtered 250 × 250 $\mu m^2$ area. A stable, constant energy (21 eV) electron beam was shot onto the sample surface during data acquisition for charge compensation. All detected secondary ions had negative polarity and with a mass resolution > 5000 (m/δm). An optical Raman system with a Verdi V2 532 nm green laser, Andor spectrometer, iCCD detector and a 1800 grating was utilized for vibrational spectroscopy measurements. Fityk (Version 0.9.8) peak fitting software was used to analyze the Raman spectra [26].

### 6.2.3 Photoelectrochemical Testing

Photoelectrochemical measurements were conducted in a glass 3-electrode cell using the $WO_3$ film as the working electrode, Ag/AgCl (1 M KCl) as the reference electrode and Pt wire as the counter electrode. All potentials reported here are versus the reversible $H_2$ electrode (RHE),

$$E_{RHE} = E_{Ag/AgCl} + 0.059\times pH + E^\circ_{Ag/AgCl}\ (1\ M\ KCl) \qquad (6.1)$$

where, $E^\circ_{Ag/AgCl}$ (1 M KCl) = 0.236 V at 25 °C [27].

and optical power meter (model 1830-C, Newport) were used to determine the incident photon to current conversion efficiency (IPCE). IPCE values were calculated using the formula [5]:

$$\mathrm{IPCE}(\lambda) = (1240 \cdot j(\lambda)) / (\lambda \cdot P(\lambda)) \times 100 \qquad (6.2)$$

where, $\lambda$ is the wavelength (nm), $j$ is the photocurrent density (mA $cm^{-2}$) and $P$ is the incident power density of the monochromated light (mW $cm^{-2}$). Illumination was from the solution-side of the PEC cell in all cases, passing through a glass window and ~3 cm of electrolyte solution.

The electrolyte solution used was 1 M methane sulfonic acid (Sigma Aldrich) with 0.1 M methanol (Fisher) added as a hole scavenger in most cases. A CH Instruments 660D potentiostat was used for all current-voltage and current-time scans. The scan rate was 10 mV $s^{-1}$.

## 6.3 Results and Discussion

### 6.3.1 Synthesis

Extreme care was taken to avoid contamination, as even small concentrations of the dopants studied had large effects on the material's properties. This involved flushing the precursor lines with clean solvent before runs and the use of separate lines for undoped, S:$WO_3$ and I:$WO_3$ samples.

Films deposited on quartz substrates were prone to excessive cracking and poor adhesion, whereas deposition on F:$SnO_2$ on glass (FTO, Pilkington) and glass slides (Corning) resulted in strongly bonded films. Thiourea was tried as an alternative sulfur

source to ammonium sulfide, but these films did not adhere strongly to the FTO substrates. Ethanol and ethylene glycol were also candidate solvents, but led to poor film coverage.

### 6.3.2 Phase and Morphology

X-ray diffraction (XRD) spectra for all samples could only be indexed to monoclinic $WO_3$ (PDF # 43–1035) and the underlying FTO substrate (Figures E.1 and E.2 in Appendix E), indicating the addition of S or I did not lead to the formation of secondary crystalline phases. At doping levels greater than 2% in the S:$WO_3$ films, peak broadening was observed, indicative of poorer crystallinity. Although both sulfur and iodide are larger than oxygen and should expand the lattice, the levels of these impurities were too low to induce crystallographic changes detectable by XRD.

Scanning electron microscopy (SEM) revealed a rough, leaf-like microstructure of the $WO_3$ films grown using spray pyrolysis (Figure 6.1). Cross-sectional SEM showed the film thickness after 25 deposition cycles was approximately 5 μm, but that the film profile was heavily corrugated, with minimum and maximum thicknesses of ~3 and ~8 um respectively (Figure 6.1b). The morphology is attributed to solvent evaporation and particle deposition from the gas phase as the spray approached the hot substrate during synthesis, and similar to other $WO_3$ films prepared by spray pyrolysis [28,29]. The incorporation of S and I did not change the morphology of the $WO_3$ appreciably (Figure 6.1c and 6.1d).

### 6.3.3 Optical Properties

For the 2% S:$WO_3$ and I:$WO_3$ films, significant color changes were observed relative to the undoped case; from pale green to yellow and brown/red respectively (Figure 6.2a). Intermediate compositions exhibited progressive visual color changes (Figure E.3) and shifts in absorption spectra (Figures E.4 and E.5). Tauc plot analyses [5] yielded indirect transitions at 2.7, 2.6 and 2.1 eV for $WO_3$, S:$WO_3$ and I:$WO_3$ respectively (Figure E.6). The addition of sulfur resulted in a slight shift of the absorption

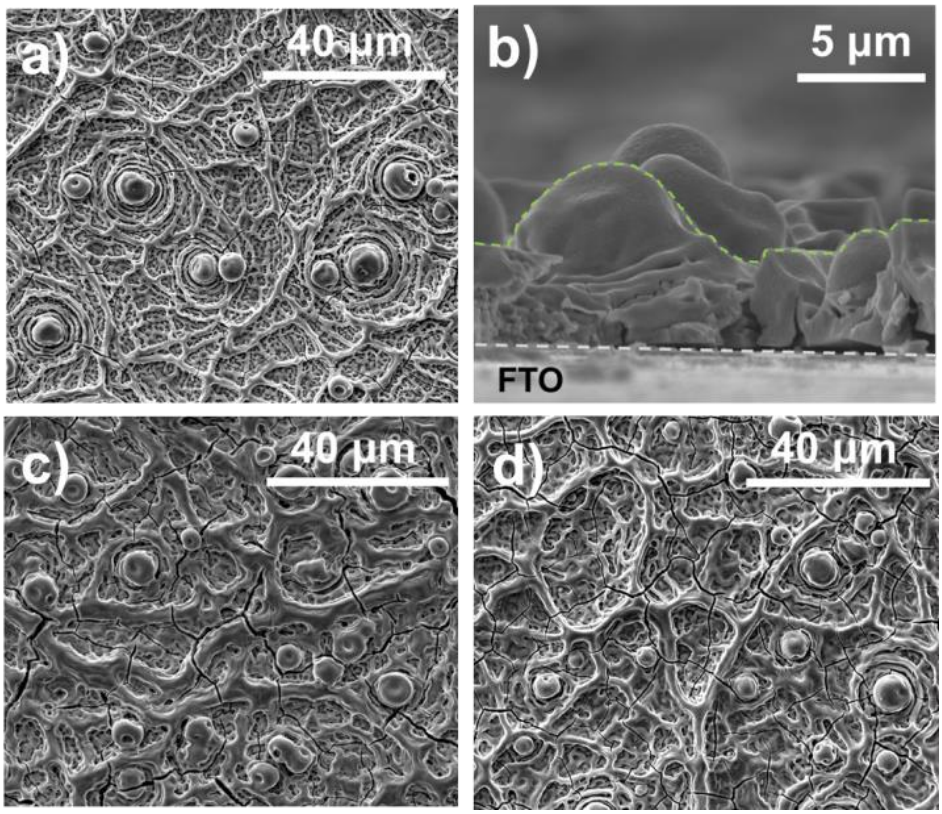


**Figure 6.1**. Scanning electron micrographs of the $WO_3$ film morphology. a) Undoped $WO_3$, b) Cross-sectional view of a $WO_3$ film, c) 2% S:$WO_3$, d) 2% I:$WO_3$.

edge to longer wavelengths, whereas iodine created what appeared to be a new and separate transition, while retaining the fundamental band gap transition of $WO_3$ at ~2.7 eV (Figure 6.2b).

We attempted to learn more about these transitions using photoluminescence (PL) spectroscopy, but no PL was observed from the samples at room temperature, indicating that recombination from these new states was non-radiative.

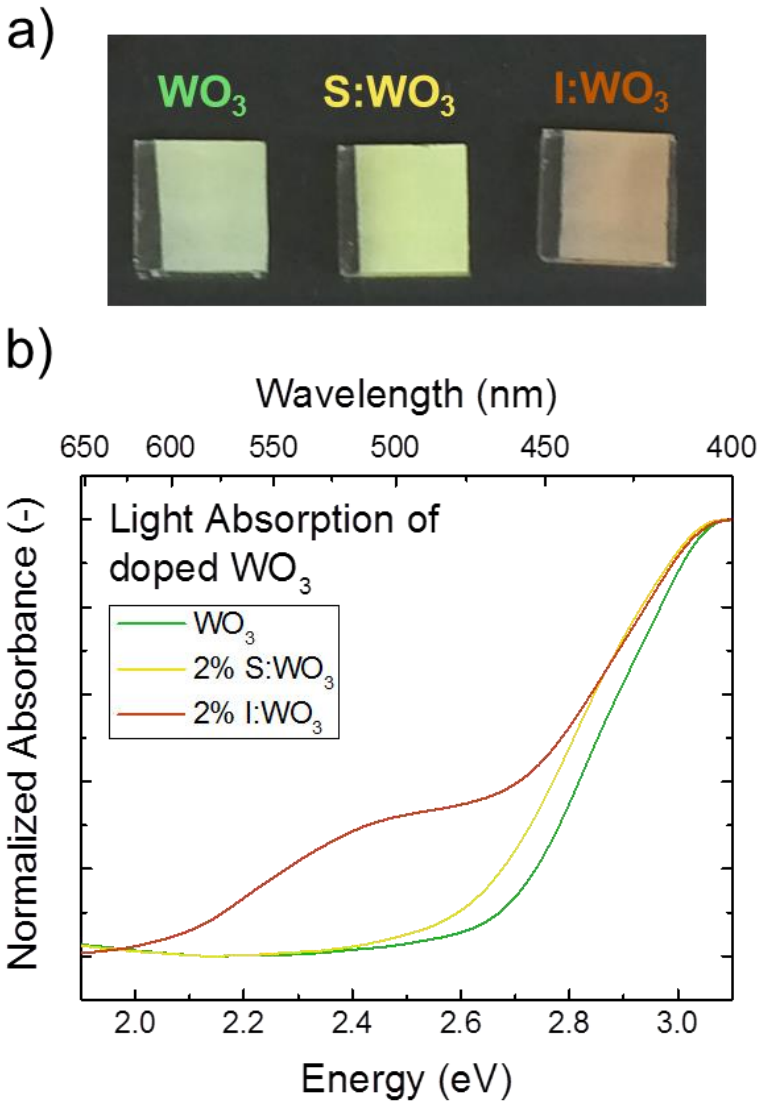


**Figure 6.2. a)** Photograph of undoped, 2% S:$WO_3$ and 2% I:$WO_3$ on 1.5 × 1.5 $cm^2$ FTO substrates. **b)** UV-Vis spectra of undoped and doped films.

### 3.4 Photoelectrochemical (PEC) Characterization

The choice of electrolyte is extremely important in PEC cell design. Recent work has shown that faradaic $O_2$ production is not achieved at $WO_3$ photoanodes in common aqueous electrolytes such as $H_2SO_4$, $HClO_4$ and HCl, with anion oxidation competing with water oxidation on the $WO_3$ surface [30-32]. Further, Hill and Choi showed that $WO_3$ was not stable in many acidic electrolytes [30]. Solarska et al. achieved stable photocurrents for up to 14 hrs using a methane sulfonic acid electrolyte after an initial loss (over 1-2 hrs) of 20% of the photocurrent for their nanostructured $WO_3$ electrodes [33]. We observed similar behavior for our films (Figure E.7). However, this initial degradation complicated the comparison of samples over repeated short–term tests. As we were primarily interested in the bulk film properties and not the kinetics of oxidation processes at its surface, 0.1 M methanol was added as a hole scavenger for most testing. This facilitated stable, consistent behavior over repeated PEC tests. Methanol oxidation is significantly easier than water oxidation and takes part in current doubling [34], so larger photocurrents were observed with its addition (Figure 6.3). Complimentary experiments without the addition of methanol showed the same trends (Figure E.8a and b). Surprisingly, no oxygen bubbles were observed during ~1 hr long tests in 1 M methane sulfonic acid (data in Figure E.8b), suggesting a significant fraction of the photocurrent did not go towards water oxidation in this electrolyte. As previously mentioned, this is often the case for $WO_3$ photoanodes and highlights the need for oxygen evolution reaction electrocatalysts for this material [35], which is a subject of further research in our laboratory.

The photocurrents achieved with our undoped $WO_3$ films (0.5 and 0.75 mA $cm^{-2}$ at 1.23 V vs. RHE with and without a hole scavenger respectively) are comparable to

other $WO_3$ films deposited by spray pyrolysis (SP), such as the work of Sun et al. (when their higher lamp intensity is taken into account) [8]. However, the performance of the samples deposited by SP is lower than other WO3 films synthesized by sol-gel [33,34], RF sputtering [15] or electrodeposition [32] under the same illumination conditions. We

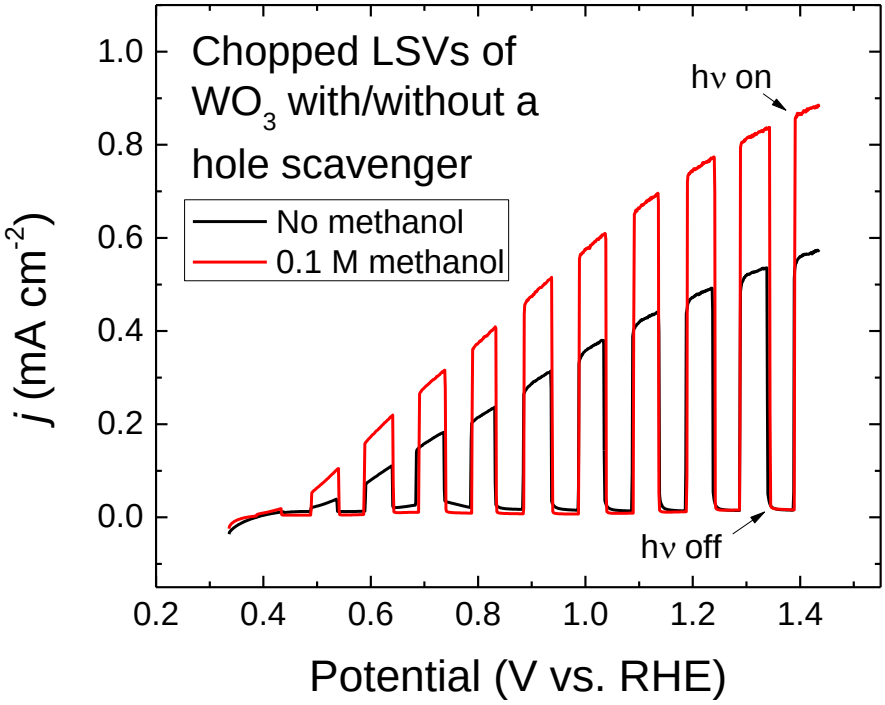


**Figure 6.3.** Chopped linear scan voltammagrams (LSV) of undoped WO3 in 1 M methane sulfonic acid with and without 0.1 M methanol as a hole scavenger under AM1.5G simulated solar light (100 mW cm-2). The scan rate was 10 mV s-1 and potential was scanned in the positive direction.

attribute this to two key differences between films grown by SP and those by other methods: the degree of nanostructuring and film thickness. The best performing $WO_3$ electrodes have features on the order of 50 nm, increasing the active surface area and minimizing carrier transport distances relative to the compact, rough microstructure

(Figure 6.1) observed in our work. Further, nanometer sized features may scatter incident light, allowing the use of thinner, more efficient films (~2.4 μm or less compared to an average of 5 μm (Figure 6.1b)). Incorporation of S and I into $WO_3$ photoelectrodes with advantageous morphologies either by optimizing the SP technique or by other synthesis methods would be an interesting avenue for future work.

The trends with increased S or I doping are shown in Figure 6.4. At very low S concentrations, photocurrents were improved compared to undoped WO3, but worsened with increasing sulfur. The large decrease in performance at 2% coincides with poorer crystallinity as seen in the XRD data (Figure E.1) Film performance was variable, especially around 1% S:$WO_3$, where a possible change in the incorporation mechanism may have occurred. Evidence for this will be provided in Section 6.3.8.

As shown in Figure 5a, 0.1% S:$WO_3$ exhibited improved full spectrum and

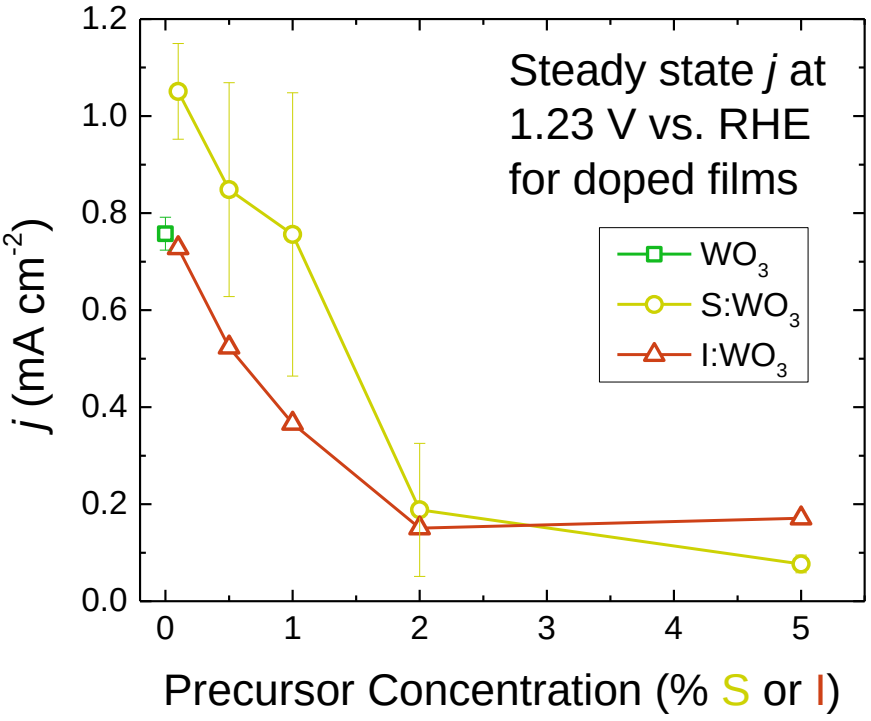

**Figure 6.4.** Steady state photocurrent under AM1.5G simulated solar light (100 mW cm-2) vs. initial sulfur and iodine precursor concentration. Points with error bars were constructed using the average of 3 films ± one standard deviation.

visible light photocurrents compared to undoped $WO_3$. Incident photon conversion efficiency (IPCE) measurements showed increased efficiency at longer wavelengths. All S:$WO_3$ films showed a similar spectral profile (Figure E.9) that is in agreement with the shift to longer wavelengths in the UV-Vis absorption spectra (Figure 6.2). We note that the 0.1% S:$WO_3$ sample exhibited a slight IPCE improvement at wavelengths less than 400 nm (Figure 6.5b) and attribute this to variations in film thickness, and hence performance, as shown by the error bars in Figure 6.4. For a full discussion see Section E3.1 in Appendix E. A typical power density spectrum for IPCE testing is located in the Appendix E (Figure E.10). Integration of the IPCE values with respect to the AM1.5G reference spectrum (ASTM G-173) [36] over-estimated the photocurrent by up to 30%, but showed the same trends as seen for photocurrents obtained with the solar simulator (Tables E.1 and E.2). This over-estimation may arise due to a decreased carrier recombination rate at low light intensity.

With increasing I incorporation, overall photocurrent decreased (Figure 6.4), possibly due to an increased number of recombination sites due to a higher concentration of defects. Despite absorbing substantially more visible light, 0.1% I:$WO_3$ exhibited only a slight increase in the visible light contribution to the total photocurrent (Figure 6.5a), which occurred with a corresponding decrease in IPCE at wavelengths less than 400 nm (Figure 6.5b). The spectral shape was maintained even as increased I incorporation hurt overall PEC performance (Figure E.11).

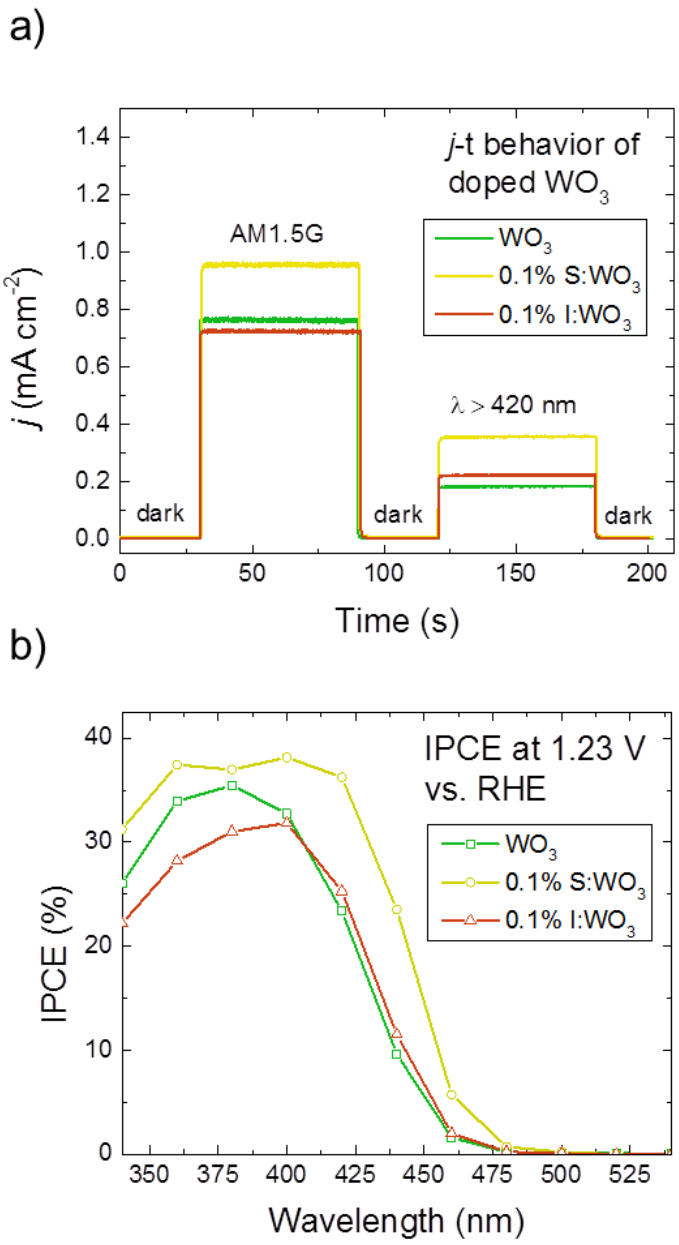


**Figure 6.5. a)** Photocurrent-time (*j-t*) data under AM1.5G simulated solar light (100 mW $cm^{-2}$) and with a long pass filter. The electrolyte was 1 M methane sulfonic acid with 0.1 M methanol. Complimentary *j-t* data without methanol showed the same trend (Figure E.8a in Appendix E).**b)** IPCE vs. wavelength at 1.23 V vs. RHE. The electrolyte in both cases was 1 M me-thane sulfonic acid with 0.1 M methanol.

### 6.3.5 ToF-SIMS

To determine the amounts and distributions of S and I in the films, sequential ToF-SIMS and XPS analyses were carried out. The samples used had not been previously PEC tested to avoid contamination with the sulfur-containing electrolyte. The selection of suitable marker ions is discussed in Appendix E (Section E.4).

Depth profiling on different areas of the samples indicated different thicknesses. As shown in Figure 1, the film is extremely rough; thus it was not practical to convert the sputtering time to a film depth. To ensure a fair analysis of the bulk film in all cases, we compared the depth profiles up to 2500 s of sputtering time, where signals from FTO substrate emerged in the thinnest areas.

Figures 6.6a and b illustrate the depth profiles for representative S:$WO_3$ and I:$WO_3$ samples. The sulfur distribution was uniform throughout the films (Figure 6.6a), and qualitatively agreed with the trend in precursor concentrations, i.e. higher S concentration in precursor, more S in the resulting film. As shown in Figure 6.6a (tabulated in Table E.3 in Appendix E), scaling was relatively close until 2%, where there was a jump in S concentration. After this point, saturation of S in the $WO_3$ lattice seems to be occurring.

Conversely, the I distribution varied as a function of sputtering depth, with a maximum at the surface that tailed off through the film. We speculate that this concentration profile was caused by the pulsed nature of the spray pyrolysis synthesis and volatile nature of iodine at the deposition temperature (~250 °C). After each deposition cycle, the as-deposited film was left at the hot plate temperature to allow for solvent evaporation, during which iodine left the sample. The final layers near the top of the film spent the least amount of time on the hot plate and so retained the most iodine. The

concentration of I scaled well with the initial concentration in the precursor, but saturated after 1% near the bottom of the films (after 1000 s in Figure 6.6b).

### 6.3.6 XPS

XPS was used to quantify the concentrations and charge states of the dopants. W 4*f* and O 1*s* regions agreed well with reported tungsten trioxide XPS spectra [37,38], with peaks at 35.7 eV ($4f_{7/2}$) and 530.5 eV respectively (Figure 6.6c and d). These indicate the presence of $W^{6+}$ and $O^{2-}$. Fitting of the W 4*f* region showed the correct peak split-ting (2.2 eV) and area ratio (0.75) between $4f_{7/2}$ and $4f_{5/2}$ peaks – thus only the 6+ oxidation state of tungsten was observed. The shoulder at higher B.E. on the main O 1*s* peak (Figure 6d) has been observed in many transition metal oxides and is attributed to either defective oxygen sites [39,40] or surface hydroxides.

Due to the low concentration of S and I in the doped samples, heavily doped samples (20% S:$WO_3$ and 2% I:$WO_3$) were used for XPS analysis of the chemical speciation within the films. With the incorporation of S and I, we saw no significant changes in the W 4*f* and O 1*s* regions compared to undoped $WO_3$. The W:O atomic ratio was ~3 for all samples.

Despite our best efforts and intense scan conditions (1.5 s dwell time, 16 sweeps), we did not observe a sulfur signal in the bulk of the 20% S:$WO_3$ sample (correspondingly, lower concentration samples also had no detectable signal). There was a surface concentration of $S^{6+}$ (Figure E.12a) which has been observed in other reports [20]. This peak disappeared after light $Ar^+$ sputtering (Figure E.12b), therefore we attribute it to surface sulfate species. Clearly, it is not the same as the bulk S observed in

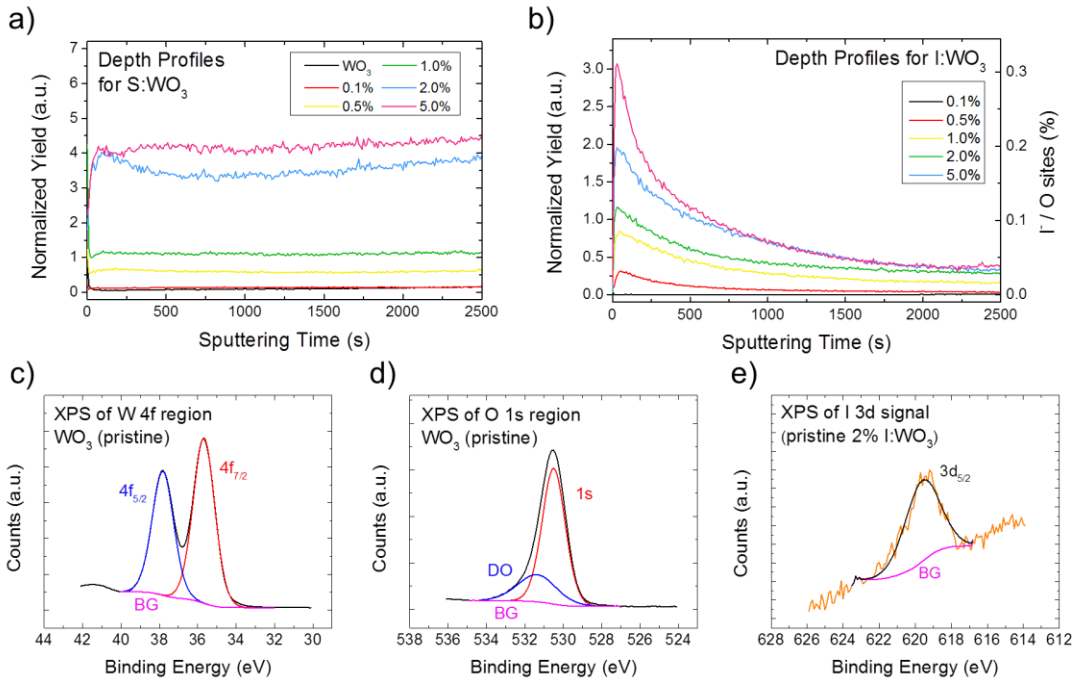


**Figure 6.6. a)** ToF-SIMS depth profiles of S:WO3, showing the fraction of the marker ions ($S^-$ / $^{180}WO_3$) vs. sputtering time for each film. **b)** ToF-SIMS depth profiles of I:$WO_3$ films, showing the fraction of the marker ions ($IO^-$ / $^{180}WO_3$) vs. sputtering time on the left *y*-axis. The normalized yield was converted to the percentage of I- of total O sites using XPS data on the right *y*-axis, where O sites = 3*$W^{6+}$ concentration from the XPS data, assuming fully oxidized $WO_3$. This was performed for comparison to the starting precursor concentrations. XPS data and fitting for pristine, undoped $WO_3$ **c)** W 4*f* region, **d)** O 1*s* region and e) pristine 2% I:$WO_3$, I 3*d* region. OH/DO: hydroxide/defect oxide, BG: background.

the ToF-SIMS data (Figure 6.6a) which was uniform throughout the film. Therefore, we could not assign charge states or quantify the sulfur concentration for the S:$WO_3$ films. We could however, estimate an upper limit of the concentration by fitting the instrumental noise. This yielded an upper limit for sulfur doping of ~0.1% compared to 20% – indicating a very low incorporation level relative to the precursor concentrations.

The I $3d_{5/2}$ peak was located at 619.5 eV (Figure 6.6e), corresponding to I in the 1- oxidation state [21]. Combined ToF-SIMS and XPS were used to quantify the

concentration of I in the films. This procedure is detailed in Section E5.3 in Appendix E. Figure 6.6b shows a maximum concentration of 0.3% relative to the oxygen sites, on the same order as the incorporation levels for the S:$WO_3$ samples. These analyses show that large excesses of both of these impurities were required to incorporate them into $WO_3$, even in small amounts. The difficulties detecting sulfur by XPS is likely due to its low relative sensitivity factor compared to iodine (0.668 for S 2*p* vs. 10.343 for I 3*d*) and the very low concentrations present.

### 6.3.7 Raman Spectroscopy

Raman spectroscopy was used to probe changes in the $WO_3$ bonding environment due to sulfur or iodine incorporation. Undoped $WO_3$ showed only characteristic peaks for the monoclinic phase (Figure 6.7) [41,42]. Note that this spectrum is quite complex 48 Raman modes are active [41] and only the main peaks have been assigned in the literature.

Upon sulfur incorporation (2% and above), shifts to lower wavenumbers of the modes at 273, 717 and 807 $cm^{-1}$ and peak broadening occurred (Figures 6.7 and E.14). These bands correspond to stretching modes of the W-O bonds, and a shift to lower wavenumbers suggests a heavier atom such as sulfur has replaced the oxygen [43]. Peak broadening in Raman spectra is associated with poorer crystallinity, as seen in the XRD data (Figure E.1). It was difficult to assign the broad peak at ~630 $cm^{-1}$, as though this slight shoulder is present in the undoped samples; it is very weak and has not been previously assigned. It does not line up with Raman bands in examples of W-S or W-O bonding as in tungsten disulfide [44] or sulfur dioxide [45,46]. A candidate feature has been observed in aqueous sulfate solutions: the deformation of the $S_2O_5^{2-}$ ion [46], but

none of the other modes for this ion were present in our spectra. Additionally, a similar feature has been seen in Raman spectra for $WO_3$ cationically doped with Sn and Si, but was not assigned [47]. Therefore, we cannot conclusively determine whether only sulfur substitution on the O-site or a combination of cation and anion sulfur substitution occurs in these heavily doped samples. Surprisingly, we did not observe peak shifts up to 1% S:$WO_3$ (Figure E.14), either because the very low concentrations could not be detected by Raman, or the nature of sulfur incorporation in the $WO_3$ lattice not substitutional at concentrations less than 2%.

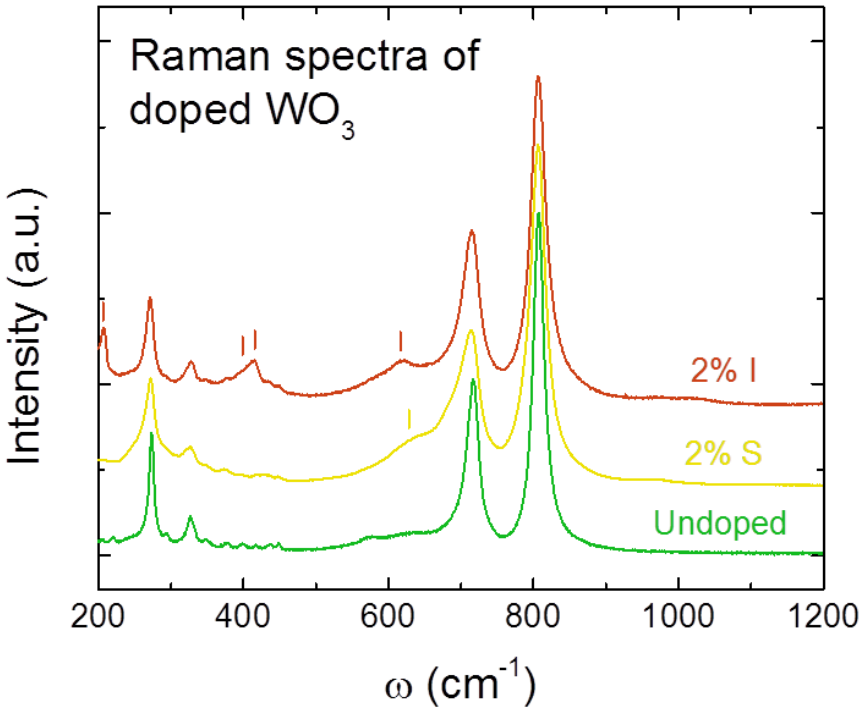


**Figure 6.7**. Raman spectra of undoped and doped films. Only traces for undoped, 2% S:$WO_3$ and 2% I:$WO_3$ films are shown for simplicity. Vertical ticks indicate peaks either not present or weaker in the undoped $WO_3$ spectrum. Spectra for all samples can be located in Appendix E.

Increasing iodine incorporation resulted in gradual peak shifts to lower wavenumber and broadening (Figures 6.7 and E15), which we attribute to substitution of I on the O-site and a lower degree of crystalline perfection. Several auxiliary peaks became more pronounced with I incorporation: at ~207, 400, 415 and 615 $cm^{-1}$ (Figure 6.7). As previously mentioned, the Raman spectra of monoclinic $WO_3$ is quite complex, so it was difficult to determine whether these are existing peaks whose intensity has increased, or new modes due to iodine in the $WO_3$ lattice (Figure E.16). As the intensity of these peaks tracks with increasing I content, we tentatively assign to them new W-I bonding modes. There is a lack of tungsten oxyiodide compounds in the literature, and hence no reference Raman patterns. Theoretical calculations will be invaluable in elucidating the nature of these peaks in both the S:$WO_3$ and I:$WO_3$ samples.

### 6.3.8 Incorporation Mechanism

Monoclinic $WO_3$ (space group $P2_1/n$, $a$ = 7.327 Å, $b$ = 7.564 Å, $c$ = 7.727 Å, $\beta$ = 90.49° [48]) adopts a distorted cubic $ReO_3$ structure, closely related to the cubic perovskite ($AMO_3$) structure, but without a cation on the A site. It consists of tilted edge-sharing $WO_6$ octahedra (Figure 6.8a). Several possible cases exist for dopant incorporation in the lattice: i) interstitially, ii) intercalation in the "empty" A-site between the $WO_6$ units, iii) substitutionally for W or iv) for O.

**Sulfur** Because bulk S could not be detected, even in heavily doped films, XPS could not be used to provide evidence for the location of S atoms. Li et al. showed the presence of $S^{6+}$ on the surface of their S:$WO_3$ powders and associated it with the substitution of $W^{6+}$ by $S^{6+}$ [20]. It is worth noting that this has been observed in the case

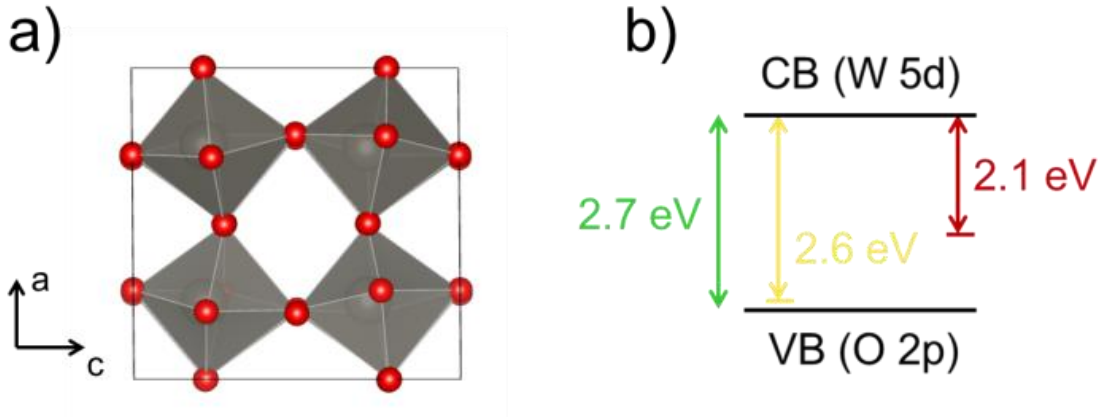


**Figure 6.8. a)** Schematic of the monoclinic $WO_3$ structure, illustrating edge-sharing $WO_6$ units (grey) and oxygen atoms (red) created with VESTA software [53]. Not to scale. **b)** Simplified band diagram showing the suggested locations of mid-gap impurity bands.

of S:$TiO_2$, where sulfur has been detected in the 2- [49], 4+ [50] and 6+ [51] oxidation states, indicating both anionic and cationic substitutions are possible. The cases of 2- and 4+ have been studied by DFT, where substitution on either site did not change the electronic density of states significantly [52], i.e., the sulfur 3*p* orbitals form impurity states close the valence band edge of $TiO_2$.

As mentioned in Section 6.3.7, no differences between the undoped and S:$WO_3$ samples was observed until 2%, after which O -- and possibly W – substitution occurred. Considering theoretical calculations for S on O site substitution in S:$WO_3$ [18,19] and by analogy with cation doped S:$TiO_2$ [52], we suggest that at these higher dopant concentrations, a relatively shallow defect state is formed ~0.1 eV above the valence band (Figure 6.8b), which caused increased visible light absorption. At these higher levels of incorporation, the crystalline quality of the lattice has been degraded (broadening of XRD and Raman peaks) leading to lower PEC performance.

Below 1% S:$WO_3$ no sulfur was detected by XPS or Ra-man up to 1200 $cm^{-1}$. This prompted us to look at other incorporation options, such as an oxidized sulfur compound (e.g. $SO_2$) in the space between the $WO_6$ octahedra, in which case Raman modes consistent with S-O bonding should be present. As an example, stable $N_2$ intercalation has been observed in monoclinic $WO_3$ [54]. However, we saw no differences in the Raman spectra up to 4500 $cm^{-1}$. Though we cannot comment on the location of sulfur in the lightly doped samples, there are large changes from 1 to 2% S:$WO_3$ in the XRD spectra (Figure E.1), Raman (Figure E.14), UV-Vis (Figure E.4, inset), ToF-SIMS (Figure 6.6a) and PEC data (Figure 6.4). It is possible that the incorporation mechanism at low concentrations may be different than the substitution seen in the heavily doped case, though the UV-Vis spectra (Figure E.4) would suggest that in both scenarios a shallow defect state is created. Sensitive analytical techniques, for example, solid state NMR, hard X-ray absorption spectroscopy or neutron scattering may help understand the role of sulfur at these low concentrations, but are out of the scope of this study.

**Iodine** Raman spectroscopy indicated I substituted for O and as only $I^-$ was present the XPS spectra, we conclude that this ion substitutionally replaced $O^{2-}$ in $WO_3$. We would expect this substitution to be quite destructive to the lattice as $I^-$ is much larger than $O^{2-}$ (2.2 Å vs. 1.4 Å for 6-fold coordination [55]) Additionally, $I^-$ should act as an electron donor, possibly resulting in $W^{6+}$ vacancies or reduced W sites so that the excess charge is balanced, further lowering the crystalline quality. No peak broadening was observed in XRD spectra, but was observed using Raman spectroscopy with progressive I doping. UV-Vis spectroscopy indicates that iodine forms a deep impurity band, ~0.6 eV above the valence band maximum (Figure 6.8b). The combination of this deep trap acting as a recombination center and disruption of the crystal lattice explains the poorer PEC performance of the I:$WO_3$ films.

## 6.4. CONCLUSIONS

In summary, we synthesized films of sulfur or iodine incorporated $WO_3$, with the aim to improve its visible light harvesting ability and PEC performance. Red-shifts of the absorption spectra were observed with S and I-incorporation (from ~2.7 to 2.6 and 2.1 eV respectively). S:$WO_3$ samples exhibited better PEC performance at low S concentrations, but worsened with increasing S addition. PEC and IPCE data showed that this initial improvement was driven by improved collection efficiency at longer wavelengths. Conversely, photocurrent decreased at all levels of I addition. IPCE measurements for these films showed only a marginal increase in efficiency at longer wavelengths, indicating that the extra absorbed photons did not contribute significantly to the photocurrent. ToF-SIMS was used to detect the very small levels of impurities and revealed a uniform concentration of S throughout S:$WO_3$ films, but a decreasing I concentration from the surface in the I:$WO_3$ samples. Raman and XPS showed that S and I substituted for oxygen, but in the case of S, other pathways – such as intercalation and cation substitution – could not be ruled out. In the case of S:WO3, the relatively shallow impurity state allowed greater visible light absorption without compromising the quality of the crystal lattice at low concentrations, while incorporation of iodine created a deep impurity band, negatively affecting the performance at all concentrations investigated in this study. Non-metal doping of metal oxides is a contentious subject in the literature and our study highlights that advanced characterization techniques and theoretical calculations will be vital in understanding these new materials.

## REFERENCES

(1) Here "$WO_3$" will refer to the high temperature monoclinic phase of $WO_3$ ($\gamma$-$WO_3$) as opposed to the low temperature monoclinic form ($\varepsilon$-$WO_3$).

(2) Grätzel, M. *Nature* **2001**, *414*, 338.

(3) Brillet, J.; Yum, J.-H.; Cornuz, M.; Hisatomi, T.; Solarska, R.; Augustynski, J.; Graetzel, M.; Sivula, K. *Nature Photonics* **2012**, *6*, 824.

(4) Miller, E. L.; Paluselli, D.; Marsen, B.; Rocheleau, R. E. *Solar Energy Materials and Solar Cells* **2005**, *88*, 131.

(5) Chen, Z.; Jaramillo, T. F.; Deutsch, T. G.; Kleiman-Shwarsctein, A.; Forman, A. J.; Gaillard, N.; Garland, R.; Takanabe, K.; Heske, C.; Sunkara, M. *J. Mater. Res* **2010**, *25*, 3.

(6) Maruthamuthu, P.; Ashokkumar, M. *Solar Energy Materials* **1988**, *17*, 433.

(7) Baeck, S. H.; Jaramillo, T. F.; Braendli, C.; McFarland, E. W. *J. Comb. Chem.* **2002**, *4*, 563.

(8) Sun, Y.; Murphy, C. J.; Reyes-Gil, K. R.; Reyes-Garcia, E. A.; Thornton, J. M.; Morris, N. A.; Raftery, D. *International Journal of Hydrogen Energy* **2009**, *34*, 8476.

(9) Zheng, H.; Tachibana, Y.; Kalantar-zadeh, K. *Langmuir* **2010**, *26*, 19148.

(10) Su, J.; Guo, L.; Bao, N.; Grimes, C. A. *Nano Letters* **2011**, *11*, 1928.

(11) Hong, S. J.; Lee, S.; Jang, J. S.; Lee, J. S. *Energy & Environmental Science* **2011**, *4*, 1781.

(12) Sivula, K.; Formal, F. L.; Grätzel, M. *Chemistry of Materials* **2009**, *21*, 2862.

(13) Chatchai, P.; Murakami, Y.; Kishioka, S.-y.; Nosaka, A. Y.; Nosaka, Y. *Electrochimica Acta* **2009**, *54*, 1147.

(14) He, H.; Berglund, S. P.; Xiao, P.; Chemelewski, W. D.; Zhang, Y.; Mullins, C. B. *Journal of Materials Chemistry A* **2013**, *1*, 12826.

(15) Cole, B.; Marsen, B.; Miller, E.; Yan, Y.; To, B.; Jones, K.; Al-Jassim, M. *The Journal of Physical Chemistry C* **2008**, *112*, 5213.

(16) Liu, Y.; Li, Y.; Li, W.; Han, S.; Liu, C. *Applied Surface Science* **2012**, *258*, 5038.

(17) Nah, Y.-C.; Paramasivam, I.; Hahn, R.; Shrestha, N. K.; Schmuki, P. *Nanotechnology* **2010**, *21*, 105704.

(18) Migas, D.; Shaposhnikov, V.; Rodin, V.; Borisenko, V. *Journal of Applied Physics* **2010**, *108*, 093713.

(19) Wang, F.; Di Valentin, C.; Pacchioni, G. *The Journal of Physical Chemistry C* **2012**, *116*, 8901.

(20) Li, W.; Li, J.; Wang, X.; Chen, Q. *Applied Surface Science* **2012**, *263*, 157.

(21) Tojo, S.; Tachikawa, T.; Fujitsuka, M.; Majima, T. *The Journal of Physical Chemistry C* **2008**, *112*, 14948.

(22) Hahn, N. T.; Hoang, S.; Self, J. L.; Mullins, C. B. *ACS Nano* **2012**, *6*, 7712.

(23) Hahn, N. T.; Self, J. L.; Mullins, C. B. *The Journal of Physical Chemistry Letters* **2012**, *3*, 1571.

(24) Miller, D.; Biesinger, M.; McIntyre, N. *Surface and Interface Analysis* **2002**, *33*, 299.

(25) Biesinger, M. C.; Payne, B. P.; Lau, L. W.; Gerson, A.; Smart, R. S. C. *Surface and Interface Analysis* **2009**, *41*, 324.
(26) Wojdyr, M. *Journal of Applied Crystallography* **2010**, *43*, 1126.
(27) Light, T. S. *Analytical Chemistry* **1972**, *44*, 1038.
(28) Enesca, A.; Duta, A.; Schoonman, J. *Thin Solid Films* **2007**, *515*, 6371.
(29) Hao, J.; Studenikin, S.; Cocivera, M. *Journal of Applied Physics* **2001**, *90*, 5064.
(30) Hill, J. C.; Choi, K.-S. *The Journal of Physical Chemistry C* **2012**, *116*, 7612.
(31) Mi, Q.; Coridan, R. H.; Brunschwig, B. S.; Gray, H. B.; Lewis, N. S. *Energy & Environmental Science* **2013**, *6*, 2646.
(32) Mi, Q.; Zhanaidarova, A.; Brunschwig, B. S.; Gray, H. B.; Lewis, N. S. *Energy & Environmental Science* **2012**, *5*, 5694.
(33) Solarska, R.; Jurczakowski, R.; Augustynski, J. *Nanoscale* **2012**, *4*, 1553.
(34) Santato, C.; Ulmann, M.; Augustynski, J. *The Journal of Physical Chemistry B* **2001**, *105*, 936.
(35) Seabold, J. A.; Choi, K.-S. *Chemistry of Materials* **2011**, *23*, 1105.
(36) NREL. Reference Solar Spectral Irradiance: ASTM G-173. http://rredc.nrel.gov/solar/spectra/am1.5/ASTMG173/ASTMG173.html (accessed October, 2013
).
(37) Yous, B.; Robin, S.; Donnadieu, A.; Dufour, G.; Maillot, C.; Roulet, H.; Senemaud, C. *Materials Research Bulletin* **1984**, *19*, 1349.
(38) Blackman, C. S.; Parkin, I. P. *Chemistry of Materials* **2005**, *17*, 1583.
(39) Biesinger, M. C.; Lau, L. W.; Gerson, A. R.; Smart, R. S. C. *Applied Surface Science* **2010**, *257*, 887.
(40) Biesinger, M. C.; Payne, B. P.; Grosvenor, A. P.; Lau, L. W.; Gerson, A. R.; Smart, R. S. C. *Applied Surface Science* **2011**, *257*, 2717.
(41) Salje, E. *Acta Crystallographica Section A: Crystal Physics, Diffraction, Theoretical and General Crystallography* **1975**, *31*, 360.
(42) Daniel, M.; Desbat, B.; Lassegues, J.; Gerand, B.; Figlarz, M. *Journal of Solid State Chemistry* **1987**, *67*, 235.
(43) Vandenabeele, P. *Practical Raman Spectroscopy: An Introduction*; John Wiley & Sons, 2013.
(44) Zabinski, J.; Donley, M.; Prasad, S.; McDevitt, N. *Journal of Materials Science* **1994**, *29*, 4834.
(45) Anderson, A.; Savoie, R. *Canadian Journal of Chemistry* **1965**, *43*, 2271.
(46) Davis, A.; Chatterjee, R. *Journal of Solution Chemistry* **1975**, *4*, 399.
(47) Solarska, R.; Alexander, B. D.; Braun, A.; Jurczakowski, R.; Fortunato, G.; Stiefel, M.; Graule, T.; Augustynski, J. *Electrochimica Acta* **2010**, *55*, 7780.
(48) Vogt, T.; Woodward, P. M.; Hunter, B. A. *Journal of Solid State Chemistry* **1999**, *144*, 209.

(49) Umebayashi, T.; Yamaki, T.; Itoh, H.; Asai, K. *Applied Physics Letters* **2002**, *81*, 454.

(50) Ohno, T.; Akiyoshi, M.; Umebayashi, T.; Asai, K.; Mitsui, T.; Matsumura, M. *Applied Catalysis A: General* **2004**, *265*, 115.

(51) Yu, J. C.; Ho, W.; Yu, J.; Yip, H.; Wong, P. K.; Zhao, J. *Environmental Science & Technology* **2005**, *39*, 1175.

(52) Matsushima, S.; Takehara, K.; Yamane, H.; Yamada, K.; Nakamura, H.; Arai, M.; Kobayashi, K. *Journal of Physics and Chemistry of Solids* **2007**, *68*, 206.

(53) Momma, K.; Izumi, F. *Journal of Applied Crystallography* **2011**, *44*, 1272.

(54) Mi, Q.; Ping, Y.; Li, Y.; Cao, B.; Brunschwig, B. S.; Khalifah, P. G.; Galli, G. A.; Gray, H. B.; Lewis, N. S. *Journal of the American Chemical Society* **2012**, *134*, 18318.

(55) Shannon, R. *Acta Crystallographica Section A: Crystal Physics, Diffraction, Theoretical and General Crystallography* **1976**, *32*, 751.

# Chapter 7: Conclusions and Future Directions

## 7.1 Overview of Completed Work

In this dissertation, we studied model systems of $BiVO_4$, $Fe_2O_3$ and $WO_3$ with the aim to improve our fundamental understanding of these materials and hence facilitate their use as photoanodes for solar water splitting. To summarize:

In Chapter 2, we synthesized single crystals of undoped and Mo or W-doped $BiVO_4$ single crystals using the floating zone technique and scrutinized their electronic and photoelectrochemical (PEC) behavior. Undoped crystals were highly resistive, so all transport and photoelectrochemistry was performed on doped crystals. Electrons were found to form small polarons around room temperature and a small (~0.2 $cm^2\ V^{-1}\ s^{-1}$ at 300 K in the *ab*-plane), temperature independent Hall mobility was measured using the AC field Hall effect. PEC characterization yielded a flatband potential of 0.03-0.08 V vs. RHE and a hole diffusion length of 100 nm using the Gartner model. Incident photo conversion efficiency testing showed that the dark coloration of the doped single crystals did not result in additional photocurrent.

In Chapter 3, we built on the work performed in Chapter 2, extending the electronic transport measurements to better understand small-polarons in $BiVO_4$. DC electrical conductivity, Seebeck and Hall coefficients are measured between 300 and 450 K on single crystals of W:$BiVO_4$. Strongly activated small-polaron hopping was implied by the activation energies of the Arrhenius conductivities (about 300 meV) greatly exceeding the energies characterizing the falls of the Seebeck coefficients' magnitudes

with increasing temperature (about 50 meV). Small-polaron hopping was further evidenced by the measured Hall mobility in the *ab*-plane ($10^{-1}$ $cm^2$ $V^{-1}$ $s^{-1}$ at 300 K) being larger and much less strongly activated than the deduced drift mobility (about 5 $\times 10^5 cm^2$ $V^{-1}$ $s^{-1}$ at 300 K). The conductivity and n-type Seebeck coefficient is found to be anisotropic with the conductivity larger and the Seebeck coefficient's magnitude smaller and less temperature dependent for motion within the *ab*-plane than that in the *c*-direction. These anisotropies were addressed by considering highly anisotropic next-nearest-neighbor (~4 Å) transfers in addition to the somewhat shorter (~4 Å), nearly isotropic nearest-neighbor transfers.

In Chapter 4, we investigated pulsed laser deposition (PLD) as a method to produce well-defined single crystalline and polycrystalline thin films of $BiVO_4$ for use as model systems. Epitaxial, c-axis oriented growth was achieved using single crystal yttria-stabilized zirconia (100), a substrate temperature of 575−600 °C, and an oxygen pressure of 7.8 mTorr. XRD confirmed a BVO (001)||YSZ (001) and BVO [100]||YSZ [100] epitaxial relationship. Film growth was 3-D, and the morphology was discontinuous, consisting of irregular, smooth grains. Additionally, dense, continuous polycrystalline films were deposited on fluorine-doped tin oxide (FTO) on glass substrates at room temperature with stoichiometric targets and postdeposition annealing in air. Evaluation of these samples as photoanodes yielded photocurrents of ~0.15 and ~0.05 mA $cm^{-2}$ at 1.23 V vs RHE under backside AM1.5G illumination with and without a hole scavenger ($Na_2SO_3$), respectively.

In Chapter 5, the electronic transport of another promising photoanode, Ti-doped hematite (Ti:α-$Fe_2O_3$) was studied. Specifically, we wanted to scrutinize the applicability

of the small-polaron model to electron transport and determine the room temperature anisotropy in doped α-$Fe_2O_3$, which has implications for PEC cell operation. Single crystals were grown using chemical vapor transport. Firstly, electronic transport (conductivity, Seebeck and Hall effects) were analyzed within the adiabatic small-polaron framework from 200-400 K in the basal plane. Above the Morin transition temperature ($T_M$ ~260 K) the conductivity activation energies and pre-factors agree well with charge carriers being small-polarons in the adiabatic regime, hopping between nearest neighbor Fe sites. Below $T_M$, in the antiferromagnetic state, the barrier to hopping increased significantly, suggesting that transfers between Fe sites with anti-parallel spins dominate in this regime. At all temperatures studied the Hall coefficient was positive, opposite to that of the Seebeck coefficient – again, a fingerprint of small polarons. Lastly, optical measurements from 8 meV to 3 eV revealed broad IR absorption upon Ti-doping and was preliminarily assigned to small-polaron absorption predicted by theory.

Surprisingly, the conductivities in and perpendicular to the basal plane and were found to be comparable, i.e. electron transport was isotropic. This is at odds with the common view in the literature: that the spin environment in hematite is responsible for a large (up to four orders of magnitude) conductivity anisotropy and hints that $Ti^{4+}$ doping has additional effects on transport, other than simply donating electrons to the lattice. However, these effects were extremely subtle – no significant structural changes were observed with Ti-incorporation or changes to the bulk magnetic properties of the material. The Seebeck coefficient was also isotropic, indicating that the electron mobilities are approximately equal. The magnitude of the Seebeck coefficient indicated that only a fraction of Fe atoms take part in hopping transport.

Finally, in Chapter 6, the feasibility of anion doping of $WO_3$ to improve its visible light absorption was studied. Films were synthesized by spray pyrolysis with either ammonium sulfide or iodide added to the aqueous $WO_3$ precursor solutions. Red shifts of the absorption spectra were observed with S and I incorporation (from ~2.7 to 2.6 and 2.1 eV respectively), likely due to the formation of intragap impurity bands. S:$WO_3$ samples exhibited enhanced photoelectrochemical (PEC) performance at low S concentrations, but this quickly deteriorated with increasing S content. Incident photon conversion efficiency (IPCE) data showed that this initial improvement was driven by improved collection efficiency at longer wavelengths. Conversely, photocurrent decreased at all levels of I addition. IPCE measurements for these films showed only a marginal increase in efficiency at longer wavelengths, indicating that the extra absorbed photons did not contribute significantly to the photocurrent. Time of flight-secondary ion mass spectrometry (ToF-SIMS) depth profiling revealed a uniform distribution of S throughout the S:$WO_3$ films, but showed surface segregation of I in the I:$WO_3$ samples. Raman and X-ray photoelectron spectrometry (XPS) showed that S and I substituted for oxygen, but in the case of S, other pathways such as interstitial incorporation and cation substitution could not be ruled out.

## 7.2 On-going Work and Future Directions

### 7.2.1 Small Polarons for Experimentalists

Since its conception, the study of small-polarons has belonged largely to the theoretical physics community, who has made great strides in predicting and explaining experimental phenomena exhibited by these quasi-particles. Although thorough, these treatises on hopping conduction are not written for an experimentalist attempting to apply

their results to his/her data, being very mathematical and abstract. A perspective covering the general aspects of small-polaron theory relevant for experimentalists working on metal oxides and including the worked examples of electron transport work on $BiVO_4$ and $\alpha$-$Fe_2O_3$ contained in this dissertation (Chapters 2, 3 and 5) is therefore warranted and in progress.

### 7.2.2 Small-Polaron Transport in Other Materials

There are many low mobility materials where our understanding of their transport would benefit from thorough single-crystal transport studies. Interestingly, many of these are copper-based. Iron and copper tungstates ($FeWO_4$, $CuWO_4$); n-type photoanode materials, copper iron oxide ($CuFeO_2$); a p-type photocathode and copper thiocyanate (CuSCN); a low cost hole transport material, are all good candidates. Bulk charge transport either limits performance or is integral to all of these materials' function and poorly understood.

### 7.2.3 Photoconductivity and Hole Transport

Traditional transport measurements (e.g., conductivity, Seebeck and Hall effect) only access majority carrier transport information. In most metal oxides the majority carriers are electrons, as oxygen vacancies are the most common native defect in these materials. However, in PEC cell operation, minority carriers (holes) are just as important and notoriously hard to measure directly. In $BiVO_4$, holes have been predicted to have band-like transport using DFT calculations that looked at the band structure and carrier localization. So far, no experimental confirmation of this exists. Photoconductivity techniques would be ideal to gain information on hole transport in metal oxides, but the

short lifetimes and low mobilities found in many of these materials make these techniques difficult to utilize. Relatively recently, pulse-radiolysis time-resolved microwave conductivity (PR-TRMC) has been developed to probe photogenerated carrier dynamics in low-mobility materials at TU Delft in the Netherlands. We have initiated a collaboration with this group to study undoped and doped $BiVO_4$ crystals. Comparison with dark conductivity transport measurements should yield information about the hole transport in this material.

### 7.2.4 Soft X-ray Spectroscopy

Single crystal samples with known orientation can be used to gain detailed band structure information, particularly observation of defect and polaron-related states using soft X-ray techniques such as X-ray emission, absorption. X-ray induced photoemission S and resonant inelastic X-ray scattering spectroscopies (XAS, XES, XPS and RIXS respectively). These experiments are on-going with Dr. Vedran Jovic at Lawrence Berkeley National Laboratory using the facilities at the Advanced Light Source.

# Appendices

## Appendix A: Combined Charge Carrier and Photoelectrochemical Characterization of $BiVO_4$ Single Crystals

### A.1 Experimental Details

#### Sample preparation

After growth, the crystal boules could be easily cleaved to reveal mirror-like (001) faces. These were cut with a diamond saw so that rectangular plate samples oriented with edges along the principal axes: *a, b* or *c*, were obtained. As shown in the Laue XRD patterns in Figure A.4, the *a* and *b* directions are highly symmetrical, which was expected as the $BiVO_4$ unit cell is a slightly distorted tetragonal structure (where $a = b$). As the properties of interest were not expected to change significantly between *a* or *b*, it was not practical to differentiate between them and they were collectively termed *ab*. *c*-plates refer to samples where (001) is the main crystal face exposed (Figure A.1) and the

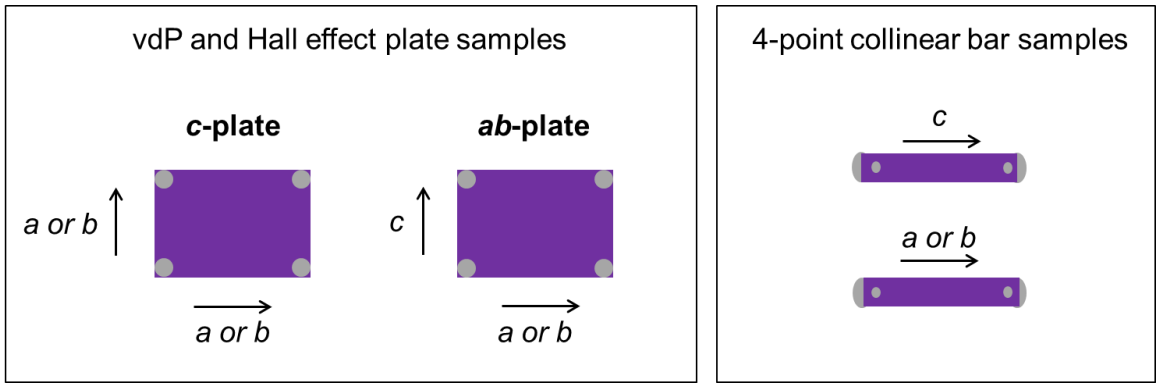


**Figure A1**: Diagram of various sample geometries. Arrows represent orientation relative to the principal crystallographic axes. Grey spots represent contact placement, which were connected to copper wire. The small inner contacts for the 4-point collinear samples were used for the voltage probes.

edges are along the *a* or *b* directions. *ab*-plates refer to samples where (100) or (010) is the main crystal face exposed (Figure A.1) and one edge is along the *c* direction, while the other is along either *a* or *b*.

**Contact application**

Small dots of liquid InGa eutectic (Sigma-Aldrich) were painted on the sample edges using a fine-tipped dental tool. Fine copper wires (California Fine Wire Company) were then stuck to the liquid dots and soldered to larger contact pads on a sample measurement board before Ag epoxy (Circuit Works) was applied over the wire and liquid InGa eutectic to hold it in place. Heat treatment in air at 150 °C for 15 mins was used to cure the Ag epoxy. Simply sticking the Cu wires to the liquid dots was observed to give Ohmic contacts with equivalent resistances but were not robust enough for repeated measurements or handling. For the Ag paste only contacts, the same procedure was employed only without painting on InGa eutectic. Indium metal pads were gently pressed into crystal surfaces that had been lightly roughened using sandpaper. All contact application was performed under an optical microscope with the sample held in place with double-sided tape (Scotch or Kapton). Figure A.2 shows that the InGa eutectic contacts were the only ones that gave Ohmic behavior.

**Electrical measurements**

For van der Pauw (vdP) resistivity experiments steady state 2- and 4-point voltage measurements were recorded at ±0.3 and ±0.9 μA at all temperatures automatically using a custom graphical interface. These data were used to form *i*-*V* curves (typical curve in

Figure A.3) at each temperature from which the resistance was obtained and used in the vdP formula.

In the AC field Hall measurements, a sinusoidal magnetic field with a frequency of 0.1 Hz was employed. The applied current is DC. Frequency dependent conductivity and Hall effect can be reasonably described using the Drude-Lorentz model. The time scale of this theory is determined by the mean free time between collisions. This time is so short (nano to picoseconds) compared to the AC field frequency that AC conductivity effects in the material can be ignored. The current was reversed to remove the inductive pickup signal from the Hall voltage.

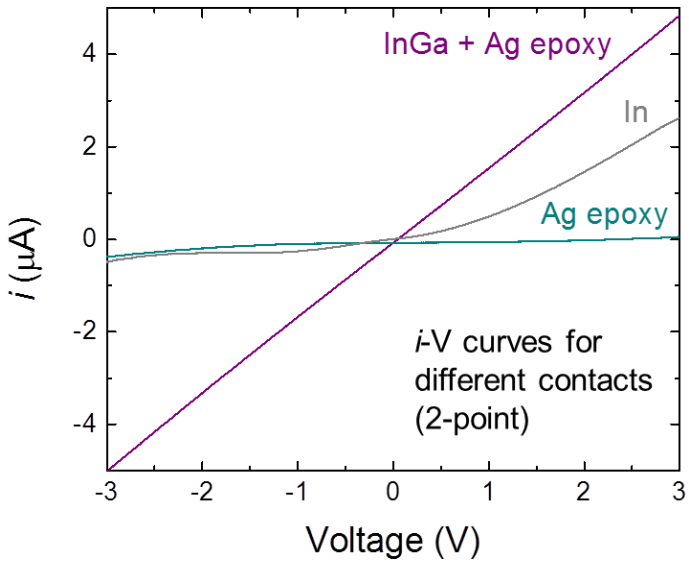


**Figure A.2:** 2-point *i*-V curves at 300 K for various contacting methods employed. Only the InGa eutectic and Ag epoxy contact showed Ohmic behavior, while In metal pads showed diode behavior. Ag epoxy only was significantly more resistive and exhibited non-Ohmic behavior.

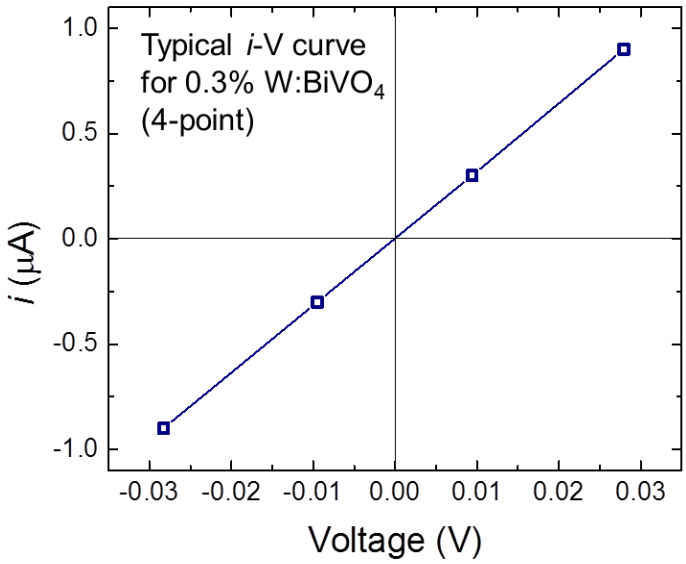


**Figure A.3:** Typical 4-point *i*-V curve for resistance measurement at 300 K (in this case for a 0.3% W:$BiVO_4$ *c*-plate). Steady state voltages were measured at ±0.3 and ±0.9 μA to generate the *i-V* curve (open symbols). The line is drawn between the points and is not fitted.

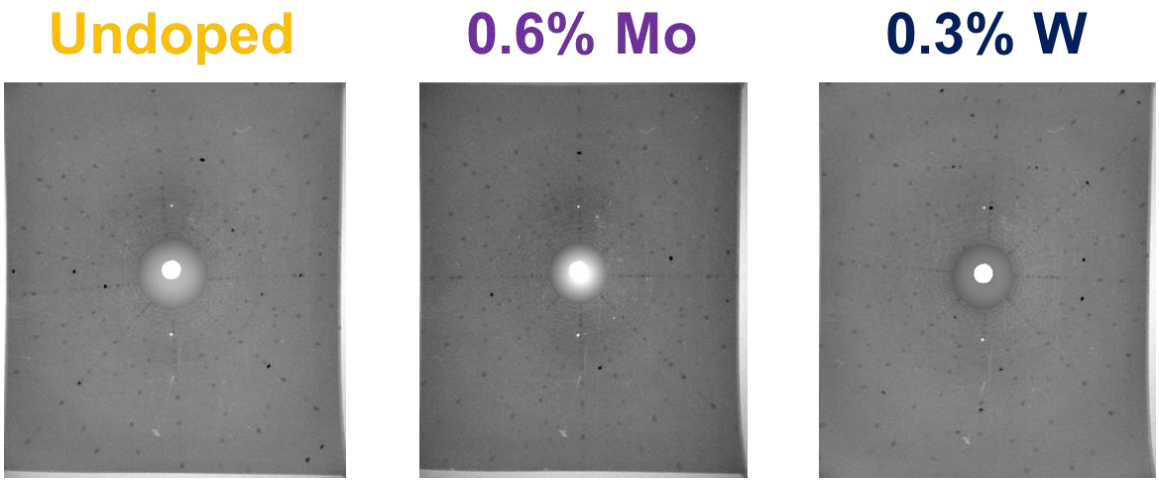


**Figure A.4**: Typical Laue back-reflection patterns for an undoped and doped $BiVO_4$ *c*-plate crystals (x-rays incident on the (001) face). To enhance the visibility of the Bragg peaks, the background pattern of the Laue image was fitted and stripped using a Mathematica image processing script.

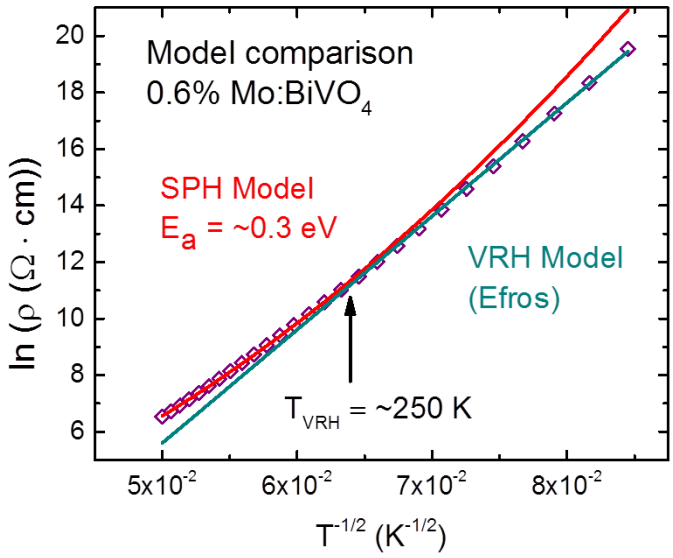


**Figure A.5:** Fits of small polaron hopping (SPH) and variable range hopping (VRH) transport models to resistivity data. Arrow indicates transition to the VRH mechanism.

| Sample | Geometry | Technique | $\rho_1$ / $\rho_2$ |
|---|---|---|---|
| 0.3% W | c-plate | vdP | 1.2 |
| 0.6% Mo | c-plate | vdP | 1.3 |

**Table A.1:** Resistivity anisotropy of doped $BiVO_4$ *c*-plates (300 K) calculated using the Kazani *et al.*'s method [1]. vdP: van der Pauw. $\rho_1$ and $\rho_2$ refer to resistivities along different plate edges, cut along either *a* or *b*, which could not be differentiated between due to close structural symmetry.

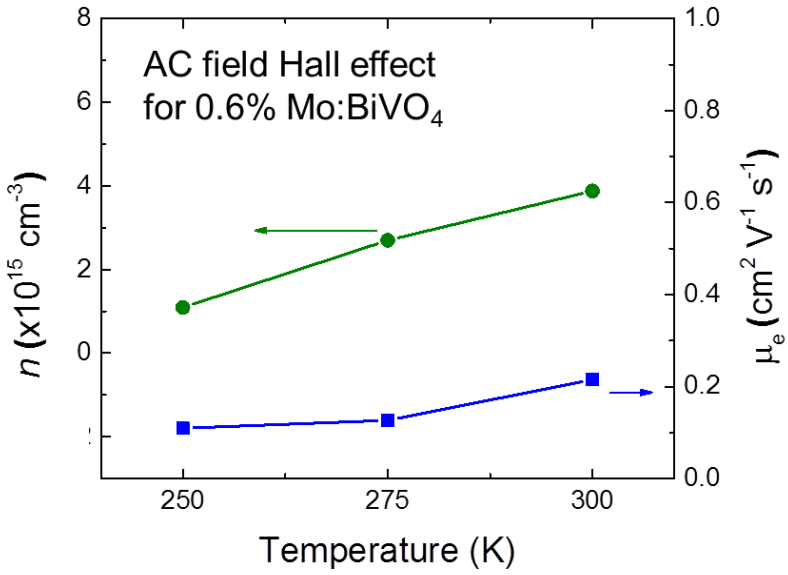


**Figure A.6**: Carrier concentration ($n$) and electron mobility ($\mu_e$) AC field Hall effect as a function of temperature for a 0.6% W:$BiVO_4$ *c*-plate.

| Sample | ρ (Ω-cm) | $n$ ($cm^{-3}$) | $\mu_e$ ($cm^2\ V^{-1}\ s^{-1}$) |
|---|---|---|---|
| 0.3% W (1) | $6.7 \times 10^3$ | $4.7 \times 10^{15}$ | 0.20* |
| 0.3% W (2) | $8.5 \times 10^3$ | $4.9 \times 10^{15}$ | 0.15 |
| 0.6% Mo | $7.1 \times 10^3$ | $4.8 \times 10^{15}$ | 0.18 |

**Table A.2:** vdP resistivity and AC field Hall effect data taken at 300 K. Two different 0.3% W samples were measured to check repeatability. *this value was an average of 3 measurements (Table A.3)

| Measurement | ρ (Ω-cm) | $n$ ($cm^{-3}$) | $\mu_e$ ($cm^2\ V^{-1}\ s^{-1}$) |
|---|---|---|---|
| 1 | $6.6 \times 10^3$ | $5.0 \times 10^{15}$ | 0.188 |
| 2 | $6.7 \times 10^3$ | $5.7 \times 10^{15}$ | 0.126 |
| 3 | $6.7 \times 10^3$ | $3.3 \times 10^{15}$ | 0.285 |
| Average | $6.7 \times 10^3$ | $4.7 \times 10^{15}$ | 0.200 |

**Table A.3:** Repeated vdP resistivity and AC Hall effect measurements on 0.3% W:$BiVO_4$ *c*-plate sample 1 at 300 K.

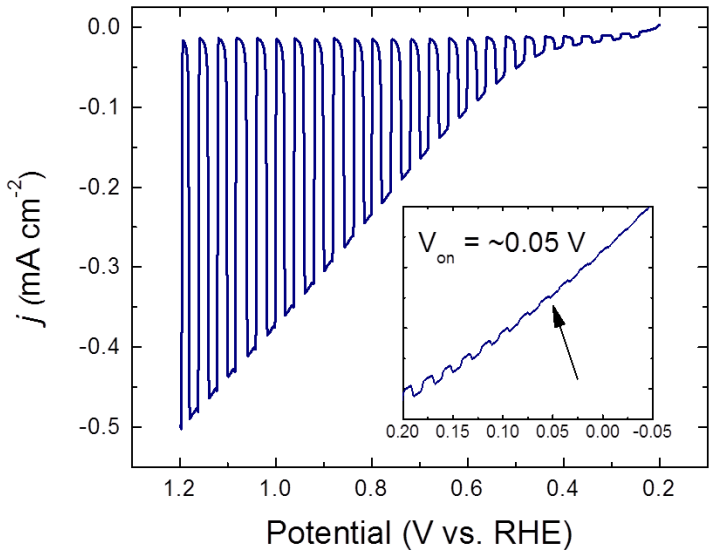


**Figure A.7**: Linear sweep voltammogram under chopped illumination with a hole scavenger ($Na_2SO_3$) using a W:$BiVO_4$ crystal with the (001) face exposed. The electrolyte solution was 0.1 M phosphate buffer with 0.1 M $Na_2SO_4$ and 0.1 M $Na_2SO_3$. Inset shows on-set potential of ~0.05 V.

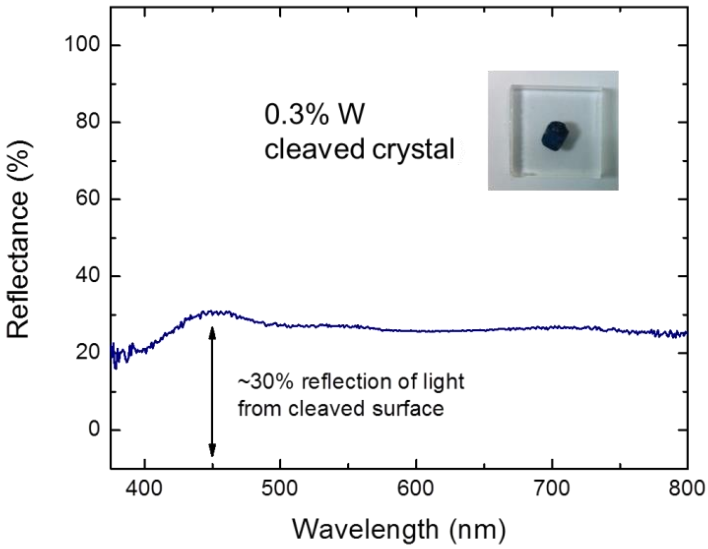


**Figure A.8**: Diffuse reflectance spectra for a cleaved 0.3% W:$BiVO_4$ single crystal.

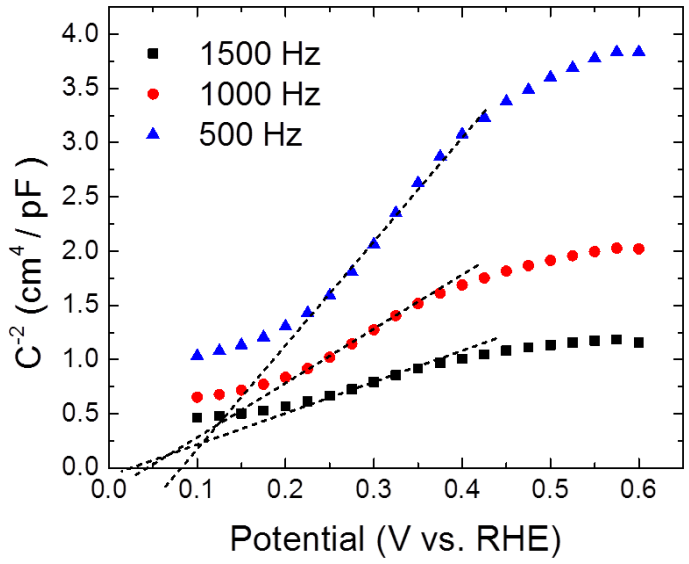


**Figure A.9:** Mott-Schottky plots generated from capacitance-voltage data using a resistor and capacitor in series. The electrolyte solution was 0.1 M phosphate buffer with 0.1 M $Na_2SO_4$ and the electrode was a W:$BiVO_4$ single crystal electrode.

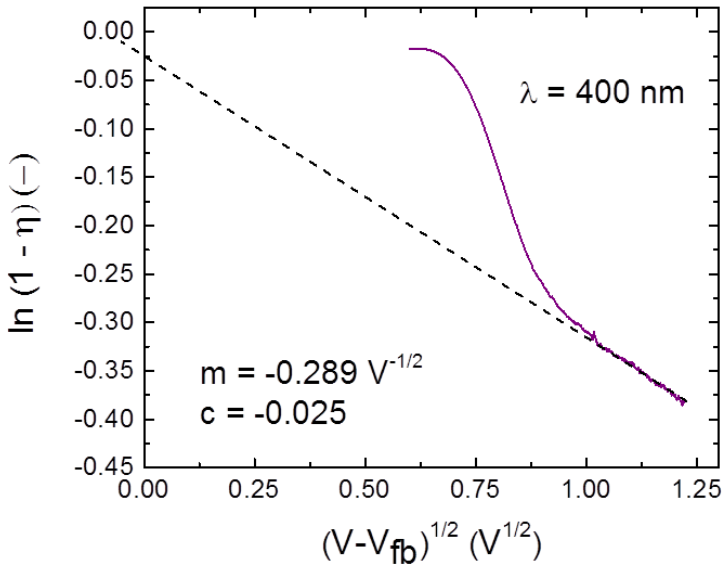


**Figure A.10:** Determination of α and $L_p$ for a W:$BiVO_4$ single crystal electrode. The gradient (m) and y-intercept (c) of the linear region used in calculations are shown. $\lambda$ = 400 nm. The electrolyte solution was 0.1 M phosphate buffer with 0.1 M $Na_2SO_4$ and 0.1 M $Na_2SO_3$.

### A.2 CALCULATION OF HOLE DIFFUSION LENGTH

LSVs using monochromated light were used to generate the plot in Figure A.7. The electrolyte solution was 0.1 M phosphate buffer with 0.1 M $Na_2SO_4$ and 0.1 M $Na_2SO_3$. The use of a hole scavenger is desired as we are interested in the electrical properties of the electrode bulk and want to minimize charge transfer limitations at the electrode surface. The surface of the crystals reflects ~20% of incident light at 400 nm (Figure A.5) and this was accounted for in calculations of $\eta$. Optical losses through the glass cell window and aqueous electrolyte were not accounted for. Using the value of n at 300 K

from AC field Hall effect measurements ($n \sim 5 \times 10^{15}$ cm$^{-3}$), $\alpha$ was determined as 2,620 cm$^{-1}$ using the gradient of the linear region and Equation 2.9 in chapter 2. The dielectric constant of undoped single crystals of $BiVO_4$ is 55 at 300 K [2] and was used in calculations.

| | Type | Growth method | Dopant | Orientation | $\mu$ (cm$^2$ V$^{-1}$ s$^{-1}$) | Reference |
|---|---|---|---|---|---|---|
| $TiO_2$ (rutile) | Single crystal | Unclear | Reduction | ∥c | 1 | 3 |
| $TiO_2$ (anatase) | Single crystal | Vapor transport | Reduction | ∥c | 10 | 4 |
| α-$Fe_2O_3$ | Epitaxial | MBE | Ti | ⊥c | 0.1 | 5 |
| γ-$WO_3$ | Single crystal | Vapor transport | Reduction | Unclear | 16 | 6 |
| $BiVO_4$ | Single crystal | Floating zone | Mo, W | ⊥c | 0.2 | Our work |

**Table A.4:** Comparison of metal oxide carrier mobility at 300K. Molecular beam epitaxy (MBE)

| | Type | Growth method | Dopant | Face exposed | $L_p$ (nm) | Reference |
|---|---|---|---|---|---|---|
| $TiO_2$ (rutile) | Single crystal | Unclear | Reduction | (001) | 20 | 7 |
| α-$Fe_2O_3$ | Polycrystalline | Solid state reaction | Ti | - | 2-4 | 8 |
| γ-$WO_3$ | Single crystal | Vapor transport | Reduction | Unclear | 500 | 9 |
| $BiVO_4$ | Single crystal | Floating zone | Mo, W | (001) | 100 | Our work |

References in Tables A.4 and A.5: [3-9]

**Table A.5:** Comparison of metal oxide hole diffusion lengths as determined by the Gärtner or equivalent model at 300 K.

## REFERENCES

### References

(1) van de Krol, R.; Grätzel, M. *Photoelectrochemical Hydrogen Production*, 2012.

(2) Lewis, N. S.; Nocera, D. G. *Proceedings of the National Academy of Sciences* **2006**, *103*, 15729.

(3) Walter, M. G.; Warren, E. L.; McKone, J. R.; Boettcher, S. W.; Mi, Q.; Santori, E. A.; Lewis, N. S. *Chemical Reviews* **2010**, *110*, 6446.

(4) Seitz, L. C.; Chen, Z.; Forman, A. J.; Pinaud, B. A.; Benck, J. D.; Jaramillo, T. F. *ChemSusChem* **2014**, *7*, 1372.

(5) James, B. D.; Baum, G. N.; Perez, J.; Baum, K. N. *DOE Report* **2009**.

(6) Pinaud, B. A.; Benck, J. D.; Seitz, L. C.; Forman, A. J.; Chen, Z.; Deutsch, T. G.; James, B. D.; Baum, K. N.; Baum, G. N.; Ardo, S. *Energy & Environmental Science* **2013**, *6*, 1983.

(7) Bard, A. J.; Fox, M. A. *Acc. Chem. Res.* **1995**, *28*, 141.

(8) Khaselev, O.; Turner, J. A. *Science* **1998**, *280*, 425.

(9) Weber, M. F.; Dignam, M. *International Journal of Hydrogen Energy* **1986**, *11*, 225.

(10) Weber, M. F.; Dignam, M. J. *Journal of the Electrochemical Society* **1984**, *131*, 1258.

(11) Bolton, J. R.; Strickler, S. J.; Connolly, J. S. *Nature* **1985**, *316*, 495.

(12) Reece, S. Y.; Hamel, J. A.; Sung, K.; Jarvi, T. D.; Esswein, A. J.; Pijpers, J. J.; Nocera, D. G. *Science* **2011**, *334*, 645.

(13) Zhong, D. K.; Choi, S.; Gamelin, D. R. *J. Am. Chem. Soc.* **2011**, *133*, 18370.

(14) Chemelewski, W. D.; Lee, H.-C.; Lin, J.-F.; Bard, A. J.; Mullins, C. B. *J. Am. Chem. Soc.* **2014**, *136*, 2843.

(15) Kim, T. W.; Choi, K.-S. *Science* **2014**, *343*, 990.

(16) Kweon, K. E.; Hwang, G. S.; Kim, J.; Kim, S.; Kim, S. *Phys. Chem. Chem. Phys.* **2014**, *advance online publication*.

(17) Emin, D. *Polarons*; 1st ed.; Cambridge University Press: New York, 2013.

(18) Jaime, M.; Hardner, H.; Salamon, M.; Rubinstein, M.; Dorsey, P.; Emin, D. *Phys. Rev. Lett.* **1997**, *78*, 951.

(19) Nagels, P. In *The Hall Effect and Its Applications*; Springer: 1980, p 253.

(20) Zhao, B.; Kaspar, T. C.; Droubay, T. C.; McCloy, J.; Bowden, M. E.; Shutthanandan, V.; Heald, S. M.; Chambers, S. A. *Phys. Rev. B* **2011**, *84*, 245325/1.

(21) Emin, D.; Seager, C.; Quinn, R. K. *Phys. Rev. Lett.* **1972**, *28*, 813.

(22) Sayer, M.; Mansingh, A. *J. Non-Cryst. Solids* **1983**, *58*, 91.

(23) Baily, S. A.; Emin, D. *Phys. Rev. B* **2006**, *73*, 165211.

(24) Yoo, K.-H.; Ha, D.; Lee, J.-O.; Park, J.; Kim, J.; Kim, J.; Lee, H.-Y.; Kawai, T.; Choi, H. Y. *Phys. Rev. Lett.* **2001**, *87*, 198102.

(25) Venkateshvaran, D.; Nikolka, M.; Sadhanala, A.; Lemaur, V.; Zelazny, M.; Kepa, M.; Hurhangee, M.; Kronemeijer, A. J.; Pecunia, V.; Nasrallah, I.; Romanov, I.; Broch, K.; McCulloch, I.; Emin, D.; Olivier, Y.; Cornil, J.; Beljonne, D.; Sirringhaus, H. *Nature* **2014**, *advance online publication*.

(26) Alexandre, S. S.; Artacho, E.; Soler, J. M.; Chacham, H. *Phys. Rev. Lett.* **2003**, *91*, 108105.
(27) Van der Pauw, L. *Philips Technical Review* **1958**, *20*, 220.
(28) Streetman, B. G.; Banerjee, S. *Solid state electronic devices*; 6th ed.; Prentice Hall New Jersey, 2006.
(29) Borup, K. A.; de Boor, J.; Wang, H.; Drymiotis, F.; Gascoin, F.; Shi, X.; Chen, L.; Fedorov, M. I.; Müller, E.; Iversen, B. B. *Energy & Environmental Science* **2015**, *8*, 423.
(30) Emin, D. *Monatshefte für Chemie-Chemical Monthly* **2013**, *144*, 3.
(31) Emin, D. *Phys. Rev. Lett.* **2008**, *100*, 166602.
(32) Nagaosa, N.; Sinova, J.; Onoda, S.; MacDonald, A.; Ong, N. *Reviews of Modern Physics* **2010**, *82*, 1539.
(33) Emin, D. In *The Hall Effect and Its Applications*; Springer: 1980, p 281.
(34) Emin, D.; Holstein, T. *Ann. Phys.* **1969**, *53*, 439.
(35) Friedman, L.; Holstein, T. *Ann. Phys.* **1963**, *21*, 494.
(36) Emin, D. *Ann. Phys.* **1971**, *64*, 336.
(37)
(38)
(39) Emin, D. *Phys. Rev. B* **1993**, *48*, 13691.
(40) National Renewable Energy Laboratory Reference Solar Spectral Irradiance: ASTM G-173. [Online Early Access]. http://rredc.nrel.gov/solar/spectra/am1.5/ASTMG173/ASTMG173.html (accessed 1st August, 2014).

## APPENDIX B: COMBINED CHARGE CARRIER AND PHOTOELECTROCHEMICAL CHARACTERIZATION OF $BiVO_4$ SINGLE CRYSTALS

### B.1 EXPERIMENTAL DETAILS

Four point collinear conductivity and AC field Hall effect experiments between 300 and 450 K were conducted at Lake Shore Cryotronics on an 8404 AC/DC Hall measurement system. Samples for these measurements were ca. $2 \times 0.5 \times 0.3$ $mm^3$ bars or ca. $2 \times 2 \times 0.3$ $mm^3$ plates respectively. Ohmic contact was achieved using In-Ga eutectic (Sigma-Aldrich), held in place with Ag epoxy (EPO-TEK). Sample dimensions were measured using phase sensitive interferometry (Veeco NT9100).

Measurement of the Seebeck coefficient, $S$ was performed using a laboratory-built apparatus at UT Austin. Samples (ca. $2 \times 1 \times 1$ $mm^3$) were sandwiched between two heaters with a piece of Ti shim and InGa eutectic on either side. This set up facilitated ohmic contact and the use of relatively small single crystal samples. Though ohmic contacts are not strictly necessary to measure $S$, in practice, cleaner data was obtained with them. Electrical contact was made using Pt pins that contacted the Ti shim. The Ti and InGa eutectic layers were very thin and therefore their contributions to the voltage were neglected. The contribution of the Pt leads was accounted for. A $\Delta T$ of 10 K was used as it resulted in the least noisy data and was still small (< 5%) compared to the absolute temperatures of the measurements. $\Delta V$-$\Delta T$ curves were excellent linear fits that passed through (0,0) (Figure B.1).

An additional W:BVO single crystal was prepared and showed similar Seebeck coeffient data and trends as observed for the sample presented in Figure 3.2 (Figure B.2).

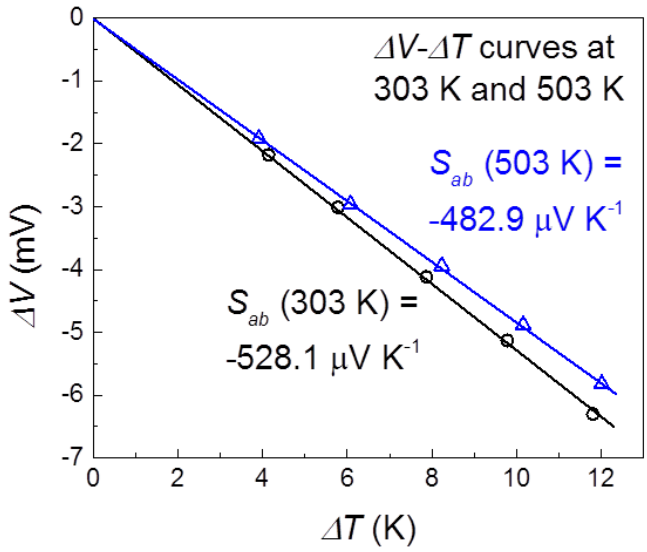


**Figure B.1:** Representative $\Delta V$-$\Delta T$ curves showing linear behavior with a y-intercept of (0,0) at 303 (○) and 503 K (△). Values of $S$ were calculated from the gradient of the fit through (0,0).

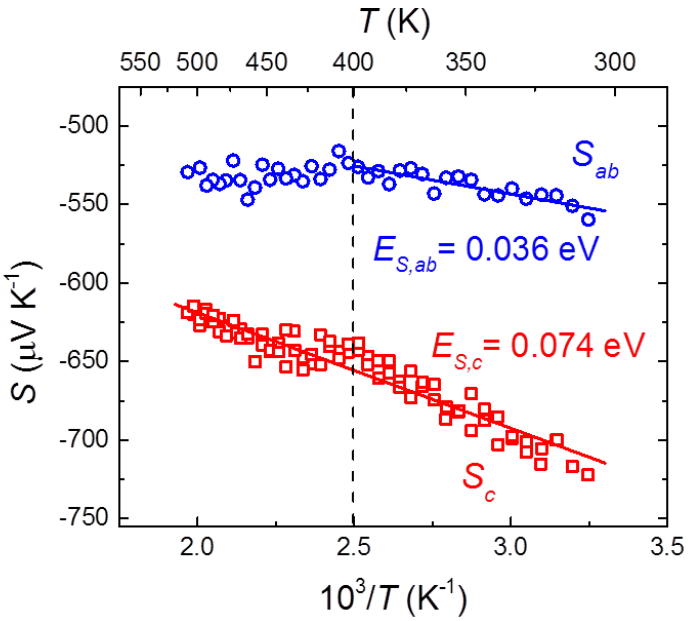


**Figure B.2:** Seebeck coefficients of the *ab*-plane ($S_{ab}$, ○) and the *c*-axis ($S_c$, □) *vs.* inverse temperature for a second W:BVO sample. The dashed line indicates a change in slope at 400 K in the *ab*-plane. Linear fits to determine the activation energies and intercepts are shown with solid lines.

For the additional sample the parameters in equation 3.2 in the main text were: $E_{S,ab}$ = 0.036 ± 0.004 eV, $E_{S,c}$ = 0.074 ± 0.003 eV, $A_{ab}$ = 5.1 ± 0.1 and $A_c$ = 5.55 ± 0.1.

### B.2 VECTOR ANALYSIS TO DETERMINE G

The drift velocity can be written generally as

$$\boldsymbol{v} = \sum_k \boldsymbol{h}_{ik}\, w(i \rightarrow k) \qquad \text{(B.1)}$$

where $\boldsymbol{h}_{ik}$ is the vector linking the initial site $i$ to its nearest neighbors $k$, and w($i \rightarrow k$) is the jump rate from the initial to the final site. w($i \rightarrow k$) is the same for all equivalent nearest neighbors (NN) in the absence of any fields (as required by symmetry), and only depends on the energetics of the system. In the case of BVO, where two of the neighboring four V sites are slightly further away than the other two, we expect the difference in distance is small enough to be neglected and to treat all 4 NNs the same. In the presence of an electric field the jump rate is modified by a factor of exp(e$\mathbf{F}$.$\boldsymbol{h}_{ik}$/2κ$T$) which biases the jump frequency in a direction opposite the field (as expected for an electron) such that the new w($i \rightarrow k$) is

$$w(i \rightarrow k) = \exp\left(-\frac{e\boldsymbol{F}\cdot\boldsymbol{h}_{ik}}{2\kappa T}\right) w^0 \qquad \text{(B.2)}$$

where $w^0$ is the jump rate in absence of a field – its form depends on whether the hopping is adiabatic or non-adiabatic, but the difference is small and unimportant at this point. In the case of an infinitesimal field the exponential can be expanded as a Taylor series about 0 which yields

$$exp\left(-\frac{e\boldsymbol{F}\cdot\boldsymbol{h}_{ik}}{2\kappa T}\right) \approx 1 - \frac{e\boldsymbol{F}\cdot\boldsymbol{h}_{ik}}{2\kappa T} + \cdots \qquad \text{(B.3)}$$

with the higher order terms reasonably neglected and the constant term also neglected because we are only interested in the rate that is proportional to the field (which we can measure). Plugging equations (B.3) and (B.2) into (B.1) we find

$$\boldsymbol{v} = -\frac{ew^0}{2\kappa T}\sum_k \boldsymbol{h}_{ik}\,(\boldsymbol{F}\cdot\boldsymbol{h}_{ik}) \qquad \text{(B.4)}$$

Now all that remains is evaluating the summation for the hopping geometry of BVO. Explicitly writing out the positions of the 4 NNs (setting the initial site as the origin and all jump distances as equal to '*a*'):

$$\boldsymbol{h}_{01} = a[\cos(47°), 0, \sin(47°)]$$
$$\boldsymbol{h}_{02} = a[-\cos(47°), 0, \sin(47°)]$$
$$\boldsymbol{h}_{03} = a[0, \cos(50°), -\sin(50°)]$$
$$\boldsymbol{h}_{04} = a[0, -\cos(50°), -\sin(50°)]$$

With the angles being between either the *a* or *b* crystal axes and the site in question.

Setting $\boldsymbol{F}$ in the [110] direction ($\boldsymbol{F}$ = *F* [0.707, 0.707, 0]) and carrying out the vector algebra we find

$$\boldsymbol{v} = \frac{-ea^2Fw^0}{\sqrt{2}\kappa T}[\cos^2(47°), \cos^2(50°), \sin(47°)\cos(47°) - \sin(50°)\cos(50°)] \qquad \text{(B.5)}$$

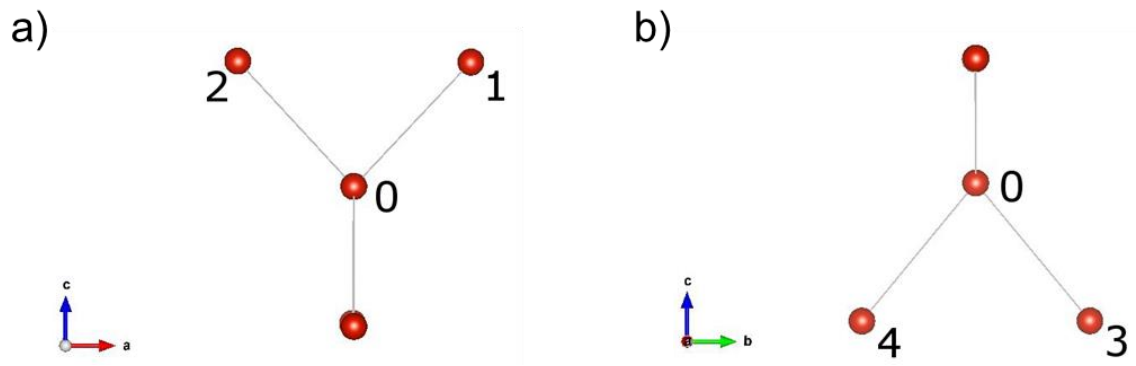


**Fig. B.3:** Possible hopping sites around a central V-site in monoclinic BVO along *a*- (a) and *b*-axes (b).

Note that the chosen direction of $\boldsymbol{F}$ is arbitrary. Then the drift mobility can be found using the scalar equation $\mu_d = v/F$ which assumes that $v$ and $F$ are collinear – translating this to a vector equation gives

$$\mu_d = \frac{\boldsymbol{v}\cdot\widehat{\boldsymbol{F}}}{F} \qquad \text{(B.6)}$$

Where $\widehat{\boldsymbol{F}}$ is the unit direction vector of $\boldsymbol{F}$ and F = |F|. Plugging (B.5) into (B.7) we find

$$\mu_d = \frac{-ea^2w^0}{\kappa T}\frac{\left(\cos^2(47°)+\cos^2(50°)\right)}{2} \qquad \text{(B.7)}$$

This is very similar to the drift velocities found for triangular lattices [2,3] (Ref. 2, equation 4.9 and Ref. 3, equation 9.5)) and square lattices [4] (Ref. 4, equation 7.5) with the only difference being the prefactors, which are geometry dependent. For the case of BVO we find a prefactor, $g_{NN}$ of 0.44. This is lower than the other cases ($g$ = 1-1.5) mostly because the hops only have one component in the same plane as the electric field.

In the case of next-nearest neighbor (NNN) hopping in the *ab*-plane (see Fig. 3.4b in the main text), the hopping geometry is a 2-D square lattice and thus, $g_{NNN} = 1$.

### B.3 DATA ANALYSIS

The variables used in determining $\sigma_0$ from the adiabatic small-polaron hopping model are summarized in Table B.1. As $N_{ab}(T)$ and $N_c(T)$ are not explicitly known but $N_{ab}(T)$, $N_c(T) > N_d$, we simply use $N_d$ to estimate lower limits for $\sigma_0$.

We make the assumption that hopping in the ab-plane is a convolution of nearest-neighbor (NN) and next-nearest-neighbor (NNN) hops, while transport in the *c*-axis is exclusively characterized by NN jumps to calculate rough values for $g_{ab}$ and $a_{ab}$. That is:

$$\sigma_{ab} = \sigma_{NN} + \sigma_{NNN},$$
$$\sigma_c = \sigma_{NN}.$$

It follows from the measured anisotropy ratio, $\sigma_{ab}/\sigma_c = 2.3$,

$$\frac{\sigma_{NNN}}{\sigma_{NN}} \approx 1.3,$$

and the average values weighted by the conductivity are given by:

$$g_{ab} = \frac{\sigma_{NNN} \cdot g_{NNN} + \sigma_{NN} \cdot g_{NN}}{\sigma_{NNN} + \sigma_{NN}} \approx 0.76,$$
$$a_{ab} = \frac{\sigma_{NNN} \cdot a_{NNN} + \sigma_{NN} \cdot a_{NN}}{\sigma_{NNN} + \sigma_{NN}} \approx 4.6 \text{ Å}.$$

**Table B1:** Calculation variables and pre-exponential factors.

| | $g$ (-) | $N_d$ (cm$^{-3}$) | $a$ (A) | $\nu_0$ (Hz) | $\sigma_0$ (S cm$^{-1}$) at 300 K |
|---|---|---|---|---|---|
| *ab*-plane | 0.76 | 3.9x10$^{19}$ | 4.6 | 2x10$^{13}$ | 7.5 |
| *c*-axis | 0.44 | 3.9x10$^{19}$ | 4.0 | 2x10$^{13}$ | 3.4 |

### B.4 RANGE OF THE CHARACTERISTIC PHONON FREQUENCY

The optical phonon dispersion in transition metal oxides is complex and the phonon frequencies that interact with small polarons are usually unknown, though a range of $10^{13}$-$10^{14}$ Hz is often used. We use two methods to narrow this range to ~ $2\times10^{13}$ Hz below:

1) Deviation from Arrhenius behavior occurs at ~250 K for W:BVO and taking this as being the thermal energy that is equivalent to 1/3 the characteristic optical phonon frequency [5]: $\nu_0 = 3*\kappa *250/h = 1.6\times10^{13}$ Hz, where $h$ is Planck's constant.

2) Iordanova et al. [6] estimate a characteristic frequency using the highest energy Raman band for hematite. Applying this to BVO, the wavenumber is 830 cm$^{-1}$, corresponding to an energy of ~0.1 eV and a frequency of $2.4\times10^{13}$ Hz.

### REFERENCES


1 A. J. E. Rettie, H. C. Lee, L. G. Marshall, J.-F. Lin, C. Capan, J. Lindemuth, J. S. McCloy, J. Zhou, A. J. Bard, and C. B. Mullins, J. Am. Chem. Soc. **135** (30), 11389 (2013).

2 L. Friedman and T. Holstein, Ann. Phys. **21** (3), 494 (1963).

3 D. Emin and T. Holstein, Ann. Phys. **53** (3), 439 (1969).

4 D. Emin, Ann. Phys. **64** (2), 336 (1971).

5 D. Emin, Adv. Phys. **24** (3), 305 (1975).

6 N. Iordanova, M. Dupuis, and K. M. Rosso, J. Chem. Phys. **122** (14), 144305 (2005).

## APPENDIX C: PULSED LASER DEPOSITION OF EPITAXIAL AND POLYCRYSTALLINE BISMUTH VANADATE THIN FILMS

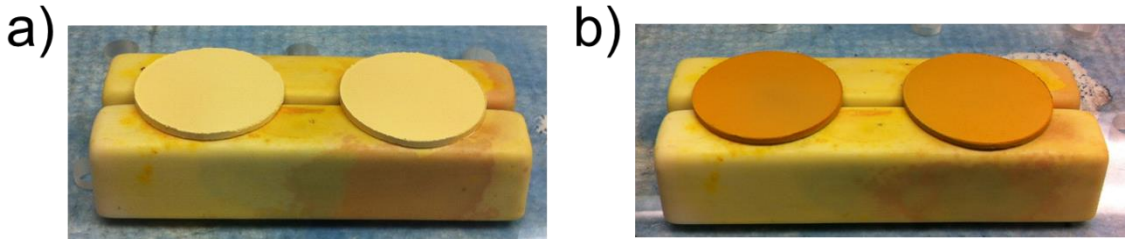


**Figure C.1:** Photographs of sintered **a)** 5:1 (L) and 6:1 (R) Bi:V targets and **b)** 1:1 (L) and 1.05:1 (R) Bi:V targets, ~1.375 in. diameter.

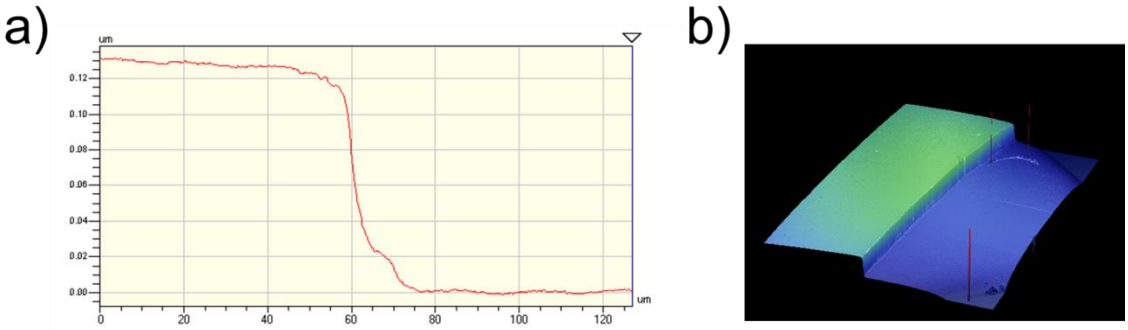


**Figure C.2: a)** Film profile from optical profilometry for a film twice the typical film thickness. Repeated measurements yielded an average thickness of 129.2 ± 1 nm, where the error is one standard deviation. **b)** 3-D image of BVO/YSZ step edge.

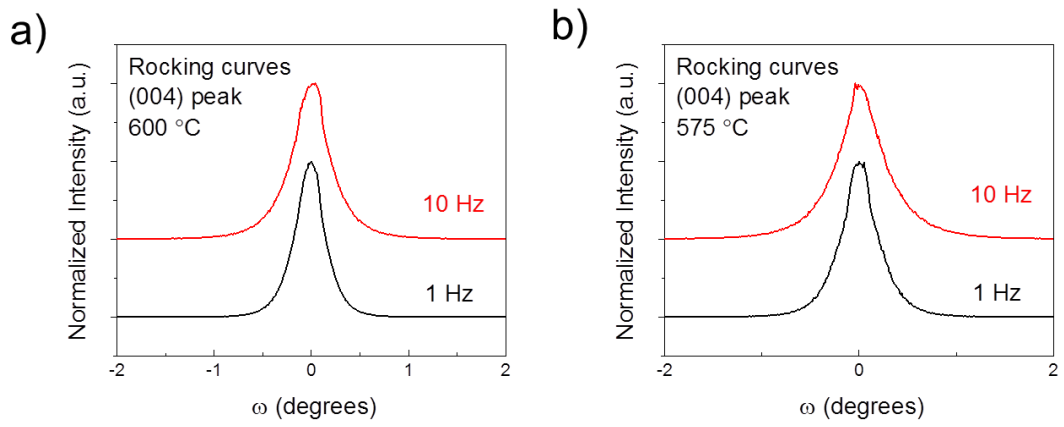


**Figure C.3**: Rocking curves around (004) peak of epitaxial BVO (65 nm)/YSZ films at **a)** 600 °C at 1 (0.3°) and 10 Hz (0.4°) and **b)** 575 °C at 1 (0.4°) and 10 Hz (0.5°).

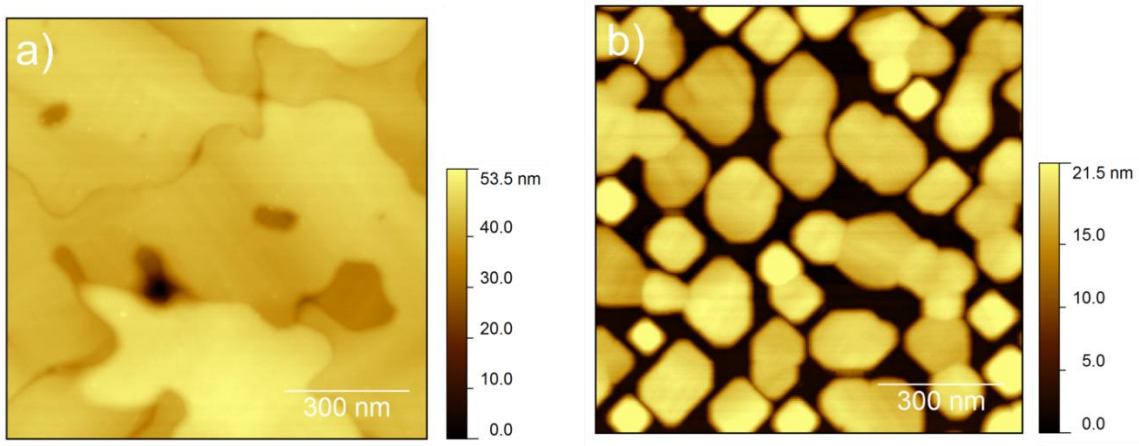


**Figure C.4: a)** Zoomed in AFM image of BVO(65 nm)/YSZ film morphology, **b)** zoomed in image at an early stage of film growth, depicting isolated islands of material.

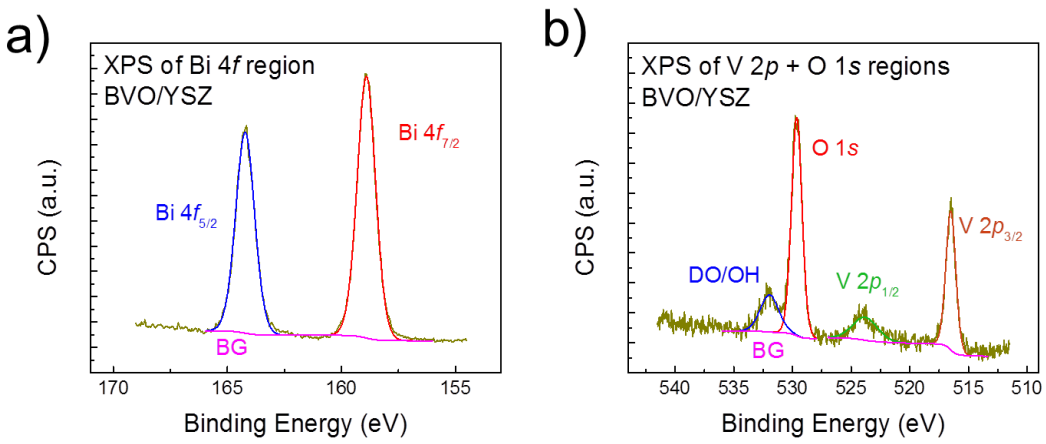


**Figure C.5:** XPS data and fitting for a BVO(65 nm)/YSZ film. **a)** Bi 4*f* and **b)** V 2*p* and O 1*s* region data with peak designations labelled. DO/OH: defect oxide or hydroxide, BG: background.

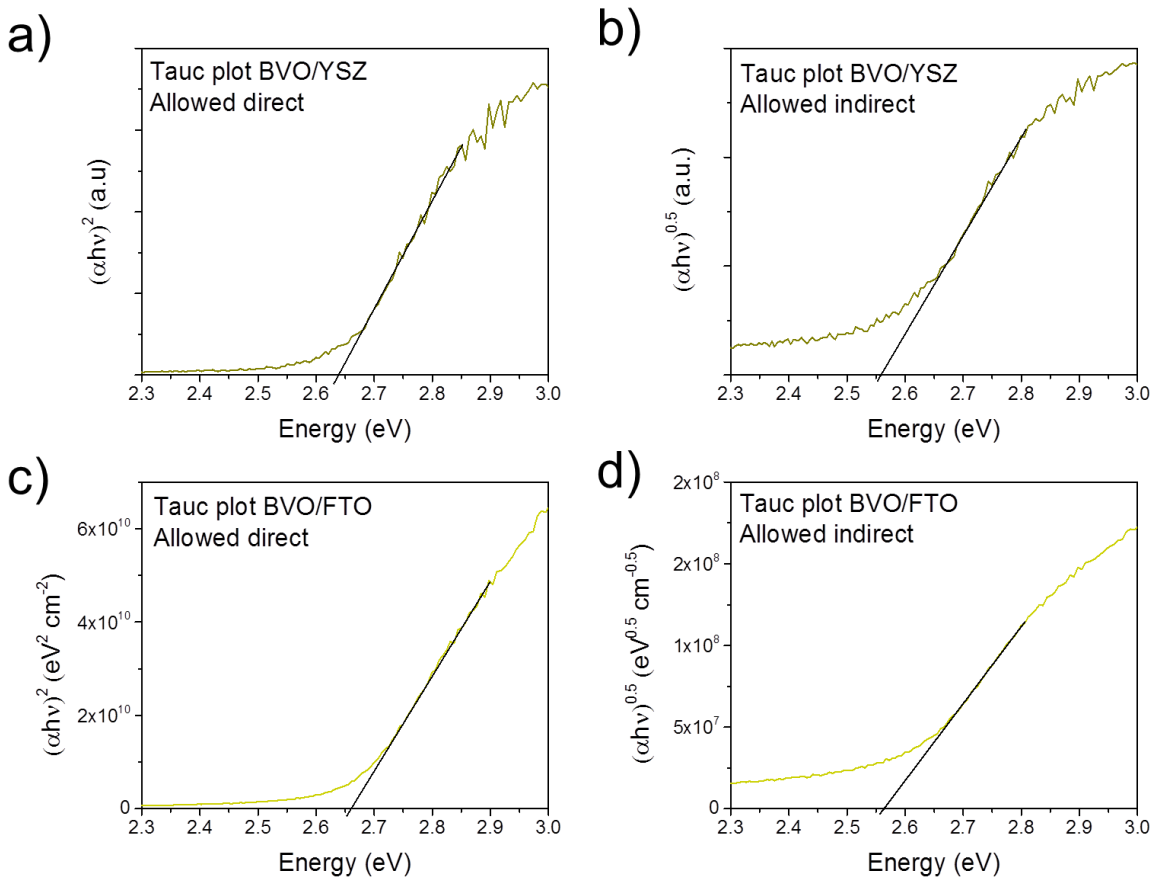


**Figure C.6:** Tauc analysis of BVO/YSZ **a)** direct and **b)** indirect transitions and BTO/FTO **c)** direct and **d)** indirect transitions. For the BVO/YSZ samples, the spectrometer light beam was likely larger than the films and so data was not quantitative.

## C1. Deposition of indium tin oxide (ITO) on YSZ

Deposition conditions similar to those of Sakanoue et al. were used[1], i.e. $T_{sub}$ = 700 °C (maximum for our system), a repetition rate of 5 Hz and 7.8 mTorr $O_2$. $\theta$-$2\theta$ XRD scans showed the ITO grew in an oriented fashion on YSZ (100) and rocking curves yielded a FWHM of ~0.3° (Figure C.6). BVO on ITO deposition was performed

immediately after ITO deposition without breaking vacuum, using conditions that resulted in the best films on YSZ.

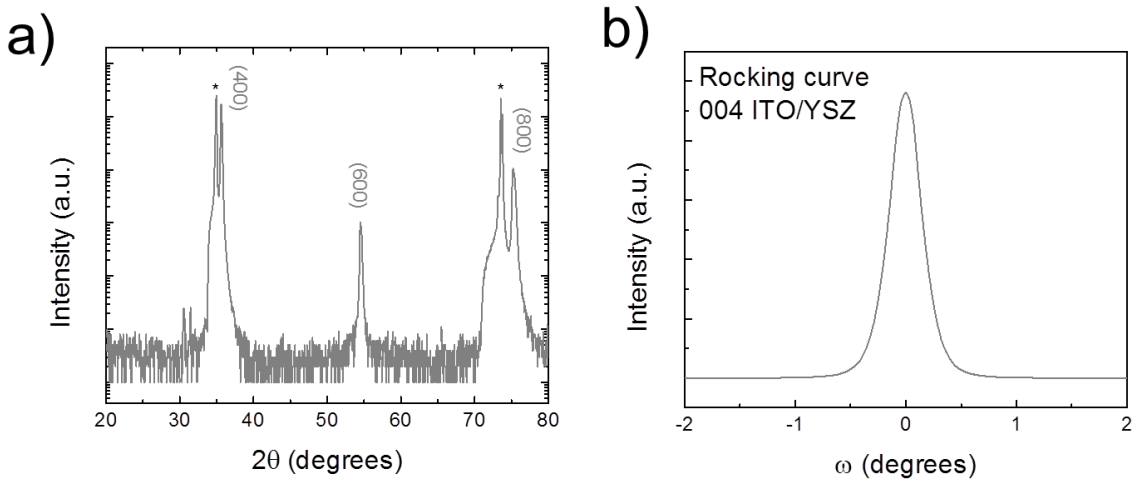


**Figure C.7: a)** $\theta$-$2\theta$ XRD scan of ITO/YSZ showing only ($h$,0,0) reflections of ITO. **b)** Rocking curve around the (004) peak of ITO, $2\theta = 36.64°$. The small peaks at ~30° in **a)** are likely from residual Cu Kβ x-rays interacting with the YSZ 200 peak at $2\theta = 35.96°$ due its high intensity. * symbol indicates peaks from the underlying substrate.

| | $j$ (mA cm$^{-2}$) | | |
|---|---|---|---|
| | AM1.5G | IPCE$_{int}$ | % Difference |
| $Na_2SO_3$ added | 0.153 | 0.134 | -12.4 |
| No $Na_2SO_3$ | 0.044 | 0.031 | -29.5 |

**Table C.1**: IPCE comparison with photocurrents from LSVs under AM1.5 G irradiation (Figures 4.6a and 4.7 in the main text).

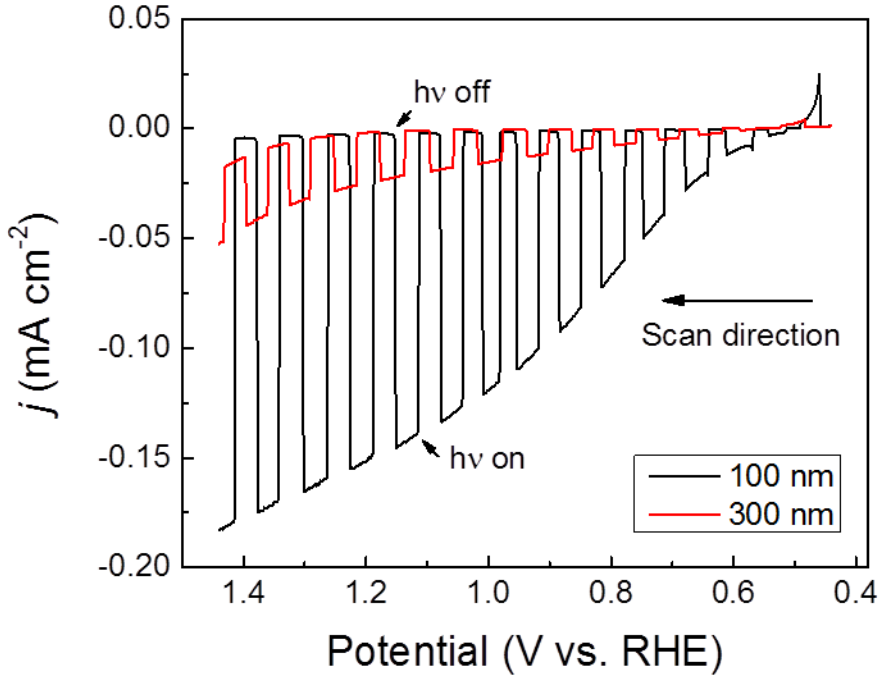


**Figure C.8:** Chopped LSVs showing the effect of film thickness on PEC performance. Both films were deposited in 7.8 mTorr of $O_2$.The electrolyte was 0.1 M phosphate buffer with 0.1 M $Na_2SO_4$ and 0.1 M $Na_2SO_4$ as a hole scavenger under AM1.5G simulated solar light (100 mWcm$^{-2}$). The scan rate was 10 mV s$^{-1}$.

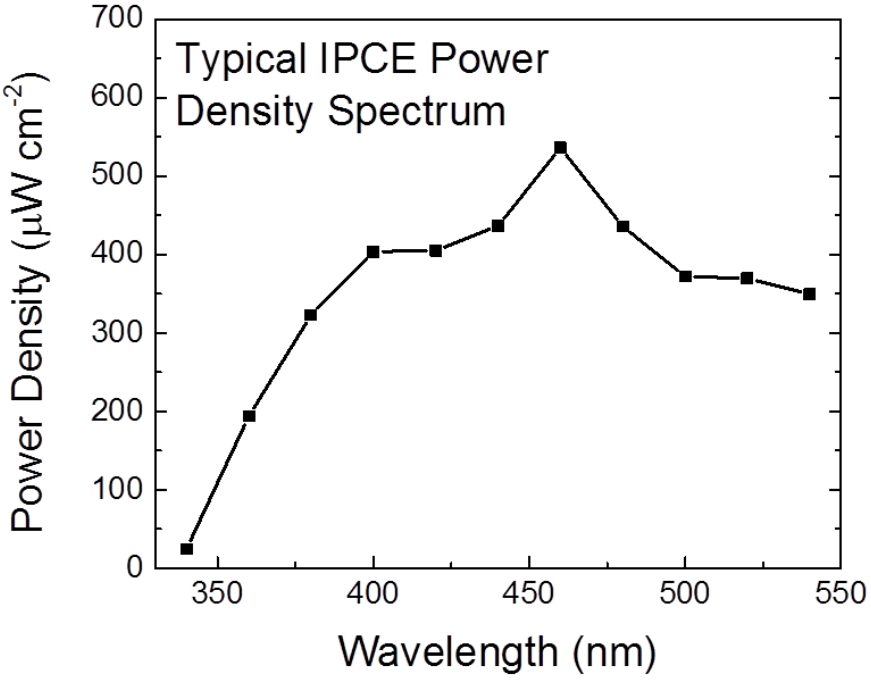


**Figure C.9:** Typical power density spectrum using for IPCE measurements. The power density was measured using a Si photodetector with a machined aluminum mask.

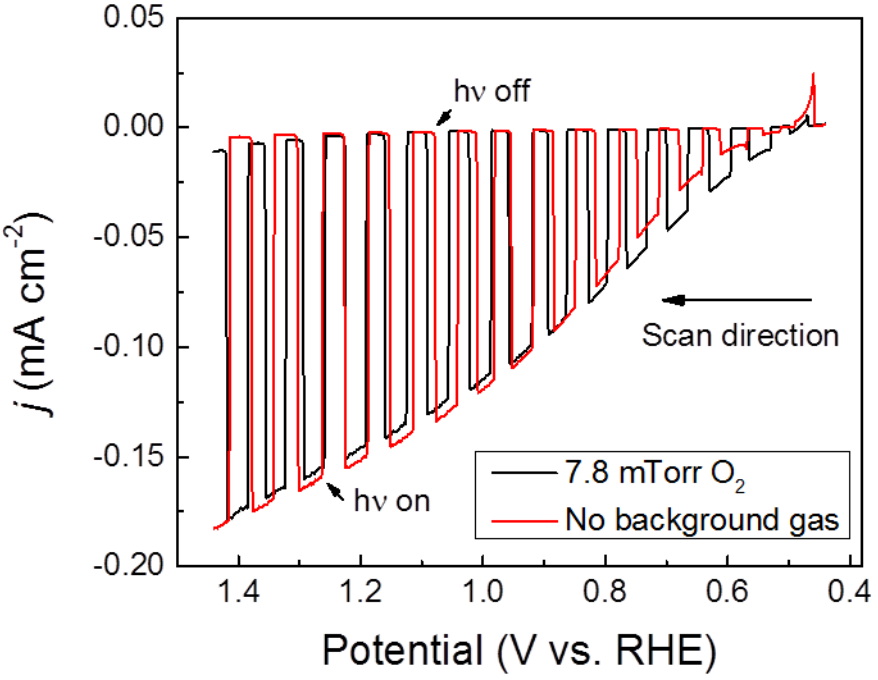


**Figure C.10:** Chopped LSVs showing the effect of background gas during deposition. Both films were ~100 nm thick. The electrolyte was 0.1 M phosphate buffer with 0.1 M $Na_2SO_4$ and 0.1 M $Na_2SO_4$ as a hole scavenger under AM1.5G simulated solar light (100 mW $cm^{-2}$). The scan rate was 10 mV $s^{-1}$.

## REFERENCES

(1) Sakanoue, T.; Nakatani, S.; Ueda, Y.; Izumi, H.; Ishihara, T.; Motoyama, M. Fabrication of Well-Ordered Indium-Tin-Oxide Film and Characterization of Organic Films Vacuum-Deposited on It. *Mol. Cryst. Liq. Cryst.* **2003**, *405*, 59-66.

## APPENDIX D: ANISOTROPIC SMALL-POLARON HOPPING IN W:$BiVO_4$ SINGLE CRYSTALS

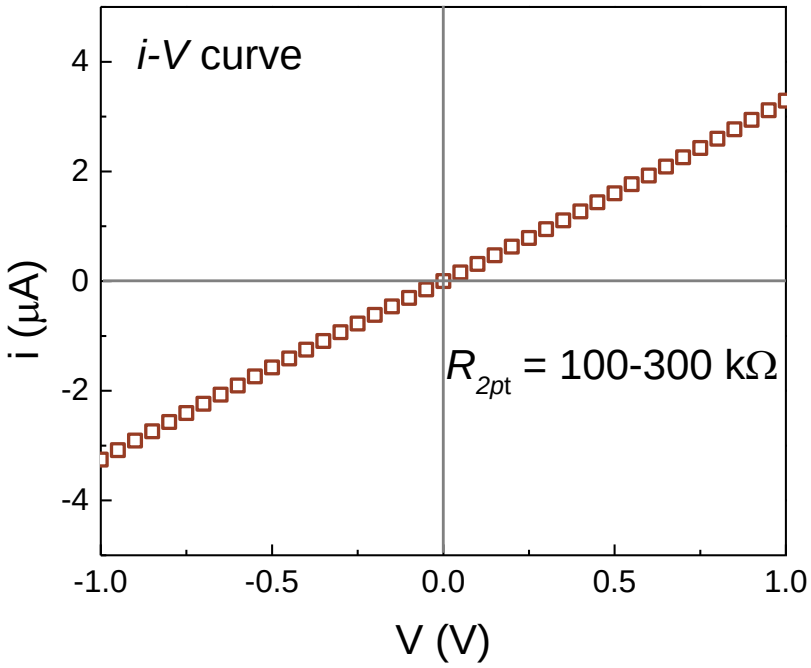


**Figure D1:** Example 2 pt *i-V* curve showing Ohmic behavior. Contacts in this case were InGa eutectic.

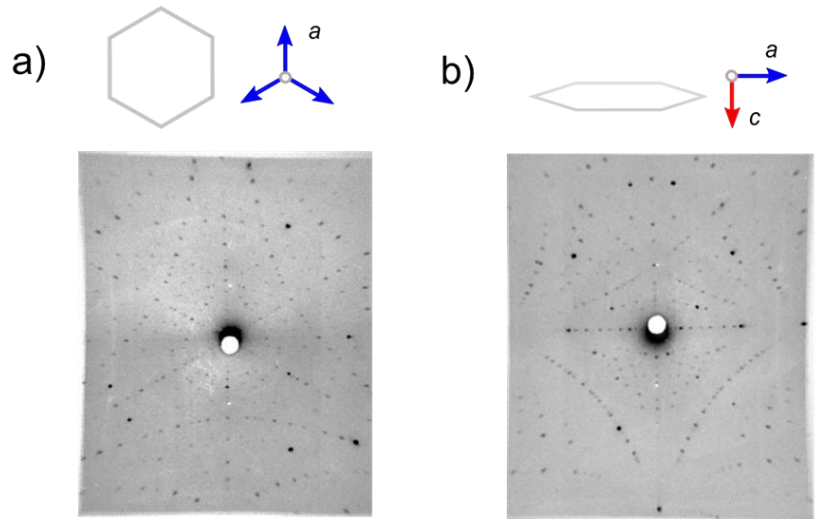


**Figure D2:** Representative Laue spot patterns showing a) (0001)-plane oriented and b) (1000)-plane oriented Ti:α-$Fe_2O_3$ single crystals.

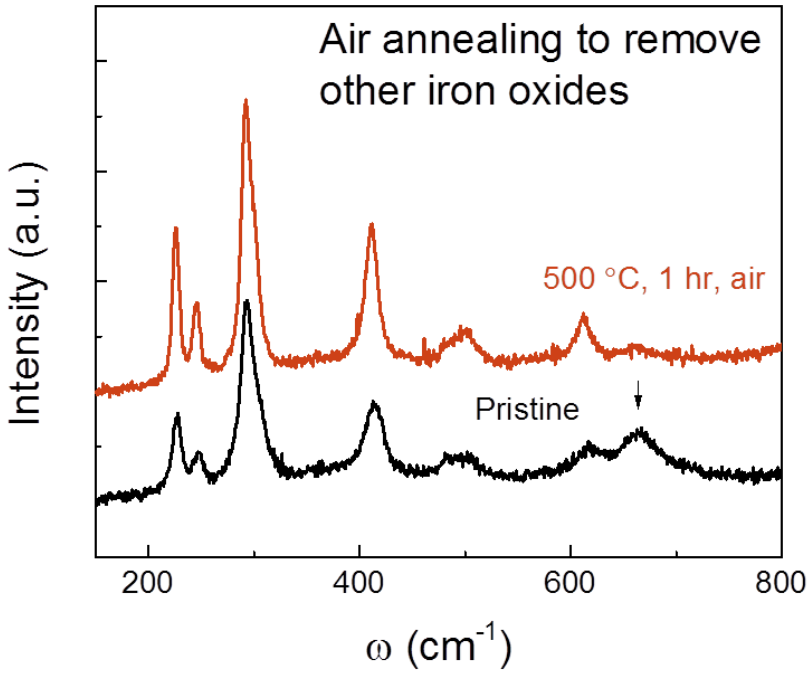


**Figure D3:** Raman spectra of one sample with small impurity peak (indicated by arrow at ~660 $cm^{-1}$) before and after thermal treatment (500 C, 1 hr in air).

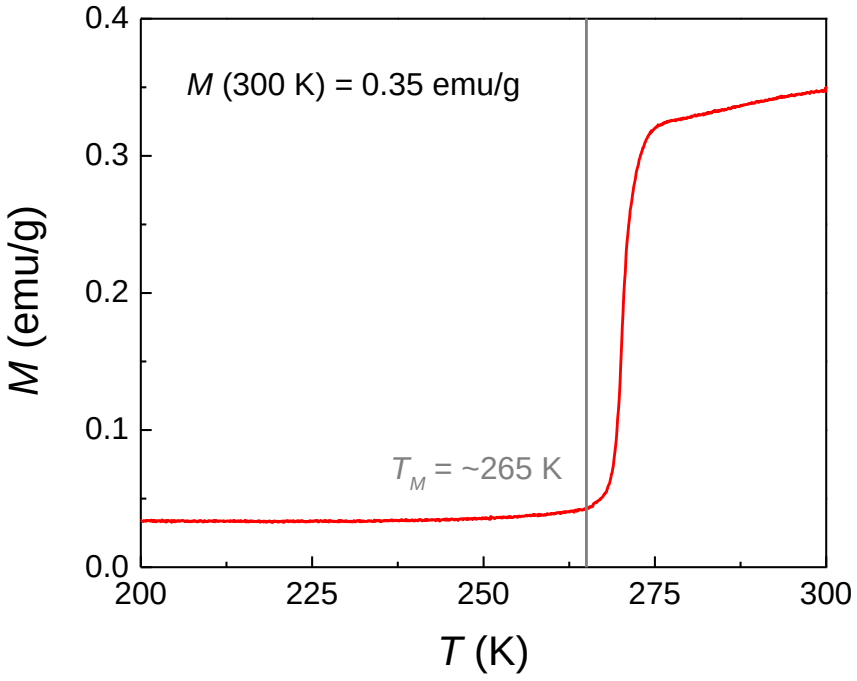


**Figure D4:** Magnetization vs. temperature for a Ti:α-$Fe_2O_3$ single crystal (ρ (300 K) = ~70 Ohm-cm). The field was applied in the basal plane (easy axis), .i.e. perpendicular to *c*-axis.

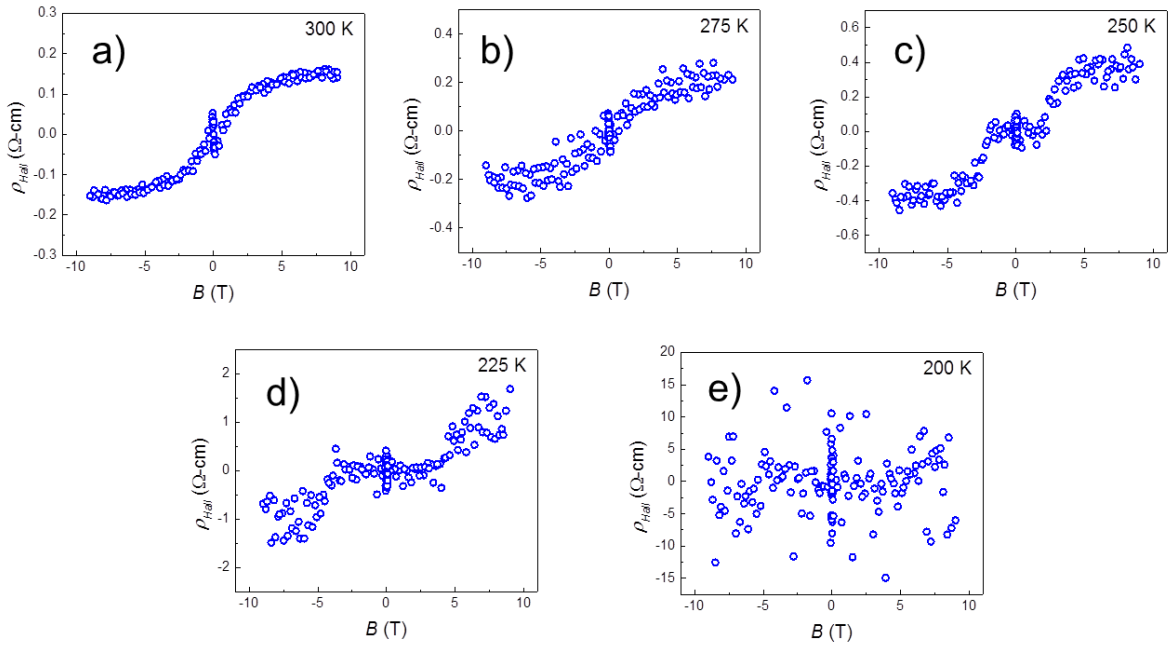


**Figure D5:** DC Hall effect, $\rho_{Hall}$ vs. $B$ at **a)** 300, **b)** 275, **c)** 250, **d)** 225 and **e)** 200 K.

### D.1 CALCULATION OF ADIABATIC PRE-FACTOR

The variables used in calculating $\sigma_0 T$ using equation D1are given in Table D1. $n_d$ was estimated from the conductivity, assuming a drift mobility of $10^{-2}$ cm$^2$ V$^{-1}$ s$^{-1}$.

$$\sigma_0 = \frac{n_d e^2 a^2 \nu_0}{\kappa T} \qquad \text{(D1)}$$

**Table D1:** Calculation variables in calculating the adiabatic pre-factor for the crystal in the main text.

| $g$ (-) | $n_d$ (cm$^{-3}$) | $a$ (A) | $\nu_0$ (Hz) | $\sigma_0$ (S cm$^{-1}$) at 300 K |
|---|---|---|---|---|
| 0.50 | 2.6x10$^{18}$ | 3.0 | 2x10$^{13}$ | 0.14 |

## APPENDIX E: IMPROVED VISIBLE LIGHT HARVESTING OF WO3 BY INCORPORATION OF SULFUR OR IODINE

### E.1 X-RAY DIFFRACTION (XRD)

Undoped $WO_3$ films showed excellent agreement with existing XRD spectra for monoclinic $WO_3$ (PDF #00-043-1235). With progressive sulfur incorporation, no significant changes were observed until 2%, where peak broadening (most noticeably of the (200), (020) and (002) peaks at 23.119, 23.586 and 24.380° respectively) occurred (Figure E.1). This indicates poorer crystallinity of these heavily doped samples.

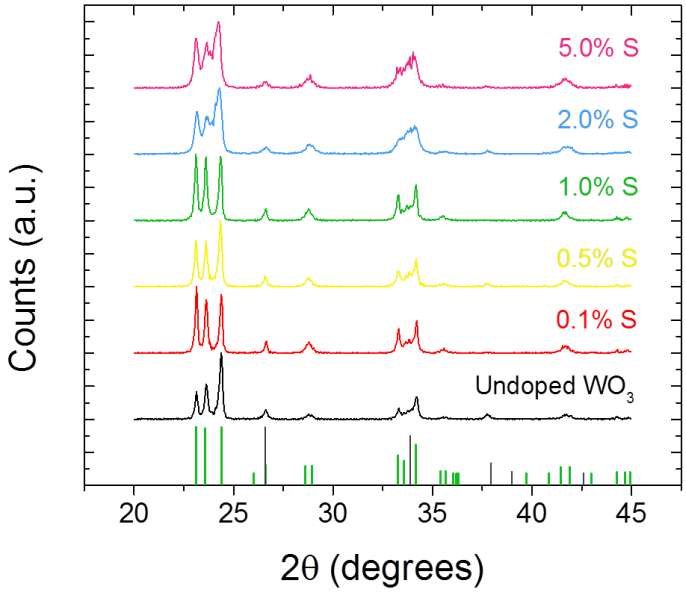


**Figure E.1:** X-ray diffraction (XRD) patterns for S:$WO_3$ films. The bars at the bottom of the plot are the reference patterns for monoclinic $WO_3$ (thick green bars, PDF #00-043-1235) and tin oxide from the substrate (thin grey bars, PDF #00-021-1250). All films were annealed at 550 ˚C for 1 hr in air.

Interestingly, there were no detectable changes in the XRD patterns with increasing iodine content (Figure E.2), despite drastic changes in the light absorption and PEC performance of these samples. We cannot rule out the formation of new amorphous phases using this technique, or changes in the crystalline perfection below the sensitivity of XRD.

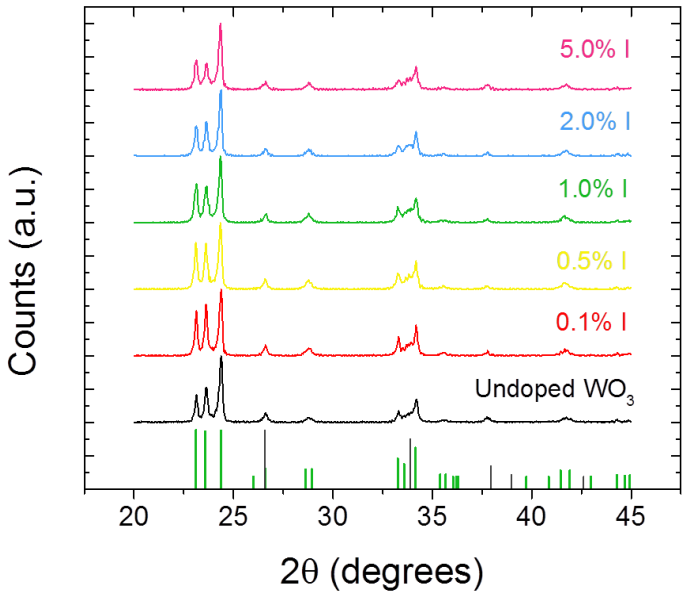


**Figure E.2:** X-ray diffraction (XRD) patterns for I:$WO_3$ films. The bars at the bottom of the plot are the reference patterns for monoclinic $WO_3$ (thick green bars, PDF #00-043-1235) and tin oxide from the substrate (thin grey bars, PDF #00-021-1250). All films were annealed at 550 ˚C for 1 hr in air.

## E.2 Optical properties

As sulfur was added to the films, the absorption was red-shifted to longer wavelengths (Figure E.5), manifesting as a shoulder at low doping concentrations that gradually changed to a longer wavelength tail. This provides evidence for sulfur acting as a shallow defect state, ~0.1 eV above the valence band.

In the I:$WO_3$ films, two transitions are clearly visible in the optical absorption spectra (Figure E.6), one close to the band gap energy for undoped $WO_3$ (2.7 eV) and another at ~2.1 eV. This is likely the combination of absorption from the band gap of $WO_3$ and the defect state related to iodine incorporation.

Tauc plot analyses [1] showed indirect transitions at ~2.7, 2.6 and 2.1 eV for undoped $WO_3$, S:$WO_3$ and I:$WO_3$ respectively (Figure E.4).

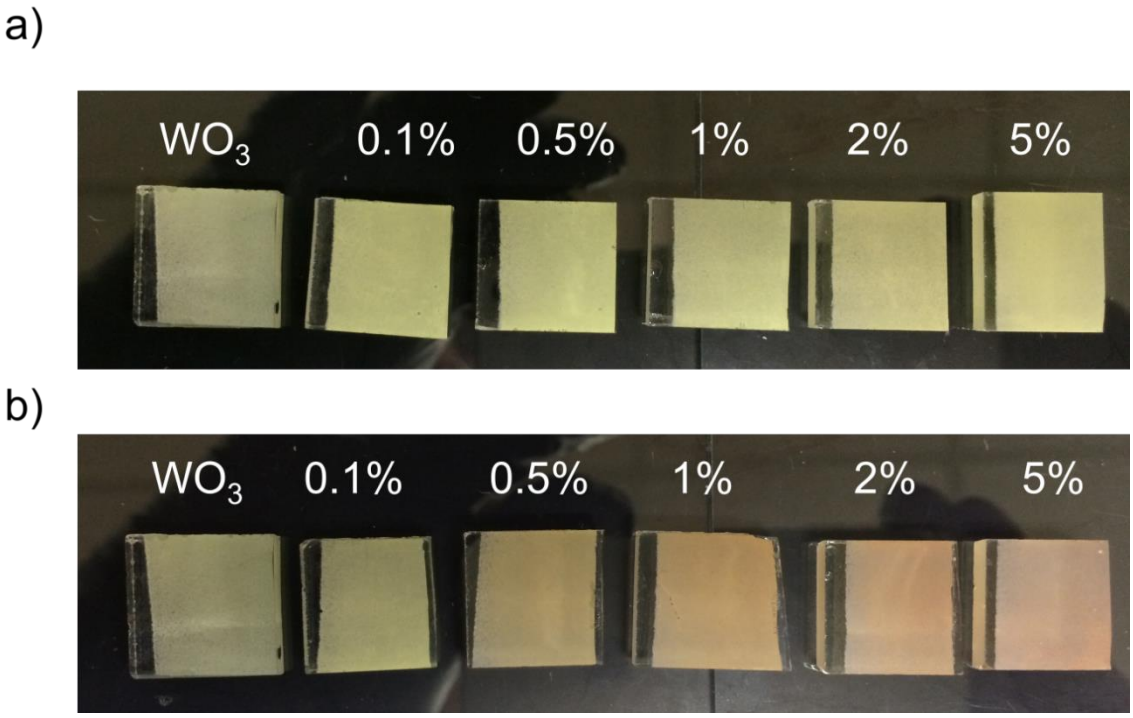


**Figure E.3:** Photographs of undoped and **a)** S:$WO_3$ and **b)** I:$WO_3$ films.

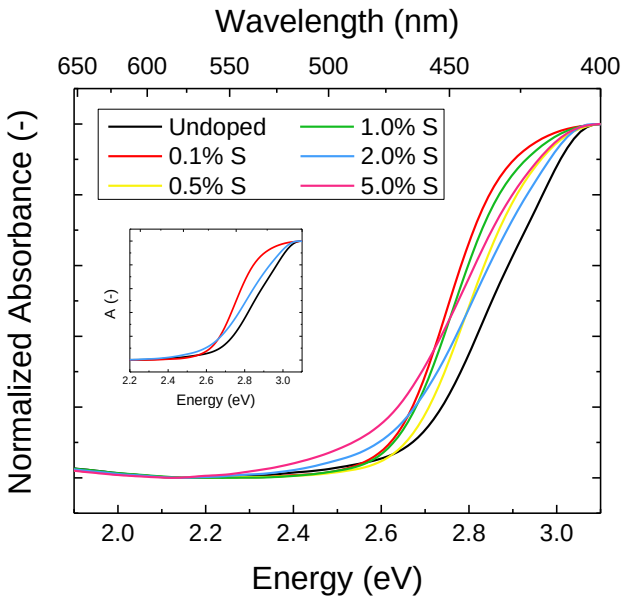


**Figure E.4:** Absorbance spectra calculated from UV-Vis diffuse reflectance data for S:$WO_3$ films. Inset shows the spectra of 0.1% and 2% S:$WO_3$ only to illustrate the differences in the spectral shape.

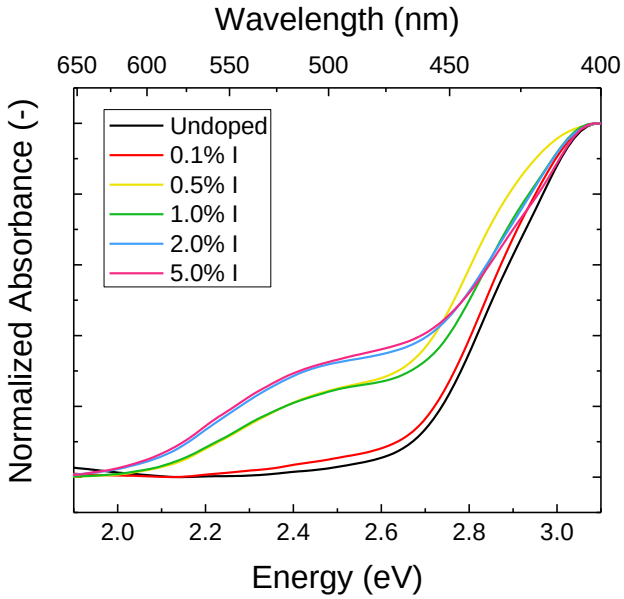


**Figure E.5:** Absorbance spectra calculated from UV-Vis diffuse reflectance data for I:$WO_3$ films.

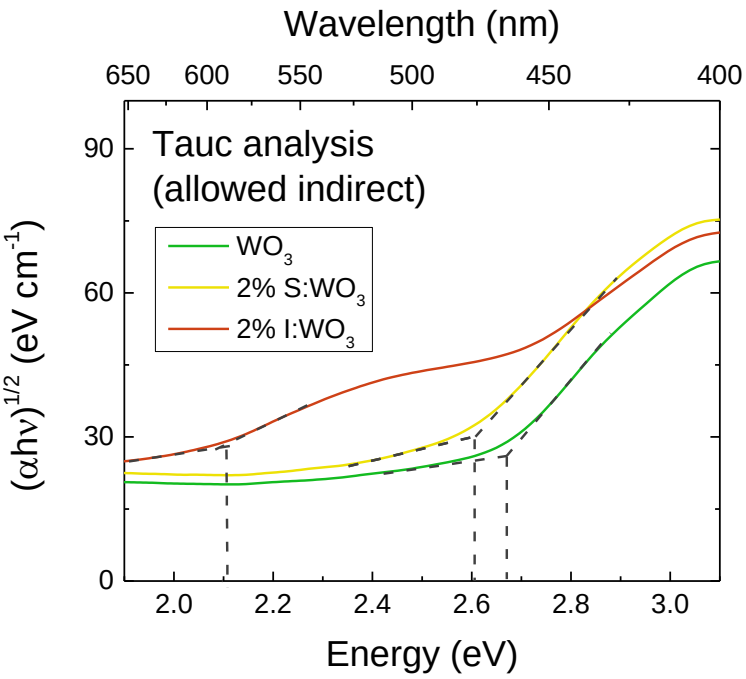


**Figure E.6:** Tauc plot for allowed indirect transitions for heavily doped $WO_3$ films.

## E.3. PHOTOELECTROCHEMISTRY

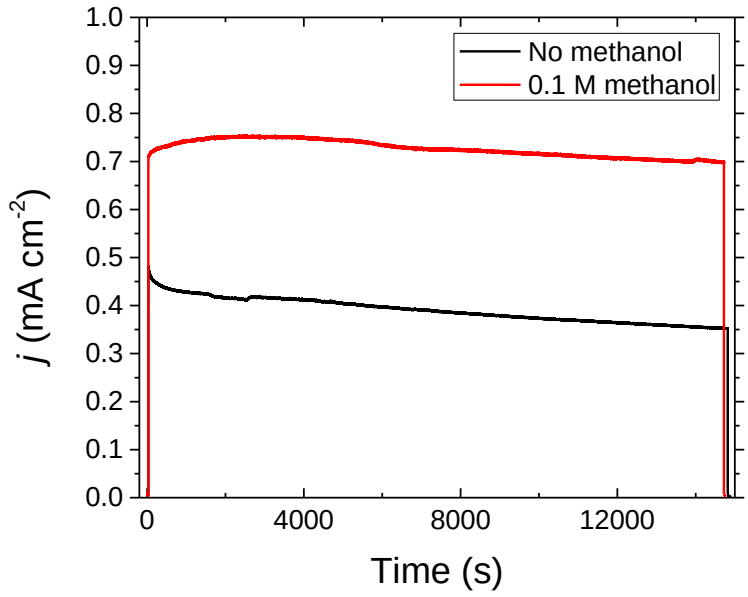


**Figure E.7:** Long term testing (~4 hrs) with and without methanol under AM1.5 G simulated solar light (100 mW $cm^{-2}$). The electrolyte was 1 M methane sulfonic acid.

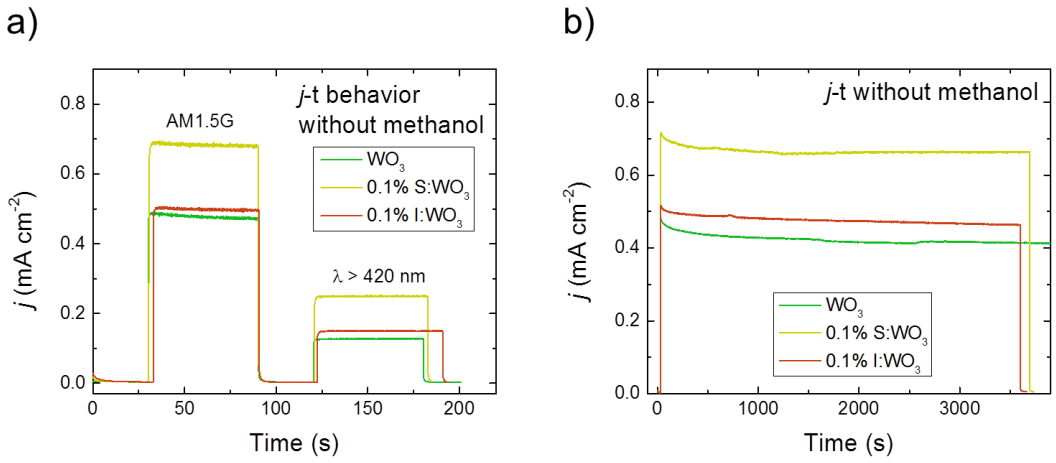


**Figure E.8: a)** Photocurrent-time (*j*-t) data under AM1.5G simulated solar light (100 mW $cm^{-2}$) and with a long pass filter. **b)** *j*-t behavior under AM1.5G simulated solar light (100 mW $cm^{-2}$) for ~1 hr. The undoped data is reproduced from Figure E.7 and so extends to longer times. The electrolyte was 1 M methane sulfonic acid in both **a)** and **b)**.

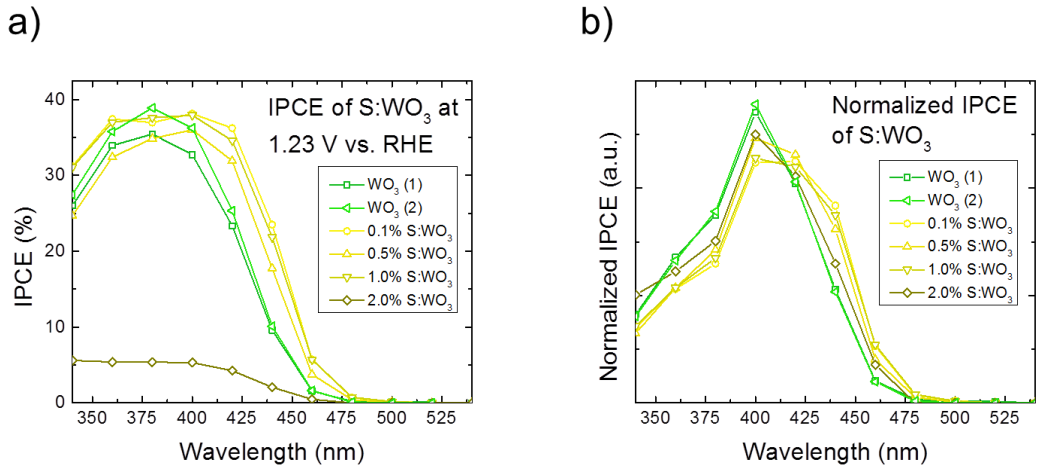


**Figure E.9: a)** IPCE vs. wavelength plots at 1.23 V vs. RHE for $S:WO_3$ films. The electrolyte was 1 M methane sulfonic acid with 0.1 M methanol**. b)** The data taken in a), integrated with respect to the AM1.5G spectrum[40] and normalized such that the integrated photocurrents for all samples were 1 mA $cm^{-2}$. This was done to compare the spectral shape of the IPCE spectra. The traces for the two undoped $WO_3$ ((1) and (2)) samples overlap closely.

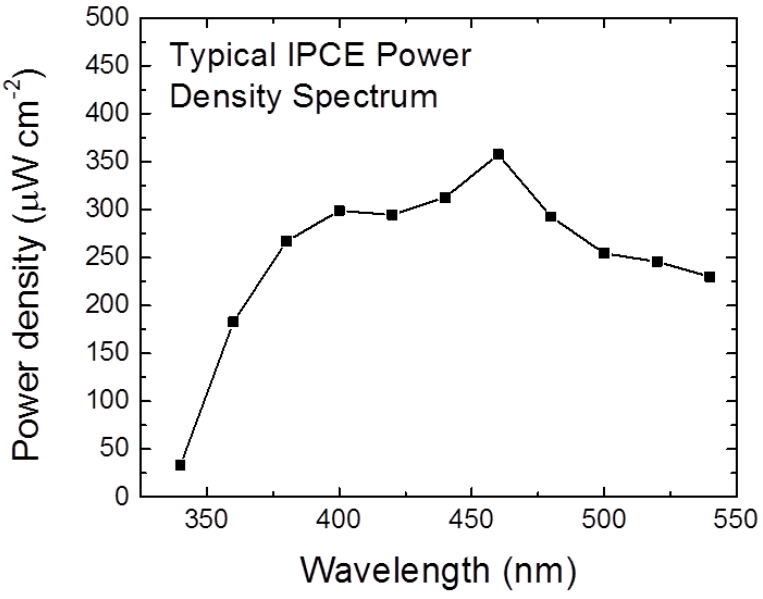


**Figure E.10:** Typical power density spectrum using for IPCE measurements. The power density was measured using a Si photodetector with a machined aluminum mask.

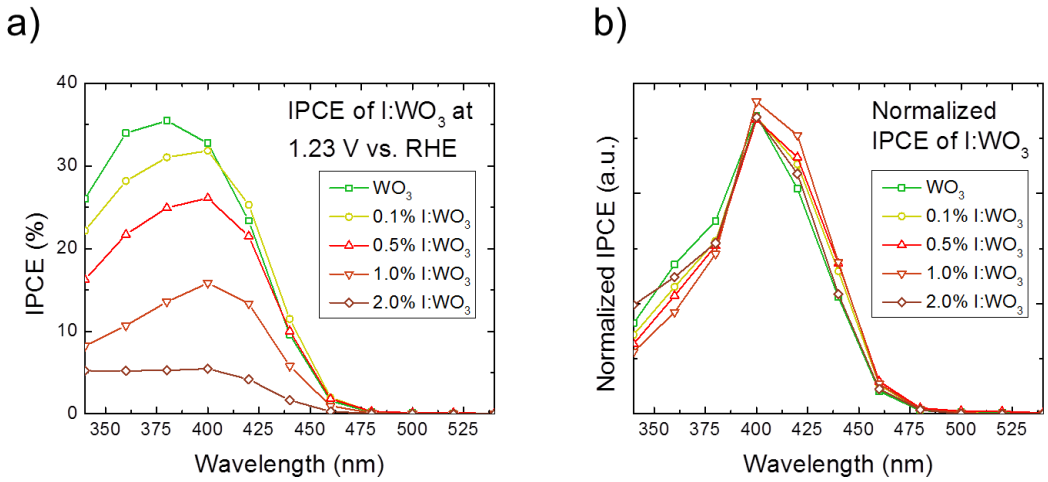


**Figure E.11: a)** IPCE vs. wavelength plots at 1.23 V vs. RHE for I:$WO_3$ films. The electrolyte was 1 M methane sulfonic acid with 0.1 M methanol. **b)** The data taken in a) ), integrated with respect to the AM1.5G spectrum[40] and normalized such that the integrated photocurrents for all samples were 1 mA $cm^{-2}$. This was done to compare the spectral shape of the IPCE spectra.

| | $j$ (mA $cm^{-2}$) | | |
|---|---|---|---|
| Sample | AM1.5G | $IPCE_{int}$ | % Difference |
| Undoped (1) | 0.76 | 0.87 | 14.5 |
| Undoped (2) | 0.80 | 0.94 | 17.5 |
| 0.1 | 1.00 | 1.23 | 23.0 |
| 0.5 | 0.81 | 1.05 | 29.6 |
| 1.0 | 1.10 | 1.20 | 9.1 |
| 2.0 | 0.13 | 0.15 | 15.4 |

**Table E.1:** Comparison between lamp and integrated IPCE photocurrent values for S:$WO_3$. Undoped (1) and (2) refer to $WO_3$ (1) and (2) in Figure E.9.

| | $j$ (mA cm$^{-2}$) | | |
|---|---|---|---|
| Sample | AM1.5G | $IPCE_{int}$ | % Difference |
| Undoped | 0.76 | 0.87 | 14.5 |
| 0.1 | 0.72 | 0.85 | 18.1 |
| 0.5 | 0.53 | 0.70 | 32.1 |
| 1.0 | 0.37 | 0.40 | 8.1 |
| 2.0 | 0.15 | 0.15 | 0.0 |

**Table E.2:** Comparison between lamp and integrated IPCE photocurrent values for I:$WO_3$.

## E.4. TIME OF FLIGHT SECONDARY ION MASS SPECTROMETRY (TOF-SIMS)

To determine the amounts and profiles of S and I in the films, combined ToF-SIMS and XPS analyses were carried out. It should be noted that these samples had not been previously tested in electrolyte to avoid contamination with sulfur species in the electrolyte.

The oxide of the lightest isotope of tungsten, $^{180}WO_3^-$, secondary ion signal was selected as a marker for the $WO_3$ matrix to avoid hydrogen signal convolution. This is a common issue arising from hydrogen combining with lighter isotopes that match the same masses as heavier isotopes. Since the $I^-$ signal saturated the detector for samples with I doping larger than 1% (nominal), the $IO^-$ signal was chosen as a marker for I in the I:$WO_3$ films. Albeit convoluted with the $O^-$ signal, the $IO^-$ signal tracked closely with the $I^-$ signal for samples with light I doping, thus proving its correct assignment as I marker. The marker for the sulfur dopant was selected as $S^-$.

Note that the similarity between the precursor S concentrations and the $S^-$ / $^{180}WO_3^-$ ratio in Table E.3 is coincidental – the precursor concentration was calculated based on the concentration of oxygen in $WO_3$, not W.

| Precursor S concentration (%) | $S^-$ / $^{180}WO_3^-$ after 1000 s (-) | BG substracted (-) |
|---|---|---|
| 0 | 0.101 | 0.000 |
| 0.1 | 0.145 | 0.044 |
| 0.5 | 0.612 | 0.511 |
| 1 | 1.138 | 1.037 |
| 2 | 3.272 | 3.171 |
| 5 | 4.053 | 3.953 |

**Table E.3:** Precursor concentrations and the corresponding ToF-SIMS $S^-$ / $^{180}WO_3^-$ value. BG: background $S^-$ signal measured on undoped sample.

## E.5. X-RAY PHOTOELECTRON SPECTROSCOPY (XPS)

In the analysis of the XPS data, the adventitious carbon 1*s* peak was used as a reference with a binding energy (B.E.) of 285 eV and the background was removed using the Shirley algorithm.

### E5.1 XPS of 20% S:$WO_3$

The S 2*p* signal was extremely weak, requiring involved scan conditions (80 eV pass energy, 1.5 s dwell time, 16 sweeps) to observe. On the pristine sample, the S $2p_{3/2}$ peak was seen at 168.9 eV, indicating $S^{6+}$ on the surface, possibly from a $SO_4^{2-}$ species (Figure E.12a). However, after brief (10s) $Ar^+$ sputtering this peak disappeared (Figure E.12b), indicating this concentration is not the same as the S signal from our ToF-SIMS measurement -- which was relatively constant throughout the film (Figure 6.6a in Chapter 6). No peaks were observed around 160 eV, the position for $S^{2-}$ when bonded to W as in $WS_2$ [3].Therefore the bulk sulfur in the most heavily doped S:$WO_3$ films was not detectable by XPS, meaning we could not quantify it or assign charge states.

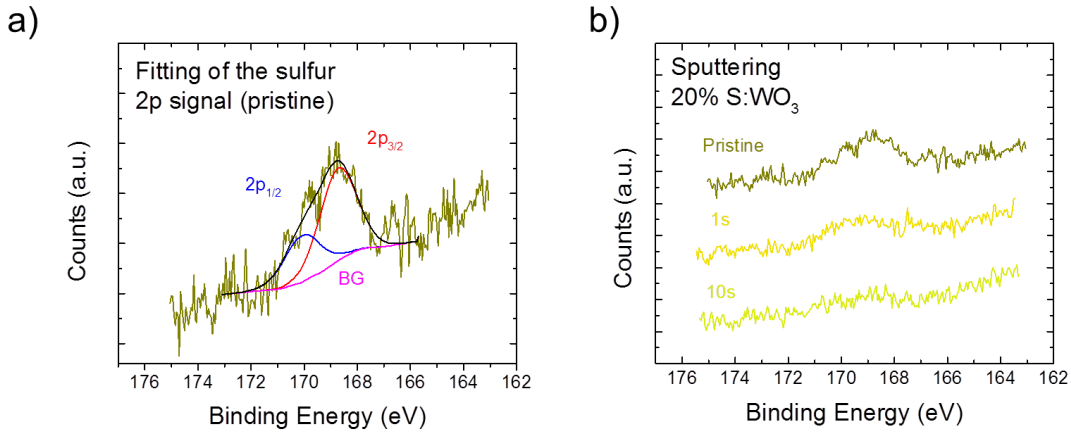


**Figure E.12: a)** Example fitting of the S 2*p* region, **b)** Decreasing I concentration with brief $Ar^+$ sputtering. BG: background.

However, we estimate an upper limit (based on fitting the instrument noise) of ~0.1% of O sites for 20% S:$WO_3$.

### S5.2 XPS of 2% I:WO3

The I $3d_{5/2}$ signal was detected at 619.5 eV (Figure E.13a), corresponding to I in the 1- oxidation state [4]. Upon $Ar^+$ sputtering, 3*d* signal increased slightly (Figure E.13b), likely due to environmental contamination (C, H, O species) on the surface of the sample. Due to the 11.52 eV peak splitting of I $3d_{3/2}$ and $3d_{5/2}$, only the $3d_{5/2}$ peak was recorded to optimize instrument time. The relative sensitivity factor was adjusted accordingly.

### S5.3 Quantification of $I^-$ concentration

In order to quantify the $I^-$ concentration (which was a function of film depth, see Figure 6.6b in the main text), a 2% I:$WO_3$ sample was sputtered to an intermediate point in the film and the signal measured by ToF-SIMS. Then, the sample was quickly (less than 5 min) transferred to the XPS system, and the sputtered area analyzed. This allowed

a direct conversion of the ToF-SIMS signal to an atomic concentration. The sputtered area was 1 × 1 $mm^2$ and clearly visible. Care was taken to align the X-ray detector and camera, so that the sputtered area was being analyzed with confidence. This value was used to convert the ToF-SIMS signal to a [$I^-$] / [O sites] value for I:$WO_3$ samples, where the [O sites] = 3* [$W^{6+}$] in $WO_3$ (Figure 6.6b in Chapter 6).

## E.6. RAMAN SPECTROSCOPY

Raman spectroscopy was used to probe small changes in the bonding environment due to sulfur or iodine incorporation. Data for all S:$WO_3$ and I:$WO_3$ films are contained in Figures E.14 and E.15 respectively. We attribute the steadily increasing background observed with increasing I incorporation (Figure E.15) to low-level fluorescence due to these impurities.

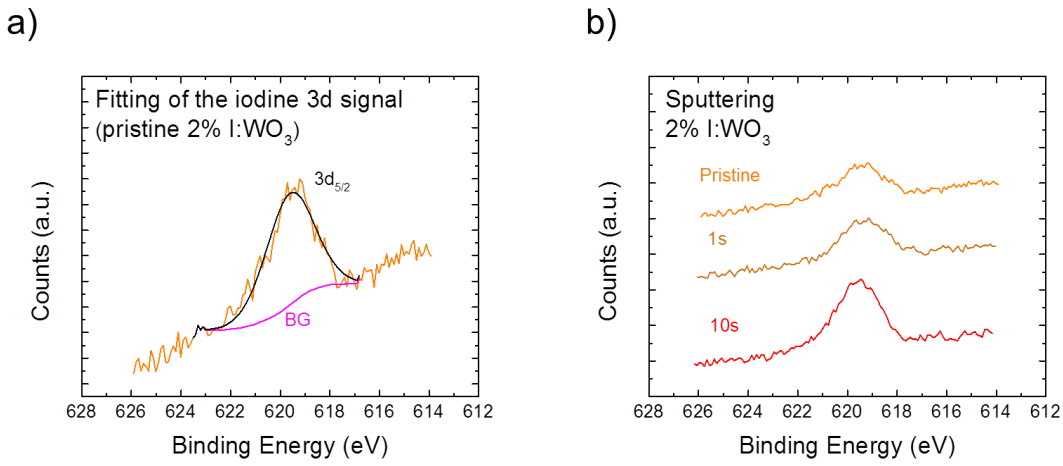


**Figure E.13: a)** Example fitting of the I $3d_{5/2}$ peak, **b)** Increasing I concentration with short $Ar^+$ sputtering. BG: background.

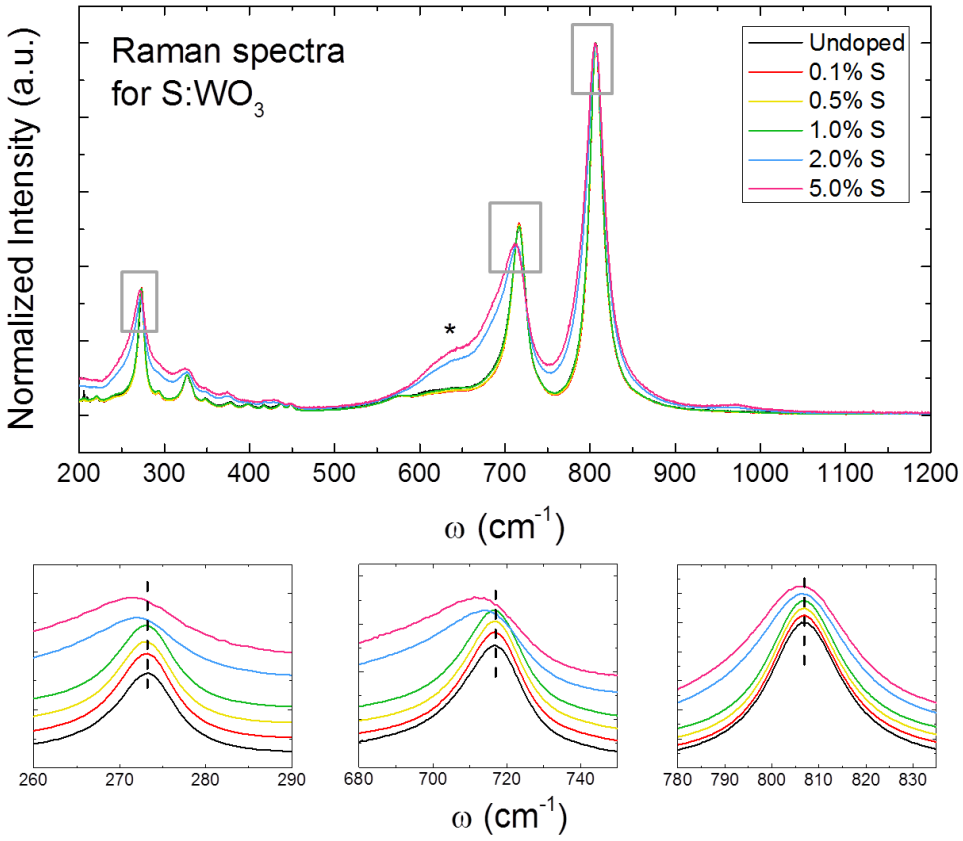


**Figure E.14:** Raman spectra for S:$WO_3$ as a function of doping level. The boxed areas have been magnified in the inset so that peak broadening and shifts can be clearly seen. Peaks not seen in the reference undoped $WO_3$ spectra have been starred with a "*" symbol. Vertical dashed lines highlight the peak centers for undoped $WO_3$.

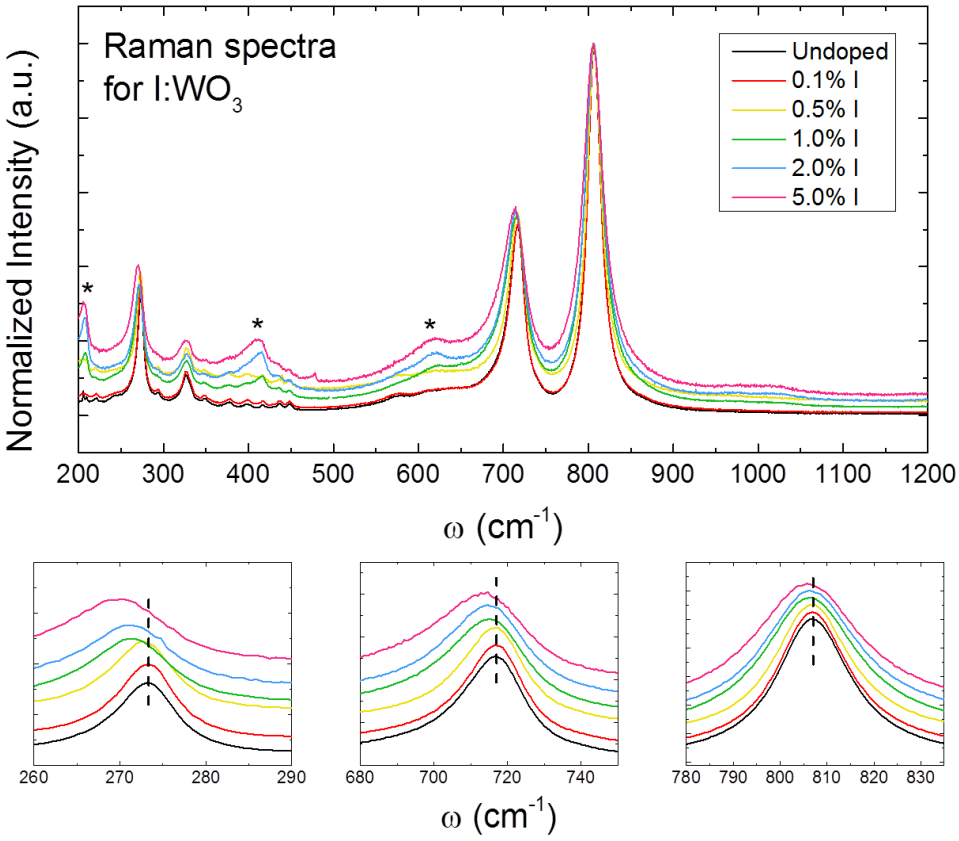


**Figure E.15:** Raman spectra for I:$WO_3$ as a function of doping level. The boxed areas have been magnified in the inset so that peak broadening and shifts can be clearly seen. New peaks not seen in the reference undoped $WO_3$ spectra have been starred with a "*" symbol. Vertical dashed lines highlight the peak centers for undoped $WO_3$ Spikes due to cosmic rays have been removed.

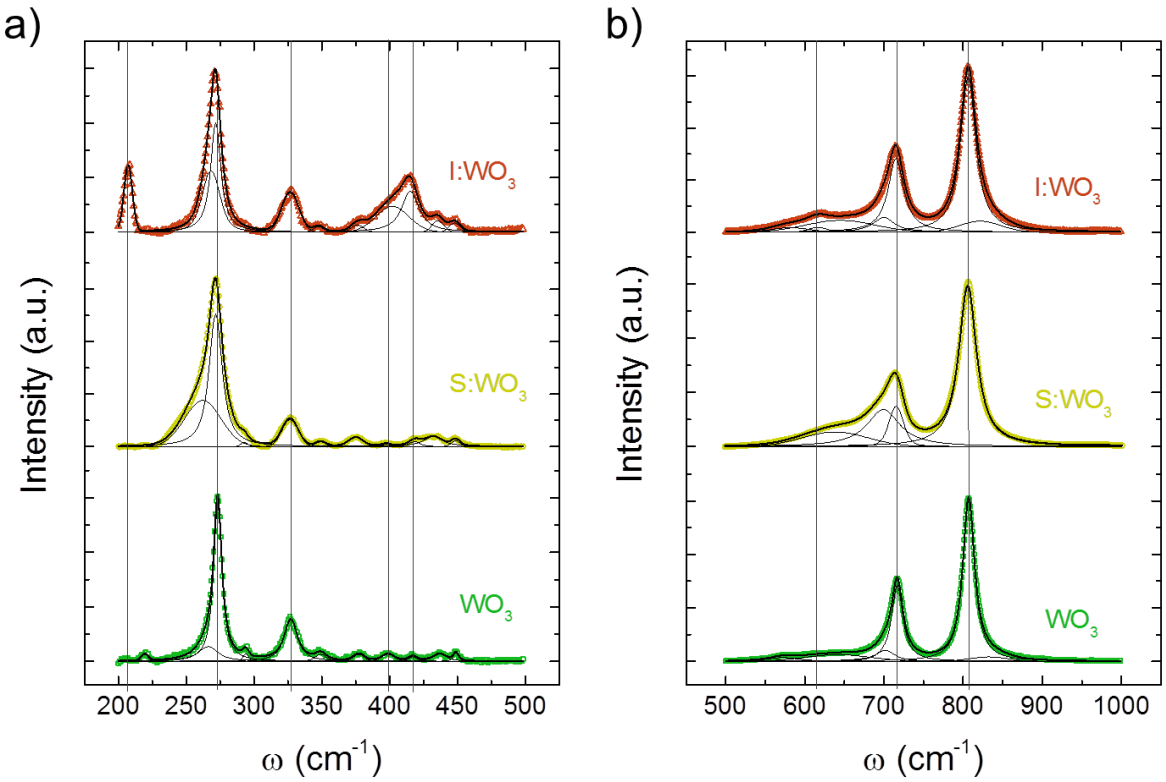


**Figure E.16:** Fitting of Raman spectra for $WO_3$, 2% S:$WO_3$ and 2% I:$WO_3$ at **a)** low and **b)** high wavenumbers. Data is represented by open symbols, the sum of the model as thick black lines and individual components as thin black lines. Vertical gray lines highlight the positions of peaks of interest. Fitting was done using Fityk software (version 0.9.8) [5], and represents the minimum number of peaks required in all cases.

## REFERENCES

(1) Chen, Z.; Jaramillo, T. F.; Deutsch, T. G.; Kleiman-Shwarsctein, A.; Forman, A. J.; Gaillard, N.; Garland, R.; Takanabe, K.; Heske, C.; Sunkara, M. *J. Mater. Res* **2010**, *25*, 3.

(2) NREL. Reference Solar Spectral Irradiance: ASTM G-173. [Online Early Access]. http://rredc.nrel.gov/solar/spectra/am1.5/ASTMG173/ASTMG173.html (accessed October, 2013).

(3) Martin-Litas, I.; Vinatier, P.; Levasseur, A.; Dupin, J.; Gonbeau, D.; Weill, F. *Thin Solid Films* **2002**, *416*, 1.

(4) Tojo, S.; Tachikawa, T.; Fujitsuka, M.; Majima, T. *The Journal of Physical Chemistry C* **2008**, *112*, 14948.

(5) Wojdyr, M. *Journal of Applied Crystallography* **2010**, *43*, 1126.

# Bibliography


Abdi, F. F.; Firet, N.; van de Krol, R. *ChemCatChem* **2013**, *5*, 490.

Abdi, F. F.; Han, L.; Smets, A. H. M.; Zeman, M.; Dam, B.; van de Krol, R. *Nat. Commun.* **2013**, *4*, 1.

Abdi, F. F.; Savenije, T. J.; May, M. M.; Dam, B.; van de Krol, R. *J. Phys. Chem. Lett.* **2013**, *4*, 2752.

Abdi, F. F.; van de Krol, R. *J. Phys. Chem. C* **2012**, *116*, 9398.

Abdi, F. F.; van de Krol, R. *The Journal of Physical Chemistry C* **2012**, *116*, 9398.

Acket, G.; Volger, J. *Physica* **1966**, *32*, 1543.

Alarcon-Llado, E.; Chen, L.; Hettick, M.; Mashouf, N.; Lin, Y.; Javey, A.; Ager, J. W. *Phys. Chem. Chem. Phys.* **2014**, *16*, 1651.

Alexandre, S. S.; Artacho, E.; Soler, J. M.; Chacham, H. *Phys. Rev. Lett.* **2003**, *91*, 108105.

Anderson, A.; Savoie, R. *Canadian Journal of Chemistry* **1965**, *43*, 2271.

Artman, J.; Murphy, J.; Foner, S. *Physical Review* **1965**, *138*, A912.

Austin, I. G.; Mott, N. F. *Advances in Physics* **1969**, *18*, 41.

Baeck, S. H.; Jaramillo, T. F.; Braendli, C.; McFarland, E. W. *J. Comb. Chem.* **2002**, *4*, 563.

Baily, S. A.; Emin, D. *Phys. Rev. B* **2006**, *73*, 165211.

Bard, A. J.; Fox, M. A. *Acc. Chem. Res.* **1995**, *28*, 141.

Beg, S.; Haneef, S.; Al-Areqi, N. A. S. *Phase Transitions* **2010**, *83*, 1114.

Benjelloun, D.; Bonnet, J.; Doumerc, J.; Launay, J.; Onillon, M. *Mater. Chem. Phys.* **1988**, *20*, 1.

Benjelloun, D.; Bonnet, J.-P.; Doumerc, J.-P.; Launay, J.-C.; Onillon, M.; Hagenmuller, P. *Mater. Chem. Phys.* **1984**, *10*, 503.

Berglund, S. P.; Flaherty, D. W.; Hahn, N. T.; Bard, A. J.; Mullins, C. B. *J. Phys. Chem. C* **2011**, *115*, 3794.

Berglund, S. P.; Rettie, A. J. E.; Hoang, S.; Mullins, C. B. *Phys. Chem. Chem. Phys.* **2012**, *14*, 7065.

Besser, P.; Morrish, A.; Searle, C. *Physical Review* **1967**, *153*, 632.

Bierlein, J. D.; Sleight, A. W. *Solid State Commun.* **1975**, *16*, 69.

Bierwagen, O.; Pomraenke, R.; Eilers, S.; Masselink, W. *Physical Review B* **2004**, *70*, 165307.

Biesinger, M. C.; Lau, L. W.; Gerson, A. R.; Smart, R. S. C. *Appl. Surf. Sci.* **2010**, *257*, 887.

Biesinger, M. C.; Payne, B. P.; Grosvenor, A. P.; Lau, L. W.; Gerson, A. R.; Smart, R. S. C. *Appl. Surf. Sci.* **2011**, *257*, 2717.

Biesinger, M. C.; Payne, B. P.; Lau, L. W.; Gerson, A.; Smart, R. S. C. *Surf. Interface Anal.* **2009**, *41*, 324.
Binnewies, M.; Glaum, R.; Schmidt, M.; Schmidt, P. *Chemical vapor transport reactions*; Walter de Gruyter, 2012.
Blackman, C. S.; Parkin, I. P. *Chemistry of Materials* **2005**, *17*, 1583.
Blank, D. H.; Koster, G.; Rijnders, G. A.; van Setten, E.; Slycke, P.; Rogalla, H. *J. Cryst. Growth* **2000**, *211*, 98.
Bolton, J. R.; Strickler, S. J.; Connolly, J. S. *Nature* **1985**, *316*, 495.
Borup, K. A.; de Boor, J.; Wang, H.; Drymiotis, F.; Gascoin, F.; Shi, X.; Chen, L.; Fedorov, M. I.; Müller, E.; Iversen, B. B. *Energy & Environmental Science* **2015**, *8*, 423.
Bosman, A.; Van Daal, H. *Advances in Physics* **1970**, *19*, 1.
Brillet, J.; Yum, J.-H.; Cornuz, M.; Hisatomi, T.; Solarska, R.; Augustynski, J.; Graetzel, M.; Sivula, K. *Nature Photonics* **2012**, *6*, 824.
Cesar, I.; Sivula, K.; Kay, A.; Zboril, R.; Grätzel, M. *J. Phys. Chem. C* **2008**, *113*, 772.
Cesari, M.; Perego, G.; Zazzetta, A.; Manara, G.; Notari, B. *J. Inorg. Nucl. Chem.* **1971**, *33*, 3595.
Chatchai, P.; Murakami, Y.; Kishioka, S.-y.; Nosaka, A. Y.; Nosaka, Y. *Electrochimica Acta* **2009**, *54*, 1147.
Chemelewski, W. D.; Lee, H.-C.; Lin, J.-F.; Bard, A. J.; Mullins, C. B. *J. Am. Chem. Soc.* **2014**, *136*, 2843.
Chen, H.; Niu, Q.; MacDonald, A. *Phys. Rev. Lett.* **2014**, *112*, 017205.
Chen, L.; Alarcón-Lladó, E.; Hettick, M.; Sharp, I. D.; Lin, Y.; Javey, A.; Ager, J. W. *J. Phys. Chem. C* **2013**, *117*, 21635.
Chen, Z.; Forman, A. J.; Jaramillo, T. F. *The Journal of Physical Chemistry C* **2013**, *117*, 9713.
Chen, Z.; Jaramillo, T. F.; Deutsch, T. G.; Kleiman-Shwarsctein, A.; Forman, A. J.; Gaillard, N.; Garland, R.; Takanabe, K.; Heske, C.; Sunkara, M. *J. Mater. Res* **2010**, *25*, 3.
Chrisey, D. B.; Hubler, G. K. *Pulsed laser deposition of thin films*; 2nd ed.; Wiley-VCH: New York, NY, 2003.
Cole, B.; Marsen, B.; Miller, E.; Yan, Y.; To, B.; Jones, K.; Al-Jassim, M. *The Journal of Physical Chemistry C* **2008**, *112*, 5213.
Cornell, R. M.; Schwertmann, U. *The iron oxides: structure, properties, reactions, occurrences and uses*; John Wiley & Sons, 2003.
Curry, N.; Johnston, G.; Besser, P.; Morrish, A. *Philosophical Magazine* **1965**, *12*, 221.
Daniel, M.; Desbat, B.; Lassegues, J.; Gerand, B.; Figlarz, M. *Journal of Solid State Chemistry* **1987**, *67*, 235.
Davis, A.; Chatterjee, R. *Journal of Solution Chemistry* **1975**, *4*, 399.
De Faria, D.; Venâncio Silva, S.; De Oliveira, M. *Journal of Raman Spectroscopy* **1997**, *28*, 873.
Deskins, N. A.; Dupuis, M. *Physical Review B* **2007**, *75*, 195212.

dos Santos, C. A. M.; de Campos, A.; da Luz, M. S.; White, B. D.; Neumeier, J. J.; de Lima, B. S.; Shigue, C. Y. *Journal of Applied Physics* **2011**, *110*, 083703.
Droubay, T.; Qiao, L.; Kaspar, T. C.; Engelhard, M. H.; Shutthanandan, V.; Chambers, S. A. *Appl. Phys. Lett.* **2010**, *97*, 1241051.
Efros, A.; Shklovskii, B. *Journal of Physics C Solid State Physics* **1975**, *8*, L49.
Emin, D. *Ann. Phys.* **1971**, *64*, 336.
Emin, D. In *The Hall Effect and Its Applications*; Springer: 1980, p 281.
Emin, D. In *Wiley Encyclopedia of Electrical and Electronics Engineering*; Webster, J. G., Ed.; Wiley: New York, 2002.
Emin, D. *Monatshefte für Chemie-Chemical Monthly* **2013**, *144*, 3.
Emin, D. *Phys. Rev. B* **1993**, *48*, 13691.
Emin, D. *Phys. Rev. Lett.* **2008**, *100*, 166602.
Emin, D. *Polarons*; 1st ed.; Cambridge University Press: New York, 2013.
Emin, D.; Holstein, T. *Ann. Phys.* **1969**, *53*, 439.
Emin, D.; Seager, C.; Quinn, R. K. *Phys. Rev. Lett.* **1972**, *28*, 813.
Emin, D.; Seager, C.; Quinn, R. K. *Physical Review Letters* **1972**, *28*, 813.
Enesca, A.; Duta, A.; Schoonman, J. *Thin Solid Films* **2007**, *515*, 6371.
Farmer, V. C. *Infrared spectra of minerals*; Mineralogical society, 1974.
Finklea, H. O. *Semiconductor electrodes*; Elsevier Science Ltd, 1988.
Flanders, P. *Journal of Applied Physics* **1972**, *43*, 2430.
Flanders, P.; Remeika, J. *Philosophical Magazine* **1965**, *11*, 1271.
Frank, S. N.; Bard, A. J. *Journal of the American Chemical Society* **1975**, *97*, 7427.
Friedman, L.; Holstein, T. *Ann. Phys.* **1963**, *21*, 494.
Frost, R. L.; Henry, D. A.; Weier, M. L.; Martens, W. *Journal of Raman Spectroscopy* **2006**, *37*, 722.
Fujishima, A.; Honda, K. *Nature* **1972**, *238*, 37.
Gärtner, W. W. *Physical Review* **1959**, *116*, 84.
Gharibi, E.; Hbika, A.; Dupre, B.; Gleitzer, C. *Eur. J. Solid State Inorg. Chem.* **1990**, *27*, 647.
Goodenough, J. B. *Prog. Solid State Chem.* **1971**, *5*, 145.
Grätzel, M. *Nature* **2001**, *414*, 338.
Hahn, N. T.; Hoang, S.; Self, J. L.; Mullins, C. B. *ACS Nano* **2012**, *6*, 7712.
Hahn, N. T.; Mullins, C. B. *Chem. Mater.* **2010**, *22*, 6474.
Hahn, N. T.; Self, J. L.; Mullins, C. B. *The Journal of Physical Chemistry Letters* **2012**, *3*, 1571.
Hahn, N. T.; Ye, H.; Flaherty, D. W.; Bard, A. J.; Mullins, C. B. *ACS Nano* **2010**, *4*, 1977.
Hao, J.; Studenikin, S.; Cocivera, M. *Journal of Applied Physics* **2001**, *90*, 5064.
Hartmanova, M.; Le, M. T.; Jergel, M.; Smatko, V.; Kundracik, F. *Russ. J. Electrochem.* **2009**, *45*, 621.

He, H.; Berglund, S. P.; Rettie, A. J. E.; Chemelewski, W. D.; Xiao, P.; Zhang, Y.; Mullins, C. B. *J. Mater. Chem. A* **2014**, *2*, 9371.
Hermann, A.; Ham, J. *Review of Scientific Instruments* **1965**, *36*, 1553.
Hill, J. C.; Choi, K.-S. *The Journal of Physical Chemistry C* **2012**, *116*, 7612.
Hoffart, L.; Heider, U.; Huggins, R. A.; Witschel, W.; Jooss, R.; Lentz, A. *Ionics* **1996**, *2*, 34.
Hoffart, L.; Heider, U.; Joerissen, L.; Huggins, R. A.; Witschel, W. *Solid State Ionics* **1994**, *72*, 195.
Hoffart, L.; Heider, U.; Jorissen, L.; Huggins, R. A.; Witschel, W. *Ionics* **1995**, *1*, 131.
Holstein, T. *Annals of Physics* **1959**, *8*, 343.
Hong, S. J.; Lee, S.; Jang, J. S.; Lee, J. S. *Energy & Environmental Science* **2011**, *4*, 1781.
Hu, Y.-S.; Kleiman-Shwarsctein, A.; Forman, A. J.; Hazen, D.; Park, J.-N.; McFarland, E. W. *Chem. Mater.* **2008**, *20*, 3803.
Ihlefeld, J.; Kumar, A.; Gopalan, V.; Schlom, D.; Chen, Y.; Pan, X.; Heeg, T.; Schubert, J.; Ke, X.; Schiffer, P. *Appl. Phys. Lett.* **2007**, *91*, 0719221.
Iordanova, N.; Dupuis, M.; Rosso, K. M. *J. Chem. Phys.* **2005**, *122*, 144305.
James, B. D.; Baum, G. N.; Perez, J.; Baum, K. N. *DOE Report* **2009**.
Joly, A. G.; Williams, J. R.; Chambers, S. A.; Xiong, G.; Hess, W. P.; Laman, D. M. *Journal of Applied Physics* **2006**, *99*, 053521.
Kaneko, T.; Abe, S. *J. Phys. Soc. Jpn.* **1965**, *20*, 2001.
Katz, J. E.; Zhang, X.; Attenkofer, K.; Chapman, K. W.; Frandsen, C.; Zarzycki, P.; Rosso, K. M.; Falcone, R. W.; Waychunas, G. A.; Gilbert, B. *Science* **2012**, *337*, 1200.
Kavan, L.; Grätzel, M.; Gilbert, S. E.; Klemenz, C.; Scheel, H. J. *Journal of the American Chemical Society* **1996**, *118*, 6716.
Kazani, I.; De Mey, G.; Hertleer, C.; Banaszczyk, J.; Schwarz, A.; Guxho, G.; Van Langenhove, L. *Textile Research Journal* **2011**, *81*, 2117.
Kennedy, J. H.; Frese, K. W. *Journal of the Electrochemical Society* **1976**, *123*, 1683.
Kennedy, J. H.; Frese, K. W. *Journal of the Electrochemical Society* **1978**, *125*, 709.
Khaselev, O.; Turner, J. A. *Science* **1998**, *280*, 425.
Kim, T. W.; Choi, K.-S. *Science* **2014**, *343*, 990.
Klein, C.; Hurlbut, C. S.; Dana, J. D. *Manual of mineralogy*; Wiley New York, 1993; Vol. 527.
Kment, S.; Schmuki, P.; Hubicka, Z.; Machala, L.; Kirchgeorg, R.; Liu, N.; Wang, L.; Lee, K.; Olejnicek, J.; Cada, M. *ACS Nano* **2015**.
Koohpayeh, S.; Fort, D.; Abell, J. *Progress in Crystal Growth and Characterization of Materials* **2008**, *54*, 121.
Kronawitter, C.; Zegkinoglou, I.; Shen, S.-H.; Liao, P.; Cho, I.; Zandi, O.; Liu, Y.-S.; Lashgari, K.; Westin, G.; Guo, J.-H. *Energy & Environmental Science* **2014**, *7*, 3100.
Kweon, K. E.; Hwang, G. S.; Kim, J.; Kim, S.; Kim, S. *Phys. Chem. Chem. Phys.* **2014**, *advance online publication*.

Lago, J.; Battle, P.; Rosseinsky, M.; Coldea, A.; Singleton, J. *J. Phys. Condens. Matter* **2003**, *15*, 6817.
Launay, J.; Horowitz, G. *J. Cryst. Growth* **1982**, *57*, 118.
Lewis, N. S.; Nocera, D. G. *Proceedings of the National Academy of Sciences* **2006**, *103*, 15729
Li, R.; Zhang, F.; Wang, D.; Yang, J.; Li, M.; Zhu, J.; Zhou, X.; Han, H.; Li, C. *Nat Commun* **2013**, *4*, 1432.
Li, W.; Li, J.; Wang, X.; Chen, Q. *Applied Surface Science* **2012**, *263*, 157.
Li, Z.; Luo, W.; Zhang, M.; Feng, J.; Zou, Z. *Energy & Environmental Science* **2013**, *6*, 347.
Liang, Y.; Tsubota, T.; Mooij, L. P.; van de Krol, R. *J. Phys. Chem. C* **2011**, *115*, 17594.
Light, T. S. *Anal. Chem.* **1972**, *44*, 1038.
Lindemuth, J., A. J. Rettie, L. G. Marshall, J. Zhou, and C. B. Mullins, presented at the MRS Proceedings, 2014 (unpublished).
Lindemuth, J.; Mizuta, S.-I. In *SPIE Solar Energy + Technology*; International Society for Optics and Photonics: 2011, p 81100I.
Ling, Y.; Wang, G.; Wheeler, D. A.; Zhang, J. Z.; Li, Y. *Nano Letters* **2011**, *11*, 2119.
Liu, N.-L. H.; Emin, D. *Phys. Rev. B* **1984**, *30*, 3250.
Liu, X.; Wang, F.; Wang, Q. *Physical Chemistry Chemical Physics* **2012**, *14*, 7894.
Liu, Y.; Li, Y.; Li, W.; Han, S.; Liu, C. *Applied Surface Science* **2012**, *258*, 5038.
Liu, Z.; Yan, F. *J. Am. Ceram. Soc.* **2012**, *95*, 1944.
Look, D. C. *Electrical characterization of GaAs materials and devices*; Wiley, 1989.
Luo, W.; Li, Z.; Yu, T.; Zou, Z. *J. Phys. Chem. C* **2012**, *116*, 5076.
Luo, W.; Li, Z.; Yu, T.; Zou, Z. *The Journal of Physical Chemistry C* **2012**, *116*, 5076.
Luo, W.; Yang, Z.; Li, Z.; Zhang, J.; Liu, J.; Zhao, Z.; Wang, Z.; Yan, S.; Yu, T.; Zou, Z. *Energy & Environmental Science* **2011**, *4*, 4046.
Marusak, L. A.; Messier, R.; White, W. B. *Journal of Physics and Chemistry of Solids* **1980**, *41*, 981.
Maruthamuthu, P.; Ashokkumar, M. *Solar Energy Materials* **1988**, *17*, 433.
Massey, M.; Baier, U.; Merlin, R.; Weber, W. *Phys. Rev. B* **1990**, *41*, 7822.
Matsushima, S.; Takehara, K.; Yamane, H.; Yamada, K.; Nakamura, H.; Arai, M.; Kobayashi, K. *Journal of Physics and Chemistry of Solids* **2007**, *68*, 206.
McCloy, J. S.; Ryan, J. V.; Droubay, T.; Kaspar, T. C.; Chambers, S.; Look, D. C. *Review of Scientific Instruments* **2010**, *81*, 063902.
Mi, Q.; Coridan, R. H.; Brunschwig, B. S.; Gray, H. B.; Lewis, N. S. *Energy & Environmental Science* **2013**, *6*, 2646.
Mi, Q.; Ping, Y.; Li, Y.; Cao, B.; Brunschwig, B. S.; Khalifah, P. G.; Galli, G. A.; Gray, H. B.; Lewis, N. S. *Journal of the American Chemical Society* **2012**, *134*, 18318.
Mi, Q.; Zhanaidarova, A.; Brunschwig, B. S.; Gray, H. B.; Lewis, N. S. *Energy & Environmental Science* **2012**, *5*, 5694.

Migas, D.; Shaposhnikov, V.; Rodin, V.; Borisenko, V. *Journal of Applied Physics* **2010**, *108*, 093713.
Migita, S.; Kasai, Y.; Ota, H.; Sakai, S. *Appl. Phys. Lett.* **1997**, *71*, 3712.
Miller, D.; Biesinger, M.; McIntyre, N. *Surf. Interface Anal.* **2002**, *33*, 299.
Miller, E. L.; Paluselli, D.; Marsen, B.; Rocheleau, R. E. *Solar Energy Materials and Solar Cells* **2005**, *88*, 131.
Momma, K.; Izumi, F. *J. Appl. Crystallogr.* **2011**, *44*, 1272.
Montgomery, H. *Journal of Applied Physics* **1971**, *42*, 2971.
Morin, F. J. *Physical Review* **1951**, *83*, 1005.
Morin, F. *Physical Review* **1954**, *93*, 1195.
Morrish, A. H. *Canted antiferromagnetism: hematite*; World Scientific, 1994.
Mott, N. F.; Davis, E. A. *Electronic processes in non-crystalline materials*; 2nd ed.; OUP Oxford, 1979.
Nagaosa, N.; Sinova, J.; Onoda, S.; MacDonald, A.; Ong, N. *Reviews of Modern Physics* **2010**, *82*, 1539.
Nagels, P. In *The Hall Effect and Its Applications*; Springer: 1980, p 253.
Nah, Y.-C.; Paramasivam, I.; Hahn, R.; Shrestha, N. K.; Schmuki, P. *Nanotechnology* **2010**, *21*, 105704.
Nakau, T. *J. Phys. Soc. Japan* **1960**, *15*, 727.
Nassu, K. *American Mineralogist* **1978**, *63*, 219.
Ni, M.; Leung, M. K.; Leung, D. Y.; Sumathy, K. *Renewable and Sustainable Energy Reviews* **2007**, *11*, 401.
Oh, S. J.; Cook, D.; Townsend, H. *Hyperfine Interact.* **1998**, *112*, 59.
Ohno, T.; Akiyoshi, M.; Umebayashi, T.; Asai, K.; Mitsui, T.; Matsumura, M. *Applied Catalysis A: General* **2004**, *265*, 115.
Ovsyannikov, S. V.; Morozova, N. V.; Karkin, A. E.; Shchennikov, V. V. *Phys. Rev. B* **2012**, *86*, 205131.
Park, H. S.; Kweon, K. E.; Ye, H.; Paek, E.; Hwang, G. S.; Bard, A. J. *J. Phys. Chem. C* **2011**, *115*, 17870.
Park, Y.; McDonald, K. J.; Choi, K.-S. *Chemical Society Reviews* **2013**.
Parker, D.; Yahia, J. *Physical Review* **1968**, *169*, 605.
Paulauskas, I. E.; Jellison, G. E.; Boatner, L. A.; Brown, G. M. *International Journal of Electrochemistry* **2011**, *2011*.
Pilli, S. K.; Furtak, T. E.; Brown, L. D.; Deutsch, T. G.; Turner, J. A.; Herring, A. M. *Energy & Environmental Science* **2011**, *4*, 5028.
Pinaud, B. A.; Benck, J. D.; Seitz, L. C.; Forman, A. J.; Chen, Z.; Deutsch, T. G.; James, B. D.; Baum, K. N.; Baum, G. N.; Ardo, S. *Energy & Environmental Science* **2013**, *6*, 1983.
Pinczuk, A.; Welber, B.; Dacol, F. *Solid State Commun.* **1979**, *29*, 515.
Price, W. *Journal of Physics D: Applied Physics* **2002**, *5*, 1127.
Quinn, R. K.; Nasby, R. D.; Baughman, R. J. *Mater. Res. Bull.* **1976**, *11*, 1011.

Ransom, C. L., Montana State University, 1968.
Reece, S. Y.; Hamel, J. A.; Sung, K.; Jarvi, T. D.; Esswein, A. J.; Pijpers, J. J.; Nocera, D. G. *Science* **2011**, *334*, 645.
Rettie, A. J. E.; Lee, H. C.; Marshall, L. G.; Lin, J.-F.; Capan, C.; Lindemuth, J.; McCloy, J. S.; Zhou, J.; Bard, A. J.; Mullins, C. B. *J. Am. Chem. Soc.* **2013**, *135*, 11389.
Rosso, K. M.; Smith, D. M.; Dupuis, M. *The Journal of chemical physics* **2003**, *118*, 6455.
Salje, E. *Acta Crystallographica Section A: Crystal Physics, Diffraction, Theoretical and General Crystallography* **1975**, *31*, 360.
Sanchez, C.; Hendewerk, M.; Sieber, K.; Somorjai, G. *J. Solid State Chem.* **1986**, *61*, 47.
Sanchez, C.; Sieber, K.; Somorjai, G. *Journal of electroanalytical chemistry and interfacial electrochemistry* **1988**, *252*, 269.
Santato, C.; Ulmann, M.; Augustynski, J. *The Journal of Physical Chemistry B* **2001**, *105*, 936.
Sayama, K.; Nomura, A.; Arai, T.; Sugita, T.; Abe, R.; Yanagida, M.; Oi, T.; Iwasaki, Y.; Abe, Y.; Sugihara, H. *J. Phys. Chem. B* **2006**, *110*, 11352.
Sayer, M.; Mansingh, A. *J. Non-Cryst. Solids* **1983**, *58*, 91.
Schlom, D. G.; Chen, L.-Q.; Fennie, C. J.; Gopalan, V.; Muller, D. A.; Pan, X.; Ramesh, R.; Uecker, R. *MRS Bull.* **2014**, *39*, 118.
Seabold, J. A.; Choi, K.-S. *J. Am. Chem. Soc.* **2012**, *134*, 2186.
Seabold, J. A.; Zhu, K.; Neale, N. R. *Phys. Chem. Chem. Phys.* **2014**, *16*, 1121.
Searle, C.; Morrish, A. *Journal of Applied Physics* **1966**, *37*, 1141.
Searle, C.; Wang, S. *Journal of Applied Physics* **1968**, *39*, 1025.
Seitz, L. C.; Chen, Z.; Forman, A. J.; Pinaud, B. A.; Benck, J. D.; Jaramillo, T. F. *ChemSusChem* **2014**, *7*, 1372.
Shannon, R. *Acta Crystallographica Section A: Crystal Physics, Diffraction, Theoretical and General Crystallography* **1976**, *32*, 751.
Shchennikov, V. V.; Ovsyannikov, S. V.; Karkin, A. E.; Todo, S.; Uwatoko, Y. *Solid State Commun.* **2009**, *149*, 759.
Shim, S.-H.; Duffy, T. S. *American Mineralogist* **2002**, *87*, 318.
Shull, C. G.; Strauser, W. A.; Wollan, E. O. *Physical Review* **1951**, *83*, 333.
Silversmit, G.; Depla, D.; Poelman, H.; Marin, G. B.; De Gryse, R. *J. Electron. Spectrosc. Relat. Phenom.* **2004**, *135*, 167.
Sivula, K. *J. Phys. Chem. Lett.* **2013**, *4*, 1624.
Sivula, K.; Formal, F. L.; Grätzel, M. *Chemistry of Materials* **2009**, *21*, 2862.
Sivula, K.; Le Formal, F.; Grätzel, M. *ChemSusChem* **2011**, *4*, 432.
Sleight, A. W.; Aykan, K.; Rogers, D. B. *J. Solid State Chem.* **1975**, *13*, 231.
Sleight, A. W.; Chen, H. Y.; Ferretti, A.; Cox, D. E. *Mater. Res. Bull.* **1979**, *14*, 1571.
Solarska, R.; Alexander, B. D.; Braun, A.; Jurczakowski, R.; Fortunato, G.; Stiefel, M.;

Graule, T.; Augustynski, J. *Electrochimica Acta* **2010**, *55*, 7780.
Solarska, R.; Jurczakowski, R.; Augustynski, J. *Nanoscale* **2012**, *4*, 1553.
Stoughton, S.; Showak, M.; Mao, Q.; Koirala, P.; Hillsberry, D.; Sallis, S.; Kourkoutis, L.; Nguyen, K.; Piper, L.; Tenne, D. *Appl. Phys. Lett. Mater.* **2013**, *1*, 0421121.
Streetman, B. G.; Banerjee, S. *Solid state electronic devices*; 6th ed.; Prentice Hall New Jersey, 2006.
Su, J.; Guo, L.; Bao, N.; Grimes, C. A. *Nano Letters* **2011**, *11*, 1928.
Sun, Y.; Murphy, C. J.; Reyes-Gil, K. R.; Reyes-Garcia, E. A.; Thornton, J. M.; Morris, N. A.; Raftery, D. *International Journal of Hydrogen Energy* **2009**, *34*, 8476.
Swanson, H. E. C.-M., M.; Evans, E. H.; Ulmer, L. *National Bureau of Standards Circular 539* **1955**, *5*, 26.
Theis, C.; Yeh, J.; Schlom, D.; Hawley, M.; Brown, G.; Jiang, J.; Pan, X. *Appl. Phys. Lett.* **1998**, *72*, 2817.
Tojo, S.; Tachikawa, T.; Fujitsuka, M.; Majima, T. *The Journal of Physical Chemistry C* **2008**, *112*, 14948.
Tokunaga, S.; Kato, H.; Kudo, A. *Chem. Mater.* **2001**, *13*, 4624.
Trassin, M.; Viart, N.; Versini, G.; Loison, J.-L.; Vola, J.-P.; Schmerber, G.; Cregut, O.; Barre, S.; Pourroy, G.; Lee, J. *Appl. Phys. Lett.* **2007**, *91*, 2025041.
Tsipis, E. V.; Patrakeev, M. V.; Kharton, V. V.; Vyshatko, N. P.; Frade, J. R. *J. Mater. Chem.* **2002**, *12*, 3738.
Umebayashi, T.; Yamaki, T.; Itoh, H.; Asai, K. *Applied Physics Letters* **2002**, *81*, 454.
van de Krol, R.; Grätzel, M. *Photoelectrochemical Hydrogen Production*, 2012
Van der Pauw, L. *Philips Technical Review* **1958**, *20*, 220.
Vandenabeele, P. *Practical Raman Spectroscopy: An Introduction*; John Wiley & Sons, 2013.
Vasylechko, L.; Senyshyn, A.; Bismayer, U. In *Handbook on the Physics and Chemistry of Rare Earths*; North Holland: Amsterdam, 2009; Vol. 39, p 113.
Venkateshvaran, D.; Nikolka, M.; Sadhanala, A.; Lemaur, V.; Zelazny, M.; Kepa, M.; Hurhangee, M.; Kronemeijer, A. J.; Pecunia, V.; Nasrallah, I.; Romanov, I.; Broch, K.; McCulloch, I.; Emin, D.; Olivier, Y.; Cornil, J.; Beljonne, D.; Sirringhaus, H. *Nature* **2014**, *advance online publication*.
Vinke, I. C.; Diepgrond, J.; Boukamp, B. A.; De, V. K. J.; Burggraaf, A. J. *Solid State Ionics* **1992**, *57*, 83.
Vlasov, K.; Rozenberg, E. *SOV. PHYS. SOL. ST.* **1980**, *22*, 967.
Vogt, T.; Woodward, P. M.; Hunter, B. A. *Journal of Solid State Chemistry* **1999**, *144*, 209.
Voskanyan, R.; Levitin, R.; Shchurov, V. *Soviet Physics JETP* **1968**, *26*.
Walsh, A.; Yan, Y.; Huda, M. N.; Al-Jassim, M. M.; Wei, S.-H. *Chem. Mater.* **2009**, *21*, 547.
Walter, M. G.; Warren, E. L.; McKone, J. R.; Boettcher, S. W.; Mi, Q.; Santori, E. A.; Lewis, N. S. *Chemical Reviews* **2010**, *110*, 6446.
Wang, F.; Di Valentin, C.; Pacchioni, G. *The Journal of Physical Chemistry C* **2012**,

*116*, 8901.
Wang, G.; Ling, Y.; Lu, X.; Qian, F.; Tong, Y.; Zhang, J. Z.; Lordi, V.; Rocha Leao, C.; Li, Y. *The Journal of Physical Chemistry C* **2013**, *117*, 10957.
Weber, M. F.; Dignam, M. *International Journal of Hydrogen Energy* **1986**, *11*, 225.
Wojdyr, M. *Journal of Applied Crystallography* **2010**, *43*, 1126.
Ye, H.; Park, H. S.; Bard, A. J. *The Journal of Physical Chemistry C* **2011**.
Yildiz, A.; Lisesivdin, S.; Kasap, M.; Mardare, D. *Physica B: Condensed Matter* **2009**, *404*, 1423
Yin, W.-J.; Wei, S.-H.; Al-Jassim, M. M.; Turner, J.; Yan, Y. *Phys. Rev. B* **2011**, *83*, 1551021.
Yin, W.-J.; Wei, S.-H.; Al-Jassim, M. M.; Turner, J.; Yan, Y. *Physical Review B* **2011**, *83*, 155102.
Yoo, K.-H.; Ha, D.; Lee, J.-O.; Park, J.; Kim, J.; Kim, J.; Lee, H.-Y.; Kawai, T.; Choi, H. Y. *Phys. Rev. Lett.* **2001**, *87*, 198102.
Yous, B.; Robin, S.; Donnadieu, A.; Dufour, G.; Maillot, C.; Roulet, H.; Senemaud, C. *Materials Research Bulletin* **1984**, *19*, 1349.
Yu, J. C.; Ho, W.; Yu, J.; Yip, H.; Wong, P. K.; Zhao, J. *Environmental Science & Technology* **2005**, *39*, 1175.
Zabinski, J.; Donley, M.; Prasad, S.; McDevitt, N. *Journal of Materials Science* **1994**, *29*, 4834.
Zhang, H. M.; Liu, J. B.; Wang, H.; Zhang, W. X.; Yan, H. *Journal of Nanoparticle Research* **2008**, *10*, 767.
Zhao, B.; Kaspar, T. C.; Droubay, T. C.; McCloy, J.; Bowden, M. E.; Shutthanandan, V.; Heald, S. M.; Chambers, S. A. *Phys. Rev. B* **2011**, *84*, 245325/1
Zheng, H.; Tachibana, Y.; Kalantar-zadeh, K. *Langmuir* **2010**, *26*, 19148.
Zhong, D. K.; Choi, S.; Gamelin, D. R. *J. Am. Chem. Soc.* **2011**, *133*, 18370.
Zhou, M.; Bao, J.; Bi, W.; Zeng, Y.; Zhu, R.; Tao, M.; Xie, Y. *ChemSusChem* **2012**, *5*, 1420.

# Vita

Alexander J. E. Rettie was born in Seattle, WA on June 8th, 1987 to Scottish parents, Allan and Annette. H has one brother, Stephen. He attended Hilltop Elementary School near Seattle before moving to Scotland, U.K. and attending Thurso High School until 2005. He then enrolled at the University of Edinburgh, graduating in 2009 with an integrated B.Eng/M.Eng. in Chemical Engineering. During his undergraduate studies he did internships at UKAEA Dounreay and Invista in Middlesborough, England. Before starting his Ph.D. in Chemical Engineering at the University of Texas at Austin in 2010 with Prof. C. Buddie Mullins, he worked in Prof. Albert Folch's lab at the University of Washington. He holds both U.S. and U.K. nationalities.

Email address: alex.rettie@gmail.com

This dissertation was typed by the author.